OPTICAL EMISSION SPECTROSCOPY AS A TOOL FOR MONITORING COLD ATMOSPHERIC PRESSURE PLASMA PROCESSES

Andrea Jurov

Doctoral Dissertation
Jožef Stefan International Postgraduate School
Ljubljana, Slovenia

Supervisor: Prof. Dr. Uroš Cvelbar, Jožef Stefan International Postgraduate School and Jožef Stefan Institute, Ljubljana, Slovenia
Co-Supervisor: Dr. Nataša Hojnik, Jožef Stefan Institute, Ljubljana, Slovenia

Evaluation Board:
Prof. Dr. Aleksander Zidanšek, Chair, Jožef Stefan International Postgraduate School and Jožef Stefan Institute, Ljubljana, Slovenia
Prof. Dr. Eva Kovačević, Member, Université d'Orléans, Orléans, France
Prof. Dr. Ana Sobota, Member, Technische Universiteit Eindhoven, Eindhoven, Netherlands

MEDNARODNA PODIPLOMSKA ŠOLA JOŽEFA STEFANA
JOŽEF STEFAN INTERNATIONAL POSTGRADUATE SCHOOL

Andrea Jurov

OPTICAL EMISSION SPECTROSCOPY AS A TOOL FOR MONITORING COLD ATMOSPHERIC PRESSURE PLASMA PROCESSES

Doctoral Dissertation

OPTIČNA EMISIJSKA SPEKTROSKOPIJA KOT ORODJE ZA SPREMLJANJE PROCESOV HLADNE PLAZME PRI ATMOSFERSKEM TLAKU

Doktorska disertacija

Supervisor: Prof. Dr. Uroš Cvelbar

Co-Supervisor: Dr. Nataša Hojnik

Ljubljana, Slovenia, November 2021

In memory of Bela, my companion.

Acknowledgments

First and foremost, I would like to thank my supervisor, Prof. Dr. Uroš Cvelbar for giving me the opportunity to work with him and our colleagues. He encouraged me to develop as a researcher and a person by giving me countless opportunities to travel and collaborate with many of our partners. I honestly appreciate everything he has done for me in the past five years. Second, I have to thank my co-supervisor Dr. Nataša Hojnik for always being the shoulder to cry on and an inexhaustible source of memes that helped my mental stability. Next, I am profoundly grateful to every member of the F6 team for all the scientific discussions, lunch breaks, beers and everything that made my days easier and more fun. Thanks to Dr. Gregor Filipič for always suggesting we burn something or throw it through the window, to Dr. Janez Zavašnik for the most amusing stories, and especially to my fellow students, our PhD support group – Aswathy, Jaka, Neel, Martin and Petra.

I would also like to express my gratitude to colleagues I met on this journey that I am always happy to see and collaborate with – Dr. Nikola Škoro, Dr. Špela Kos and Dr. Anton Nikiforov. I am grateful for the opportunity to work with you and learn from your expertise.

Special thanks go to my lovely friend Ivana Sremački who I am most grateful to have met. It is an amazing feeling when you meet someone as nice as you, who understands your position and is such a great host, and most importantly, is always up for going on an adventure.

I would also like to express my gratitude to people I had met before my PhD, who helped me get to this point in my life – Dr. Nikša Krstulović and Dr. Dean Popović. Both of you made me fall in love with what I do and pushed me to pursue my goals.

I cannot forget the first ladies who were there for me when I moved to Ljubljana – Tifa and Fadila. Both of them fed me their perfect Bosnian specialities and were always up for a conversation. Fadila was both a friend and a mother that I needed at the time, and I appreciate it more than she knows.

I want to thank all my friends who have been there for me – Sonja, Sanja, Nika, Šime, Ana Marija, Nevena, Ivan, Marin, Nina, Željka and Anja. Thanks for all the conversations, drinks, trips, parties, food and games!

I want to express my indescribable gratitude to my family, especially my parents Aida and Davor. I am not sure how they find the will to comfort me again and again, but I am grateful. I also have to thank my grandparents Neda and Tonko for feeding me all the nice fish.

In the end, I have to thank the love of my life Neven who is always there for me. He always makes me feel better, even when he doesn't know what to say. In the end, he helped me stay sane and finished sentences when my brain wasn't cooperating. He even noticed he was the only one I missed to include in this list!

Abstract

Non-equilibrium atmospheric pressure plasmas are used in many areas, such as food and agriculture, plasma medicine, plasma surface modification, material synthesis and deposition. Because of their versatility, many plasma setups have been developed. Of greater interest are those that operate at atmospheric pressure, like atmospheric pressure plasma jets (APPJs). Regarding applications, there are two main advantages of this type of plasma – simplicity and availability that comes with operation at atmospheric pressure, and low operating temperature that enables treatments of temperature-sensitive materials and substrates. Versatility and wide application of APPJs make detailed and standardized diagnostics a necessity.

This dissertation tries to prove that optical emission spectroscopy is an efficient method for observing plasma properties generated within inert gases of argon and helium, and can provide all necessary data on plasma parameters and conditions. Consequently, optical emission spectroscopy enables *in situ* monitoring to understand physical and chemical processes occurring on surfaces, during synthesis or deposition. Therefore, the goal of the dissertation is to follow and investigate two objectives: (i) tracking APPJ surface modifications by optical emission spectroscopy for improved functionalization of nanomaterial surfaces or nanoparticles in colloidal solutions, and (ii) monitoring treatment of biological substrates with optical emission spectroscopy for the safe APPJ treatment of skin, decontamination of surfaces and removal of bacteria, as well as mitigations of plasma damages on cells relevant to clinical practice.

In order to test the hypothesis, the research is based on three steps – setting up a plasma system, implementing plasma diagnostic tools and monitoring different changes in materials, either biological responses or chemical and morphological change. The used plasma setups are APPJs with different power sources, either operating in radio frequency or kHz regimes, with a possibility of aerosol injection. Implementation of plasma diagnostic tools means that gas-phase diagnostics are combined with electrical characterization of the power source. Optical diagnostics consist of optical emission spectroscopy, spatial and time-resolved, and fast intensified charged coupled device imaging of the plasma streamer. Electrical characterization and power measurements are performed by HV probes and current monitoring. Lastly, to uncover plasma properties indirectly, we look at different analyses and responses of substrates based on chemical (liquid chemistry), morphological (scanning electron microscopy, transmission electron microscopy, atomic force microscopy, X-ray photoelectron spectroscopy, ultraviolet–visible spectroscopy, Fourier-transform infrared spectroscopy) and biological analysis (cell viability tests, determination of viable bacteria after the plasma treatment, fluorescence microscopy for evaluation of skin damage and infrared imaging of the mouse skin surface).

The results support our hypothesis – optical emission spectroscopy is a great multipurpose tool for monitoring and tracking atmospheric pressure plasma processes in jets and changes when accompanied with appropriate and detailed substrate analysis. If we want to gain even more, other diagnostic techniques should be added to the research. However, the optical emission spectroscopy will be a future cornerstone sensor for monitoring and controling the atmospheric pressure plasma processes initiated by jets in either nanofabrication or treatments of biological materials.

Povzetek

Uporaba ne-ravnovesnih atmosferskih plazem zajema številna področja, kot so npr. plazemska medicina, prehrana in kmetijstvo, plazemska obdelava površin ter sinteza materialov in nanos nanomaterialov. Zaradi raznovrstnosti plazem, je bilo do sedaj razvitih mnogo plazemskih sistemov. Pri tem nas najbolj zanimajo atmosferske plazme, kot so atmosferski plazemski curki. Prednosti tovrstnih plazemskih sistemov pri uporabi v različnih aplikacijah sta predvsem njihova preprostost in razpoložljivost, ki sta posledici uporabe plazem pri atmosferskem tlaku in nizki delovni temperaturi, kar omogoča obdelavo termično nestabilnih materialov in substratov. Zaradi raznovrstnosti in mnogih aplikacij atmosferskih plazemskih curkov, je nujna njihova podrobna in standardizirana diagnostika.

Namen te disertacije je dokaz da je optična emisijska spektroskopija učinkovita metoda za opazovanje lastnosti argonovih in helijevih plazem in lahko priskrbi vse potrebne podatke o plazemskih parametrih in pogojih. Prav tako omogoča optična emisijska spektroskopija *in situ* spremljanje fizikalnih in kemijskih procesov, ki se dogajajo na površinah ob plazemskih sintezah ali nanosih. Cilj disertacije je torej raziskovanje dveh področij: (i) opazovanje površinskih sprememb z optično emisijsko spektroskopijo za izboljšavo površinske funkcionalizacije nanomaterialov ali nanodelcev v koloidnih raztopinah, in (ii) monitoring plazemske obdelave bioloških substratov z optično emisijsko spektroskopijo za varno obdelavo kože z atmosferskim plazemskim curkom, dekontaminacijo površin in odstranjevanje bakterij, kot tudi ublažitev plazemskih poškodb na celicah, pomembnih za klinično delo.

Za preizkus hipotez, je raziskava razdeljena na tri korake – postavitev plazemskega sistema, implementacija plazemskih diagnostičnih orodij in spremljanje različnih sprememb v materialih – bodisi bioloških odzivov, bodisi kemijskih in morfoloških sprememb. Uporabljeni plazemski sistemi generirajo atmosferske plazemske curke z možnostjo injiciranja aerosola, generirani z različnimi viri napetosti, ki delujejo v radiofrekvenčnem ali kHz razponu. Implementacija plazemsko diagnostičnih orodij se nanaša na kombinacijo diagnostike plinske faze z električno karakterizacijo vira napetosti. Optična diagnostika sestoji iz prostorsko in časovno ločljive optične emisijske spektroskopije ter karakterizacije plazemskih curkov s CCD napravami. Električna karakterizacija in meritve moči so izvedeni z visokonapetostnimi sondami in tokovnim monitoringom. Nazadnje je za indirektno odkrivanje plazemskih lastnosti, pridobljen vpogled v različne analize in odzive substratov, ki temelji na kemijski (tekoča kemija), morfološki (vrstična elektronska mikroskopija, presevna elektronska mikroskopija, mikroskopija na atomsko silo, rentgenska fotoelektronska spektroskopija, UV-VIS spektroskopija, Fourier-transformirana infrardeča spektroskopija) in biološki analizi (testi celične viabilnosti, določanje viabilnih bakterij po plazemski obdelavi, fluorescenčna mikroskopija za evaluacijo kožnih poškodb in infrardeče slikanje površine mišje kože).

Rezultati podpirajo naše hipoteze – optična emisijska spektroskopija je odlično večnamensko orodje za spremljanje in preučevanje procesov in sprememb v atmosferskih plazemskih curkih, če ga spremlja primerna in podrobna analiza substrata. Za pridobitev več informacij, bi bilo potrebno raziskavi dodati še druge diagnostične tehnike. Kljub temu pa bo v prihodnosti optična emisijska spektroskopija temeljni senzor za zaznavanje in nadzor procesov v atmosferskih plazmah bodisi pri izdelavi nanomaterialov ali plazemski obdelavi bioloških materialov.

Contents

List of Figures

Abbreviations

2D	...	Two-Dimensional
AC	...	Alternating Current
AFM	...	Atomic Force Microscopy
APPJ	...	Atmospheric Pressure Plasma Jet
Ar	...	Argon
AuNP	...	Gold Nanoparticle
CNT	...	Carbon Nanotube
CRM	...	Collisional-Radiative Model
DBD	...	Dielectric Barrier Discharge
DC	...	Direct Current
DFE	...	Dielectric-Free Electrode
FTIR	...	Fourier-Transform Infrared Spectroscopy
H_2O_2	...	Hydrogen Peroxide
He	...	Helium
ICCD	...	Intensified Charged Coupled Device
LAL	...	Laser Ablation in Liquids
LIF	...	Laser Induced Fluorescence
MEM	...	Minimal Essential Medium
MWCNTs	...	Multi-Walled Carbon Nanotubes
N_2	...	Nitrogen
NO_2	...	Nitrogen Dioxide
NPs	...	Nanoparticles
O_2	...	Oxygen
OES	...	Optical Emission Spectroscopy
OH	...	Hydroxyl Group
PVC	...	Polyvinyl Chloride
RF	...	Radio Frequency
RNS	...	Reactive Nitrogen Species
ROS	...	Reactive Oxygen Species
SE	...	Single Electrode
SEM	...	Scanning Electron Microscopy
TEM	...	Transmission Electron Microscopy
UV–Vis	...	Ultraviolet–Visible Spectroscopy
XPS	...	X-Ray Photoelectron Spectroscopy

Chapter 1

Introduction

1.1 Atmospheric Pressure Non-Equilibrium Plasma

Plasma is the fourth state of matter, after solid, liquid and gas, and the most abundant form of matter in the universe. When a substantial amount of energy is delivered to a gas, electrons start to escape atoms and molecules and produce even more electrons and ions by collisions induced by a growing electric field. Energy needed for such ionization can come through different mechanisms, such as applying high temperatures or electrical discharges to the gas. Finally, when the number of collisions is high enough that the time between electron–neutral collisions is large compared to the characteristic time during which the physical plasma parameters are changing, the electrical properties of gas change and it becomes an ionized gas or plasma [1], [2].

Even though plasmas exist mostly in intergalactic regions, such as stars and the intracluster medium of galaxy clusters, they can be generated in the laboratory under different conditions, for instance using different pressures. In the early days of plasma technology, low-pressure plasmas were more common than plasmas induced at atmospheric pressure because they were easier to ignite and maintain [3]. Soon, it became obvious that atmospheric pressure plasmas have some advantages compared to low-pressure plasmas, which, from a practical point of view, is most evident in the lack of expensive and complicated vacuum systems [1], [4].

Aside from pressure, temperature – which represents the mean translational energy of plasma species – is another defining plasma parameter. When using electrical discharge to ignite plasma, if the generated electric field is strong enough, electrons obtain more energy from the electric field than they lose in collision with heavier neutral particles. This enables electrons to accelerate, resulting in an avalanche that finally induces the breakdown of the gas. However, the number of electron–neutral collisions is high and energy is transferred from fast accelerated electrons to heavy neutral particles. In this case, when the electron temperature is similar to the neutral particle temperature, the plasma is classified as equilibrium plasma [1], [5]. However, in laboratory conditions at atmospheric pressure, it is possible to induce a different kind of plasma – non-equilibrium or cold plasma. As the name suggests, a non-equilibrium plasma is a gas discharge where plasma species, electrons and heavy particles, do not have the same temperature. The mean kinetic energy of electrons, electron temperature, is higher than the gas temperature ($T_e \gg T_g$). This is possible because energy transfer is much faster from the induced electric field to electrons than energy transferred in collisions of electrons and heavy particles due to their large mass difference. For a plasma sustained in an atomic gas, such as noble gases used in this dissertation, the gas temperature T_g can be estimated by the previously mentioned energy transfer relation between electric field, electrons and heavy particles as:

$$T_g = T_e\left(1 - \frac{m_g}{4m_e}\frac{(\lambda_e e E)^2}{\varepsilon_e^2}\right) \tag{1}$$

where m_g is the heavy particle mass, m_e the electron mass, ε_e the electron energy, e the elementary charge and λ_e the electron mean free path [6]. This equation shows that keeping low gas temperature can be challenging with increasing pressure, which is evident in atmospheric pressure plasma systems like arcs. However, there are numerous methods to minimize gas heating that include the use of noble gases, different gas flows, reduced plasma size and more [6].

Non-equilibrium plasmas at atmospheric pressure have a wide application range in many fields that are focused on temperature sensitive materials, like agriculture and the food industry [7]–[13], material synthesis and deposition [5], [14]–[19], and especially plasma medicine [20]–[26]. In order to be used in such a variety of areas, atmospheric pressure non-equilibrium plasmas come in many forms, some of which are shown in Figure 1.

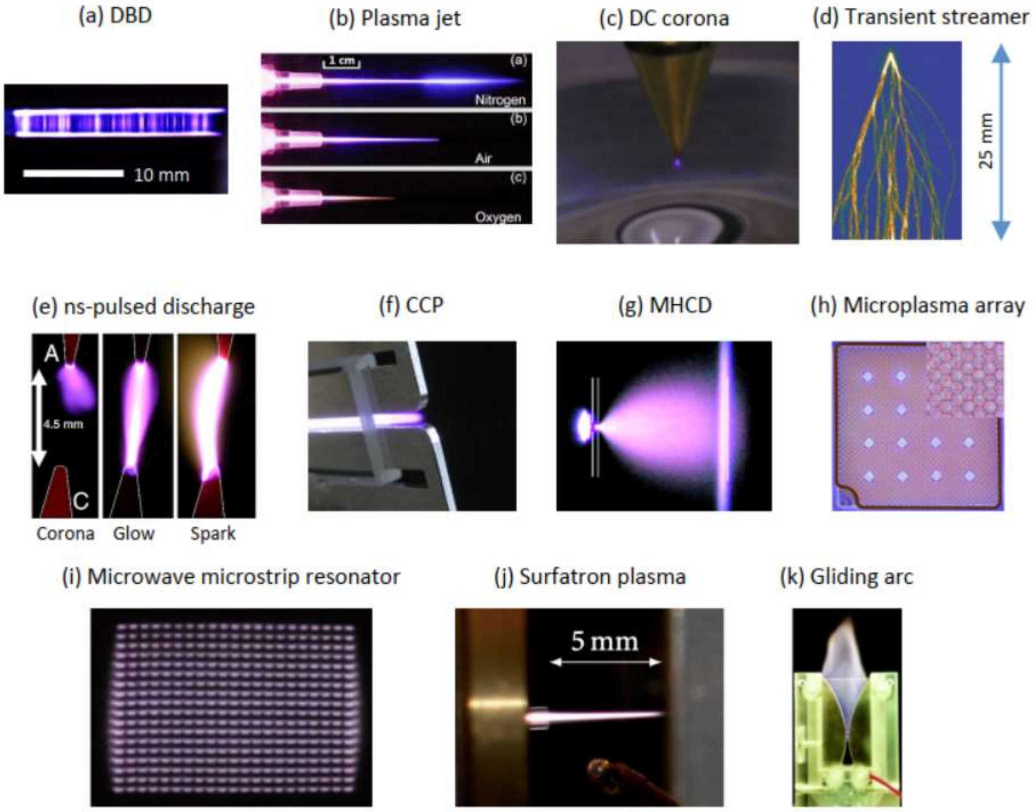

Figure 1: Examples of atmospheric pressure non-equilibrium plasmas from [6].

1.1.1 Atmospheric pressure plasma jets

Plasmas are generated when an applied electric field is strong enough to initiate a breakdown over a discharge gap. At atmospheric pressure, that electric field needs to be quite high so the discharge gaps are usually small – from a mm to a few cm. To increase the size limit of treated objects, plasmas confined between electrodes are replaced by plasmas generated in open space – plasma jets. There are two main challenges that hinder the generation of non-equilibrium atmospheric pressure plasma jets (APPJs) – high electron/heavy particle collision frequency and low applied electric field [1]. These challenges can be overcome with different designs and power supplies. Most jets use noble gases with the possible addition of small amounts of reactive gases, such as oxygen (O_2) or nitrogen (N_2). Based on their design, non-thermal plasma jets are divided into dielectric-free electrode (DFE) jets, dielectric barrier discharge (DBD) jets, DBD-like jets and single-electrode (SE) jets, as in [1], [27]. A schematic representation of most jet configurations is presented in Figure 2–5. APPJs can also be classified by excitation frequencies into direct current (DC) plasma jets, pulsed-DC plasma jets, kHz-operated plasma jets, radio frequency (RF)-operated plasma jets and microwave-driven plasma jets [3].

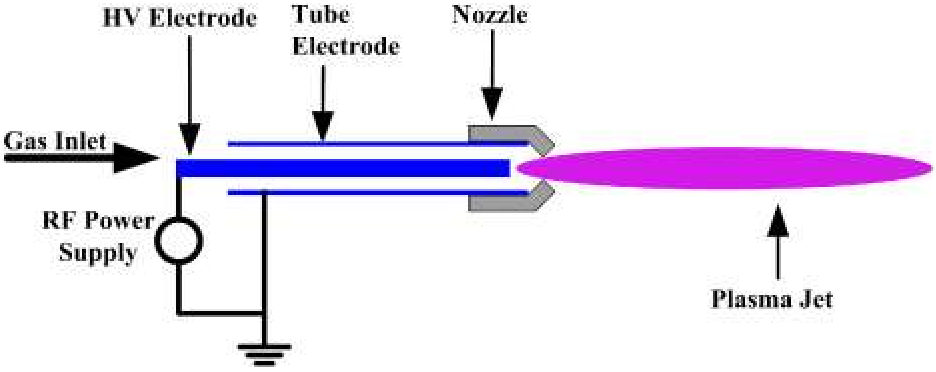

Figure 2: Schematic representation of DFE jets from [27].

DFE jets, powered by a radio frequency (RF) source, have one inner electrode coupled to that source and a grounded outer electrode [17], [28]. The setup has to be cooled down by water so as not to overheat, and the gas temperature goes from 50°C to 300°C. The gas temperature is quite high because of the high power delivered to plasma, which reduces possible applications in biomedicine. The upside of this setup is the resultant highly reactive plasma and its suitability for material processing, as long as the materials are not temperature sensitive.

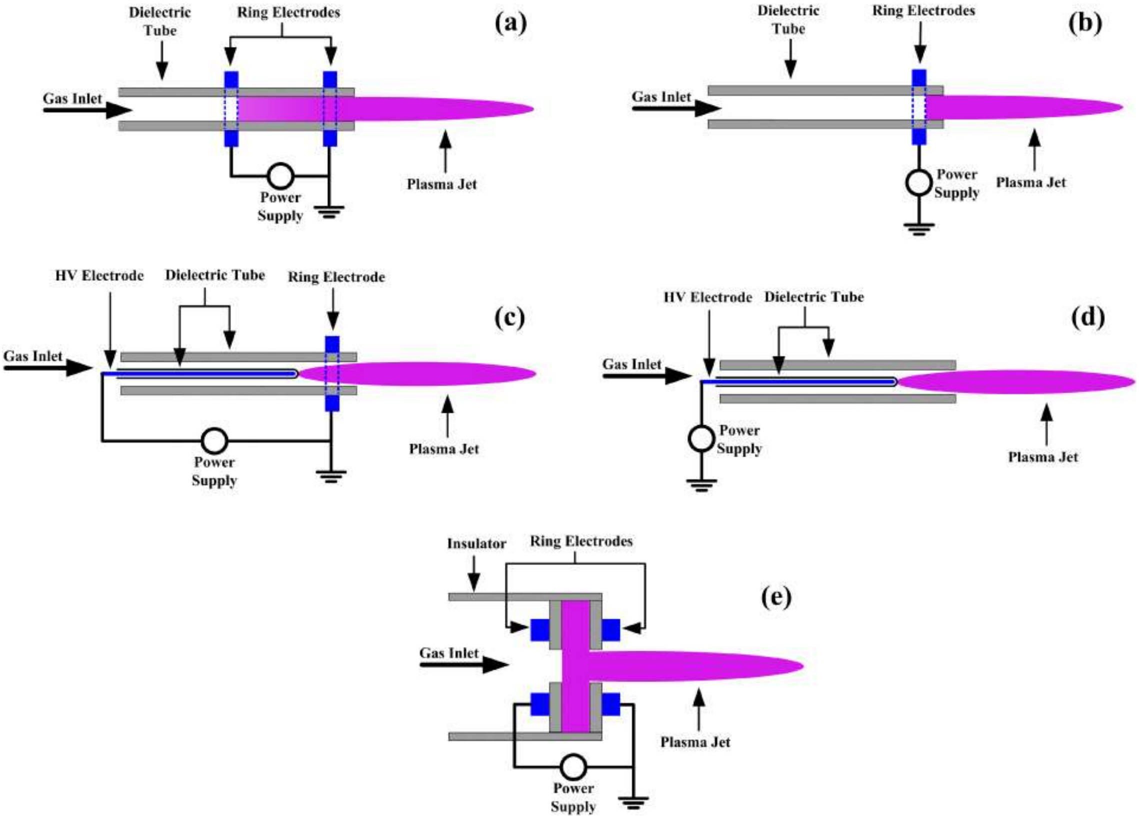

Figure 3: Schematic representation of different DBD jets: (a) with two external ring electrodes; (b) with a single ring electrode; (c) with an axial pin electrode and an external ring electrode; (d) with a single axial pin electrode; and (e) with two annular ring electrodes on centrally perforated dielectric disks from [27].

DBD jets have many different configurations, but common to all is that every jet has an electrode that is not in direct contact with the gas flow but is separated with a dielectric (usually a glass tube) [29]–[31]. All DBD jets can be operated by pulsed DC or kHz alternating current (AC) power supply. Gas temperature remains low and the plasma plume can have lengths of several cm, sometimes over 10 cm, which makes them perfect candidates for applications in plasma medicine [32].

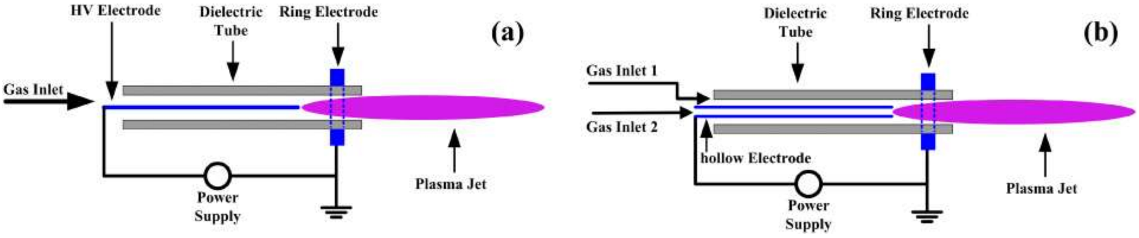

Figure 4: Schematic representation of DBD-like plasma jets: (a) with an axial pin electrode and an external ring electrode; (b) with a hollow tube electrode, an external ring electrode and two gas inlets from [27].

DBD-like jets are quite similar to DBD jets when they are treating a non-conductive material [33]. However, when the plasma plume makes contact with a conductor, the discharge starts running between a high-voltage electrode and a conductive substrate and the jet changes properties. DBD-like jets can be operated by kHz AC, pulsed DC or RF power sources [34]. Their configuration makes them useful in treating conductive materials when there is a need for more power delivered to the substrate. However, when treating biological samples, such as cells or tissue, there is a possibility of arcing.

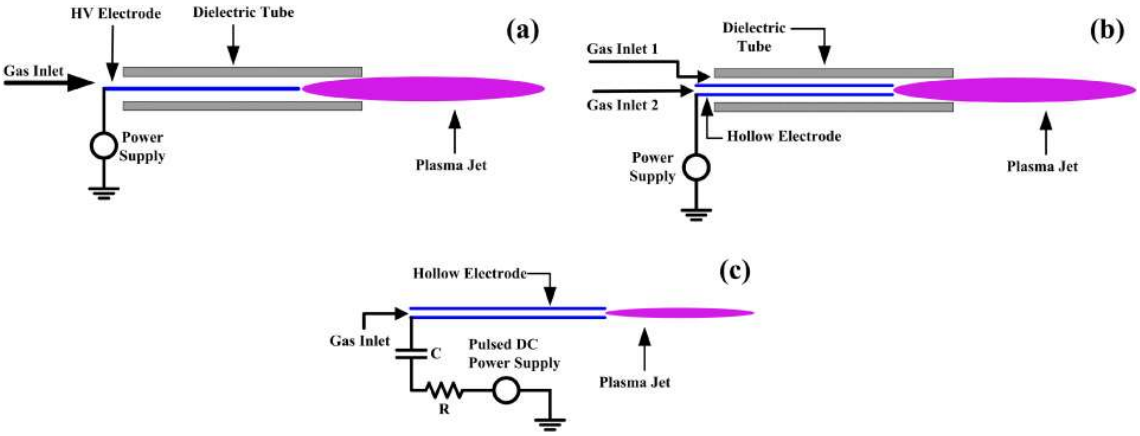

Figure 5: Schematic representation of SE plasma jets: (a) with an axial pin electrode inside a dielectric tube; (b) with one hollow tube electrode from [27].

In this thesis SE jets were used, paired with different power sources, mostly operated in the kHz region. SE jets have one electrode inside a glass tube that guides the gas flow, and there is no ground electrode. These jets have a similar disadvantage to DFE and DBD-like jets: there is a possibility of arcing between plasma and the treated substrate. Nonetheless, there are many different setups of SE jets that can overcome this danger. The biggest advantage of SE jets is low gas temperature and the possibility of safely touching the plasma plume, making them a good candidate for applications in plasma medicine [21], [22].

1.2 Plasma Diagnostics and Spectroscopy

Plasma consist of many species, such as atoms, molecules and their ions. Every plasma emits and absorbs electromagnetic radiation in a wide wavelength range, but there are some limitations for spectroscopy. Below 200 nm, the air starts to absorb electromagnetic radiation. To avoid this absorption, the diagnostic system requires an evacuated light path, which complicates diagnostics drastically. Above 1000 nm, the thermal background noise becomes too high for common spectrometers to distinguish from the real plasma spectrum, and it can only be compensated with expensive detection equipment [35], [36]. For those reasons, optical plasma diagnostics is usually conducted in the spectral region between 200 nm to 1000 nm.

Plasma spectroscopy detects plasma radiation. There are three different contributions to overall plasma radiation – bremsstrahlung, recombination radiation and line radiation. Bremsstrahlung and recombination radiation are detected as continuum radiations. They occur when electrons are deflected in the energy field of ions and when electrons recombine with ions, respectively. In contrast, line radiation corresponds to transitions of electrons between levels of atoms, ions and molecules (at low temperatures) [36]. A possible representation of plasma radiation is presented in Figure 6: Simulated spectrum representing plasma radiation – dense hydrogen plasma of $k_B T_e = 10\ eV$ with impurities, $n_e = 10^{19} cm^{-3}$, thickness 1 mm [36], where a simulated spectrum of a dense hydrogen plasma is shown, with contributions from bremsstrahlung, recombination and line radiation, alongside a blackbody limit.

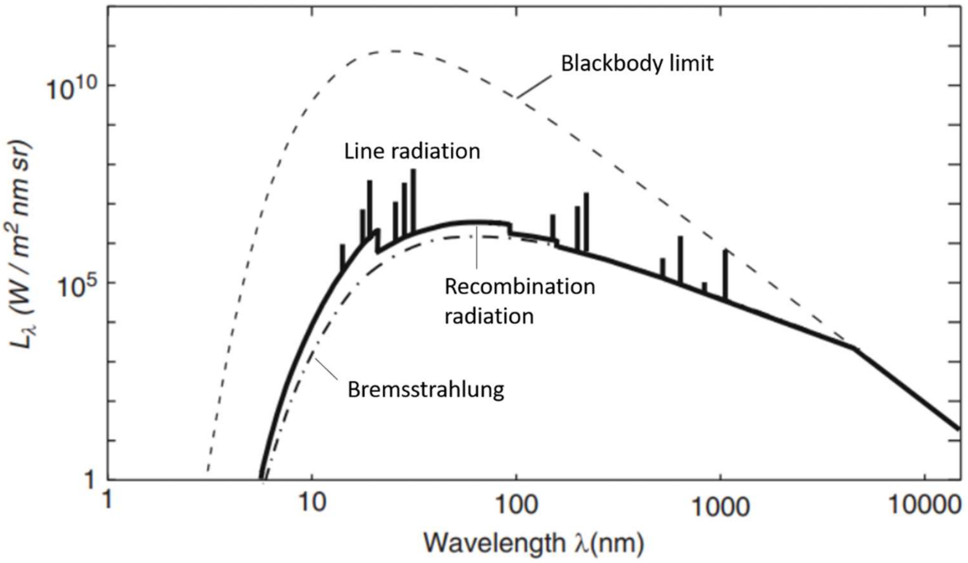

Figure 6: Simulated spectrum representing plasma radiation – dense hydrogen plasma of $k_B T_e = 10\ eV$ with impurities, $n_e = 10^{19} cm^{-3}$, thickness 1 mm [36].

Continuum radiation can be used to determine electron density and temperature. This radiation comes from the free electrons that have Coulomb interactions with ions and neutrals in plasma [37]. When the electrons are interacting with ions either free–free bremsstrahlung or free–bound recombination occurs. In contrast, when the electrons interact with neutrals only free–free bremsstrahlung exists. In essence, bremsstrahlung is radiation that originates when a charged particle decelerates and interacts with another charged particle or a neutral. Sometimes, continuum radiation is sufficient to measure electron properties in atmospheric pressure plasmas [37]–[39].

Line radiation gives a lot of information about plasma composition and can be used to determine plasma parameters. There are different aspects of a spectral line that give information about the observed medium – position, intensity, line shape and broadening. Positions of the spectral lines are used for the identification of atoms and molecules, whereas intensity, if absolutely calibrated, can be used to determine species concentrations. The line shape of a spectral profile is determined by a handful of factors dictated by the spectroscopic properties of the observed species and by experimental conditions like the temperature and pressure of the gas along with electric and magnetic fields. All of these factors influence the line shape but some affect every element present in the sample in an identical way (homogenous) and sometimes those effects are not identical to every species (non-homogenous). Ideal line shapes are described by Lorentzian, Gaussian and Voigt functions, presented in Figure 7Figure 7: Line profiles used in plasma spectroscopy [1], where a Voigt profile is dominated by the Gaussian component near the center (core), and resembles the Lorentzian component on the wings. Parameters that describe each profile are the line position, maximum height and half-width. As the half-width varies with the temperature and pressure of the system, it is often used for plasma parameter determination.

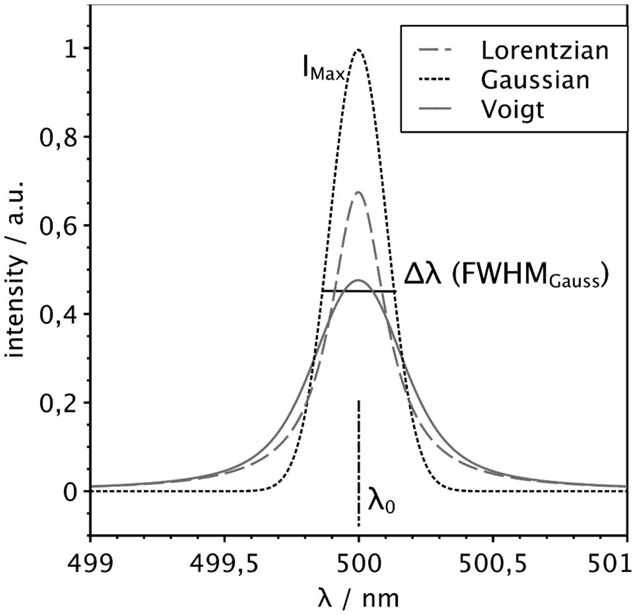

Figure 7: Line profiles used in plasma spectroscopy [1].

If we observe one particle in plasma, its interaction with the plasma changes the energies and lifetime of the observed particle. Those fluctuations in energy are observed as line broadenings in the optical spectrum of the system. In essence, different atoms in plasma have different interactions with the rest of the plasma species, which is observed as different types of broadenings [40].

Natural line broadening and collisional broadening are examples of homogenous contributions to spectral line broadenings. Natural line broadening occurs due to the natural lifetime of the emitting state of observed transitions. This type of broadening has a Lorentzian line shape but is usually negligible compared to other broadening contributions in low-temperature plasma [36]. Collisional broadening develops as a result of reduction of the natural lifetime of the transitions due to many collisions occurring in a gaseous sample. The contribution of collisional broadening depends on the nature of the energy transfer during collision (pressure or van der Waals broadening) and on the natural lifetime of the transition compared to the frequency of collisions (resonance or self-broadening) [1], [41], [42]. Even though collisional broadening dominates at atmospheric pressure, not all collisions have the same contributions. Pressure broadening by neutral particles and resonance broadening are negligible compared to charged particle interactions. The dominant type of broadening, pressure broadening of charged particles, is Stark broadening. It is a result of the interaction of molecules with electrons and ions. When the contribution of electrons is much higher than the contribution of ions, Stark broadening is described by a Lorentzian profile whose half-width is directly related to the electron density [43]–[45].

An example of inhomogeneous broadening would be Doppler broadening occurring as a result of the shift in frequency of the absorbed radiation during a transition – any motion of the emitter. The contribution of Doppler broadening becomes significant only at higher temperatures, when it is used for translation temperature determination [1], [36], [46].

1.2.1 Optical diagnostics for low-temperature plasmas – passive and active spectroscopic techniques

Most general plasma spectroscopy is divided into passive and active techniques. Passive optical diagnostic techniques record spontaneous plasma emission whereas active optical diagnostic techniques observe intensity changes after stimulating plasma with an external light source.

The most commonly used passive diagnostic technique is emission spectroscopy that uses radiation emitted by excited species when they spontaneously relax to a lower energy state. Emission spectra can, under the right conditions, give information about particle densities and temperatures. More on optical properties of plasma and how to utilize them for plasma parameter determination is presented in subchapters 1.2 and 1.2.2.

In order to use active spectroscopic techniques, one needs to introduce light into plasma and determine the correlation between the two – absorption, reflection or transmission. The most prevalent active spectroscopic technique is absorption spectroscopy, which is based upon measuring the light intensity before and after its interaction with plasma. Another way to measure absorption is to record light emitted by the excited species, that is absorbed induced light, decaying to a lower energy state. This indirect measurement of absorbed light is called laser induced fluorescence (LIF).

Other active spectroscopic techniques utilize the process of light scattering – Thomson, Rayleigh and Raman. Thomson scattering is elastic scattering from free electrons, Rayleigh scattering is elastic scattering from heavy particles and Raman scattering is inelastic scattering from molecules [47]. Based on the process of distinguished species they measure, each method gives different information. Thomson scattering can help determine electron temperature and density, Rayleigh scattering can be used to determine total density and temperatures of heavy particles, and Raman scattering gives information about density and temperature of a particular molecule.

Rayleigh scattering. This method utilizes the fact that the intensity of the scattered light depends on the intensity and polarization of the incident light and the density of the scatterers n_g^i. The relation is

$$I \sim \sum_i \sigma^i n_g^i = \sum_i \sigma^i \frac{p^i}{k_B T_g} \qquad (2)$$

where σ^i is the Rayleigh scattering cross-section of the light on i scatterer and p^i is the partial pressure of the scatterer in the gas mixture [48], [49]. In order to measure plasma gas temperature T_g, two signals obtained for the same conditions have to be recorded: the reference signal I_0 of working gas without plasma at a reference temperature T_0, and the signal obtained from plasma I_P with unknown gas temperature. Gas temperature comes from the following ratio of these values:

$$T_g = \frac{I_0}{I_P} T_0. \qquad (3)$$

The recorded signal originates from different heavy particles present in plasma. In the case of argon (Ar) plasma operating in ambient air, that signal can come from Ar, N_2 and O_2 and since these species have similar cross-sections for Rayleigh scattering, the signal can be considered independent of the mixture and air present in the effluent [49], [50].

1.2.2 Temperature measurements of species in non-equilibrium plasma with optical emission spectroscopy

Species in non-equilibrium plasma – electrons, ions, neutrals, radicals – do not share the same temperature. This means that the electron temperature is much higher than temperatures of heavy neutral species. Moreover, different degrees of freedom (rotation, vibration, translation and electronic excitation) in molecule are also not in equilibrium. This inequality of temperatures can be presented as: $T_{trans} \leq T_r \leq T_{vib} \leq T_{ex} \leq T_e$ [51].

1.2.2.1 Gas temperature

Gas temperature is a very important plasma parameter as it is essential information for technological and biomedical applications. Since APPJs have a small plasma region, it is virtually impossible to directly measure the gas temperature. However, there are different techniques that enable gas temperature measurements that can be divided based on their physical principles into rotational distribution of molecules, line profiles, neutral density and thermal probes [51].

Rotational distribution of molecules. The rotational temperature of ground state molecules is a good representation of gas temperature, as the lifetime of the molecules in the ground state is usually larger than the characteristic time between collisions. The downside of using the ground states is the need for an active diagnostic, such as absorption spectroscopy, LIF or Raman scattering, to deliver sufficient energy to excite molecules that are in the ground state. As these techniques require an additional light source, they are neither simple nor widely available. An additional drawback is that active diagnostics influence the observed medium (invasive diagnostic method). However, the rotational temperature of excited states can also be a good representation of gas temperature, especially if obtained from thermometric methods. In this case, the required information is easily obtained with simple optical emission spectroscopy (OES) [42]. To obtain the rotational temperature of diatomic gas molecules, the measured rotational spectrum has to be compared with a simulated one where a Boltzmann plot method is used, often with the help of specialized software like Specair, Lifbase or MassiveOES [52]–[54]. When picking a molecule or radical, the important factor is to choose a system that has no interference, like overlapping transition, so as not to overestimate the neutral gas temperature. Rotational temperature determination is often based on the use of emission lines from OH radical or N_2 molecule and ion, as they are present in most atmospheric pressure plasmas. OES temperature measurements revolve around relative intensity measurements of rotational lines in the same vibrational band. An example of a suitable emission spectrum for rotational temperature determination is presented in Figure 8; an OH(A–X) band from an atmospheric pressure Ar plasma jet generated by a 5 kV power source. Comparison of different neutral gas temperature determination approaches is presented in Chapter **Error! Reference source not found.**.

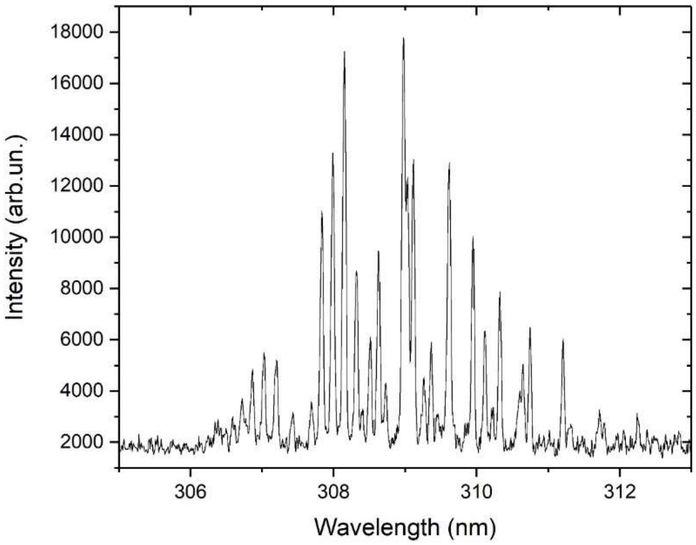

Figure 8: OES spectrum: rotational lines of OH(A–X) in Ar APPJ where gas temperature was estimated to be 388 K with Lifbase.

Line profiles. Radiation of atomic and molecular transitions has specific energies corresponding to the energy difference between upper and lower levels of the transition, and are observed at distinct wavelengths. As mentioned in section 1.2, there is always a spectral width present due to different mechanisms like natural broadenings, Doppler broadening, Stark broadening, van der Waals broadening or resonance (pressure) broadening. Some of the broadening can be successfully utilized for electron temperature and electron density measurements, which is further explained in section 1.2.2.2.

Neutral density. When plasma does not show significant changes in the composition of the neutral species, measurements of neutral species density can give information of gas temperature. Rayleigh scattering is the most direct technique of neutral density measurement, as the cross-section is species dependent and the scattered light is proportional to the concentration of neutrals in the scattered volume [55]–[57]. This method assumes an ideal gas law where at constant pressure the amount of scattered light is inversely proportional to the gas temperature. Moreover, this method is most accurate at moderate gas temperatures and at high pressure (non-equilibrium atmospheric pressure plasmas).

Thermal probes. In atmospheric pressure conditions, where the plasma region is small, it is hard to use thermal probes of any kind. First, most probes are composed of metal, which is strongly influenced by electromagnetic fields present in plasma environments. Second, even when using non-conductive fibers for temperature measurements, they can significantly modify the discharge. Ultimately, gas temperature in atmospheric pressure plasmas can have strong gradients in space and time, and influencing the discharge in any way is not appropriate for measurements. However, some gas temperature measurements have been made utilizing probes [58], [59].

1.2.2.2 Electron temperature and density

Other than electron and gas temperatures, particle density, especially electron density, is an important plasma parameter. The efficiency of plasma processes is generally dependent directly on the density of charged particles [5]. Moreover, electrons are the main factor responsible for energy transfer from the electric field that ignites plasma to the plasma discharge. The external electric field interacts with all charged particles and accelerates them. The electrons, as the lightest charged particles inside plasma, are easiest to accelerate, consequently absorbing the most energy from the applied electric field. Therefore, electrons participate in most collisions and by that transfer the most energy to gas molecules and cause their ionization and dissociation.

Electron temperature and electron density play a major role in active species generation in a non-equilibrium plasma, but their measurement is not as simple as measurements of other plasma parameters. Even though probes are not a good solution as a diagnostic tool for small scale non-equilibrium plasmas, there are some studies of applying Langmuir probes to microplasmas with various degrees of success [60]–[64]. The biggest issue with Langmuir probe analysis is that it is based on standard collisions theory, which is not applicable to atmospheric pressure plasmas as they are highly collisional as the ion–neutral mean free path becomes smaller than the Debye length [60], [65]. Another issue with probes is that their voltage disturbs the discharge conditions, which can highly influence plasma parameters [66]. As a consequence, optical diagnostics, especially OES, is used for electron temperature and density measurements. Optical diagnostics cause no disturbance to the plasma but in the case of non-equilibrium plasmas the excited-state number densities that correspond to the line intensities cannot be described with a Boltzmann distribution [65]–[67]. Thus, excitation kinetics in the plasma must be considered and densities of the excited states should be mathematically formulated with electron temperature and density, as they are well associated parameters.

Electron density can be measured from OES by three different methods – Stark broadening, analysis of the continuum radiation and the line-ratio method. Electron density is usually calculated from Stark broadening of hydrogen from the Balmer series [68]. Balmer lines, when present in plasma, are most appropriate because the broadening of hydrogen lines is a result of the linear Stark effect and is the most sensitive to electron density variations [42], [45]. Another reason to use hydrogen Balmer lines is the fact that they practically show no self-absorption and are not broadened by any dynamic processes in plasma. When an electron density is lower than $\sim 10^{13} cm^{-3}$, Stark broadening is not applicable because other broadening, like van der Waals and Doppler, become dominant [44], [69]. If observed, electron density can be measured from continuum radiation, usually present in some recombining plasmas [70]. The continuum radiation in APPJs is mostly generated by electron–atom collisions and can be used for electron density measurement in the case of plasma with low ionization degree [71]. Along with line broadening and continuum radiation measurements, temperature and density can be measured from line intensity ratios, often from nitrogen or He [67], [72], [73]. In this method, the intensity ratio of emission lines is related to the electron density by a collisional-radiative model (CRM), which is explained elsewhere [74]–[76].

More complex optical diagnostics are also used for electron temperature and density measurements like Thomson and Rayleigh scattering, already mentioned in section 1.2.1.

1.3 Thesis Objectives and Outline

The previous sections revealed the background of atmospheric pressure plasma and its diagnostics, which are important for understanding plasma processes. This thesis tries to prove a hypothesis that OES can be used as a multipurpose sensorics tool for monitoring and controlling APPJ characteristics and processes though different applications. While OES is a versatile technique, it has limitations that are dependent both on the spectroscopy system and the plasma source. This is obvious in different parameters obtained from different applications. Always, OES is supported with other diagnostic and analytical methods fo the plasma power source, plasma discharge and plasma-treated substrate, and with combined results we hope to pinpoint parameters responsible for specific processes.

After the introduction, focused on optical plasma diagnostics, the thesis is divided into two sets of applications – plasma surface modifications and treatment of biological samples.

Thesis objectives are:

1. **Tracking APPJ surface modifications by OES.**

An APPJ is used for inflicting surface modifications by changing surface properties of a polymer to prepare it for nanoparticle impregnation and creating a polymer/nanoparticle composite, and modifying surface properties of a carbon nanotube (CNT)-based gas sensor to improve sensing properties. In both applications, a setup with a kHz-driven plasma jet that operates in Ar or He will be used. We will apply OES for tracking changes inside inert gas plasma induced by substrate–discharge interactions. Along with OES, the gas phase will be analyzed in detail by fast intensified charged coupled device (ICCD) imaging and complete electrical characterization of the plasma power source. This information will be accompanied with thorough surface morphology analysis in order to understand the physical and chemical processes occurring on the surface during and after plasma treatment. The results, presented in Chapter 3, reveal our plasma systems to be energetically soft, as no evidence for changes in the bulk were found.

2. **Monitoring treatment of biological substrates by OES.**

Biological systems can be quite sophisticated and their interaction with atmospheric pressure plasmas are complex. Therefore, many different techniques are required to obtain comprehensive characterization and analysis of every step in the process. This implies a complete diagnostics and analysis is required of the power source, plasma gas phase, plasma–substrate interaction and substrate itself. This thesis covers three different applications when biological substrates are treated with APPJ – bacteria, murine fibroblast and mouse skin. Since each substrate is quite different and has a high interaction with plasma discharge, we propose implementing a standard for plasma diagnostics by means of OES as that significantly adds value to the research and allows a better understanding and faster improvement of this field. OES gives an abundance of information, making it easier to control and repeat plasma treatments, and is supported with electrical characterization of the power source to assure stability and repeatability. Since most biological samples treated in this dissertation are suspended in a liquid medium, liquid chemistry is analyzed as it should give information on the gas–liquid interaction. Moreover, all substrates are monitored after treatment and analyses are repeated after 24 or 48 h to make sure the obtained effect does not change through time. These applications are documented in Chapter 4.

Chapter 2

Diagnostics of an Atmospheric Pressure Plasma Jet

This chapter serves as an introduction to atmospheric pressure plasma diagnostic techniques. Low-temperature atmospheric pressure plasmas are a powerful source of chemically active species and can be used in applications such as processing heat-sensitive materials, chemical synthesis, material surface modifications and functionalization, cleaning, sterilization, etching, coating, etc. For the purpose of applications in the biomedical field, an RF plasma jet that operates at atmospheric pressure was constructed. The constructed jet could inject aerosol directly in the gas discharge, which could potentially be used for medical implementation. The reason behind choosing the RF range is the fact that RF-operated jets produce a large amount of reactive species, which is essential for the desired applications.

In order to evaluate suitability of an RF-driven Ar plasma jet for biomedical applications, thorough electrical characterization and optical diagnostics of the discharge were performed. Since temperatures are important parameters for biomedical application due to treatments of temperature-sensitive materials, such as skin, a detailed measurement of gas and rotational temperatures was performed. A comparison of spectroscopy and direct laser scattering methods for measuring gas temperature was made – OES, Rayleigh and Raman scattering. The gas temperature was measured from OES both from OH and N_2 emission spectra and compared with Rayleigh and Raman spectroscopy measurements. Gas temperature measured on the N_2 molecule was higher when measured with OES than complementary methods. However, gas temperature measured on the OH radical was in good agreement for all used techniques.

Regarding my contribution: I participated in performing electrical characterization and OES measurements. After the original draft of the manuscript was prepared, I helped with the refinement.

IOP Publishing Plasma Sources Science and Technology

Plasma Sources Sci. Technol. **29** (2020) 035027 (14pp) https://doi.org/10.1088/1361-6595/ab71f7

On diagnostics of annular-shape radio-frequency plasma jet operating in argon in atmospheric conditions

Ivana Sremački[1], Andrea Jurov[2], Martina Modic[2], Uroš Cvelbar[2], Lei Wang[1], Christophe Leys[1] and Anton Nikiforov[1]

[1] Department of Applied Physics, Ghent University, Sint-Pietersnieuwstraat 41, Gent, 9000, EU, Belgium
[2] Jozef Stefan Institute, Jamova cesta 39, Ljubljana, 1000, EU, Slovenia

E-mail: ivana.sremacki@ugent.be

Received 10 May 2019, revised 24 January 2020
Accepted for publication 30 January 2020
Published 19 March 2020

Abstract

One of the driving forces behind the development of cold plasma sources at atmospheric pressure is their application in the biomedical field. In this respect, radio-frequency (RF) plasma jets are of particular importance due to their possible safe operation on humans and the generation of the high amount of reactive species. For this reason, we designed an RF plasma jet in co-axial geometry with the possibility of aerosol introduction, where its characteristics were evaluated by electrical diagnostics, optical emission and laser scattering spectroscopy. The RF plasma jet operation and stability of diffuse mode were analysed based on energy balance. It was observed that α-mode diffuse discharge characterised by an effluent length up to 5 mm was sustained at a power density below 30 W cm^{-3}. The gas and rotational temperature were determined by means of spectroscopy methods and compared with the results of direct laser scattering. It was established that the gas temperature obtained from N_2 emission of transition $C^3\Pi_u \rightarrow B^3\Pi_g$ (0, 2) is highly overestimated whereas the gas temperature estimated from OH transition $A^2\Sigma+ \rightarrow X^2\Pi_i$ (0, 0) gave a reasonable agreement with both Rayleigh and Raman spectroscopy. Based on the Rayleigh scattering method, uniform gas temperature distribution in the discharge effluent was found at a power below 15 W with the average temperature below 340 ± 15 K. The low gas temperature of argon plasma jets would allow use of this source in temperature-sensitive material applications including skin treatments.

Keywords: radio-frequency plasma jet, cold plasma, plasma diagnostics, laser scattering, Rayleigh spectroscopy, Raman spectroscopy

1. Introduction

Low-temperature atmospheric pressure plasmas are a powerful source of chemically active species that are used for processing different heat-sensitive material, gas cleaning and synthesis, chemical synthesis, materials surface functionalisation, cleaning, etching, coating, etc [1, 2]. Interest in these plasmas as a tool has increased over the years due to their various applications in plasma medicine. Their capability to generate reactive oxygen and nitrogen species has enabled them to be used for the inactivation of micro-organisms, the stimulation of cell proliferation, tissue regeneration, and even inactivating cells by initialising apoptosis [3]. During the last years, two basic plasma device principles have been established in medical research and application [4–6], known as dielectric barrier discharge (DBD) and the atmospheric pressure plasma jet (APPJ). The safe application of plasma requires the generation of stable and reproducible plasma which is capable of operating in atmospheric conditions. Furthermore, plasma needs to be cold (below temperatures that could induce skin burning) and electromagnetically compatible (there should be no EM coupling between the source and substrate) [3]. Here, APPJs are especially interesting due to the plasma effluent created in the surrounding air being suitable for the direct treatment of substrates [7, 8]. The fact that plasma is in direct contact with air makes plasma physics and chemistry of atmospheric pressure jets rather complex, and brings a number of complications into its evaluations with plasma diagnostics.

To design a source that meets the previous requirements, a set of experimental plasma diagnostics is needed. For this reason, the present work was focused on electrical and temperature characterisation of an argon (Ar) atmospheric pressure RF plasma jet. The plasma source was designed in so-called co-axial electrode geometry, first introduced by Selwyn *et al* [9] and Döbele *et al* [10]. In contrast to the aforementioned works where discharge in He was studied, an attempt is made in the current study to generate stable plasma in Ar gas. It has to be noted that for industrial and medical applications, cold plasmas in Ar have an advantage over expensive He gas. However, the design of the reactor should enable safe and stable operation which is often not the case for APPJs operating in Ar because of the filament formation [11]. The source developed here is based on previous works [9, 12, 13] and it is an RF plasma up-scaled in the form of a ring-shaped jet of 14 mm diameter operating in pure Ar under atmospheric conditions. The source is intended to be used for skin treatment to support safe and fast wound healing and plasma/aerosol-assisted topical drug introduction. Accordingly, it is constructed in a way that simultaneous application of water-soluble pharmaceutical compounds and plasma is possible. Hereby, the aim of this work is to study a source operating in Ar and suitable for combination with an aerosol, to investigate its electrical characteristics and compare the temperature diagnostic methods applied to accurately measure the gas temperature (T_g) in the plasma effluent. The most convenient way to measure gas temperature in non-equilibrium plasmas is rotational optical emission spectroscopy (OES) of molecules. Temperature diagnostics by OES have been examined for rotational lines of the same vibrational band for N_2 transition $C^3\Pi_u \rightarrow B^3\Pi_g$ (0, 2) and OH transition $A^2\Sigma+ \rightarrow X^2\Pi_i$ (0, 0) [14, 15]. This technique is based on the fact that plasma has to fulfil rotational-translational equilibrium described by the Maxwell–Boltzmann distribution of populated rotational levels. However, in atmospheric pressure plasmas, due to quenching effects and ro-vibrational coupling of states, overpopulation of higher rotational levels has been noticed in many cases. This overpopulation is manifested as non-Boltzmann behaviour resulting in the overestimation of T_g [16]. The complexity of OES analysis for gas temperature determination is coupled with a low spatial resolution of the method due to the line-of sight detection. This is also a disadvantage of the method, and its validity needs to be improved by other techniques such as laser radiation scattering. Better spatial resolution and higher sensitivity are obtained by Rayleigh scattering with a scattered signal intensity directly proportional to the heavy particle density. The method of laser scattering has been applied to measure the gas temperature in a high-pressure arc [17] and recently to APPJs [18]. The approximation of the negligible effect of plasma on the gas flow is not always valid. In many cases, the gas flow is strongly affected by plasma and even controlled by the discharge, as done for example in plasma actuators [19, 20]. To confirm that the effect of plasma on gas dynamics in our RF discharge is negligible, the Rayleigh temperature measurements are confirmed by Raman scattering spectroscopy. The advantage of the Raman scattering technique is based on inelastic scattering of laser light on molecules in ground states and is independent of gas-phase dynamics [21]. Armed with these data, we were able to precisely determine the set of operational conditions at which the RF jet is safe for the treatment of skin, and at the same time re-validate the capability of spectroscopy methods for gas temperature measurements under conditions of an RF APPJ propagating in ambient air.

2. Materials and methods

In the presented paper, an RF plasma jet for the treatment of large-size objects and compatible with direct injection of an aerosol is studied. The main focus is given to the analysis of the RF plasma jet's electrical characteristics and the operational window for stable operation in diffuse α-mode. The gas temperature T_g as a key parameter for biomedical applications is studied by a combination of different methods. The chosen methods are applied in a way that they cannot affect the properties of the plasma. They are considered non-invasive, whereas T_g in the plasma afterglow is determined by three different spectroscopic techniques: OES, Rayleigh and Raman scattering spectroscopy. The application of methods is based on the analysis of different physical processes, which allows comparison and validation of diagnostic methods in the high-pressure non-equilibrium discharges.

2.1. RF plasma jet source and its electrical characterisation

The plasma source presented in figure 1 consists of two co-axial electrodes with an internal one made as a hollow cylinder of $d_{\text{in}} = 10$ mm and $d_{\text{out}} = 12$ mm. The internal electrode from stainless steel, powered by RF voltage, was surrounded by a grounded external electrode of 14 mm diameter. The grounded outer electrode was made of aluminium. As can be seen from figure 1 the conical reductions were made in the source body for practical reasons of the source installation and its holding. Additionally conical reduction in the lowest part of the source was made of a size that fits a standard 12-well plate for bio-tests. The plasma source was powered with the RF generator CESAR 136 (Advanced Energy Industries) operating at 13.56 MHz with an L-type matching box. The inter-electrode gap of 1 mm width and 10 mm length was formed by reduction of the grounded electrode diameter from 20 mm to 14 mm as shown in figure 1(b). The gas was fed into the gap through two inlets mounted symmetrically 10 cm above the electrodes that ensured a laminar flow of the gas at the outlet of the source. For the purposes of plasma diagnostics, N_2 (99.999% purity) or dry air (78.999% N_2 and 21% O_2) was added to the gas mixture at an amount of 0.05%–0.2% of Ar flow. This very small amount of admixing gas ensured that the effect of the admixing gas was negligible on the electrical and temperature properties of the discharge. Depending on the jet application,

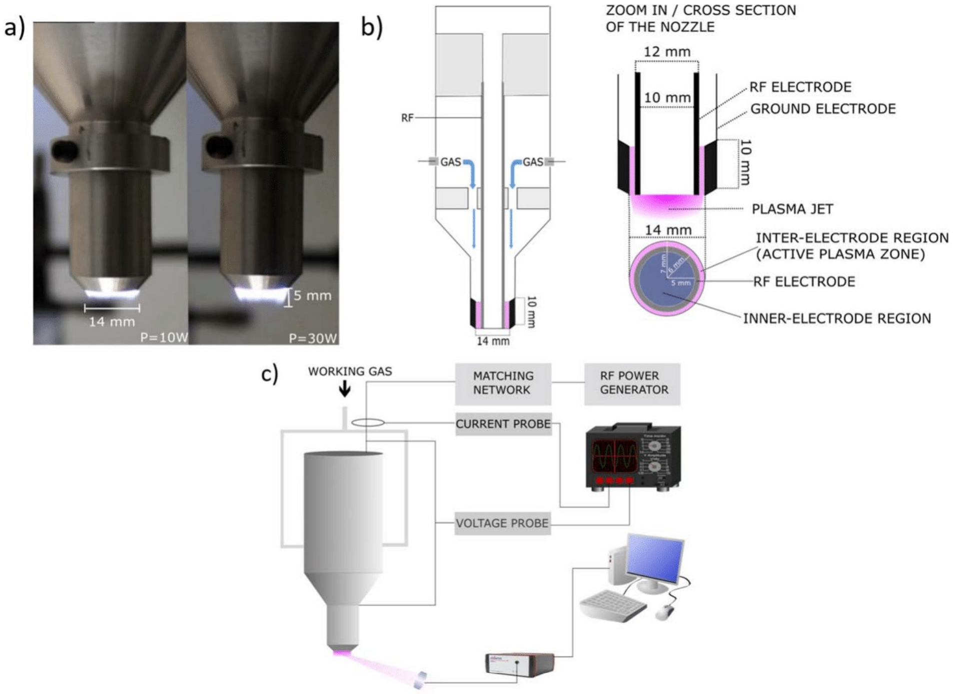

Figure 1. (a) Visual view of the jet effluent in ambient air indicating the effluent formation of a length of 5 mm for the highest RF power applied at Ar flow of 2 slm. (b) Cross-section of the reactor, enlarged nozzle and its cross-section with indicated regions of interest. (c) Experimental setup schematics used for optical and electrical characterisation of RF plasma jet.

an Ar flow of 2, 3 or 4 standard litres per minute (slm) was chosen, which corresponds to Reynolds numbers of 120, 180 and 240 indicating the laminar gas flow. In case of gas flow higher than 4 slm, the discharge cannot be sustained in stable mode. Electric current and voltage of the discharge were measured with an IV probe (Vigilant) and were recorded with an oscilloscope (LeCroy Wavesurfer). Fast imaging with 5 ns resolution in single-shot mode was performed with the use of a Hamamatsu ICCD camera with a bandpass filter with a transparency of 10 nm full width at half maximum (FWHM) centred at 750 nm. The camera was placed in front of the plasma jet and focused on the edge of the nozzle. The ICCD camera was synchronised with the RF generator with use of a delay generator Stanford Research DG535. The visual image of the plasma effluent, cross-section of the reactor and the nozzle with indicated regions of interest, and the experimental setup of the electrical and optical characterisation of the plasma jet are presented in figures 1(a), (b).

2.2. OES

APPJs are non-equilibrium plasmas with present constituents that have different temperatures (electronic, T_e; vibrational, T_{vib}; translational, T_t; and rotational temperature, T_{rot}). In the case of non-equilibrium atmospheric plasmas, the rotational temperature can be used as an indicator of the gas translational temperature due to the very high frequency of the collisions leading to establishment of the equilibrium between different rotational states of the colliders. Indeed, as the lifetime of the molecules in the excited states is normally significantly larger than the characteristic time between collisions, the rotational temperature of the excited state is usually a good representation of the gas temperature [14, 16]. Accordingly, establishing the gas temperature in an APPJ involves the determination of T_{rot} of the present molecules. Most atmospheric pressure plasma diagnostics are based on the use of emission from OH(A) states or N_2 as an indicator of T_{rot}, considering their presence in many atmospheric pressure plasmas. OES temperature measurements are based on relative intensity measurements of rotational lines in the same vibrational band. Following the Boltzmann distribution of rotational states, it is possible to directly infer the translation temperature from the rotational temperature. Here, the measurements of the gas temperature were done from partially rotationally resolved emission from OH radical transition

$A^2\Sigma+ \rightarrow X^2\Pi_i$ (0, 0) with a maximum of emission around 309 nm [14, 22] as well as from N_2 $C^3\Pi_u \rightarrow B^3\Pi_g$ (0, 2) band with a maximum at 380 nm. Molecule rotational spectra were recorded using an Avantes spectrometer with a resolution of 0.05 nm with the optical fibre directed to the effluent where plasma properties have been measured. Considering the axial symmetry of the plasma source, it is expected that plasma radiation is collected from the region corresponding to the inter-electrode area, e.g. at an area 6 to 7 mm across from the jet as shown in figure 1(b).

OES is an experimentally simple, non-invasive, inexpensive as well as fast method for estimation of the plasma parameters. Despite its simplicity, the method provides a line-of-sight measurement of the T_g and relies on the approximation that T_g is equivalent to T_{rot} of the excited states. Such an approach can lead to pitfalls and drastic overestimation of the gas temperature [16]. Typically the use of OH (A) emission leads to an overestimation of gas temperature due to non-Boltzmann behaviour of the rotational states with high J numbers ($J > 12$) [15, 22]. However, the use of N_2 emission can also result in incorrect estimates of the gas temperature, especially in the case of discharges operating in Ar gas [23]. Since this work is focused on accurate temperature measurements of the plasma jet, two direct methods of plasma diagnostics by laser scattering were applied to validate the results of OES. Laser-based spectroscopy methods, namely Rayleigh and Raman scattering spectroscopy, overcome the disadvantages of the OES method. Both methods are well spatially resolved, based on elastic laser scattering on heavy particles (Rayleigh) or inelastic laser scattering (Raman) and capable of direct measurements of the translation temperature of ground states.

2.3. Rayleigh scattering laser spectroscopy

Rayleigh scattering spectroscopy is an active spectroscopic method based on the elastic scattering of laser light on heavy particles. A detailed description of the Rayleigh scattering theory is found in [24, 25]. The intensity of the scattered light depends on the intensity and polarisation of the incident light, and the density of the scatterers ${n_g}^i$.

$$I \sim \sum_i \sigma^i n_g^i = \sum_i \sigma^i \frac{p^i}{k_B T_g}, \qquad (1)$$

where σ^i is the Rayleigh scattering cross-section of the light on i scatterer and p^i is the partial pressure of the scatterer in the gas mixture. The direct dependence of the scattering signal on the density of heavy particles allows using the method for spatially and temporally resolved gas temperature measurements. For plasma temperature measurements, two signals in the same conditions need to be recorded: the reference signal I_0 in the working gas without plasma at referent temperature T_0, and the signal from the plasma I_P with unknown T_g. Accordingly, the temperature T_g is calculated as:

$$T_g = \frac{I_0}{I_P} T_0. \qquad (2)$$

The recorded scattered signal is a signal originating from different heavy particles present in the discharge. In Ar plasma operating in ambient air, the following species are considered: Ar, N_2 and O_2. Since these species have a similar cross-section for Rayleigh scattering, the signal can be considered independent of the mixture and air entrainment in the effluent [26].

For temperature measurements, a pulsed Nd:YAG laser (Litron nano-S) was used at a wavelength of 532 nm. The repetition rate was 10 Hz, the energy of the pulse was set to 8 mJ and the pulse duration was 8 ns. The laser beam had a Gaussian shape with a diameter of 8 mm. At 532 nm, light scattered cross-sections on Ar atoms and air are $4.5 \cdot 10^{-27}$ and $5.245 \cdot 10^{-27}$, respectively, in units of $\mathrm{cm}^2/\mathrm{molecule}$ [25]. A fast imaging gated Hamamatsu digital camera with 532 nm filter with FWHM of 10 nm was used to record the scattered signal from the region of interest when the plasma was OFF and ON in order to measure the signal I_0 and I_p, respectively. The synchronisation between the laser pulse and the camera gate unit was achieved using a Stanford Research DG535 delay generator. The experimental setup for Rayleigh scattering spectroscopy is shown in figure 2(a).

A quartz prism was used to deflect the direction of beam propagation to 90°. After deflection, the beam was reduced using an Edmund Optics telescope of power 10X, so the beam diameter in the plasma region was 0.8 mm. Temperature measurements were done at a distance 1.5 mm from the nozzle in the effluent with spatial resolution along the jet greater than 50 μm. The rationality in the choice of distance is dictated by biomedical applications of the developed source as, typically, treated objects are located at 1.5 mm from the nozzle. Experiments were carried out in ambient air. Only the region of interest, defined later on in the paper, was used for Rayleigh scattering analysis. In order to perform a proper comparison of the Rayleigh scattering results with space-averaged results of the OES the Rayleigh signal was averaged over a 1 mm region corresponding to the inter-electrode region of elevated temperature. It has to be emphasised that equations (1) and (2) are applicable only in the case when the electrical discharge operation does not affect the gas flow dynamics. Otherwise, the observed Rayleigh signal during the plasma operation has to be attributed not only to the change of T_g but also to the change of p^i in equation (2), which appears due to the plasma effect on the gas flow. To this end, the applicability of the Rayleigh scattering method applied for T_g measurements was furthermore validated by the Raman laser scattering. Since RF APPJ is designed to be used for medical treatment, all experiments were carried out in conditions as close to the real situation as possible, without any shielding gas. It is known that Mie scattering can strongly affect both Rayleigh and Raman measurements. In order to suppress the Mie scattering effect, only an area underneath the nozzle free of Mie scattering was analysed in laser scattering tests.

2.4. Raman laser scattering spectroscopy

Raman scattering spectroscopy is based on the inelastic scattering of laser light on molecules, and for this purpose,

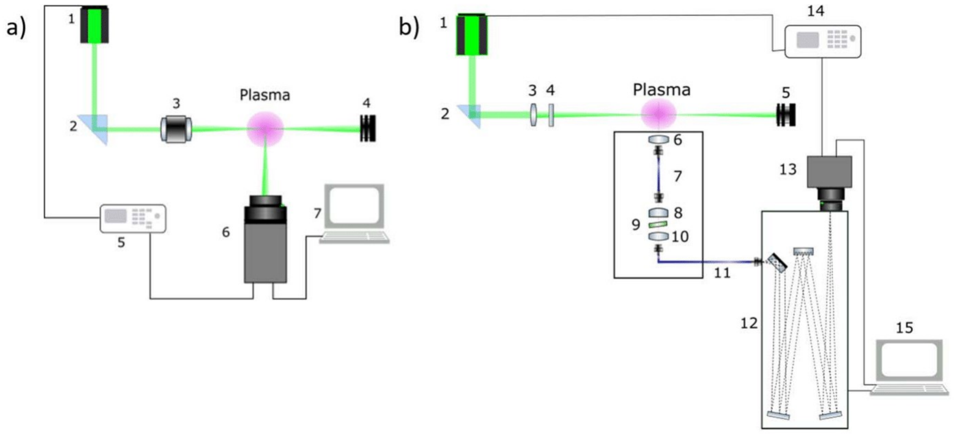

Figure 2. Experimental schematic of setup for (a) Rayleigh scattering spectroscopy with 1-Nd:YAG laser at 532 nm, 2-90 degree rotation prism, 3-telescope, 4-beam dump, 5-delay generator, 6-camera, and 7-PC; (b) Raman scattering spectroscopy with 1-Nd:YAG laser at 532 nm; 2-prism, 3-lens, $f = 500$ mm, 4-polariser, 5-beam dump, 6,10-collecting lens, $f = 50$ mm, 7,11-optical fibre with diameter of 300 μm, 8-collimation lens, $f = 30$ mm, 9-BNF 532 nm, 12-monochromator, 13-ICCD camera, 14-delay generator, and 15-PC.

dry air was added at 0.2 v% to the feed gas. A spectrum consists of two symmetrical wings called the Stokes and anti-Stokes components with lines shifted relative to the central incident wavelength (λ_L). The challenging task of rotational Raman spectroscopy is the very low scattering signal intensity and partial overlap of the central lines with about 10^4 times higher Rayleigh signal that requires filtering out the elastically scattered light in order to avoid saturation of the detector. Details of Raman scattering spectroscopy are found in the literature [21, 27–29]. Since Raman rotational spectra are characteristics of a specific molecule, the spectra are species-dependent, and so the method is free of the disadvantage of Rayleigh scattering spectroscopy. Wavelengths of the anti-Stokes and Stokes component for transitions J–J' are calculated using the expression [30]:

$$\lambda_{J-J'} = \lambda_L + \frac{\lambda_L^2}{hc} B_v((J'^2 + J') - (J^2 + J)), \tag{3}$$

where h an c are the Planck constant and the speed of light, respectively, B_v is the rotational constant of molecules N_2 and O_2, and J and J' are quantum numbers of the initial and final rotational state. The light intensity of the Raman transition J–J' is calculated as [31]:

$$I_{J-J'} = C n_J \frac{\mathrm{d}\sigma_{J-J'}}{\mathrm{d}\Omega}, \tag{4}$$

where C is the experimental constant, n_J is the density of molecules in states J and $d\sigma_{J-J'}/d\Omega$ is the differential cross-section for the transition J–J'. The density of molecules in state J is given as [32]:

$$n_j = \frac{n}{Q}(2J + 1)\, g_J\, e^{-\frac{B_v J(J+1)}{kT}} \tag{5}$$

Table 1. Molecular constants of N_2 and O_2 used in the simulation of the Raman signal [29].

Parameter	N_2	O_2
B_v (eV)	$2.467 \cdot 10^{-4}$	$1.783 \cdot 10^{-4}$
γ^2 (F^2m^4)	$3.95 \cdot 10^{-83}$	$1.02 \cdot 10^{-82}$
g_j (odd/even)	3/6	1/0
I	1	0

where n is the density of Raman active molecules, and the partition function Q is expressed by [25]:

$$Q = (2I + 1)^2 \frac{kT}{2B_v}. \tag{6}$$

Where g_j is the nuclear spin degeneracy, and I is the nuclear spin quantum number. The differential cross-section for perpendicularly scattered light is [31]:

$$\frac{\mathrm{d}\sigma_{J-J'}}{\mathrm{d}\Omega} = \frac{64}{45}\frac{\pi^4}{\varepsilon_0^2} b_{J-J'} \frac{\gamma^2}{\lambda^4_{J-J'}}, \tag{7}$$

where the Placzek–Teller coefficient for diatomic molecules $b_{J-J'} = \frac{3(J+J')(J+J'+2)}{8(2J+1)(J+J'+1)}$, and γ^2 is the anisotropy of the equilibrium polarisability tensor [33]. For diatomic molecules allowed transitions are $\Delta J = \pm 2$ (positive sign for Stokes and negative sign for anti-Stokes components), whereas all molecular constants for both N_2 and O_2 are given in table 1.

In order to detect rotationally resolved Raman spectra transmission, a Bragg notch filter (BNF; OptiGrate) was used as a narrow band filter to reduce the Rayleigh scattered light by at least 10^3 times. The laser light at 532 nm was focused with a plano-convex lens of $f = 500$ mm 1.5 mm below the nozzle, the same distance as in the case of Rayleigh scattering spectroscopy. The line-integrated scattered signal along the jet width (radius of 7 mm) was collected with a lens of $f = 50$ mm and focused on the fibre of diameter 300 μm. The other end of the fibre was used as a point light source to perform collimation of the scattered light, which plays a crucial role in filtration via the BNF. The filter BNF-532 is designed in a way that 532 nm light is filtered if the light passes the filter at an angle of $6 \pm 1°$. This method of Raman scattering spectroscopy using volume Bragg grating as a notch filter has recently been applied elsewhere [21, 34]. After passing the filter, the light is collected with a lens and projected to a 0.75 m spectrometer Zolix Omni-λ. A grating of 1200 grooves/mm (blazed on 500 nm) is used to resolve the Raman spectrum with resolution greater than 0.11 nm. The spectrum is recorded via the ICCD Andor camera synchronised with the laser. The laser energy was set at 20 mJ, and 16 000 laser shots were accumulated for each recording of the Raman scattering spectra. The rotational temperature was calculated via a comparison of the experimental spectra with simulation using equations (3)–(7). The fitting parameters were the density of the scatterers, the laser energy, resolution of the spectrometer and T_g. The experimental setup for Raman scattering spectroscopy is exhibited in figure 2(b). It has to be noted that in comparison with Rayleigh scattering, the method of Raman scattering detection is devoid of the disadvantage of the results' dependence on gas flow dynamics. The method relies on collective inelastic scattering of light by particles and, correspondingly, the effect of plasma on gas flow is neglected which makes it a perfect candidate to validate Rayleigh scattering. It has to be noted that the Raman scattering-based calculated temperatures are averaged along the laser line passing through the plasma, and thus only used for validation of the Rayleigh results which also are averaged over the same region of interest. Taking into account the region of averaging of the Raman signal, direct comparison of the gas temperature measured by the OES method and Raman scattering is not feasible and not considered in the current work.

3. Experimental results and discussion

3.1. Electrical characterisation of RF plasma jet

The electrical discharge was sustained by the application of RF forward power in the developed APPJ at a level below 30 W. At RF input power above 30 W, the discharge was transferred to γ-mode. This manifests as highly localised discharge, which is sustained primarily by a secondary emission of the electrons from hot contact spot-localised to one of the electrodes. In this work only α-mode mode uniform discharge was studied. The discharge is formed at the lowest power just on the edge of the electrodes. The increase of the power to 30 W leads to expansion of the discharge, propagating over the whole length of the electrode which is 10 mm long as indicated in figure 1. Similar expansion of the RF plasma was also noticed in our previous work on coplanar RF plasmas [35]. Further increase of the power leads to the discharge transformation to γ-mode. In α-mode at a power of 30 W the discharge fills the whole area between the electrodes. The *V–I* characteristics of the discharge are presented in figure 3(a). Power dissipation in the discharge when the plasma is off and on is shown in figure 3(b) based on the methodology described in [36]. According to the measurements the plasma source stable operating range is from 10 W (minimum RF power to sustain plasma) to 30 W (γ-mode transition). In the case of adding nitrogen/air to the gas flow, due to OES measurements, the α-mode is still in the range of power from 13 W to 30 W. The length of the visible effluent depends on the power (see figure 1) and is in the range of 2.5–5 mm, which corresponds to a minimum and maximum power. An example of the discharge appearance in α- and γ-mode is presented in the insets in figure 3.

It is interesting to note that the increase in the gas flow rate from 2 to 4 slm has very little impact on the electrical characteristics of the plasma source. However, at a flow rate above 4 slm it is not possible to sustain the discharge in a stable regime, and the plasma is randomly completely extinguished or transferred to γ-mode. There is a small increase of the V_{RMS} value for the lowest power range from 96 to 102 V with an increase in the flow rate from 2 to 4 slm. However, the current of the jet in α-mode is independent of the gas flow, with current density in the range of 0.2–0.37 $\mathrm{A\,cm^{-2}}$ for all working powers. Considering the almost linear *V–I* characteristics of the discharge with the positive slope of $110\ \mathrm{V\,A^{-1}}$ it can be expected that the plasma operates in the glow-like mode sustained by Ohmic electron heating [37]. This indicates that the main ionisation processes are driven by fast electrons accelerated in an oscillating RF field [38]. Sustained RF glow discharge is characterised by a constant V/I phase difference of about 88° that implies the stability of α-mode and discharge capacitive character. The reason for a slight deviation of $-2°$ from the pure capacitive coupling is due to the decreasing capacitive contribution and increase of the resistive one with an increase of the power similar to that observed by others [39, 40]. A observation of stable α-mode formation in Ar plasma has been also found for the plasma jet described in [41]. The evolution of plasma constituents during an RF cycle was experimentally studied by use of fast imaging of the discharge emission presented in figure 4. For this purpose, the fast imaging camera was used with a maximum transparent filter at 750 nm, which corresponds to Ar I transition $4\mathrm{p}(^2\mathrm{P}^0_{1/2}) \rightarrow 4\mathrm{s}(^2\mathrm{P}^0_{1/2})$. This is an excited state with a radiative lifetime of $\tau \approx 22$ ns [42], which is reduced to less than 5 ns due to quenching at high pressures. This intensive line is therefore suitable for RF imaging because the lifetime of atoms in excited levels is shorter than the duration of the RF cycle of 74 ns and so the emission of Ar I should be directly related to the electron kinetics in the discharge. Emission of OH $\mathrm{A}^2\Sigma+ \rightarrow \mathrm{X}^2\Pi_{\mathrm{i}}$ transition was also recorded but no temporal evolution within the RF cycle is noticed due to the longer radiative lifetime of OH radicals $\tau \approx 0.6$–$0.7\ \mu$s. Imaging of APPJ, presented in figures 4(a), (b) was performed at five different time points during the RF cycle corresponding to the applied voltage: $V_{\mathrm{RF}} = 0$ ($T_1 = 0$ ns), $V_{\mathrm{RF}} = +\mathrm{V}_0$ ($T_2 = 18.44$ ns), $V_{\mathrm{RF}} = 0$ ($T_3 = 36.87$ ns), $V_{\mathrm{RF}} = -\mathrm{V}_0$

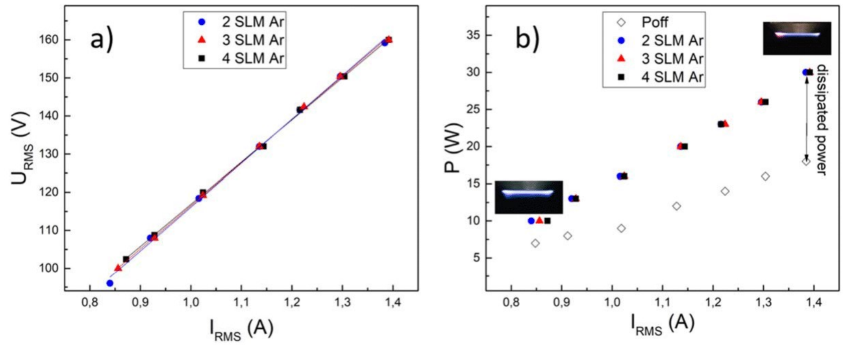

Figure 3. Electrical characterisation of RF jet (a). *I*–*V*characteristics of the RF plasma jet operating in α-mode recorded with increasing the RF forward power from 10 to 30 W. (b) Forwarded power with gas flow, and forwarded power without gas flow (P_{OFF}) as a function of the current, with a visual representation of the discharge in α- and γ-mode.

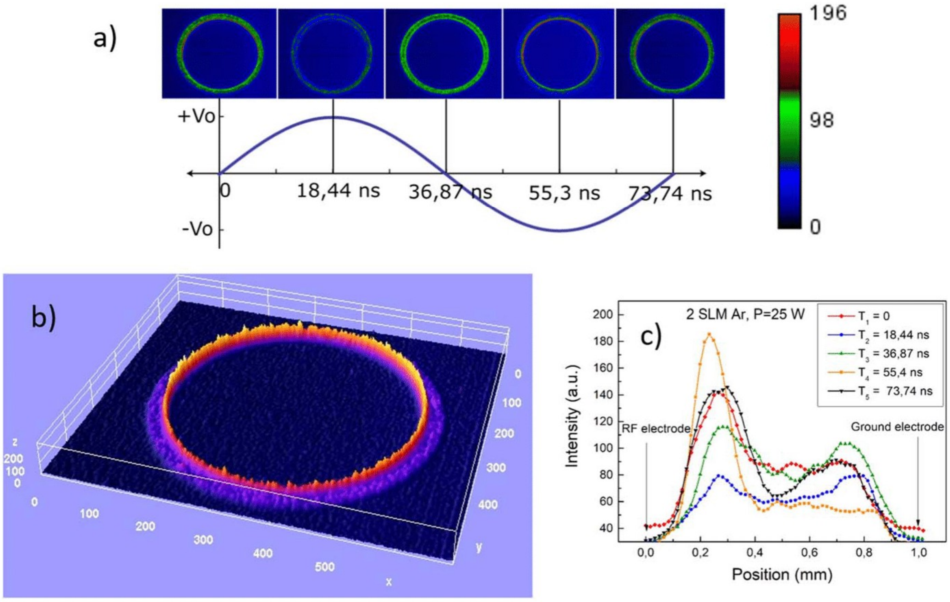

Figure 4. Time-resolved imaging of the RF APPJ with 5 ns exposure time in single-shot mode. (a) The images are recorded through a bandpass filter of 10 nm FWHM centred at 750 nm that corresponds to Ar I emission. Time of the records is indicated in the insets. (b) 3D map of intensity for the case of 55.4 ns time frame with an indication of the sheath formed near powered electrode. (c) Intensity distribution in the inter-electrode gap and near RF-powered and ground electrodes.

($T_4 = 55.3$ ns) and $V_{\mathrm{RF}} = 0$ ($T_5 = 73.74$ ns). The imaged bulk plasma was uniform in all the time frames, whereas the formed sheath exhibited a strong emission near the RF electrode. The sheath width is calculated from the image corresponding to the highest Ar emission near the RF electrode when its voltage reaches a negative amplitude as indicated in figure 4(b). The sheath is here considered to be a width of the illuminating zone near the electrode where Ar I emission drops by 90% from the peak intensity I_{peak}. Moreover, the RF imaging indicates a higher intensity of Ar I lines in the electrode area (sheaths) with respect to the bulk plasma (figure 4). The length of the developed sheath, corresponding to time 55.4 ns, is estimated to be around 200 μm, which is in good agreement with the results of particle-in-cell (PIC) simulation of RF plasmas operating at high current [43].

It should be noted that in contrast to the symmetrical sheath formation observed in PIC simulation, the sheath in APPJ is strongly asymmetrical with a barely visible sheath formed at the ground electrode (virtual cathode at 18.4 ns) and very strong sheath at the RF-powered electrode (virtual cathode at 55.4 ns). Stronger light emission on the RF electrode was also noted in our earlier work with RF planar discharge [44]. This effect is partially explained by the fact that the APPJ electrode system is asymmetrical with a 5:6 ratio of electrode areas. However, the area ratio of the electrodes cannot fully explain the observed strong asymmetry of the discharge. Correspondingly, other processes, unknown at the moment, may have an important contribution to the asymmetry, and additional research is required which is out of the scope of this work. The presence of the sheath in RF plasma can have strong impact on the stabilisation of the discharge and the generation of uniform α-mode plasma without filaments or transition to γ-mode.

Opposite to atmospheric pressure DBDs sustained in kHz frequency range in Ar, which usually operate in filamentary mode, our APPJ is a uniform-stable plasma operating in diffuse α-mode. This is obviously an advantage of the source especially in terms of biomedical treatments. Operation of the discharge in diffuse α-mode requires a mechanism to stabilise the discharge and suppress heating instabilities which would otherwise result in the transition of the discharge to γ-mode of operation. Sustaining of the source is analysed based on the balance between processes of dissociation/recombination and the diffusion of ions $\mathrm{Ar_2}^+$ and electrons in the bulk of the discharge [45]. In the case where recombination processes are dominant, the steady α-mode switches to filamentary γ-mode sustained by the secondary electron emission from the electrodes. If processes of diffusion are dominant over recombination, then one can conclude that the heating dissipation is suppressed and uniform α-mode is realised. In self-sustained low-ionisation-degree discharges, as we studied here, a major loss of the input RF power P dissipated in the discharge of volume V is because of elastic processes. Correspondingly, the electron density in the bulk is estimated using power balance for free electrons in plasma assuming only elastic collisions as [46]:

$$\frac{P}{V} = n_{\mathrm{e}} \cdot n_{\mathrm{Ar}} \cdot \frac{3m_{\mathrm{e}}}{m_{\mathrm{Ar}}} \cdot k_{\mathrm{el}} \cdot T_{\mathrm{e}}. \qquad (8)$$

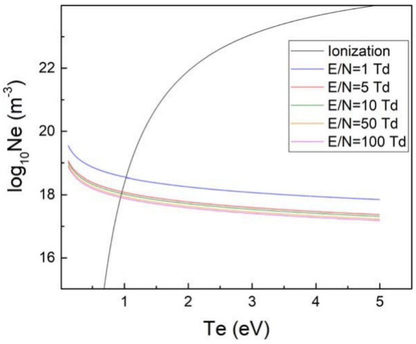

Figure 5. Electron density and temperature estimation plots from power and ionisation/recombination balance. Curves for reduced *E/N* in the range 1–100 Td represents power balance due to elastic collisions.

In equation (8) the term responsible for heating the gas is neglected as T_{g} is much lower compared with T_{e}.

The parameters n, $m$and T are the density, mass and temperatures of species, respectively. The coefficient k_{el} stands for the rate coefficient of elastic collisions between electrons and Ar atoms obtained from BOLSIG+ for characteristic electric fields E/N 1, 5, 10, 50 and 100 Td ($1\ \mathrm{Td} = 10^{-21}\ \mathrm{Vm^2}$). The maximum energy density is considered as $30\ \mathrm{MW\,m^{-3}}$ based on the results presented in figure 3(b). On the other hand, the self-sustaining operation of the discharge should fulfil the ionisation/recombination balance [33]:

$$10^{-14} n_{\mathrm{e}} n_{\mathrm{Ar}} e^{-\frac{E_i}{kT_{\mathrm{e}}}} = n_+ n_{\mathrm{e}} k_{\mathrm{d}}. \qquad (9)$$

Here k_{d} stands for the dissociative recombination rate and is typically $10^{-14}\ \mathrm{m^3 s^{-1}}$ [39]. Considering the condition of quasineutrality, equation (9) is simplified to the ionisation balance equation:

$$n_{\mathrm{e}} = n_{\mathrm{Ar}} e^{-\frac{E_i}{kT_{\mathrm{e}}}}, \qquad (10)$$

where E_i is the first ionisation energy of $\mathrm{Ar_2}$ as $\mathrm{Ar_2}^+$ is a dominant molecular ion APPJ at atmospheric pressure. Dependence of the electron density on T_{e} for the range of characteristic values for atmospheric pressure plasmas (few eV) is presented in figure 5, indicating the steady-state value for $n_e = 3.2 \cdot 10^{18}\ \mathrm{m^{-3}}$ and $T_{\mathrm{e}} = 1$ eV for the experimental condition of 5 Td. This very rough estimation of plasma parameters is in good agreement with previous works of our group based on COMSOL simulation and continuum radiation calculations [44, 47].

The results of power and ionisation/recombination balance can be used to estimate characteristic times for both diffusion and recombination of charged particles. Obviously, in high-pressure plasmas, the dominant processes of charge particle loss are dissociative recombination of electrons with $\mathrm{Ar_2}^+$ ions and diffusion of particles from the bulk [39]. The dissociative recombination described as $\mathrm{Ar}_2^+ + e^- \leftrightarrow \mathrm{Ar} + \mathrm{Ar}$ has a characteristic time given as:

$$\tau_{\mathrm{diss}} = \frac{1}{n_e \cdot k_{\mathrm{e-i}}}, \qquad (11)$$

where $k_{\mathrm{e-i}}$ is a coefficient describing the electron–ion recombination. On the other hand, the characteristic time for Ar cluster ions to leave plasma due to diffusion can be expressed as:

$$\tau_{\mathrm{diff}} = \left(\frac{l}{2.4}\right)^2 \cdot \frac{e}{\mu k T_{\mathrm{e}}}, \qquad (12)$$

where l is the characteristic diffusion length and μ is $\mathrm{Ar_2}^+$ mobility in Ar [41]. Calculations using of n_e and T_{e}, estimated from figure 5, indicate that τ_{diss} is close to 4.5 μs. This is about 30 times faster than diffusion processes with $\tau_{\mathrm{diff}} \sim 140$ μs. Such a large difference between τ_{diff} and τ_{diss} should lead to thermal instabilities and transfer of the RF discharge to γ-mode. This is contradictory with experimental results and leads to the conclusion that another process of RF discharge stabilisation should exist [48]. Both estimations of τ_{diff} and τ_{diss} are made for the bulk plasma. In contrast to DBDs or pulsed plasmas operating at high pressure, the sheath regions near the electrodes are formed in the RF APPJ as presented in figure 4. The sheath plays an important role in discharge sustaining and can stabilise the α-mode regime. High electrical potential in the sheath repeals fast electrons directing them to the bulk. A PIC simulation by Lieberman *et al* [43] demonstrated electron density decrease in the sheath, and the sheath behaviour even at high pressure is similar to the Child–Langmuir sheath in low-pressure capacitively coupled RF discharges. The decrease of n_e affects processes of dissociation/recombination and leads to an increase of τ_{diss}. On the other hand PIC simulation exhibits a high reduced field E/N in sheaths estimated to be up to 1 MV m^{-1} [43]. This results in an increase in ion mobility which causes a decrease in τ_{diff} and leads to discharge stabilisation in the sheath, where the condition $\tau_{\mathrm{diff}} \sim \tau_{\mathrm{diss}}$ is reached. The sheath effect in the stabilisation of the RF APPJ is important for sustaining the discharge in a uniform mode, which is a key issue in the generation of low-temperature active media for biomedical applications of the plasmas.

3.2. Temperature characterisation by OES method

The RF source presented in this study was developed for the purpose of trans-epidermal drug delivery. In respect to its targeted application, the source is required to fulfil: (i) safe operation without initiating thermal damage to the tissue in contact with plasma, (ii) compatibility with aerosol injection, and (iii) ability of large-area treatment. Among the different plasma properties, the gas temperature is considered to be a key parameter for its application. To this end, a well-known technique based on OES gas temperature measurements was applied. The method is based on rotational temperature calculations of OH $\mathrm{A}^2\Sigma+ \rightarrow \mathrm{X}^2\Pi_{\mathrm{i}}$ (0, 0) and $\mathrm{N_2}$ $\mathrm{C}^3\Pi_{\mathrm{u}} \rightarrow \mathrm{B}^3\Pi_{\mathrm{g}}$ (0, 2) molecules from the partially resolved ro-vibrational bands. In the first case, T_{g} was measured in the power range of 10–30 W for an Ar flow of 2, 3 and 4 slm from the OH partially rotationally resolved band. LIFBASE simulation and its comparison of the measured spectra are presented in figure 6(a). In the second case, the $\mathrm{N_2}$ transition $\mathrm{C}^3\Pi_{\mathrm{u}} \rightarrow \mathrm{B}^3\Pi_{\mathrm{g}}$ (0, 2) was used for rotational molecular temperature calculation, which is based on MassiveOES software [49] where only the linear part of the Boltzmann plot has been taken into account, similar to [22]. The slope of Boltzmann plot for J numbers in the range of 4–20 was used for the determination of N2 rotational temperature presented in figure 6(b).

The OH rotational temperature of the effluent of Ar plasma which propagates into the ambient air was estimated to be in the range of 310–350 K, at a distance of 1.5 mm from the nozzle. Interestingly, the RF power increase had a negligible impact on the rotational temperature of OH(A) radicals, which is in agreement with previous results from our group [35]. This is explained by the increase of RF power in α-mode which results in plasma expansion between the electrodes along with the gas flow, and the effluent that leads to almost constant power density W/cm^3 [35]. The OES measurements presented in figures 6(a), (b) are line-of-sight integrated across the effluent correspondingly providing the spatially averaged value of T_{g}. In the case of $\mathrm{N_2}$ admixing up to 0.2%, no change in the visual appearance or *V–I* characteristics of the discharge was detected. However, the rotational temperature estimated from the linear slope of the Boltzmann plot indicates T_{g} in the range of 450–480 K. It has to be noted that the $\mathrm{N_2}$ distribution shows Boltzmann behaviour for rotational levels up to $J = 20$ with the temperature indicated in figure 6(b), whereas fitting the vibrational band 0–2 with J numbers up to 32 leads to an unrealistically high rotational temperature of 580–680 K. Correspondingly, only the range of rotational numbers $J = 4$–20 with linear Boltzmann slope was analysed. The results of figure 6 indicate a discrepancy between T_{g} obtained from OH (A–X) emission and $\mathrm{N_2}$(C–B). Moreover, there was almost no tendency in T_{g} as a function of gas flow in the case of using $\mathrm{N_2}$ band emission. In a number of studies [16, 23] it was indicated that an often-encountered issue in non-equilibrium plasmas is the energy transfer from Ar metastable atoms in Ar($^3\mathrm{P}_2$) and Ar($^3\mathrm{P}_0$) states to $\mathrm{N_2}$(X) producing electronically excited $\mathrm{N_2}$(C) molecules, which are not in equilibrium with the rest of the molecules. As this reaction is a near-resonance process, it is often a dominant production mechanism of $\mathrm{N_2}$ excited states in Ar discharges with small additions of $\mathrm{N_2}$ or air [16]. The effect of Ar metastable energy transfer to $\mathrm{N_2}$ species is noticeable by introducing $\mathrm{N_2}$ to the feeding gas as shown in figure 7. With the addition of $\mathrm{N_2}$ to the working gas there is an increase in the intensity of nitrogen lines (second positive system) and a reduction of Ar lines from the transition 4p–4s. This behaviour may be related to an efficient energy transfer from Ar excited states to nitrogen

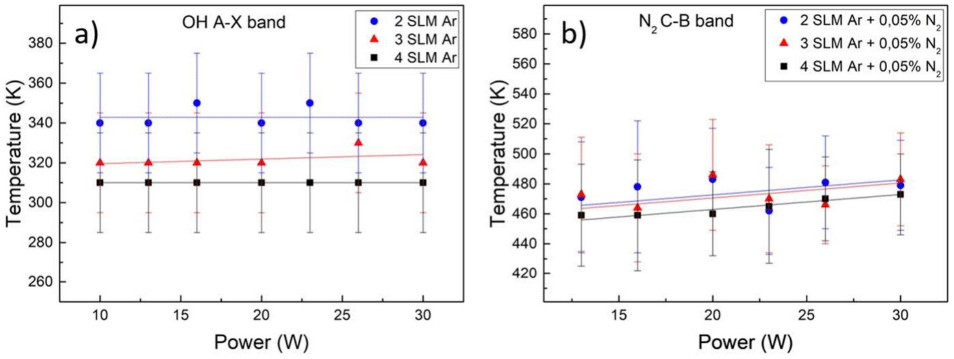

Figure 6. The gas temperature in plasma calculated via (a) LIFBASE software fitting of OH (A–X) band for different gas flow and RF forward power; (b) Boltzmann plot of N_2 transition (C–B) with the use of MassiveOES [49].

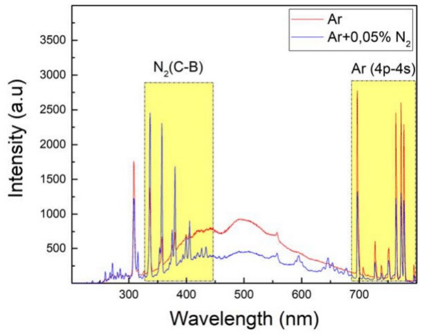

Figure 7. Example of RF APPJ spectra in pure Ar (red), and Ar in mixture with 0.05% nitrogen (blue).

species inducing overpopulation of N_2 (C) level and so non-Boltzmann distribution.

This fact can lead to the overestimation of gas temperature from the N_2 band. This could then be a reason for the discrepancy of results in our study. On the other hand, the use of OH(A–X) emission as a proper indicator of T_g is also very questionable [22, 50], and has to be revalidated based on direct methods of neutral translation temperature detection. To this end, two other methods based on laser scattering detection are applied. However, it has to be noted that the laser scattering methods presented in section 3.3 are more experimentally demanding and have other limitations, e.g. they cannot be applied in the case when an aerosol is injected into plasma. For this reason, we used them only for validation of the OES results and revealing insights into the gas heating inside the RF plasma jet.

3.3. Temperature characterisation by laser scattering

Rayleigh scattering allows direct measurement of gas density proportional to T_g through equation (2) with a high spatial and temporal resolution. A typical example of a Rayleigh scattering image taken with the ICCD camera in pure Ar plasma of 10 W at 1.5 mm distance from the nozzle is given in figure 8(a). Only part of the signal free of Mie scattering, indicated by the dotted area ROI in figure 8(a), was analysed hereinafter. No laser synchronisation with RF voltage was applied as no temporary dependence of T_g is expected because the characteristic time of RF signal (~74 ns) is too short for gas heating to follow the RF cycle. The spatially resolved gas temperatures in Ar and Ar + N_2 plasma effluent are presented in figures 8(b), (c) for the case of RF power of 20 and 30 W in Ar and Ar + N_2 mixtures, respectively. Based on the spatially resolved profile of T_g it can be assumed that the gas temperature is constant along the jet radial cross-section at power below 20 W. Higher T_g in a position that corresponds to the space between the electrodes was noted at higher power as indicated in figure 8(b). The small asymmetry of the temperature profiles that can be seen in figures 8(b), (c), is explained by the very small misalignment of the electrodes that results in the shorter gap and correspondingly more intensive discharge in that location. This effect was also observed during fast imaging (see figure 4, time frame 55.4 ns, bottom part of the inter-electrode gap).

The Rayleigh radial resolved signal presented in figure 8(b) was averaged along the regions corresponding to plasma effluent formed in the inter-electrode area, e.g. a region of 1 mm width located at the position from 6 to 7 mm for 2 slm flow. It has to be emphasised that position of the maximum of the gas temperature depends on the gas flow and a shift towards the inner-electrode region was observed with an increase of the flow as shown in figure 8. Due to the shift of the high-temperature region the area of Rayleigh signal averaging has been adjusted depending on the flow, keeping the width of the averaging at 1 mm. The described methodology of the Rayleigh signal averaging was applied in order to determine the space-averaged T_g which can be directly compared with the OES measurements presented in section 3.2. The obtained results for both Ar and Ar + N_2

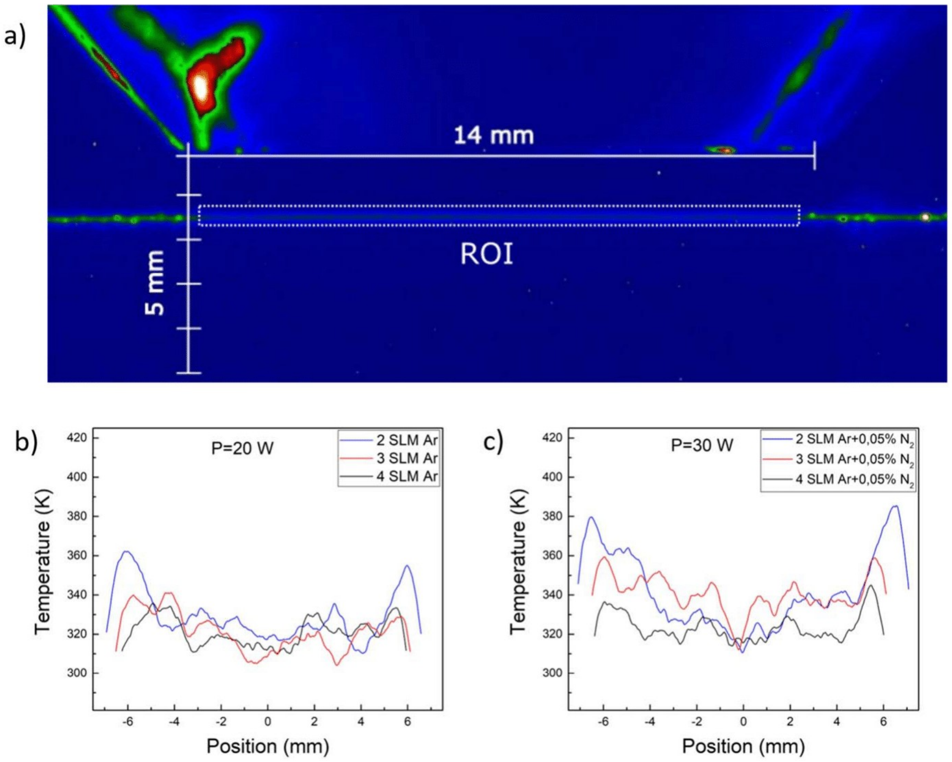

Figure 8. Rayleigh scattering of the laser light of 532 nm at 1.5 mm distance from the nozzle. (a) The image was taken with an ICCD camera of the laser beam passing through Ar plasma for $P = 10$ W. The dotted area represents the region free of Mie scattering and only this region was analysed for the temperature estimations. (b) Spatially resolved temperature measurements via Rayleigh scattering (Ar gas) at plasma power of 20 W. (c) Spatially resolved temperature measurements via Rayleigh scattering (Ar + N_2 gas) at plasma power of 30 W.

mixtures as a function of the gas flow rate and forward RF power are exhibited in figure 9. The temperature profile analysis shows uniform temperature distribution at the lowest power of 10 W. With increasing input power, the higher temperature region corresponding to the effluent region starts to be noticeable, as shown in figures 8(b), (c). As expected, the highest temperature difference is for the lowest flow. With increasing of the flow, the shape of the effluent is more conical and there is effective heat transfer towards the middle of the plasma jet leading to thermalisation and a more uniform temperature profile.

The obtained results indicate that T_g in both the Ar and Ar + 0.05% N_2 plasma is in the range of 300–370 ± 15 K, depending on the applied flow and power. Figure 8(c) confirms an approximation of the negligible impact of N_2 admixing used for OES experiments on T_g. The method of Rayleigh scattering has higher sensitivity compared to OES, and T_g can be estimated with an uncertainty of ±15 degrees. This allows us to see the effect of the input RF power on the gas temperature which was undetectable in OES measurements. As presented in figures 9(a), (b), the RF power increase results in an almost linear increase in the gas temperature of the effluent. The maximum increase of temperature was found for the smallest flow rate of Ar gas due to less effective heat transfer at 2 slm. The radial averaged value of T_g measured by Rayleigh scattering is in very good agreement with the OES method based on OH(A–X) emission. On the other hand, the disagreement with results obtained through the use of N_2 emission is almost 100 K for all conditions. This leads to the conclusion of a strong overestimation of T_g in the case of utilisation of emission of the second positive system of N_2 for the determination of T_g.

Despite the good agreement of the Rayleigh scattering results and OES method based on OH(A–X) emission, elastic laser scattering is not free of one well-known intrinsic problem: the scattering is dependent on the species density, and

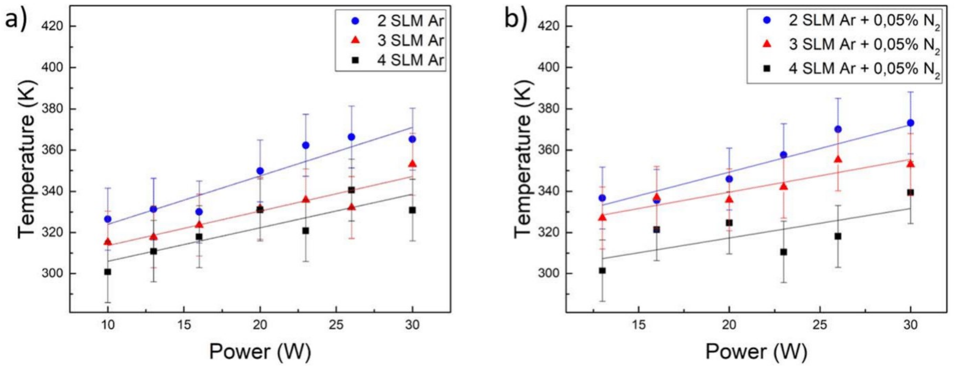

Figure 9. The gas temperature T_g that corresponds to the inter-electrode region analysed through averaging the Rayleigh scattering signal in (a) Ar gas; (b) Ar + N_2 mixture.

so it requires the validity of the condition that gas flow dynamics are not affected by plasma. In this work, the aforementioned problem was checked, and the effect of the gas flow dynamics on elastic scattering was validated by inelastic Raman scattering of the laser light on N_2 and O_2 molecules appearing in the effluent due to ambient air diffusion. The Raman spectrum was measured in Ar plasma with 0.2% admixing of molecular gas (air) at a position 1.5 mm beneath the nozzle. It has to be noted that due to the Bragg grating used to filter out the Rayleigh line at 532 nm, the detection scheme presented in figure 2(b) has a low radial resolution. To this end the spatially averaged Raman signal was detected and compared with the Rayleigh scattering results. As mentioned earlier, the Raman signal-based gas temperature was only used to validate the applicability of the Rayleigh scattering method in order to clarify the effect of the discharge on the gas flow dynamics. Accordingly, the spatially averaged Raman signal over the region indicated as ROI in figure 8(a) was used as an indicator of the average temperature of the plasma jet effluent and was compared with the Rayleigh scattered signal averaged over the same length.

The strongest influence of plasma on gas flow dynamics is expected at the lowest gas flow and high power. For this reason, Raman spectroscopy was performed at 2 slm Ar flow. In order to calculate T_g from the Raman spectra, theoretical Raman spectra were fitted to the experimental results with input parameters: the resolution of the spectrometer, N_2 and O_2 density, and T_g. Both anti-Stokes and Stokes signals were observed but due to the stronger Stokes signal, only this part of the Raman spectra was analysed. The experimental and fitted Stokes components of the Raman spectra are presented in figure 10.

During experiments, it was found that the first three lines in Stokes components with $J \leqslant 3$ were partially affected by the strong Rayleigh signal which was still present even after filtration by the single BNF-532 filter. All three lines were excluded from the fitting procedure as well as lines above 535.2 nm (corresponding to $J > 14$) as the S/N ratio was too low for high J-number lines due to the low line intensity. The Raman spectrum fitting indicates T_g of 320 ± 25 K for 15 W RF power, which is in good agreement with the Rayleigh scattering result of 330 ± 15 K obtained by averaging the scattered signal over the ROI −7 to +7 mm, indicated in figure 8(a). Considering the good agreement between Rayleigh and Raman spectroscopy results it can be concluded that RF discharge in α-mode does not affect the dynamics of the gas flow and the method of Rayleigh scattering is applicable to similar plasmas.

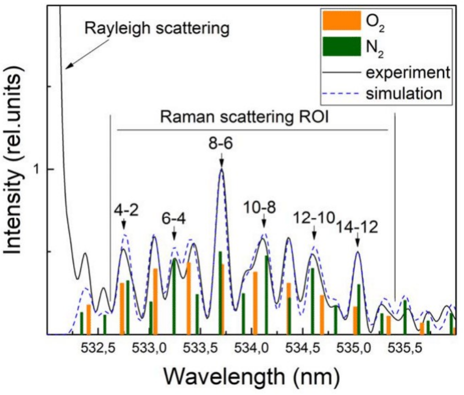

Figure 10. Example of normalised experimental and simulated Raman spectra (Stokes component) for Ar plasma with 0.2% molecular gas admixing for RF forward power of 15 W. Raman components attributed to O_2 and N_2 are presented with red and green colour with an indication of the rotational numbers of the lines.

In summary, the rotational temperature measured by emission of the OH(A) band effectively represents the gas temperature evaluated by the direct detection of Rayleigh scattering. The method based on emission spectroscopy of ro-vibrational bands of OH radicals can be used in future tests of the developed source in biomedical tests and treatment of skin surfaces where the applicability of other methods is technically challenging.

4. Conclusions

An annular-shape RF APPJ was characterised with electrical and temperature diagnostics. The plasma device was designed for biomedical application in wound healing and topical drug delivery with possible aerosol introduction through a hollow inner-electrode. For this reason, the aim was to obtain uniform and cold plasma in order to prevent any damage to the skin. The obtained results showed that this could be achieved with RF capacitively coupled discharge operating in a uniform diffuse α-mode at RF power below 30 W. In order to explain the stability of the uniform α-mode of the discharge, the processes of diffusion and recombination were analysed. It is proposed that stabilisation of the discharge operation in α-mode is achieved due to the presence of the sheath.

The gas temperature in the plasma was determined using the OES technique based on the rotational temperature of OH radicals $A^2\Sigma+ \rightarrow X^2\Pi_i$ (0,0) band and N_2 $C^3\Pi_u \rightarrow B^3\Pi_g$ (0, 2) band. The temperature obtained by the fitting method of the OH $A^2\Sigma^+$-$X^2\Pi$ (0,0) band indicated T_g of 340, 320 and 310 K for a flow of 2, 3 and 4 slm of Ar. Considering the safety limit of the source applicability of 333 K (60 °C), for a short treatment time, it can be concluded that the operational range of the APPJ is limited by a flow rate above 2 slm in the case of α-mode. However, the measurements for N_2 and OH bands yield discrepant results of almost 100 K, where the highest temperatures of 450–480 K are obtained in the case of N_2. For this reason, the temperature measurements by the OES technique were revalidated by two other independent techniques based on laser scattering. Rayleigh scattering has shown uniform temperature distribution at RF forwarded below 20 W while at higher powers the inner-electrode region is noticeable for low flow. For a flow higher than 2 slm, mixing with middle part starts to be significant, thermalisation occurs and the temperature distribution is close to uniform. The radially averaged T_g determined by the Rayleigh method is in good agreement with the OH temperature determined by emission spectroscopy. The assumption of the negligible effect of plasma ignition on gas flow dynamics and so on the results of Rayleigh scattering was validated by Raman scattering. It was revealed that both methods agree well with OES results based on OH (A–X) measurements. The low gas temperature of the RF plasma source combined with the uniform and diffuse afterglow and possibility of the source coupling with aerosol injection is considered to be beneficial for a variety of biomedical applications, including topical drug injection and wound healing.

Acknowledgements

The research work performed was supported by the FWO/ARRS agencies project ‘Plasma-skin interactions: from wound treatment to topical introduction of molecules’, numbers G084917N and N3-0056, respectively.

ORCID iDs

Ivana Sremački https://orcid.org/0000-0001-9263-2002
Lei Wang https://orcid.org/0000-0002-8341-2881

References

[1] Penkov O V *et al* 2015 A review of recent applications of atmospheric pressure plasma jets for materials processing *J. Coat. Technol. Res.* **12** 225–35
[2] Tendero C *et al* 2006 Atmospheric pressure plasmas: a review *Spectrochim. Acta B* **61** 2–30
[3] Weltmann K D and von Woedtke T 2017 Plasma medicine-current state of research and medical application *Plasma Phys. Controlled Fusion* **59** 11
[4] Weltmann K D *et al* 2010 Atmospheric-pressure plasma sources: Prospective tools for plasma medicine *Pure Appl. Chem.* **82** 1223–37
[5] Isbary G *et al* 2013 Non-thermal plasma—More than five years of clinical experience. Clinical Plasma *Medicine* **1** 19–23
[6] Von Woedtke T, Metelmann H R and Weltmann K D 2014 Clinical plasma medicine: state and perspectives of *in vivo* application of cold atmospheric plasma *Contrib. Plasma Phys.* **54** 104–17
[7] Winter J, Brandenburg R and Weltmann K D 2015 Atmospheric pressure plasma jets: an overview of devices and new directions *Plasma Sources Sci. Technol.* **24** 19
[8] Park G Y *et al* 2012 Atmospheric-pressure plasma sources for biomedical applications *Plasma Sources Sci. Technol.* **21** 21
[9] Selwyn G *et al* 2001 Materials processing using an atmospheric pressure, RF-generated plasma source *Contrib. Plasma Phys.* **41** 610–9
[10] Niemi K, Schulz-Von Der Gathen V and Döbele H 2005 Absolute atomic oxygen density measurements by two-photon absorption laser-induced fluorescence spectroscopy in an RF-excited atmospheric pressure plasma jet *Plasma Sources Sci. Technol.* **14** 375
[11] Brandenburg R 2017 Dielectric barrier discharges: progress on plasma sources and on the understanding of regimes and single filaments *Plasma Sources Sci. Technol.* **26** 053001
[12] Wang S, Schulz-Von der Gathen V and Döbele H 2003 Discharge comparison of nonequilibrium atmospheric pressure Ar/O_2 and He/O_2 plasma jets *Appl. Phys. Lett.* **83** 3272–4
[13] Schutze A *et al* 1998 The atmospheric-pressure plasma jet: a review and comparison to other plasma sources *IEEE Trans. Plasma Sci.* **26** 1685–94
[14] Laux C O *et al* 2003 Optical diagnostics of atmospheric pressure air plasmas *Plasma Sources Sci. Technol.* **12** 125–38
[15] Sarani A, Nikiforov A Y and Leys C 2010 Atmospheric pressure plasma jet in Ar and Ar/H_2O mixtures: optical emission spectroscopy and temperature measurements *Phys. Plasmas* **17** 8
[16] Bruggeman P J *et al* 2014 Gas temperature determination from rotational lines in non-equilibrium plasmas: a review *Plasma Sources Sci. Technol.* **23** 32
[17] Murphy A and Farmer A 1992 Temperature measurement in thermal plasmas by Rayleigh scattering *J. Phys. D: Appl. Phys.* **25** 634

[18] Van Gessel A *et al* 2012 Laser scattering on an atmospheric pressure plasma jet: disentangling Rayleigh, Raman and Thomson scattering *Plasma Sources Sci. Technol.* **21** 015003

[19] Kuhn M *et al* 2017 Plasma actuators for active flow control based on a glow discharge *14th High-Tech Plasma Processes Conf.* ed D Uhrlandt, P Teulet and J Schein (Bristol: IOP Publishing Ltd)

[20] Neretti G, Ricchiuto A C and Borghi C A 2018 Measurement of the charge distribution deposited by an annular plasma synthetic jet actuator over a target surface *J. Phys. D: Appl. Phys.* **51** 9

[21] Klarenaar B L M *et al* 2018 A rotational Raman study under non-thermal conditions in a pulsed CO_2 glow discharge *Plasma Sources Sci. Technol.* **27** 12

[22] Bruggeman P *et al* 2009 Characterization of a direct dc-excited discharge in water by optical emission spectroscopy **18** 13

[23] Sobolev N 1985 Electron-excited molecules in a nonequilibrium plasma *Proc. Lebedev Physics Institute, Academy of Sciences of the USSR* 157 (New York: Nova Science)

[24] Miles R B, Lempert W R and Forkey J N 2001 Laser Rayleigh scattering *Meas. Sci. Technol.* **12** R33–51

[25] Sneep M and Ubachs W 2005 Direct measurement of the Rayleigh scattering cross section in various gases *J. Quant. Spectrosc. Ra.* **92** 293–310

[26] deRegt J M *et al* 1996 Air entrainment in an inductively coupled plasma measured by Raman and Rayleigh scattering *Spectrochim. Acta B* **51** 1527–34

[27] Brehmer F *et al* 2015 Gas temperature in transient CO_2 plasma measured by Raman scattering *J. Phys. D: Appl. Phys.* **48** 6

[28] Jia F D *et al* 2011 Laser scattering diagnosis of a 60-Hz non-equilibrium atmospheric pressure plasma jet *Appl. Phys. Express* **4** 3

[29] Penney C M, Stpeters R L and Lapp M 1974 Absolute rotational Raman cross-sections for N_2, O_2, and CO_2 *J. Opt. Soc. Am.* **64** 712–6

[30] Penney C, Peters R S and Lapp M 1974 Absolute rotational Raman cross sections for N_2, O_2, and CO_2 *JOSA* **64** 712–6

[31] Long D A and Long D 1977 *Raman Spectroscopy* vol 206 (New York: McGraw-Hill)

[32] Hoskins L C 1975 Pure rotational Raman spectroscopy of diatomic molecules *J. Chem. Educ.* **52** 568

[33] Eckbreth A C 1996 *Laser Diagnostics for Combustion Temperature and Species* vol 3 (Boca Raton, FL: CRC Press)

[34] Klarenaar B L M *et al* 2015 Note: rotational Raman scattering on CO_2 plasma using a volume Bragg grating as a notch filter *Rev. Sci. Instrum.* **86** 3

[35] Deng X *et al* 2015 Absolute and relative emission spectroscopy study of 3 cm wide planar radio frequency atmospheric pressure bio-plasma source *Appl. Phys. Lett.* **107** 053702

[36] Hofmann S *et al* 2011 Power dissipation, gas temperatures and electron densities of cold atmospheric pressure helium and argon RF plasma jets *Plasma Sources Sci. Technol.* **20** 065010

[37] Lieberman M A and Lichtenberg A J 2005 *Principles of Plasma Discharges and Materials Processing* (New York: Wiley)

[38] Winchester M R and Payling R 2004 Radio-frequency glow discharge spectrometry: a critical review *Spectrochim. Acta B* **59** 607–66

[39] Nilsson J W and Riedel S A 2001 *Introductory Circuits for Electrical and Computer Engineering* (London: Pearson Education)

[40] Yanguas-Gil A *et al* 2007 Optical and electrical characterization of an atmospheric pressure microplasma jet for Ar/CH_4 and Ar/C_2H_2 mixtures *J. Appl. Phys.* **101** 103307

[41] Reuter S 2008 *Formation Mechanisms of Atomic Oxygen in an Atmospheric Pressure Plasma Jet Characterised by Spectroscopic Methods* (Göttingen, Germany: Cuvillier Verlag)

[42] Cullen P J and Milosavljevic V 2015 Spectroscopic characterization of a radio-frequency argon plasma jet discharge in ambient air *Prog. Theor. Exp. Phys.* **2015** 063J01

[43] Kawamura E *et al* 2014 Particle-in-cell and global simulations of α to γ transition in atmospheric pressure Penning-dominated capacitive discharges *Plasma Sources Sci. Technol.* **23** 0963–0252

[44] Wang L *et al* 2017 Mechanisms of sustaining a radio-frequency atmospheric pressure planar discharge *Plasma Sources Sci. Technol.* **26** 075012

[45] Fridman A 2008 *Plasma Chemistry* (Cambridge: Cambridge University Press)

[46] Mitchner M and Kruger C 1973 *Partially Ionized Gasses* (New York: Wiley)

[47] Nikiforov A Y *et al* 2015 Characterization of a planar 8 mm atmospheric pressure wide radiofrequency plasma source by spectroscopy techniques *Plasma Phys. Controlled Fusion* **58** 014013

[48] Raizer Y P, Shneider M N and Yatsenko N A 1995 *Radio-Frequency Capacitive Discharges* (Boca Raton, FL: CRC Press) p 42

[49] Vorac J *et al* 2017 Batch processing of overlapping molecular spectra as a tool for spatio-temporal diagnostics of power modulated microwave plasma jet *Plasma Sources Sci. Technol.* **26** 025010

[50] Bruggeman P *et al* 2010 Electronic quenching of OH(A) by water in atmospheric pressure plasmas and its influence on the gas temperature determination by OH(A-X) emission *Plasma Sources Sci. Technol.* **19** 7

Chapter 3

Tracking Plasma Surface Modifications of Materials

This chapter is focused on tracking plasma parameters during plasma surface modifications of materials, more precisely designing polymer/nanoparticle composites and improving electrical properties of carbon-based gas sensors. Surface modifications are made to improve or influence surface properties by changing the physical, chemical or biological characteristics of the original material. Modifications can be inflicted by different means – physical or chemical procedures – depending on the required result. One promising way to modify the surface is by atmospheric pressure plasma, which holds many beneficial properties. The main feature of plasma jets is that plasma is not confined between electrodes, but the plasma plume can be adjusted and used to treat confined spaces (such as cavities, inner walls of wells or other narrow spaces). Another feature is its low gas temperature, which makes a plasma jet perfect for treatment of thermally sensitive materials like polymers and papers. Plasma can help change surface properties, like wettability, adhesion or functionalization, or participate in impregnation of different materials onto the treated surface. Usually a plasma gas is selected that can achieve the desired effect in surface treatment. The selection of the gas combined with the plasma setup and power source can bring about desired results. Other parameters that are of importance are distance between the plasma plume and treated surface, and treatment time.

In this chapter, OES was used to analyze the optical content of the plasma jet, monitor plasma–material interaction processes, and detect and track possible related energetically excited volatile degradation products. APPJ systems used in these experiments performed stable and uniform surface treatments that were energetically soft, as OES did not detect any energetically excited states of volatile compounds from the treated material.

A detailed description and results are described in the following subchapters:

0.

Atmospheric Pressure Plasma Jet-Assisted Impregnation of Gold Nanoparticles into Polyvinyl Chloride Polymer for Various Applications

3.2. Improving Sensing Properties of Entangled Carbon Nanotube-Based Gas Sensors by Atmospheric Plasma Surface Treatment

This chapter addresses thesis Objective 1.

3.1 Atmospheric Pressure Plasma Jet-Assisted Impregnation of Gold Nanoparticles into Polyvinyl Chloride Polymer for Various Applications

As polymers are a relatively inexpensive materials with good bulk properties and many possible applications, there is a need to improve their surface properties to tailor them for specific applications they are used for. This chapter shows the creation of gold nanoparticle impregnated polyvinyl chloride (PVC) polymers that could be utilized for various applications, such as antibacterial substrates, nanoplasmonic sensing devices, improved dose measurements, catalysis, immunoassay systems, photovoltaic devices, polymeric nanocomposite membranes and fuel cells. This research focused on preparing nanoparticle impregnated polymers from scratch – nanoparticles were synthesized by laser ablation and impregnation was achieved with the help of a kHz-operated He APPJ.

This research introduces a new method for APPJ-assisted impregnation of Au nanoparticles into PVC surfaces in order to fabricate polymer/nanoparticle composites. Nanoparticles are synthesized by pulsed laser ablation of a metallic target immersed in liquid (laser ablation in liquids (LAL)). This technique provides non-inhalable colloidal nanoparticles with no residues or by-products, and no further purification is needed. Plasma impregnation of nanoparticles to polymer kept the bulk material unchanged. This impregnation method is rapid, energy-efficient, non-toxic, and a low-cost route to impregnation that needs only a small amount of nanoparticles due to two-dimensional dispersion on the surface. Produced polymer/nanoparticle composites had a relatively homogenous surface at the microsized scale due to increased surface roughness, which prevailed the size of synthesized nanoparticles making them mechanically confined within the ripples of the surface.

In order to track changes inside plasma and induced by plasma, various diagnostic techniques were implemented both on the gas discharge and on the polymer/nanoparticle composite. OES showed the difference in intensities of detected reactive species during polymer/nanoparticle treatment, but no new excited species were detected when plasma was in contact with the colloidal solution.

Regarding my contribution: I performed laser ablation in liquids for synthesis of colloidal gold nanoparticles, plasma-assisted impregnation of those nanoparticles to PVC polymer and OES diagnostics of plasma. I wrote the paper with the co-authors.

The International Journal of Advanced Manufacturing Technology
https://doi.org/10.1007/s00170-018-2988-4

ORIGINAL ARTICLE

Atmospheric pressure plasma jet–assisted impregnation of gold nanoparticles into PVC polymer for various applications

Andrea Jurov[1,2] · **Dean Popović**[1] · **Iva Šrut Rakić**[1,3] · **Ida Delač Marion**[1,3] · **Gregor Filipič**[4] · **Janez Kovač**[4] · **Uroš Cvelbar**[4] · **Nikša Krstulović**[1]

Received: 23 July 2018 / Accepted: 4 November 2018

Abstract
Atmospheric pressure plasma jet is used as a tool to design polymer/nanoparticle composite materials for various applications. The aim of this research is to get a cheap and green method for nanoparticle impregnation into polymer surfaces. The proposed route consists of nanoparticle synthesis by laser ablation in water and their impregnation into polymers assisted by atmospheric pressure plasma jet. The impregnation is achieved by increased roughness of treated samples containing nanoparticles which are embedded into such rough structures. This proof-of-concept method is based on pre- or post-treatment of PVC polymer drop-coated with Au nanoparticles by helium atmospheric pressure plasma jet.

Keywords Atmospheric pressure plasma jet · Polymer nanocomposites · Nanoparticles impregnation · Polymer treatments · Poly(vinyl chloride) (PVC)

1 Introduction

Polymers are relatively inexpensive materials with good bulk properties for a wide range of applications. However, the physical and chemical properties of polymer bulk material may be modified, improved, and tailored either by changing their surface properties (like wettability, adhesion, functionalization) or by impregnation of some metal nanoparticles making a new class of polymer composite materials [1, 2]. Such polymer/nanoparticle hybrid materials have drawn much attention having excellent properties for many applications in nanobiotechnology, nanobiomedicine, nanochemistry, optoelectronics, and food industry. Those applications include gold nanoparticles (AuNPs) impregnated into bulk polymers or polymer particles for development of anti-bacterial substrates (anti-biofilms) [3], nanoplasmonic sensing devices [4], improved radiation dose measurements [5], catalysis [6], immunoassay systems [7], photovoltaic devices [8], polymeric nanocomposite membranes [9], and fuel cell electrocatalysis [10].

PVC (polyvinyl chloride) polymer is biocompatible for wide variety of applications in nanobiomedicine for blood contact–related supplies like blood bags and drug delivery systems [11, 12]. Plasma treatment of PVC polymers is widely used for achieving anti-microbial polymer properties for various applications in biomedicine or in medical devices [13–16]. Moreover, AuNP-modified PVC is used for development of biosensors for detection of phenols [17] or glucose [18], amperometric [19, 20] and colorimetric [21] sensors, and as a multi-functional flexible sensor [22].

In this paper, we introduce a new proof-of-concept method for atmospheric pressure plasma jet (APPJ)-assisted impregnation of AuNPs into PVC surfaces in order to fabricate polymer/nanoparticle composites. APPJ, as a cold (non-thermal) plasma, is ideal for treatment of surfaces of thermally sensitive materials such as polymers. It operates at the ambient pressure, and it is highly reactive due to a presence of various reactive species [23–25]. We propose a route of polymer

---

Electronic supplementary material The online version of this article (https://doi.org/10.1007/s00170-018-2988-4) contains supplementary material, which is available to authorized users.

✉ Nikša Krstulović
niksak@ifs.hr

[1] Institute of Physics, Bijenička cesta 46, HR-10000 Zagreb, Croatia

[2] Jožef Stefan International Postgraduate School, Jamova 39, 1000 Ljubljana, Slovenia

[3] Center of Excellence for Advanced Materials and Sensing Devices, Institute of Physics, Bijenička cesta 46, 10000 Zagreb, Croatia

[4] Jožef Stefan Institute, Jamova 39, 1000 Ljubljana, Slovenia

surface modification which is based on a combination of APPJ and AuNPs synthesized ex situ by laser ablation of gold in water. Laser synthesis of nanoparticles in liquids is based on the process of pulsed laser ablation of metallic target immersed in liquid (laser ablation in liquids (LAL)) [26–28]. This technique is known as one of "green synthesis" techniques as it provides not inhalable colloidal nanoparticles with no residues or by-products, while often no further purification is required [29]. LAL technique is capable of nanoparticle synthesis from a wide variety of materials [30–34].

With this method, AuNPs are impregnated into the surface of the polymer keeping the bulk material unchanged. It is a rapid, energy-efficient, non-toxic, and low-cost route for the impregnation that needs only a small amount of nanoparticles due to 2D dispersion and impregnation into the polymer surface. PVC polymer appeared as a representative candidate for this case study of AuNP impregnation because of its huge roughness increase under the influence of APPJ which would appear as positive repercussion for AuNP impregnation.

2 Experimental section

2.1 Nanoparticle synthesis route

A colloidal solution of AuNPs was synthesized through the process of pulsed laser ablation in deionized water using Nd:YAG laser (Quantel, Brilliant). Laser specifications are as follows: pulse duration 5 ns, wavelength 1064 nm, output energy 290 mJ, repetition rate 5 Hz, and total number of applied laser pulses 2000. The target was a gold plate (purity 99.99%) with a thickness of 0.1 mm. Target was fixed on the target holder and immersed in a quartz cuvette ($2 \times 4 \times 4$ cm^3) filled with 30 ml of deionized water. Laser beam was directed by a system of prisms and focused by a lens (with focal length of 10 cm) onto the target surface. Laser pulse energy in front of the target was 210 mJ while a diameter of a focused pulse on the target surface was 1 mm which yields a laser fluence of 27 J/cm^2. The thickness of a water layer above the target was kept constant at 1.5 cm during the experiment in order to keep the ablation efficiency, and thus nanoparticle properties, constant [35]. A scheme of experimental setup for LAL is depicted in details in recent work [36]. The target was moved every 500 pulses by 2 mm relative to the incident laser beam to avoid drilling of a crater through whole sample. Instead, four craters were produced for further analysis. The obtained AuNP colloidal concentration is estimated to be of order or 4×10^8 ml^{-1} while the calculation procedure is described in [37, 38].

A colloidal solution of laser-synthesized AuNPs was analyzed using a spectrophotometer (Perkin Elmer, Lambda 25) to assess the UV-Vis absorption spectrum. Zeta potential (Malvern Zetasizer) of Au colloidal solution is measured to be − 18 mV which makes a colloidal solution of moderate stability. The photoabsorption peak at 526 nm decreases for 15% after 10 days due to precipitation and agglomeration of colloidal AuNPs.

2.2 PVC treatment with atmospheric pressure plasma jet

The experimental scheme of APPJ used for treatment of PVC is presented in Fig. S1. It is a type of single-electrode plasma jet operating with the power source with the sinusoidal output signal whose peak-to-peak voltage and frequency are 7 kV and 20 kHz, respectively [39]. Power electrode was a copper wire with a diameter of 0.15 mm. The wire was inserted inside of the borosilicate glass capillary tube and ended near the orifice of the tube. The capillary tube was 75 mm long with 1.2-mm inner diameter and 1.5-mm outer diameter. Working gas was He 4.6 (purity 99.996%). Gas flow was measured and controlled using a digital flow meter (Cole-Parmer). The gas flow was 2 slm while the visible length of the jet was 1.2 cm. All samples were positioned at 1 cm from the end of capillary orifice intersecting the visible end of jet and then exposed to an APPJ for 2 min. Sample holder was made of glass to avoid the effect of second electrode or grounding of single-electrode jet. Plasma jet was monitored by optical emission spectroscopy (OES). For this purpose, 16-bit Avantes Sens CCD spectrometer was used and it recorded spectra in the wavelength range from 200 to 750 nm with spectral resolution of 0.5 nm. Spectra were not corrected to spectral response as they were used qualitatively for species identification only. PVC samples' dimension was 1×1 cm^2. Imaging was performed from the 0.5×0.5-cm^2 area around the center of the PVC. During APPJ treatment of PVC, a temperature measurement of samples was performed using infrared thermometer (Cole-Parmer). Also, voltage and current waveforms of APPJ were acquired using voltage (Tektronix P6015A) and current (Pearson current monitor model 2877) probes.

The inset in Fig. S1 presents a photograph of a helium atmospheric pressure plasma jet in contact with PVC polymer. Optical emission spectra were recorded at the point of interaction of the jet and the polymer, while optical fiber was inclined by 45° with respect to the target surface to collect the signal from plasma jet affected area, and at the same point but without polymer sample for comparison (free jet).

There are generally two standard routes to impregnate nanoparticles into polymers: the first is based on addition of nanoparticles into the polymer as a dispersion/reaction medium, and the second is based on deposition of nanoparticles onto the pre-synthesized polymer (onto the surface or into the bulk; in that case polymer acts as a dispersion medium). In both cases, nanoparticles can be synthesized ex situ by a variety of chemical methods and in situ particularly by chemical reduction, ion exchange, and sol-gel methods [40, 41].

In Fig. S2, general nanoparticles impregnation/incorporation routes into polymers are sketched including standard techniques (a) and (b) and a method proposed in this work (c):

(a) In situ synthesis/impregnation of nanoparticles into polymers matrix with various chemical methods (3D impregnation)
(b) Ex situ synthesis of nanoparticles and impregnation/dispersion into polymers by deposition where polymers as dispersion medium are in liquid phase or in form of a casting solution (it usually yields 3D impregnation, but rarely 2D is also possible)
(c) Ex situ synthesis of nanoparticles by LAL and further APPJ-assisted surface impregnation of nanoparticles before or after the drop-coating of colloidal nanoparticle solution onto the polymer surface (2D impregnation). This method is described with steps (iv) and (v) of treatment cases presented in Fig. 1.

In Fig. 1, AuNP impregnation scheme is presented: (i) untreated sample (control sample), (ii) AuNPs deposited onto polymer surface by drop-coating method (drop of colloidal AuNPs left at the polymer surface until the water evaporates), (iii) polymer surface treated by APPJ (without AuNPs addition), (iv) polymer surface pre-treated with APPJ and then drop-coated with AuNP colloidal solution, and (v) AuNPs deposited by drop-coating onto the polymer surface and subsequently post-treated by APPJ. In case (iii), polymer surface roughness increased solely due to APPJ treatment, the roughness of samples in cases (iv) and (v) changed due to combination of APPJ treatment and AuNP presence, while in case (ii), roughness may be changed only due to a presence of AuNPs. Note that the first two steps in case (iv) correspond to case (iii) while the first two steps in case (v) correspond to case (ii).

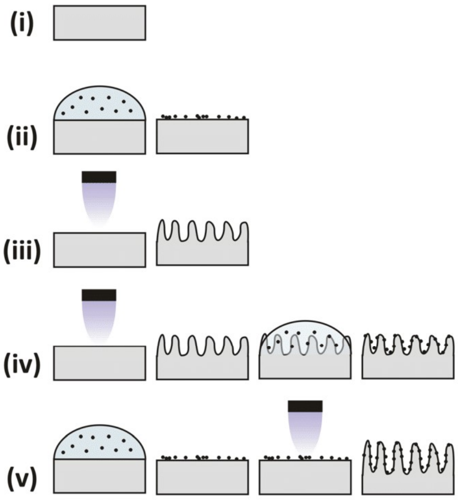

Fig. 1 APPJ treatment cases: (i) untreated sample, (ii) AuNPs colloid drop-coating, (iii) APPJ treatment, (iv) AuNPs colloid drop-coating onto APPJ pre-treated surface, and (v) APPJ treatment of polymer surface containing AuNPs

The contact angle was measured using an optical microscope and determined by image editing program GIMP. The contact angle was measured for drop of deionized water and colloidal solution of AuNP at PVC surface before and after the APPJ treatment.

2.3 PVC and AuNP characterization

PVC was characterized with atomic force microscopy (AFM), scanning electron microscopy (SEM), and X-ray photoelectron spectroscopy (XPS).

AFM measurements were carried out with Nanosurf FlexAFM in a dynamic force mode in air using AppNano silicon tips (nominal spring constant of 36–90 N/m, a tip radius less than 10 nm, and nominal resonant frequency of 160–225 kHz). AFM images were analyzed using WSxM 5.0 program in order to quantify the roughness of the samples [42].

The size distribution of AuNPs was obtained using AFM imaging where a drop of colloidal solution was placed onto the Si substrate. The AFM imaging was performed after the water evaporates by measuring the height of AuNPs (diameter) with the assumption that the AuNPs are not deformed due to the applied force of a tip [43].

The SEM analysis was done on a field emission Jeol JSM-7600F microscope. The electron accelerating voltage was 10 kV. Before the observations, samples were coated with a thin layer of amorphous carbon (PECS 682) to prevent charge accumulation on the surface. Observation mode was set to low-energy secondary electron detection.

The XPS analyses were carried out on the PHI-TFA XPS spectrometer produced by Physical Electronics Inc. Samples were mounted on the metallic sample holder. The analyzed area was 0.4 mm in diameter, and the analyzed depth was about 3–5 nm. Sample surfaces were excited by X-ray radiation from monochromatic Al source at a photon energy of 1486.6 eV. The high-energy resolution spectra were acquired with energy analyzer operating at the resolution of about 0.6 eV and pass energy of 29 eV. During data processing, the spectra were aligned by setting the C 1s peak at 285 eV, characteristic for C-C/C-H bonds in polymers. The accuracy of binding energies was about ± 0.3 eV. Quantification of surface composition was performed from XPS peak intensities taking into account relative sensitivity factors provided by instrument manufacturer [44]. We estimate that the relative error of calculated concentrations is about 20% of reported values. XPS spectra were analyzed by a Multipak software (version 8.0, Physical Electronics Inc.).

3 Results and discussion

In order to analyze the optical emission content of APPJ and to monitor the interaction process with PVC, the OES was used as it is a versatile technique to monitor plasma-material interaction processes and related energetically excited volatile degradation products [45–48].

Optical emission spectra of free-standing He APPJ and APPJ in interaction with PVC are presented in Fig. 2a. Both spectra show the same emission content with the only difference in intensity. OES spectrum of APPJ during treatment of PVC containing AuNPs was the same as in the case of pure PVC and was omitted from the graph for better clarity. The identified emission lines are as follows: He, O, and Hα (Balmer series) atomic lines, OH band ($A^2\Sigma$-$X^2\Pi$), N_2 2nd positive band ($C^3\Pi_u$-$B^3\Pi_g$), and N_2^+ 1st negative band ($B_2\Sigma_u^+$-$X^2\Sigma_g^+$). Temporal evolution of emission line intensities of OH at 309 nm, O at 777 nm, He at 706 nm, Hα at 656 nm, N_2 at 315 nm, and N_2^+ at 428 nm was performed and shown in Fig. 2b for free APPJ (full line and full symbols). Corresponding emission line intensities when APPJ interacts with PVC are also shown for comparison (dotted line, empty symbols). It can be seen that all lines show 2-fold enhancement in emission when APPJ interact with PVC, except for N_2 when the enhancement is three times higher. The intensity of nitrogen molecules dominates in both cases which is due to a diffusion of a surrounding air into the plasma jet. In the case of interaction of plasma jet with the polymer, plasma is dispersed and accumulated outside the region of intersection of jet and surface what yields increased N_2 diffusion rate (increased plasma affected area) resulting in 3-fold emission signal enhancement. The N_2^+ does not follow the same 3-fold enhancement as it appears through the Penning ionization involving N_2 molecules and He metastable atoms while an amount of He is insufficient (observed is a 2-fold enhancement) to make 3-fold enhancement of N_2^+ [49, 50]. It is expected that He metastable atoms around 389 nm also exist in APPJ, but they are either of low density (low emission signal) or overlap with N_2^+ broad line at 391 nm [51, 52]. However, emission intensities from APPJ interacting with the PVC are stable in time showing no alteration in intensities. It implies that the performed treatment is uniform and stable in time but energetically soft as there are no volatile compounds in energetically excited states which can be detected by OES. Anyway, such compounds in ground energetic state are expected as APPJ interacts with PVC mainly through etching processes (described later). These observations are expected as temperature of the sample does not reach high values which can be seen from temperature dependence on treatment time which is shown on the right *y*-axis in Fig. 2b. It is shown that temperature of PVC sample is increasing rapidly in the first 30 s from initial 23 to 40 °C reaching a final temperature of 42 °C at the end of treatment. Temperature increase obviously did not affect the OES signal which confirms that APPJ interact softly with PVC. The temperature dependence was not changed when PVC containing AuNP was used instead of control PVC. Also, voltage and current waveforms were identical both during the treatment of PVC with and without AuNPs (results not shown here). Typically, the change in discharge current is accompanied with a change in OES signal [53], none of which was observed in our experiments. Therefore, the presence of AuNPs does not lead to a stronger OES signal of APPJ interacting with PVC samples. That is because either single AuNPs or agglomerates (if exist) are scattered onto the polymer surface with no contact to each other. Thus, they cannot act as a second electrode which will certainly increase the OES signal. UV-Vis absorption spectrum

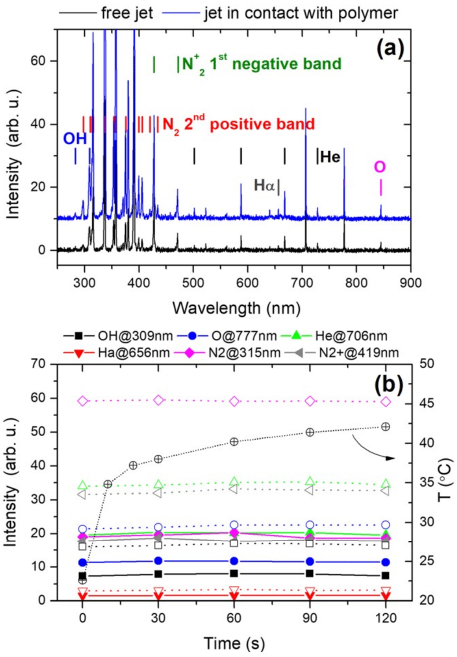

Fig. 2 **a** Optical emission spectra of He APPJ: free jet and jet in contact with PVC. **b** Temporal evolution of selected emission lines (left axis) and PVC temperature dependence on treatment time (right axis). Temporal evolution of selected optical emission lines in free jet is shown with full symbols and full line while of jet in contact with the PVC with empty symbols and dotted line

of the colloidal solution of AuNPs synthesized by LAL and the size distribution of colloidal AuNPs is presented in Fig. 3a, b, respectively. Orthogonal blue lines correspond to root mean square (RMS) roughness of PVC (shown afterwards in Fig. 5) obtained by a procedure depicted in Fig. 1(i)–(v). The size of roughness could be directly compared to the size of AuNPs to get insight into the impregnation mechanism. The absorbance exhibit distinct maximum at 526 nm typically for AuNPs sized of few tens of nanometers while the shape of the absorbance curve indicates that the AuNPs in the solution are spherical [54–57]. From Fig. 3b, it can be seen that the average AuNP diameter is 30 nm.

Representative AFM images of PVC polymer samples are presented in Fig. 4. Samples (i)–(v) correspond to the treatment cases presented in Fig. 1. It is evident that the surface morphology and AuNP distribution is highly influenced by the treatment procedure. This can be further corroborated by RMS roughness of PVC surface and by SEM imaging. The RMS roughness of polymer surface for different cases of APPJ treatment and AuNP impregnation is presented in Fig. 5. It is obvious that RMS roughness increases dramatically when APPJ treatment is applied in any form. It is reflected on the contact angle and consequently on AuNP distribution on the PVC surface. Measured water contact angle for untreated PVC (case (i), roughness is 12 nm) is 78° while for APPJ-treated PVC (case (iii), roughness is 131 nm) is 61°. Contact angle for drop of AuNPs decreases from 81° to 69° for cases (i) and (iii), respectively. The decrease in contact angles after APPJ treatment indicates that hydrophilicity (wettability) of the polymer increases due to increased roughness. It is worth to note that the contact angle for both liquids of the untreated surface of sample (iii) was the same as for sample (i) which means that APPJ treatment did not affect the lower surface of the sample but just upper (exposed) one. Moreover, the roughness of untreated surface of sample (iii) was the same as for sample (i). The other effect of APPJ treatment is that drop of either deionized water or AuNP colloid stays still on an untreated sample for approximately 2 h, while in APPJ-treated samples, it spreads onto the sample surface immediately giving better homogeneity and dispersion of AuNPs over the sample surface. AuNP dispersion onto the PVC ((ii) case) shows low distribution homogeneity due to a higher hydrophobicity of flat polymer surface than in APPJ-treated rough surfaces. Namely, during slow-drying process (evaporation of water) of drop of AuNPs, smaller and unevenly distributed drops were formed leaving zones of AuNP agglomerates or larger islands on the polymer surface behind. That promotes the final formation of unevenly distributed irregular agglomerations as is shown in Fig. 4(ii). Single AuNPs can also be observed. Unlike in case (ii), drop of AuNPs during drying on APPJ-treated polymer surface (lower hydrophobicity) is immediately distributed when applied onto the surface leaving evenly distributed single AuNPs with no agglomerates. PVC treated with APPJ (case (iii)) shows homogenously distributed ripples and rough structures which is important for further AuNP distribution and impregnation. Thus, one can expect for PVC pre-treated with APPJ and impregnated with AuNPs (case (iv)) to have a more uniform and smoother distribution with respect to case (ii). In case (iv) in Fig. 4, a sparse concentration of single AuNPs settled among ripples and forming relatively homogeneous distribution without dominating agglomerations. The dispersion is evidently more homogeneous than in case (ii). That is due to increase in surface roughness (or decrease in contact angle) allowing colloidal AuNP drop of solution to even and rapid spread onto the surface during drying without formation of agglomerations. In case (v) in Fig. 4, AuNPs cannot be easily identified as dimension of ripples (roughness is order of magnitude higher than AuNP size) far prevail their size. Possible agglomerates

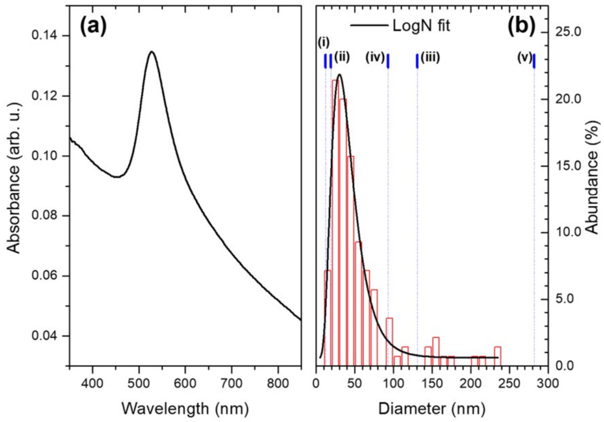

Fig. 3 **a** UV-Vis absorbance spectrum of colloidal AuNPs. **b** Size distribution of AuNPs (column bars) and LogN fit (black curve). Vertical blue lines represent RMS roughness of samples (i)–(v)

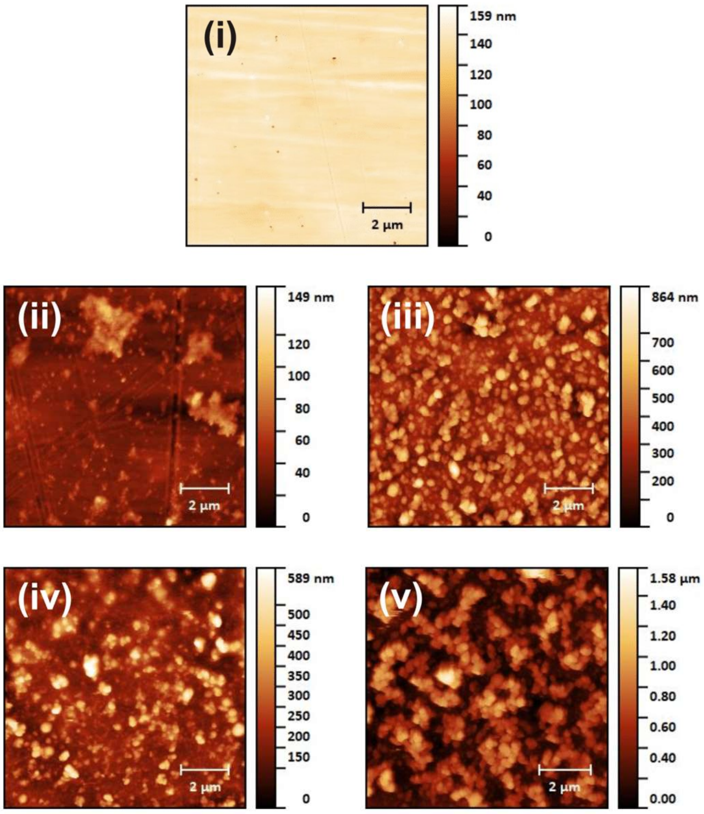

Fig. 4 AFM images of PVC polymer: (i) untreated sample, (ii) Au colloid drop-coating, (iii) APPJ treatment, (iv) Au colloid drop-coating onto APPJ pre-treated surface, and (v) APPJ treatment of polymer surface containing AuNPs

are also not identified. In that case, AuNPs were drop-coated onto the PVC surface forming case (ii) with uneven AuNP distribution. After dropping and evaporation, sample (ii) was treated with APPJ inducing redistribution of AuNPs together with formation of rough structure on the PVC surface and leading to a formation of AuNP impregnated surfaces. As the AuNP redistribution and formation of high ripples (and rough structure) is happening together in time, one can assume that AuNPs are impregnated into the polymer chains of newly formed ripples and rough structures.

In Fig. 3b, a size distribution of AuNPs is shown together with RMS roughness for cases (i)–(v) for comparison. The average size AuNPs (30 nm) is larger but comparable to the surface roughness of untreated PVC sample (which is 12 nm), case (i). When PVC was treated with APPJ, an RMS roughness increases dramatically making the roughness far larger than the size of AuNPs (cases (iii)–(v)). In cases when roughness is

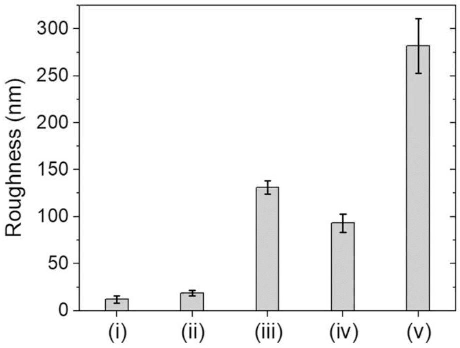

Fig. 5 The RMS roughness of PVC polymer samples (i)–(v)

smaller and comparable to AuNP size, the contact area between the AuNPs and polymer is small and they can easily drift on the polymer surface upon drying process which yields to formation of agglomerations. As the roughness becomes higher than the AuNPs size, the contact area is higher and the AuNPs are more readily impregnated and trapped into the elevated polymer ripples. In that case, it is hard to de-attach them from the polymer. For example, roughness for case (v) is 282 nm which is ten times higher than AuNP mean diameter, making AuNPs to settle among the rough structures. Therefore, the higher the roughness, the better the distribution of impregnated AuNPs into PVC surfaces, and the better the mechanical resistivity and the AuNP dispersion. Mechanical resistivity was provisionally tested by scratching the PVC with impregnated AuNPs. However, high roughness increases the attachment sites for nanoparticles or generally for any other coatings [58]. It was found that the stability of entrapped nanoparticles deposited onto the polymer matrix of filtration membranes is very high (mitigation test of sludge filtration) due to entrapment of nanoparticles in polymer matrix of membrane, especially as compared with other methods [59–61].

SEM morphology of PVC impregnated with AuNPs is shown in Fig. 6 for cases (ii), (iv), and (v) at two magnifications. SEM images reveal similar findings which are obtained from AFM imaging. Again, it can be seen that the morphology of PVC surface significantly depends on the treatment procedure. Drop-coated PVC in (a) and (b) images shows distinct AuNPs on top of irregular agglomerations which were agglomerated during drying. Visually, the surface is much dimmer than that of the control sample. APPJ-treated PVC surface in Fig. 6c has more regularly distributed elevated ripples and structures than that in Fig. 6a. Note that white spots in Fig. 6c, d are elevated ripples and structures formed upon (iv) APPJ treatment. Here, single AuNPs are difficult to identify due to high roughness. Therefore, the APPJ pre-treated PVC impregnated with AuNPs by drop-coating shows even and regular distribution of elevated ripples while single AuNPs are settled among them avoiding formation of agglomerates. The similar findings apply to the case (v) shown in Fig. 6e, f.

We assume that the AgNPs are incorporated in the surface of the polymers as they can penetrate into the polymer material only through voids in polymer chains. SEM images obtained with higher energies (not shown here) show either the same nanoparticles imaged with low energies or absence of nanoparticles which implies that AuNPs did not penetrate deep into the bulk polymer.

Elemental composition obtained with XPS of PVC polymer treated with APPJ and AuNPs is shown in Table 1 for all

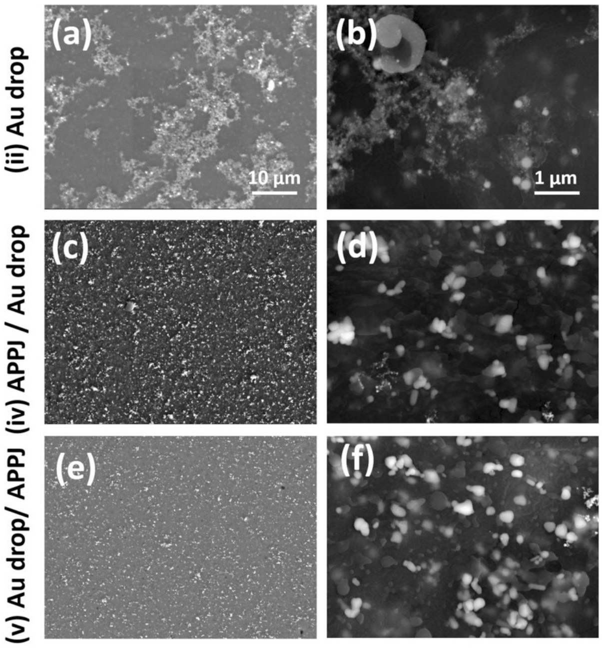

Fig. 6 SEM images of PVC (ii), (iv), and (v) samples. Scale bar is 10 µm in the first column and 1 µm in the second. Arrows are pointed to identified AuNPs

Table 1 XPS elemental composition of PVC polymer treated with different treatment cases

APPJ treatment case Element	(i) Concentration (at%)	(ii)	(iii)	(iv)	(v)
C	81	69	61.7	59.8	59.7
O	13	22	23	30	27
Cl	6	8.8	12.3	9.6	11.3
Au	0	0.2	0	0.2	0.5
N	0	0	3	0.4	1.5

treatment cases (i)–(v). It can be seen that composition depends on treatment case. Results shows that samples (ii), (iv), and (v) contain AuNPs as expected, while sample (v) reveal the highest relative concentration of AuNPs. One can observe that the C concentration in case (i) is high with respect to Cl as it would not be expected for clean PVC sample. This is probably partially related with atmospheric contamination of PVC foil with CH.

In Fig. 7, ratios O/C, Cl/O, and Cl/O are presented. APPJ interaction with sample surface induces also some kind of surface oxidation recognized by increase of oxygen surface concentration for samples (iii), (iv), and (v), in particular with respect to carbon concentration. Similar to the surface oxidation, an increase of chlorine concentration was observed for APPJ-treated samples (iii), (iv), and (v). This can be partially explained by APPJ cleaning/etching process of the polymer surface. Cl/O ratio is varying depending on the oxidation/etching rate.

Carbon XPS C 1s spectra from all samples are shown in Fig. 9. Carbon C 1s was reported in literature to have four peaks: at 284.6 eV assigned to C-C and C-H groups, at 285.8 eV assigned to C-O and C-Cl groups, at 287.5 eV assigned to N-C=O and C=O groups and at 289 eV assigned to O-C=O groups [16, 62]. Peaks were deconvoluted into different peaks marked as C1, C2, C3, and C4 as is shown in Fig. 8(i). The results of fitting of carbon spectra C 1s are given in Table 2 where binding energies, relative concentrations of fitted peaks, and assignment of carbon bonds are shown. We should note that some charging effect might take place during XPS analyses resulting in small shifts of binding energies of acquired spectra and fitted peaks**.**

From Fig. 8 and Table 2, it can be seen that carbon C 1s spectrum from sample (i) is characterized by a strong C1 peak which is probably related with surface contamination layer consisting mainly of C-C/C-H bonds. Part of the peaks C2 and C3 recognized in C 1s spectrum originate from PVC structure. From Fig. 8, one can observe similarity of shape of carbon C 1s spectra from samples (ii) and (iv) on one side and from sample (iii) and (v) on another side. Samples (ii) and (iv) have similar strong C2 peaks and similar relative intensity of C1 peaks, which are lower than C2 peaks. These features are mainly related with a deposition of the AuNPs on surfaces as being the last step in treatment of samples (ii) and (iv). Probably, a strong peak C2 (C-O/C-Cl) from these samples reflects that AuNPs are embedded in an oxidized carbon polymer surface.

As mentioned before, carbon C 1s spectra from samples (iii) and (v) have also similar shape reflecting a high relative concentration of the C1 peaks (C-C/C-H) and lower concentration of C2 peaks (C-O/C-Cl). It is explained as APPJ plasma treatment being the last step of treatment of these samples, which gives the most significant feature to the surface. We

Fig. 7 The elemental ratio of PVC samples obtained by XPS method

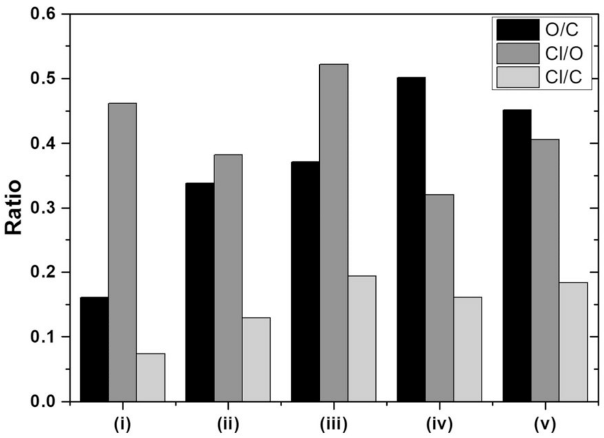

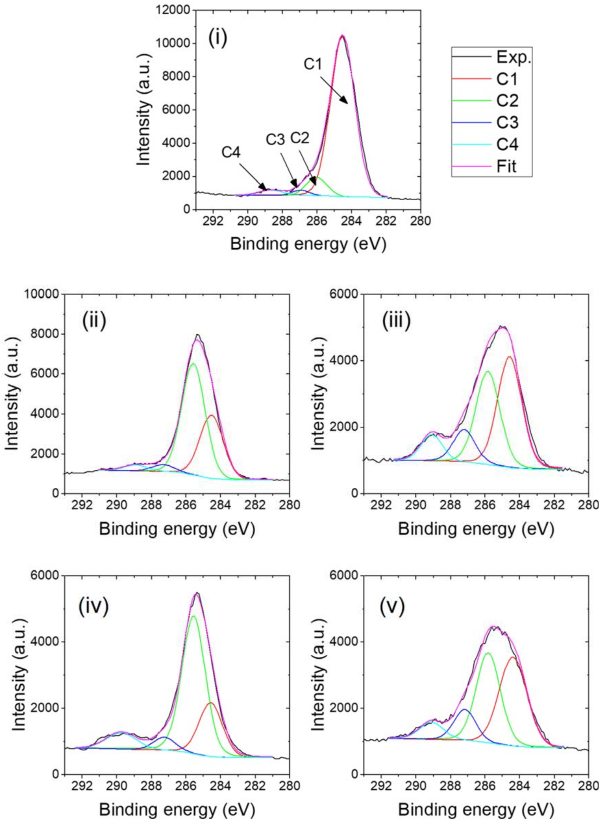

Fig. 8 Carbon XPS C 1s spectra deconvoluted into C1, C2, C3, and C4 peaks

assume that APPJ plasma treatment first induces a chain session in the PVC matrix and afterwards a cross-linking of the chains. The last process is reflected by increase of C-C/C-H bonds observed in C 1s spectra and relative concentrations of C1 peaks are higher for samples (iii) and (v) than for (ii) and (iv).

Au 4f spectra from samples (ii), (iv), and (v) are shown in Fig. 9. The Au 4f spectrum consists of a double peaks Au $4f_{7/2}$ and $4f_{5/2}$ separated by 3.67 eV. The XPS spectra shown in Fig. 7 of Au 4f from samples (ii) and (iv) show only the metallic Au $4f_{7/2}$ peak at binding energy of 84.0 eV, which indicates that AuNPs do not react with the PVC surface. APPJ

Table 2 Binding energies (eV) of peaks fitted in C 1s spectra, their relative concentrations in %, and assignments of chemical bonds of carbon atoms

APPJ treatment case			(i)	(ii)	(iii)	(iv)	(v)
C1s component	Functional groups (bonds)	Binding energy (eV)	Concentration (at%)				
C1	C-C/C-H	284.6 ± 0.5	87	33	43	21	42
C2	C-O/C-Cl	285.8 ± 0.5	10	59	36	62	39
C3	N-C=O/C=O	287.5 ± 0.5	0	4	12	7	12
C4	O-C=O	289.0 ± 0.5	3	4	9	10	8

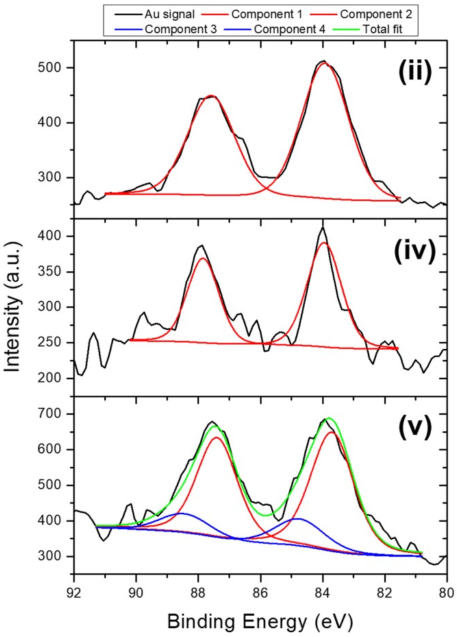

Fig. 9 XPS spectra of Au 4f of samples (ii), (iv), and (v)

treatment of sample (v) presumably yields interaction of AuNPs with APPJ resulting in new type of the Au bond ($4f_{7/2}$ peak at 84.8 eV) in addition to metallic Au bonds ($4f_{7/2}$ peak 84.0 eV). It is possible that Au-oxide like or some other Au-C species are formed on the Au-core nanoparticles. Note that in case (v), APPJ interact with AuNPs and PVC samples in the same time together promoting the interaction between AuNPs and activated PVC surface. APPJ interaction with the sample was also reflected by nitrogen signal N 1s in XPS spectra of samples (iii), (iv), and (v). Evidently, N_2 molecules are present in (or close to) the APPJ and they interact with activated PVC surface. The relative N concentration is the highest for sample (iii) which can be explained by stronger plasma–surface interaction. It can be seen from Fig. 2 that OES signal from N_2 molecules is significantly intensified with respect to all other observed lines when APPJ interacts with the PVC. The presence of nitrogen in PVC APPJ-treated surfaces indicates a surface grafting of reactive species [63, 64].

The surface roughness of polymers treated with low-temperature plasma is generally increased due to a compositional change of the surface induced via two mechanisms of etching [65–67]. The first mechanism is etching induced by oxidation, and it can be ascribed to cases (iii)–(v) as in all those cases increased concentration of oxygen is observed by XPS. The other mechanism is etching via oxidation of AuNPs, and it can be ascribed to (v) case only. That can explain why roughness is extremely increased in (v) case where contribution of those two mechanisms combines. It is supported with XPS results where certain oxidation level of AuNPs is revealed (formation of Au-oxide-like species).

Generally, when PVC is treated by APPJ, the sample surface becomes rich in C-O (C2 peak), C=O, and N-C=O groups (peak C3) with respect to untreated sample (i) [68]. The surface of PVC is oxidized, i.e., functionalized with oxygen-rich functional groups due to incorporation of oxygen atoms onto the PVC surface. It was found that as long as the temperature of polymer is low, the concentration of oxygen-rich functional group is constant but when oxidation became severe and the heating of the sample increases, the oxygen-rich functional group concentration decreases [69]. In our case, a heating of material is well below glass transition temperature (which is 85 °C) and significantly below degradation (240 °C) and melting temperatures (280 °C) (as can be seen from Fig. 2b) [70]. There was no effect of heating on untreated sample surface as well as no change in contact angle of untreated sample surface which would be expected if heating plays a role. Therefore, the role of thermal effects on the APPJ-treated PVC surface properties are neglected and morphological change may be ascribed solely to etching via mentioned oxidation mechanisms.

4 Conclusion

A novel method to impregnate AuNPs onto the PVC surface is proposed. It is based on either APPJ pre-treatment of PVC surface and then drop-coated with AuNPs or on APPJ post-treatment of AuNPs colloidal drop-coated PVC surface. In both cases, surface roughness significantly increases while roughness value far prevail the size of applied AuNPs making them mechanically tightly confined within the ripples of the rough surface. APPJ-assisted PVC impregnated with AuNPs synthesized by LAL technique is mechanically stable and resistive while the AuNP distribution onto the PVC surface is relatively homogeneous at microsized scale due to increased hydrophilicity (roughness).

The proposed method should further allow wide variety of polymers to be impregnated with different types of nanoparticles as no thermal damage occur using APPJ. It makes proposed method a versatile tool for nanoparticle impregnation into the polymer surfaces for various applications. Further mitigation, scratch, and tribological testings are planned.

Acknowledgements N.K. acknowledges COST Action TD1208 "Electrical Discharges with Liquids for Future Applications" which provided relevant discussions.

Funding This work was partially supported by the project "Laser-Cold Plasma Interaction and Diagnostics" (HrZZ-IP-11-2013-2753) funded by the Croatian Science Foundation and partially from "Laser synthesis of Au nanoparticles in liquids" funded by the Croatian Academy of Science and Arts. A.J., G.F., and U.C. are supported by grants M.ERA-Net "PlasmaTex" and L2-6769 ARRS (Slovenian Research Agency).

References

1. Hanemann T, Szabó DV (2010) Polymer-nanoparticle composites: from synthesis to modern applications. Materials 3:3468–3517
2. Bleach R, Karagoz B, Prakash SM, Davisn TP, Boyer C (2014) In situ formation of polymer−gold composite nanoparticles with tunable morphologies. ACS Macro Lett 3:591–596
3. Sawant SN, Selvaraj V, Prabhawathi V, Doble M (2010) Antibiofilm properties of silver and gold incorporated PU, PCLm, PC and PMMA nanocomposites under two shear conditions. PLoS One 8(e63311):1–9
4. Polavarapua L, Liz-Marzán LM (2013) Towards low-cost flexible substrates for nanoplasmonic sensing. Phys Chem Chem Phys 15: 5288–5300
5. Rahman WN, Wong CJ, Ackerly T, Yagi N, Geso M (2012) Polymer gels impregnated with gold nanoparticles implemented for measurements of radiation dose enhancement in synchrotron and conventional radiotherapy type beams. Australas Phys Eng Sci Me 35:301–309
6. Liao W, Wu BZ, Nian H, Chen HY, Yu JJ, Chiu KH (2012) Fabrication of a form- and size-variable microcellular-polymer-stabilized metal nanocomposite using supercritical foaming and impregnation for catalytic hydrogenation. Nanoscale Res Lett 7(283):1–7
7. Hirsch LR, Jackson JB, Lee A, Halas NJ, West JL (2003) A whole blood immunoassay using gold nanoshells. Anal Chem 75:2377–2381
8. Du H, Cao Y, Bai Y, Zhang P, Qian X, Wang D, Li T, Tang X (1998) Photovoltaic properties of polymer/Fe_2O_3/polymer heterostructured microspheres. J Phy Chem B 102:2329–2332
9. Homayoonfal M, Mehrnia MR, Mojtahedi YM, Ismail AF (2013) Effect of metal and metal oxide nanoparticle impregnation route on structure and liquid filtration performance of polymeric nanocomposite membranes: a comprehensive review. Desalin Water Treat 51:3295–3316
10. Zhang RC, Sun D, Zhang R, Lin WF, Macias-Montero M, Patel J, Askari S, McDonald C, Mariotti D, Maguire P (2017) Gold nanoparticle-polymer nanocomposites synthesized by room temperature atmospheric pressure plasma and their potential for fuel cell electrocatalytic application. Sci Rep 7:1–9
11. Modjarrd K, Ebnesajjad S (2014) Handbook of polymer applications in medicine and medical devices. William Andrew Publishing, Chadds Ford
12. Fedorov K, Jankowski A, Sheikh S, Blaszykowski C, Reheman A, Romaschin A, Nid H, Thompson M (2015) Prevention of surface-induced thrombogenesis on poly(vinyl chloride). J Mater Chem B 3:8623–8628
13. Favia P, d'Aggostino R (1998) Plasma treatments and plasma deposition of polymers for biomedical applications. Surf Coat Technol 98:1102–1106
14. Balazs DJ, Triandafillu K, Wood P, Chevolot Y, van Delden C, Harms H, Hollenstein C, Mathieu HJ (2004) Inhibition of bacterial adhesion on PVC endotracheal tubes by RF-oxygen glow discharge, sodium hydroxide and silver nitrate treatments. Biomaterials 25:2139–2151
15. Zhang W, Chu PK, Ji J, Zhang Y, Liu X, Fu RKY, Ha PCT, Yan Q (2006) Plasma surface modification of poly vinyl chloride for improvement of antibacterial properties. Biomaterials 27:44–51
16. Miao H, Jierong C (2009) Inactivation of Escherichia coli and properties of medical poly(vinyl chloride) in remote-oxygen plasma. Appl Surf Sci 255:5690–5697
17. Sánchez-Obrero G, Mayén M, Rodríguez-Mellado JM, Rodríguez-Amaro R (2012) New biosensor for phenols compounds based on gold nanoparticle-modified PVC/TTF-TCNQ composite electrode. Int J Electrochem Sci 7:10952–10964
18. Sánchez-Obrero G, Cano M, Ávila JL, Mayén M, Mena ML, Pingarrón JM, Rodríguez-Amaro R (2009) A gold nanoparticle-modified PVC/TTF-TCNQ composite amperometric biosensor for glucose determination. J Electroanal Chem 634:59–63
19. García-Pineda I, Mayén M, Rodríguez-Mellado JM, Rodríguez-Amaro R (2013) NADH electrocatalytic oxidation on gold nanoparticle-modified PVC/TTF-TCNQ composite electrode. Application as Amperometric Sensor. Electroanalysis 25:1981–1987
20. Sánchez-Obrero G, Mayén M, Rodriguez Mellado JM, Rodríguez-Amaro R (2011) Electrocatalytic oxidation of acetaminophen on a PVC/TTF-TCNQ composite electrode modified by gold nanoparticles: application as an amperometric sensor. Int J Electrochem Sci 6:2001–2011
21. Lee KY, Kim DW, Heo J, Kim JS, Yang JK, Cheong GW, Han SW (2006) Novel colorimetric sensing of anion with gold nanoparticles-embedded plasticized polymer membrane. Bull Kor Chem Soc 27: 2081–2083
22. Segev-Bar M, Landman A, Nir-Shapira M, Shuster G, Haick H (2013) A tunable touch sensor and combined sensing platform: towards nanoparticle-based electronic skin. ACS Appl Mater Interfaces 5:5531–5541
23. Tendero C, Tixier C, Tristant P, Desmaison J, Leprince P (2006) Atmospheric pressure plasmas: a review. Spectrochim Acta B 6:2–30
24. Laroussi M, Akan T (2007) Arc-free atmospheric pressure cold plasma jets: a review. Plasma Process Polym 4:777–788
25. Lu X, Naidis GV, Laroussi M, Reuter S, Graves DB, Ostrikov K (2016) Reactive species in non-equilibrium atmospheric-pressure plasmas: generation, transport, and biological effects. Phys Rep 630:1–84
26. Yang G (2012) Laser ablation in liquids: principles and applications in the preparation of nanomaterials. Pan Stanford Publishing, Singapore
27. Barcikowski S, Mafuné F (2011) Trends and current topics in the field of laser ablation and nanoparticle generation in liquids. J Phys Chem C 115:4985–4985
28. Zhang D, Gökce B, Barcikowski S (2017) Laser synthesis and processing of colloids: fundamentals and applications. Chem Rev 117:3990–4103
29. Besner S, Kabashin AV, Winnik FM, Meunier M (2008) Ultrafast laser based "green" synthesis of non-toxic nanoparticles in aqueous solutions. Appl Phys A Mater Sci Process 93:955–959
30. Bärsch N, Jakobi J, Weiler S, Barcikowski S (2009) Pure colloidal metal and ceramic nanoparticles from high-power picosecond laser ablation in water and acetone. Nanotechnology 20(445603):1–9
31. Zhang J, Post M, Veres T, Jakubek ZJ, Guan J, Wang D, Normandin F, Deslandes Y, Simard B (2006) Laser-assisted synthesis of superparamagnetic Fe@Au core-shell nanoparticles. J Phys Chem B 110:7122–7128
32. Anikin KV, Melnik NN, Simakin AV, Shafeev GA, Voronov VV, Vitukhnovsky AG (2002) Formation of ZnSe and CdS quantum dots via laser ablation in liquids. Chem Phys Lett 366:357–360

33. Amendola V, Riello P, Meneghetti M (2011) Magnetic nanoparticles of iron carbide, iron oxide, iron@iron oxide, and metal iron synthesized by laser ablation in organic solvents. J Phys Chem C 115:5140–5146
34. Tarasenko NV, Butsen AV, Nedelko MI, Tarasenka NN (2012) Laser-aided preparation and modification of gadolinium silicide nanoparticles in liquid. J Phys Chem C 116:3897–3902
35. Krstulović N, Shannon S, Stefanuik R, Fanara C (2013) Underwater-laser drilling of aluminum. Int J Adv Manuf Technol 69:1765–1773
36. Krstulović N, Umek P, Salamon K, Capan I (2017) Synthesis of Al-doped ZnO nanoparticles by laser ablation of ZnO:Al$_2$O$_3$ target in water. Mater Res Express 4(105003):1–6
37. Krstulovic N, Salamon K, Budimlija O, Kovac J, Dasovic J, Umek P, Capan I (2018) Parameters optimization for synthesis of Al-doped ZnO nanoparticles by laser ablation in water. Appl Surf Sci 440:916–925
38. Krstulovic N, Milosevic S (2010) Drilling enhancement by nanosecond–nanosecond collinear dual-pulse laser ablation of titanium in vacuum. Appl Surf Sci 256:4142–4148
39. Lu X, Laroussi M, Puech V (2012) On atmospheric-pressure non-equilibrium plasma jets and plasma bullets. Plasma Sources Sci Technol 21:034005
40. Zhao P, Li N, Astruc D (2013) State of the art in gold nanoparticle synthesis. Coord Chem Rev 257:638–665
41. Zang Z, Tang X (2015) Enhanced fluorescence imaging performance of hydrophobic colloidal ZnO nanoparticles by a facile method. J Alloy Compd 619:98–101
42. Horcas I, Fernández R, Gómez-Rodríguez JM, Colchero J, Gómez-Herrero J, Baro AM (2007) WSXM: a software for scanning probe microscopy and a tool for nanotechnology. Rev Sci Instrum 78(013705):1–8
43. Guo D, Xie G, Luo J (2014) Mechanical properties of nanoparticles: basics and applications. J Phys D Appl Phys 47:013001
44. Moulder JF, Stickle WF, Sobol PE, Bomben KD (1995) Handbook of X-ray photoelectron spectroscopy, Physical Electronics Inc. Eden Prairie, Minnesota
45. Vesel A, Mozetic M, Drenik A, Milosevic S, Krstulovic N, Balat-Pichelin M, Poberaj I, Babic D (2006) Cleaning of porous aluminium titanate by oxygen plasma. Plasma Chem Plasma Process 26: 577–584
46. Vesel A, Mozetic M, Hladnik A, Dolenc J, Zule J, Milosevic S, Krstulovic N, Klanjšek-Gunde M, Hauptmann N (2007) Modification of ink-jet paper by oxygen-plasma treatment. J Phys D Appl Phys 40:3689–3696
47. Vujošević D, Mozetič M, Cvelbar U, Krstulović N, Milošević S (2007) Optical emission spectroscopy characterization of oxygen plasma during degradation of Escherichia coli. J Appl Phys 101(103305):1–7
48. Krstulović N, Cvelbar U, Vesel A, Milošević S, Mozetič M (2009) An optical-emission-spectroscopy characterization of oxygen plasma during the oxidation of aluminium foils. Mater Tehnol 43:245–249
49. Olenici-Craciunescu SB, Muller S, Michels A, Horvatic V, Vadla C, Franzke J (2011) Spatially resolved spectroscopic measurements of a dielectric barrier discharge plasma jet applicable for soft ionization. Spectrochim Acta B 66:268–273
50. Xiong Q, Lu X, Liu J, Xian Y, Xiong Z, Zou F, Zou C, Gong W, Hu J, Chen K, Pei X, Jiang Z, Pan Y (2009) Temporal and spatial resolved op0tical emission behaviors of a cold atmospheric pressure plasma jet. J Appl Phys 106:083302
51. Zaplotnik R, Bišćan M, Krstulović N, Popović D, Milošević S (2015) Cavity ring-down spectroscopy for atmospheric pressure plasma jet analysis. Plasma Sources Sci Technol 24(054004):1–14
52. Zaplotnik R, Bišćan M, Popović D, Mozetič M, Milošević S (2016) Metastable helium atom density in a single electrode atmospheric plasma jet during sample treatment. Plasma Sources Sci Technol 25(035023):1–10
53. Zaplotnik R, Bišćan M, Kregar Z, Cvelbar U, Mozetič M, Milošević S (2015) Influence of a sample surface on single electrode atmospheric plasma jet parameters. Spectrochim Acta B 103–104:124–130
54. Link S, El-Sayed MA (1999) Size and temperature dependence of the plasmon absorption of colloidal gold nanoparticles. J Phys Chem B 103:4212–4217
55. Haiss W, Thanh NTK, Aveyard J, Fernig DG (2007) Determination of size and concentration of gold nanoparticles from UV-vis spectra. Anal Chem 79:4215–4221
56. Near RD, Hayden SC, Hunter RE Jr, Thackston D, El-Sayed MA (2013) Rapid and efficient prediction of optical extinction coefficients for gold nanospheres and gold nanorods. J Phys Chem C 117: 23950–23955
57. Schlücker S (2009) SERS microscopy: nanoparticle probes and biomedical applications. Chem Phys Chem 10:1344–1354
58. Junkar I, Vesel A, Cvelbar U, Mozetič M, Strnad S (2010) Influence of oxygen and nitrogen plasma treatment on polyethylene terephthalate (PET) polymers. Vacuum 84:83–85
59. Molinari R, Palmisano L, Drioli E, Schiavello M (2002) Studies on various reactor configurations for coupling photocatalysis and membrane processes in water purification. J Membr Sci 206:399–415
60. Bae TH, Tak TM (2005) Effect of TiO$_2$ nanoparticle on fouling mitigation of ultrafiltration membranes for activated sludge filtration. J Membr Sci 249:1–8
61. Rahimpour A, Madaeni SS, Taheri AH, Mansourpanah Y (2008) Coupling TiO$_2$ nanoparticles with UV irradiation for modification of polyethersulfone ultrafiltration membranes. J Membr Sci 313: 158–169
62. Beamson G, Briggs D (1992) High resolution XPS of organic polymers. John Wiley & Sons Ltd., New York
63. Zheng X, Chen G, Zhang Z, Beem J, Massey S, Huang J (2013) A two-step process for surface modification of poly(ethylene terephthalate) fabrics by Ar/O2 plasma-induced facile polymerization at ambient conditions. Surf Coat Technol 226:123–129
64. Rangel EC, dos Santos NM, Bortoleto JRR, Durrant SF, Schreiner WH, Hondac RY, de Cássia R, Rangel C, Cruz NC (2011) Treatment of PVC using an alternative low energy ion bombardment procedure. Appl Surf Sci 258:1854–1861
65. Phan LT, Yoon SM, Moon MW (2017) Plasma-based nanostructuring of polymers: a review. Polymers 9(417):1–24
66. Cvelbar U, Pejovnik S, Mozetič M, Zalar A (2003) Increased surface roughness by oxygen plasma treatment of graphite/polymer composite. Appl Surf Sci 210:255–261
67. Slepička P, Slepičková Kasálková N, Stránská E, Bačáková L, Švorčík V (2013) Surface characterization of plasma treated polymers for applications as biocompatible carriers. Express Polym Lett 7:535–545
68. Suganya A, Shanmugavelayutham G, Serra Rodríguez C (2016) Study on structural, morphological and thermal properties of surface modified polyvinylchloride (PVC) film under air, argon and oxygen discharge plasma. Mater Res Express 3:095302
69. Krstulovic N, Labazan I, Milošević S, Cvelbar U, Vesel A, Mozetič M (2006) Optical emission spectroscopy characterization of oxygen plasma during treatment of a PET foil. J Phys D Appl Phys 39: 3799–3804
70. Bonadies I, Avella M, Avolio R, Carfagna C, Gentile G, Immirzi B, Errico ME (2012) Probing the effect of high energy ball milling on PVC through a multitechnique approach. Polym Test 31:176–181

3.2 Improving Sensing Properties of Entangled Carbon Nanotube-Based Gas Sensors by Atmospheric Plasma Surface Treatment

Gas sensors are used in many different industries and their fabrication mainly depends on the desired application. This subchapter focuses on the effect of APPJ treatment on the surface of CNT-based gas sensor that we produced. APPJ surface treatment allows surface functionalization and defect generation of carbon nanostructures simultaneously. Those modifications can be controlled by choosing appropriate plasma parameters. A thorough study was conducted on the effect of plasma treatment on electrical conductivity, surface properties and chemical functionalities of carbon nanostructures.

To improve the gas sensor properties, the surface itself was treated with a He- and Ar-operated APPJ, while OES was used for monitoring changes in plasma processes. Surface analysis revealed that plasma treatment did not make significant morphological changes; a result supported by OES as it showed no considerable changes in emission spectra. On the other hand, we showed that plasma-treated sensors possess higher sensitivity than non-treated sensors. We concluded that plasma induced defects in the sensor that led to enhanced sensing capabilities.

Regarding my contribution: I performed OES measurements of plasma discharge and scanning electron microscopy (SEM) for morphology analysis of the gas sensors. I co-wrote the interpretation of all results and prepared an original draft of the manuscript.

Microelectronic Engineering 232 (2020) 111403

Contents lists available at ScienceDirect

Microelectronic Engineering

journal homepage: www.elsevier.com/locate/mee

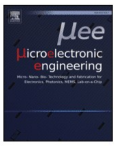

Research paper

Improving sensing properties of entangled carbon nanotube-based gas sensors by atmospheric plasma surface treatment

Neelakandan M. Santhosh[a,b], Aswathy Vasudevan[a,b], Andrea Jurov[a,b], Anja Korent[a,b], Petr Slobodian[c,d], Janez Zavašnik[a], Uroš Cvelbar[a,b,*]

[a] *Jožef Stefan Institute, Jamova cesta 39, 1000 Ljubljana, Slovenia*
[b] *Jožef Stefan International Postgraduate School, Jamova cesta 39, 1000 Ljubljana, Slovenia*
[c] *Tomas Bata University, University Institute, Centre of Polymer Systems, Tr. T. Bati 5678, 760 01 Zlin, Czech Republic*
[d] *Tomas Bata University, Faculty of Technology, Polymer Centre, T.G.M. 275, 760 01 Zlin, Czech Republic*

ARTICLE INFO

Keywords:
Multi-walled carbon nanotubes
Plasma-treatment
Gas sensor
Sensor response
Composite

ABSTRACT

Entangled multi-walled carbon nanotubes (MWCNTs) on polyurethane (PUR) after Ar plasma-treatment and He plasma-treatment have been tested as gas sensors for ethanol sensing. It was found that plasma-treated sensors exhibit higher sensitivity compared to the non-treated samples along with different ethanol concentration. Non-treated sensors exhibit similar sensor response with the increase in ethanol concentration, while Ar plasma-treated sensors displays ~5 times improvement and He plasma-treated sensors show ~3 times improvement with an increase in ethanol concentration. The sensitivity of the plasma-treated sensors is also stable for following two-weeks after the preparation compared to the non-treated sensor. Entangled nanotube network exhibits a significant shift in the baseline resistance after both plasma-treatments. The response time of the sensor was increased after the plasma-treatment, while the recovery was rather quick. Surface analyses revealed that plasma-treatment did not make any significant morphological changes. Thus, the improvements in stability and sensitivity after plasma-treatment are attributed to the plasma-enhanced surface modification and formation of functional bonds on the surface of nanotubes, which are sensitive to the ethanol vapour.

1. Introduction

A gas sensor is a device that detects a particular concentration of gases in its environment. Fabrication of gas sensors mainly depends on the application, mostly on the type of gas that should be detected, its concentration and environment. In general, gas sensors should satisfy many requirements such as high stability, selectivity, good responsivity and quick recovery time [1]; at the same time the product should be low-cost, made from non-toxic and easy to use materials. Besides this, a sensor that operates at room/low temperatures is in high demand since heating of a sensor is more complex and expensive [2]. However, the main challenge for sensors operating at low temperatures remains due to their slow recovery after the sensor response. Along with the requirement for sensors operating at low temperatures, there is a continuous need for high sensitivity, which is dependent on the active surface that the sensing gas can occupy [1,3–7]. Recent studies exhibit that improving sensing performance at low temperatures can be done by using nanostructures [8–10], by layering materials [11–13] and by modifying surface or inducing hybrid structures [14–16]. Unique properties of nanostructures such as gas adsorption capacity due to high surface-to-volume ratio, high structural and thermal stability, high modulation of the electrical charge upon gas exposure, and the possibility of changing the electrical properties by surface modifications can be used for improving the stability and sensitivity of the sensors [17]. Mostly, nanomaterial-based gas sensors are made of metal oxides, carbon nanotubes and graphene. Among them, CNTs possess quick response time, high sensitivity, good reversibility and stability [18].

CNTs are composed of graphene layers rolled into cylindrical geometry, which is classified as single-walled carbon nanotubes (SWCNT) composed of a single layer of graphene and multi-walled carbon nanotubes (MWCNT) composed of multiple layers of graphene with the same central axis [1]. Depending on the tube diameter and chirality, SWCNT can either be metallic or semiconducting in which case they are p-type semiconductors [17]. However, pure crystalline SWCNTs are inert to some volatile organic gases. In the case of MWCNT gas adsorption happens on the outer surface where a molecule connects with the sensor with Van der Waals forces. The molecule changes the electrical charge flow in the sensor, which can be measured as the change in

---

[*] Corresponding author at: Jožef Stefan Institute, Jamova cesta 39, 1000 Ljubljana, Slovenia.
E-mail address: uros.cvelbar@ijs.si (U. Cvelbar).

https://doi.org/10.1016/j.mee.2020.111403
Received 1 March 2020; Received in revised form 7 July 2020; Accepted 19 July 2020

the sensor resistivity [19]. In the case of adsorption of oxidising gas molecules on sensors surface, the electric resistance of CNT decreases with the number of adsorbed gas molecules, due to the creation of additional positive holes as an electric current carrier and *vice versa* [20]. Moreover, sensor response or other sensor properties can be improved by modifying the structure and morphology of the CNTs by combining with different nanostructures [17,21–23], by adding a transition metal [22], by plasma-treatment [19,24–27], *etc.* Compared to other surface modification techniques, plasma-treatment gives the possibility of defect generation and surface functionalisation of CNTs simultaneously, which can be controlled by plasma and treatment conditions. Research done with the plasma-enhanced surface modification of CNTs suggests that both, low and atmospheric pressure plasma can be used for the surface treatment to improve the stability and sensitivity. Depending on the sensor material, one can choose proper plasma type and plasma parameters for the surface modification. These treatment techniques allow changing the chemical composition of the CNT surface without destructing the morphology. Besides the functionalising gases, plasma generated by inert gases such as helium and argon provides higher ion bombardment and creates defects on the CNT surface due to the plasma-assisted etching. Furthermore, plasma-treatment can introduce free electrons to the sensor structure or creating free bonds inside the material, thus making them more sensitive when exposed to analyte vapours.

A variety of CNT based gas sensors are already reported to detect alcohols, where the sensing properties are improved by depositing metal oxides, metals and organic molecules. Among all the alcohol-based sensors, ethanol gas sensors are of considerable interest. Ethanol (C_2H_5OH) is a volatile, flammable, colourless organic compound (VOC) detrimental to the environment, plants, organisms and people [18,23]. Additionally, detection of ethanol fumes is essential in industries, alcohol storage facilities, fruit transportation, and many more. Ethanol is reductive, and when adsorbed on CNT surface, its electrons occupy positively charged holes and consequently increase the resistivity of the material [23,28–31], which results in the p-type sensor response.

In this work, we have designed a simple sensing device using entangled COOH-functionalised MWCNTs for the detection of ethanol at room temperature. Additionally, the effect of atmospheric pressure plasma-treatment on the CNTs using inert gases for improving the sensing properties were investigated. Also, we presented a systematic study on the changes in response and recovery time of the sensors by the effect of plasma-assisted surface modification. The gas sensors were prepared by simple vacuum filtration of MWCNTs on polyurethane (PUR) membrane to form entangled MWCNT sensor, and then they were treated with Ar or He plasma generated at atmospheric pressure. Changes in sensitivity of all sensors were measured by two-point electrical measurements while using ethanol vapours as the target gas. Stability of all prepared sensors was investigated by repeating all the measurements after two weeks. Structural and morphological analysis were obtained by Raman spectroscopy and scanning electron microscopy (SEM) analysis. Changes in the functional entities of the sensors were investigated using Fourier Transform Infrared (FTIR) spectroscopy. Finally, all the results were considered to explain the effect of inert gas plasma-treatment at atmospheric conditions on the sensing properties of entangled MWCNTs.

2. Experimental methods

2.1. Gas sensor preparation

Preparation of bucky paper (BP) was done by a vacuum filtration technique and reported elsewhere [32]. A surfactant solution of pH ≈ 10 was prepared with 46.2 g sodium dodecyl sulphate (Sigma-Aldrich), and 0.14 M water solution of pentanol (Alfa Aesar) in 300 ml deionised water. Separately, 0.8 g of 8% COOH-functionalised MWCNT (Sigma-Aldrich, average diameter × length is 9.5 nm × 1.5 μm) was weighed out and mixed with 250 ml deionised water. The above-prepared surfactant solution and MWCNT-water suspensions were mixed and sonicated for 1 h at room temperature to ensure the fine dispersion of MWCNTs. The suspension was vacuum filtrated through a PUR membrane (GSM 3 g/m^2, Pardam Nanotechnology, Czech Republic) to achieve a flat homogeneous sheet of entangled carbon nanotubes with a thickness of 0.03 ± 0.02 mm, also called the BP (Fig.S1 (a)). To remove the impurities, BP was washed several times with ethanol and distilled water. Prepared BP was left to dry overnight at room temperature. Finally cuts 1.5 × 1.5 cm from prepared BP to fabricate the gas sensors.

2.2. Plasma-treatment

Since the PUR membrane is a temperature-sensitive material, low-temperature atmospheric pressure plasma jet (APPJ) was used for the surface treatment to improve the sensitivity. APPJ system consisted of a single copper electrode without grounding and was powered by a kHz high-voltage signal source. This system allows smooth operation and produces low-temperature plasma, which is suitable for the temperature-sensitive sensors. Inert gases such as argon and helium were used to generate plasma. Compared to mono-functional specific grafting using specific gases like NH_3, O_2 or N_2; atmospheric pressure plasma-treatment using inert gases allows the possibility of surface functionalisation by the functional groups present in the atmosphere [33,34]. Surface treatment was carried out with a gas flow rate of 100 sccm for a fixed time of 3 min. The distance between the sensor and the exit of the APPJ's orifice was fixed at 2.5 cm, meaning that the sensors were treated in the after-glow region of the plasma. Plasma dissipated over the surface, and uniform treatment is assumed.

2.3. Electrical and gas sensing characterisation

I-V characteristics of the sensors were measured by an easy two-point method. We forced a voltage (0-10 V) and measured the current. The gas sensor properties were determined by measuring the change in resistance of sensor during the sensing experiment by a two-point method using a Keithley 2460-high current source meter at a constant input current of 10 mA. Ethanol (ACS reagent for analysis) was used as the sensing gas for investigating the effect of plasma surface treatment on the gas sensor sensitivity. 5 ml volume of ethanol was measured and transferred to a conical flask of 250 ml capacity, and the rest of the flask was filled with ambient air. The sensor was placed to the saturated vapour above the ethanol liquid during the sensing cycle (gas in phase) and placed to an identical conical flask of 250 ml filled with air during the recovery process (gas off phase). The gas in and gas off during the sensing measurements were assigned with an interval of 180 s. The measurements were performed at different temperatures, starting from the room temperature (20 ± 2 °C), then at 35, 50 and 65 °C. The sensor response was calculated using the following equation:

$$\text{Sensor Response} = \frac{R_g - R_a}{R_a} \tag{1}$$

where R_g is the resistance of a sensor after inserting ethanol and R_a is the resistance of the sensor in air. The concentration C_{et} of ethanol, inside the sensing chamber was controlled by heating the ethanol volume to different temperatures. Since the sensing chamber is filled with a mixture of gases (air and ethanol vapour), Dalton's law was used for the estimation of volume-based concentration of ethanol as per the following equation:

$$p_{et} = p_{tot}\, c_{et} \tag{2}$$

where p_{et} is the vapour pressure of ethanol, p_{tot} is atmospheric pressure (101,325 kPa) and c_{et} is the volume-based concentration of ethanol. Calculation of ethanol vapour pressure is well researched, and the values for specific temperatures can be obtained from many databases. In this study, we have used the vapour pressure described in Dortmund Data Bank (http://www.ddbst.com/en/EED/PCP/VAP_C11.php) for the calculation of ethanol concentration. The volume-based concentration of ethanol is estimated as 5.71% at 20 °C, 13,58% at 35 °C, 29,1% at 50 °C, and 57,68% at 65 °C. The concentration is increased by approximately 50% from room temperature to the highest temperature, which opens up an opportunity to explore the influence of ethanol concentration on the sensing measurements. Schematic diagram of the experimental setup was shown in Fig. S1(b). The stability of the prepared sensors was investigated by conducting all the measurements after two weeks.

2.4. Characterisation techniques

Surface morphology of the gas sensors was characterised by SEM analysis (JSM-7600F and JSM-5800, Jeol Inc.), operating at an acceleration voltage 10 kV. Chemical and phase composition of the samples were analysed by transmission electron microscope (TEM, JEM-2010F, Jeol Inc.) operating at 200 kV. The micrographs were recorded by a slow-scan CCD camera (Orius SC1000, Gatan). Raman spectra of the sensors were recorded using NTEGRA confocal Raman spectrometer at an excitation wavelength of 633 nm with an incident power ~ 3 mW and objective of 20× at a spot size of 10 µm. The spectrum was recorded at three different spots of each sensor to eliminate the variations and investigated the structural changes after the plasma-treatment. FTIR spectrum was recorded to analyse the changes in the functional entities of the sensors before and after plasma-treatment using Spectrum GX FTIR spectrometer by Perkin Elmer that was equipped with a photoacoustic detector with 64 scan runs average at 8 cm^{-1}. All the analysis was done right after the sensor preparation and repeated two weeks later to monitor the ageing effect.

3. Results and discussion

3.1. Resistance measurements

The resistance of the as-prepared sensor was measured as (1041 ± 5) Ω. However, the resistance of the sensor is decreased to (702 ± 7) Ω after He plasma-treatment and to (553 ± 10) Ω after Ar plasma-treatment. In addition to the decrease in the resistance, the stability of the resistance after the plasma-treatment should also be noted. Fig. 1 (a) exhibits the steadiness of the resistance of both the non-treated and plasma-treated sensors at the room temperature (20 ± 2 °C). The significant change in the resistance might be due to the surface modification either by plasma-enhanced etching or by the functionalisation of CNT surface. Typical current-voltage (I-V) characteristics of the non-treated and plasma-treated sensors at room temperature are presented in Fig. 1 (b). The linear I-V relationship confirms the ohmic nature of the sensors.

The repeatability of the sensing cycle of the sensors was checked at different concentration of ethanol by heating at different temperatures as 20 °C, 35 °C, 50 °C and 65 °C, and the stability of the sensor was investigated by repeating all the measurements after two weeks. The sensor response measurements are presented in Fig. 2, which suggests that the plasma-treated sensors acquired more stable sensor response than the non-treated sensor. The non-treated sensor possesses an unstable response at room temperature, which slightly turns into a stable response with an increase in temperature. Nevertheless, the change in the sensor response with temperature is not significant. In the case of both plasma-treated sensors, the sensor response became stable and increased with the temperature. He plasma-treated sensors possess similar sensor response at low-temperature, which increases with the temperature and attained ~3 times improvement at 65 °C. Whereas Ar plasma-treated sensors exhibit a substantial improvement of sensor response (~5 times) even at low-temperature and increase with the temperature. A higher concentration of analyte after heating makes the sensor more stable during the sensing cycle. However, the stability studies after two weeks indicated that the maximum response of all the sensors were decreased, especially for non-treated and He plasma-treated sensors.

Average of maximum sensor response was calculated to understand more about the response and repeatability of the sensors changing with temperature. This response is presented in Fig. 3, where the average response of the sensors at different concentration of ethanol (at each temperature calculated using Eq. (2)) at as-prepared and two weeks later conditions. At higher concentrations of ethanol (increase with the elevation of temperature), plasma-treated sensors show better response than the non-treated sensor. Among all the tested sensors, the non-treated sensor exhibits a constant sensor response for all concentrations. For He plasma-treated samples, the response was almost similar to the non-treated sensor but slightly improved with higher concentrations. The highest sensor response was shown by Ar plasma-treated sensor, which could be attributed to the greater extent of surface modifications done by the Ar plasma. However, the stability studies on the average response after two weeks suggest that the maximum sensor response of all the sensors become lower than the as-prepared conditions. In the

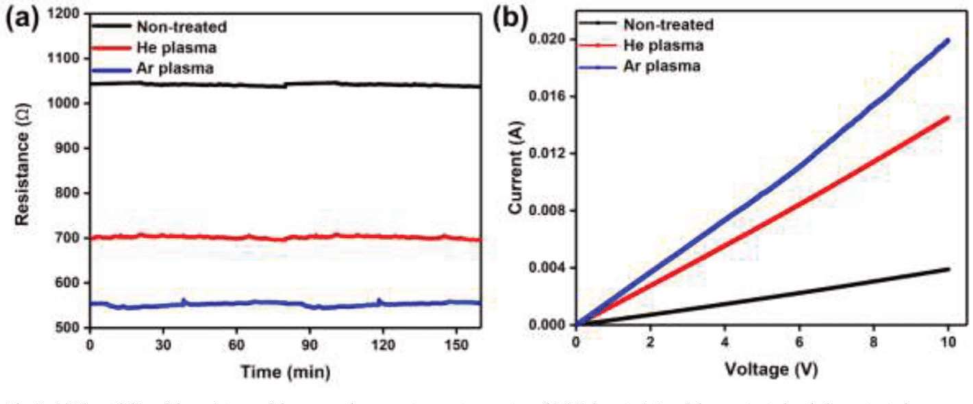

Fig. 1. (a) The stability of the resistance of the prepared sensors at room temperature, (b) I-V characteristics of the non-treated and plasma-treated sensors.

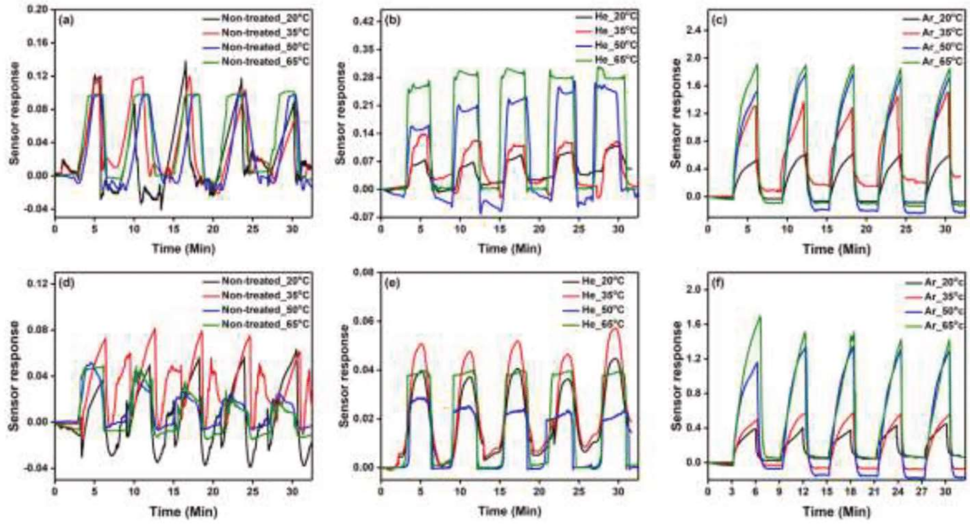

Fig. 2. The repeatability of vapour detection on (a) non-treated and (b) He plasma-treated and (c) Ar plasma-treated sensors; and corresponding measurements of stability in performance after two weeks for (d) non-treated, (e) He plasma-treated and (f) Ar plasma-treated sensors.

case of non-treated and He plasma-treated sensors, the sensor response was negligible after two weeks, even when the ethanol concentrations increased. On the other hand, Ar plasma-treated samples disclosed a stable response after two weeks and the sensor response increases with increasing the ethanol concentration.

The response and recovery curve of the sensors are presented in Fig. 4. The gas in and gas off during the sensor measurements are assigned with an interval of 180 s. The results show that the Ar plasma-treated sensors have higher sensor response, and the recovery to the initial resistance is quicker for the non-treated and He plasma-treated sensors. These results indicate that Ar plasma-treatment has made significant changes in the properties of sensor. Moreover, Ar plasma-treated sensors appear to be the most stable in both response and recovery even after two weeks. On the contrary, the non-treated sensor displays a behaviour where the response drops instantaneously to the value below the initial resistance and then recovers to the original value after the gas off. The response and recovery appear to be better after two weeks, which could be explained by the surface interaction with the surroundings. However, He plasma-treated sensors have much longer recovery time than the response time. Since the change in sensor response is minimal, it implies that the capability of the sensor to adsorb ethanol vapour is comparatively low even after the plasma-treatment. During the recovery, the resistance falls below the original value and then recovered to the initial value similar to non-treated sensor. However, the response curves after two weeks displays similar behaviour as the initial response.

A comparison between the response and recovery times of all the sensors at the room temperature is given in Fig. 5. The response time T_{res}, of the sensors, was defined as the time taken to achieve 90% of the maximum change in resistance. In contrast, recovery time T_{rec} was calculated as the time taken to recover to 90% of the initial resistance from the maximum resistance change occured during the sensing cycle. A schematic explanation for the calculation of T_{res} and T_{rec} from our results is shown in Fig. S2. It was observed that the as-prepared He

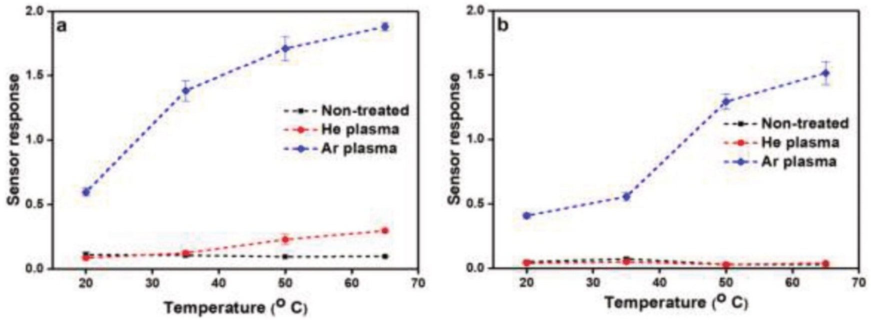

Fig. 3. The average sensor response compared to the concentration of ethanol for all the sensors (a) as-prepared and (b) two weeks later.

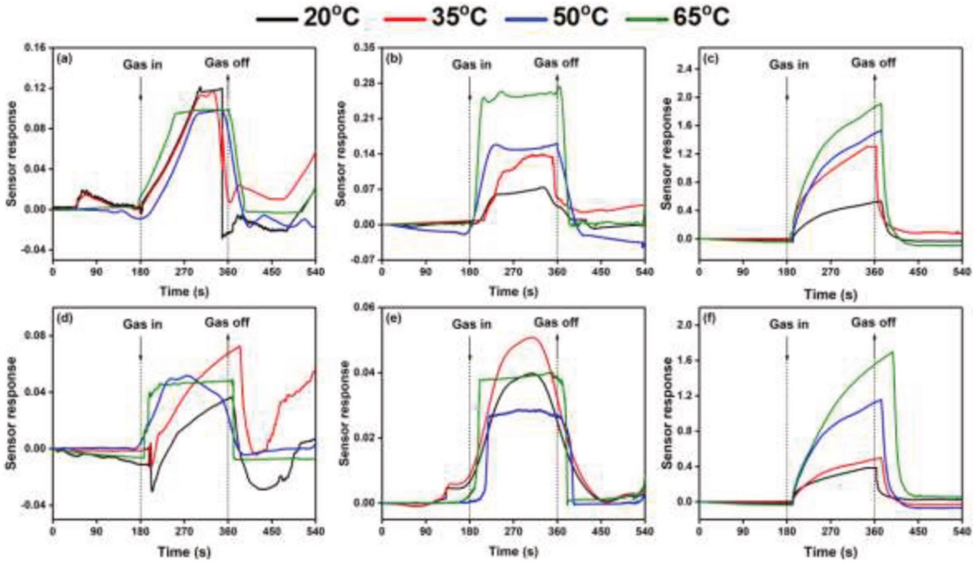

Fig. 4. The response curve for the first sensing cycle of the sensors at different temperatures: (a) non-treated, (b) He plasma-treated and (c) Ar plasma-treated; two weeks later: (d) non-treated, (e) He plasma-treated and (f) Ar plasma-treated sensors.

plasma-treated sensor had the fastest response time of 114 s, whereas the highest response time of 152 s was observed for Ar plasma-treated sensor. On the other hand, in the case of recovery, Ar plasma-treated sensor had the fastest recovery time of 40 s, where the non-treated sensor was displayed the slowest recovery time of 152 s. After two weeks, the non-treated sensors took the longest time to respond as well as to recover (156 s and 142 s respectively). He plasma-treated sensor had the fastest response of 88 s and Ar plasma-treated sensor demonstrates the fastest recovery time of 79 s. These results are indicating that the different plasma-treatments using inert gases are causing different effects on the surface of sensors, which allows tuning the gas sensing properties.

Since both the electrical resistance and sensing properties of the sensors change with plasma-treatment, which also varies after two weeks of repeated measurements, sensors required a detailed investigation of the structural and morphological changes. Thus, the surface of sensors was analysed with different characterisation techniques to get a better insight into the effect of plasma surface treatment.

3.2. Morphology analysis

To analyse surface modifications of all non-treated and plasma-treated samples, SEM was used, and the results are presented in Fig. 6. Nanotubes did not seem to be affected by plasma, and no visual damages were observed on the entangled structure (Fig. S3 and S4), which means that the surface of sensors is the same before and after the plasma-treatment.

Detailed TEM and HR-TEM analysis were done to get an insight into

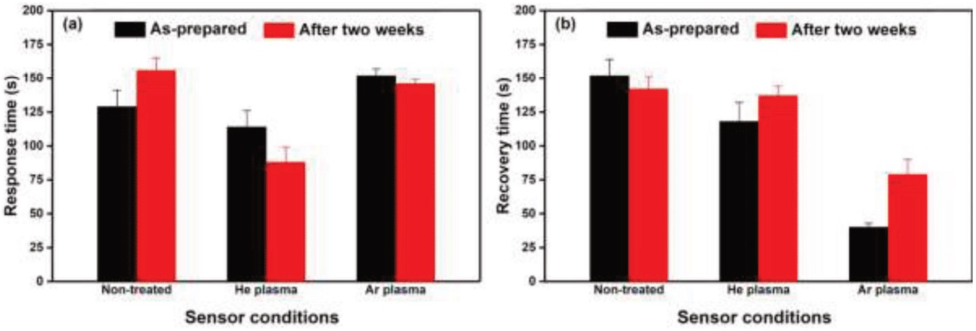

Fig. 5. Comparison of sensor (a) response time and (b) recovery time of non-treated, He plasma-treated and Ar plasma-treated sensors at the room temperature.

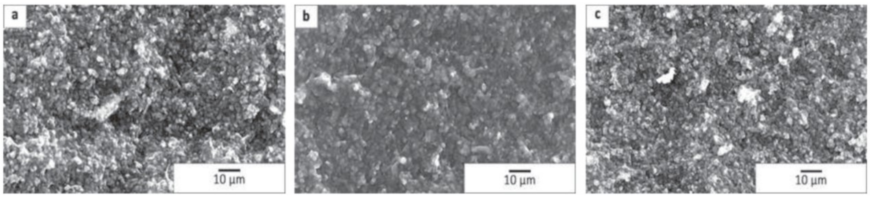

Fig. 6. Characteristic SEM micrographs of (a) non-treated, (b) He and (c) Ar plasma-treated sensor surface.

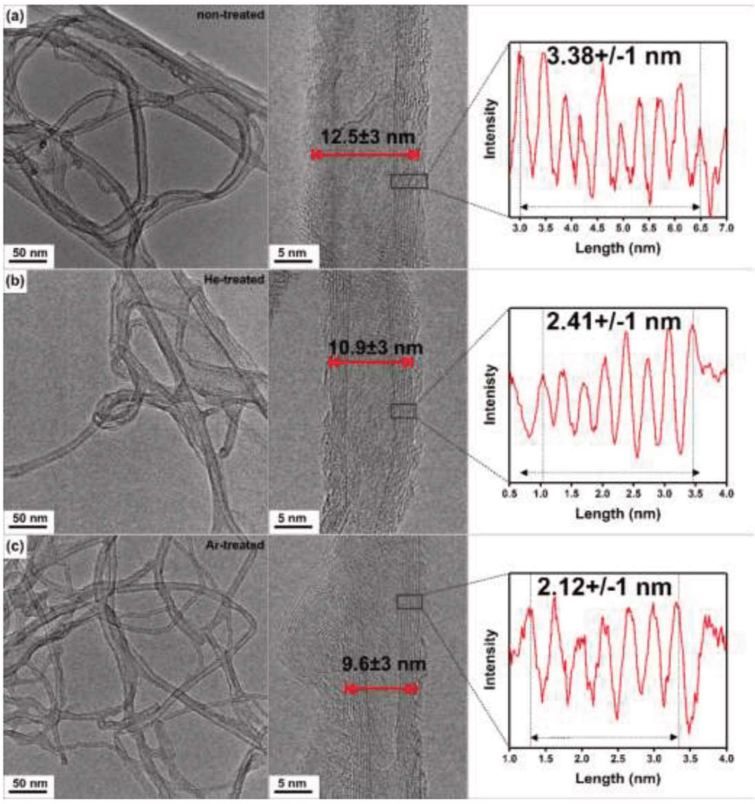

Fig. 7. Overview and high-resolution TEM micrographs of carbon nanostructures and intensity profile from the marked area of the (a) non-treated, (b) He-treated and (c) Ar treated sensor.

the changes that occurred on the surface of BPs after plasma-treatment (Fig. 7 (a–c)). The individual nanotubes are multi-walled with an average diameter of 10–15 nm. The surface of the nanotubes is covered with a wrinkled amorphous layer of carbon. The diameter of the nanotubes in the non-treated sensor was 12.57 ± 3 nm, and it was reduced to 10.9 ± 3 nm after He plasma-treatment and 9.6 ± 3 nm after Ar plasma-treatment. This slight reduction in the diameter can be ascribed to the plasma-enhanced etching effect, which also affects the thickness of the carbon layers. The intensity profile obtained from the carbon layers (Fig. 7 (a–c)) is indicating that the layer thickness is also slightly decreasing with plasma-treatment, which can be due to the removal of the top layer. Additionally, the continuous amorphous wrinkled layer visible on the non-treated sensor is completely removed after He plasma-treatment and partially removed after the Ar plasma-treatment. These effects can improve the conductivity of the BPs after the plasma-treatment and enhance the interaction of the carbon layer with ethanol vapour during the sensor cycle, which in turn improve the response of the sensor.

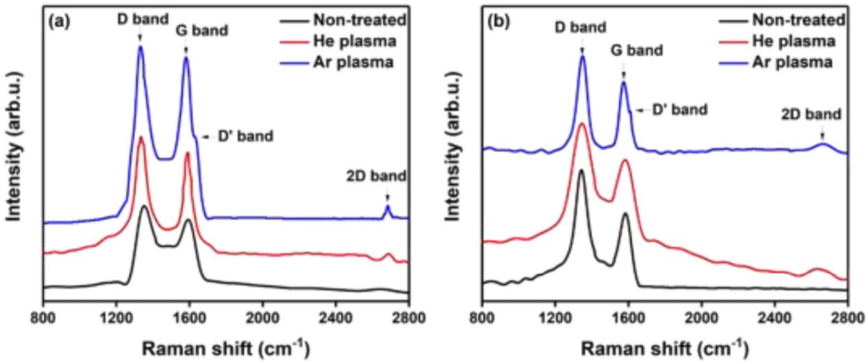

Fig. 8. Raman spectra of the non-treated, He and Ar plasma-treated sensors (a) as-prepared and (b) two weeks later.

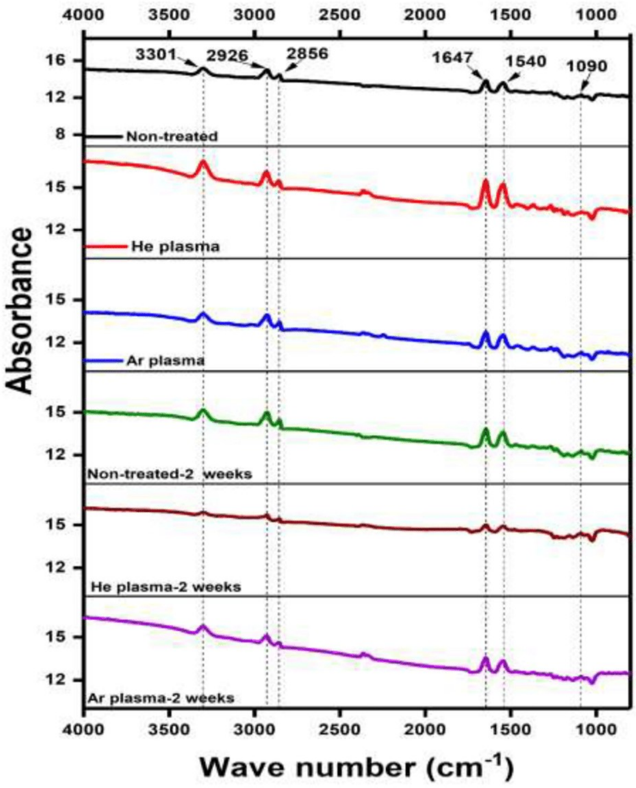

Fig. 9. FTIR spectra of the non-treated, He plasma-treated and Ar plasma-treated sensors

3.3. Raman spectroscopy

Raman spectroscopy was used for the qualitative characterisation of structural defects in CNTs, by comparing the ratio between the intensities of the defect and graphitic bands. The results of this analysis are presented in Fig. 8. The Raman spectra of the non-treated sensor display two well-distinguished peaks approximately at 1343 cm^{-1} and 1587 cm^{-1}, D and G peak, respectively, which are the typical characteristics of graphitic carbon. The D peak is induced by the disorder or defect due to the distortion of graphite lattice [35–37] and the G peak forms due to the crystallite graphite [38]. There was no 2D band (around 2675 cm^{-1}) observed in the Raman spectrum of the non-treated sensor, which is the second-order two-phonon process in a graphitic sp^2 material and indicates that the disordered graphene layers were overlapped with plenty of oxygenated functional groups. Lack of this peak indicates that the non-treated sensors possess more amorphous behaviour than the treated ones. The Raman characteristics of sensors were changed both with He and Ar plasma-treatments. The D peak is shifted to 1338 cm^{-1} and 1336 cm^{-1} after He and Ar plasma-treatment, respectively, which could be due to the formation of reactive edges on CNTs caused by plasma etching [39]. The evolution of a 2D band that was observed after He and Ar plasma-treatment around 2678 cm^{-1} and 2673 cm^{-1} indicates that the plasma-treatment causes the removal of amorphous carbon from the surface and progression of more graphitic behaviour. There was an additional shoulder peak observed along with the G peak at 1618 cm^{-1} after the Ar plasma-treatment, which is known as D' peak, a disorder peak frequently seen in microcrystalline graphite usually produced from the thin edges of graphitic layers.

Comparison of the I_D/I_G ratio of different sensors exhibits the change in structural quality. The I_D/I_G ratio for the as-prepared sensor was 1.1, which slightly decreases to 1.09 after He plasma-treatment and further decreases to 1.03 after Ar plasma-treatment. These results imply that the defect density of CNTs decreases with the plasma-treatment by the etching of disordered carbon atoms. There is no significant change observed in the Raman spectrum after two weeks, which means there is no substantial change in the structure of the sensors. Considering the changes observed in the TEM micrographs and Raman characteristics of the sensors, the improvement in sensor properties can be explained as the improvement in graphitic behaviour of sensors after the plasma-treatment.

3.4. Fourier-transform infrared spectroscopy

FTIR analysis was carried out to understand the effect of plasma-treatment on the functional entities (Fig. 9). All the spectra exhibit similar characteristic behaviour with akin vibrations of functional entities. The distinct peak around 3301 cm^{-1} refers to the $O{-}H$ stretching of the hydroxyl group, that may arise from the oscillation of the carboxyl group. The peaks at 2926 cm^{-1} and 2856 cm^{-1} can be associated with the symmetric and asymmetric stretching of $C{-}H$ group. The peak observed at 1647 cm^{-1} can be due to the stretching of the carbon nanotube backbone [40]. The peak signal formed at 1540 cm^{-1} was due to the stretching of $C{=}C$ group in the CNTs [41]. A weak peak observed at 1090 cm^{-1} could be assigned to $O{-}H$ bending deformation mode of the carboxyl groups [42]. The peak intensities of functional groups increased after the plasma-treatment, which indicates the increased surface functionalisation. Additionally, a peak at 2360 cm^{-1} was observed after the plasma-treatment, which corresponds to the stretching of carbon dioxide. A small peak at 2245 cm^{-1} appeared only in the Ar plasma-treated sensor and is attributed to the stretching of nitrile or alkynes groups. Also, the change of different weak peaks is observed in the range of 1500–1100 cm^{-1} for plasma-treated sensors that could arise because of the bending of alkane and aldehyde groups attached to the CNT network. However, the intensity of all the peaks from the He plasma-treated sensor decreased after two weeks, which shows that the stability of the sensor changed with time. Whereas, the intensity of the Ar plasma-treated sensor did not change significantly, which implies its better stability. Since all the sensors show almost similar infrared spectrum, the difference observed in the sensor response after plasma-treatment is mostly associated with the vibrations of either improved graphitic behaviour or O-terminated and H-terminated functional groups, which can enhance the sensitivity of the prepared sensors.

4. Mechanism of ethanol sensing and the influence of plasma-treatment

The non-treated sensor shows a poor and irregular sensor response that improved and stabilised after the plasma-treatment, which may be due to the interaction of plasma-activated species with the surface of carbon nanotubes. Atmospheric pressure plasma surface treatment causes the removal of amorphous carbon, the formation of H/O-terminated groups and dangling bonds, all of which are improving the absorption of ethanol molecules to the surface of the sensor. No significant morphological changes observed from SEM images confirm the capability of plasma-treatment for improving the performance without any structural damage. Detailed analysis by TEM is suggesting that the plasma-treatment leads to the removal of amorphous wrinkled structures from the nanotube surface, which eventually improves the crystalline behaviour of the carbon nanostructures. Raman and FTIR spectra analysis are also confirming that the plasma-treatment mainly improves the graphitic behaviour of the CNTs rather than causing significant chemical modification. Improvement in the graphitic characteristics can be attributed to the plasma-enhanced etching by creating vacancies with the removal of amorphous carbon, which finally improves p-type conductivity of the sensor. Moreover, removal of the amorphous structures from the outer layer of the individual nanotube surface can enhance the adsorption of ethanol to the carbon nanotube and they donate electrons to the conduction state, which increases resistance. The removal of the amorphous structure is more prominent after Ar plasma-treated sensors, in which higher ethanol vapours were adsorbed to the nanotubes and shows higher response compared to other sensors. The other possible reason for the increase of resistance is the change of contact resistance between individual nanotubes and increases the macroscopic resistance of the sensor. The sensor performance after Ar and He plasma-treatment is vividly different and indicating that plasma surface modification using various inert gases at atmospheric conditions is also considerably different. Considering Ar and He as inert gases, the surface functionalisation is only carried out by the excitation of functional groups present in the atmospheric conditions. There is no considerable change in FTIR spectra, suggesting that state of functionalisation after the plasma-treatment is similar before and after plasma-treatment. Thus, the significant factor that influences the surface modification is the bombardment of plasma species on the CNT surface, which affect the electrical conductivity of the sensors. Compared to helium, argon is much heavier and carries more reactive species to the surface of the sensor and creates severe surface modifications by plasma-enhanced etching which results in the formation of more conductive channels. Also, the stability measurements of the sensors show that the changes made by Ar plasma-treatment are persistent even after two weeks but not in the case of He plasma-treatment. Based on the analysis of the experimental data, we can conclude that plasma-treatment makes the sensors more sensitive to the environment. Moreover, the stability of the sensors after plasma-treatment can be recognised as the formation of stable defect channels facilitating the ethanol vapours to access all parts of the sensor. In plasma-treated samples, the dangling bonds, which are formed by the plasma-treatment, might be responsible for the enhanced sensing properties.

5. Conclusion

It was found that the sensitivity to ethanol vapours of the entangled

COOH-functionalised MWCNTs networks was improved by the atmospheric pressure plasma-treatment using inert gases. The resistance of the sensors was decreased after the plasma-treatment. All the sensors were able to detect the ethanol vapour, whereas the non-treated sensor exhibits an inferior sensing ability. Sensor response and stability of the He plasma-treated samples were improved by 3 times, and that of Ar plasma-treated samples were improved by 5 times with an increase in ethanol concentration. Evaluation of response time and recovery time shows that the time of response increased after the plasma-treatment due to the higher sensor response while the time of recovery was fast. Surface morphology analysis confirms that the plasma-treatment did not destroy the tubular structure of CNTs. Raman spectra and TEM analysis confirm the improvement of graphitic behaviour after the plasma-treatment. Infrared spectrum suggests similar bond vibrations for all the sensors, but the presence of additional peaks after plasma-treated sensors indicates the improved functional entities in the CNT network. It is evident that the plasma-treatment improves the graphitic nature of nanotubes, the formation of defects, and the presence of functional groups of the sensors, which is enhancing the sensing properties. Exploring the selectivity of the prepared sensor towards different gases needs to be investigated for the future applications of the entangled carbon nanotube-based sensors.

Credit author statement

Neelakandan M Santhosh planned the experiments, contributed to the data curation, analysis of physical and chemical properties of the samples and manuscript preparation. Aswathy Vasudevan helped with the experiments and manuscript preparation. Andrea Jurov prepared the original draft of the manuscript and carried out the morphology analysis. Anja Korent helped with the morphology analysis and manuscript preparation: Petr Slobodian contributed to the editing of manuscript and proofreading. Janez Zavašnik carried out the TEM analysis of the samples and interpretation. Uroš Cvelbar planned the main conceptualization of the work, reviewing results and editing of the manuscript.

Declaration of Competing Interest

The authors declare that they have no known competing financial interests or personal relationships that could have appeared to influence the work reported in this paper.

Acknowledgements

The research was co-financed by the Slovenian Research Agency (ARRS) program P2-0082 and project L2-6769. P.S. acknowledges the support of the Ministry of Education, Youth and Sports of the Czech Republic-Program NPU I (LO1504); the Operational Program Research and Development for Innovations co-funded by the European Regional Development Fund; the National budget of the Czech Republic, within the framework of the project CPS-strengthening research capacity (reg. number: CZ.1.05/2.1.00/19.0409). N.M.S. and A.V. acknowledges the support of AD FUTURA, Public Scholarship, Development, Disability, and Maintenance Fund of the Republic of Slovenia.

Appendix A. Supplementary data

Supplementary data to this article can be found online at https://doi.org/10.1016/j.mee.2020.111403.

References

[1] J.T.W. Yeow, Y. Wang, A review of carbon nanotubes-based gas sensors, J. Sensors. (2009), https://doi.org/10.1155/2009/493904.
[2] W. Yu, Y. Sun, T. Zhang, K. Zhang, S. Wang, X. Chen, N. Dai, CuO/WO3 hybrid nanocubes for high-responsivity and fast-recovery H2S sensors operated at low temperature, Part. Part. Syst. Charact. 33 (2016) 15–20, https://doi.org/10.1002/ppsc.201500178.
[3] B.S. Dakshayini, K.R. Reddy, A. Mishra, N.P. Shetti, S.J. Malode, S. Basu, S. Naveen, A.V. Raghu, Role of conducting polymer and metal oxide-based hybrids for applications in ampereometric sensors and biosensors, Microchem. J. (2019), https://doi.org/10.1016/j.microc.2019.02.061.
[4] N.P. Shetti, S.J. Malode, D. Ilager, K. Raghava Reddy, S.S. Shukla, T.M. Aminabhavi, A novel electrochemical sensor for detection of molinate using ZnO nanoparticles loaded carbon electrode, Electroanalysis (2019), https://doi.org/10.1002/elan.201800775.
[5] N.P. Shetti, S.D. Bukkitgar, K.R. Reddy, C.V. Reddy, T.M. Aminabhavi, Nanostructured titanium oxide hybrids-based electrochemical biosensors for healthcare applications, Colloids Surf. B: Biointerfaces (2019), https://doi.org/10.1016/j.colsurfb.2019.03.013.
[6] P. Slobodian, U. Cvelbar, P. Riha, R. Olejnik, J. Matyas, G. Filipič, H. Watanabe, S. Tajima, H. Kondo, M. Sekine, M. Hori, High sensitivity of a carbon nanowall-based sensor for detection of organic vapours, RSC Adv. (2015), https://doi.org/10.1039/c5ra12000d.
[7] G. Filipič, J. Gruenwald, Temperature influence on the diethylamine sensing abilities of CuO nanoparticles deposited by atmospheric pressure plasma, J. Technol. Sp. Plasmas. (2020), https://doi.org/10.31281/jtsp.v1i1.10.
[8] H.G. Moon, Y.S. Shim, D.H. Kim, H.Y. Jeong, M. Jeong, J.Y. Jung, S.M. Han, J.K. Kim, J.S. Kim, H.H. Park, J.H. Lee, H.L. Tuller, S.J. Yoon, H.W. Jang, Self-activated ultrahigh chemosensitivity of oxide thin film nanostructures for transparent sensors, Sci. Rep. (2012), https://doi.org/10.1038/srep00588.
[9] X. Pan, X. Zhao, J. Chen, A. Bermak, Z. Fan, A fast-response/recovery ZnO hierarchical nanostructure based gas sensor with ultra-high room-temperature output response, Sensors Actuators B Chem. 206 (2015) 764–771, https://doi.org/10.1016/j.snb.2014.08.089.
[10] D. Zhang, Z. Liu, C. Li, T. Tang, X. Liu, S. Han, B. Lei, C. Zhou, Detection of NO2 down to ppb levels using individual and multiple In2O3 nanowire devices, Nano Lett. (2004), https://doi.org/10.1021/nl0489283.
[11] Y. Zhou, G. Xie, T. Xie, H. Yuan, H. Tai, Y. Jiang, Z. Chen, A sensitive film structure improvement of reduced graphene oxide based resistive gas sensors, Appl. Phys. Lett. (2014), https://doi.org/10.1063/1.4890843.
[12] F. Niefind, W. Bensch, M. Deng, L. Kienle, J. Cruz-Reyes, J.M. Del Valle Granados, Co-promoted MoS2 for hydrodesulfurization: new preparation method of MoS2 at room temperature and observation of massive differences of the selectivity depending on the activation atmosphere, Appl. Catal. A Gen. (2015), https://doi.org/10.1016/j.apcata.2015.03.003.
[13] J.D. Fowler, M.J. Allen, V.C. Tung, Y. Yang, R.B. Kaner, B.H. Weiller, Practical chemical sensors from chemically derived graphene, ACS Nano (2009), https://doi.org/10.1021/nn800593m.
[14] M. Zhao, J.X. Huang, C.W. Ong, Room-temperature resistive H 2 sensing response of Pd/WO 3 nanocluster-based highly porous film, Nanotechnology. 23 (2012) 315503, https://doi.org/10.1088/0957-4484/23/31/315503.
[15] H.T. Wang, B.S. Kang, F. Ren, L.C. Tien, P.W. Sadik, D.P. Norton, S.J. Pearton, J. Lin, Hydrogen-selective sensing at room temperature with ZnO nanorods, Appl. Phys. Lett. (2005), https://doi.org/10.1063/1.1949707.
[16] Z.S. Hosseini, A. Mortezaali, A. Iraji Zad, S. Fardindoost, Sensitive and selective room temperature H2S gas sensor based on Au sensitized vertical ZnO nanorods with flower-like structures, J. Alloys Compd. (2015), https://doi.org/10.1016/j.jallcom.2014.12.163.
[17] T. Zhang, S. Mubeen, N.V. Myung, M.A. Deshusses, Recent progress in carbon nanotube-based gas sensors, Nanotechnology. (2008), https://doi.org/10.1088/0957-4484/19/33/332001.
[18] K. Xu, C. Fu, Z. Gao, F. Wei, Y. Ying, C. Xu, G. Fu, Nanomaterial-based gas sensors: a review, Instrum. Sci. Technol. (2018), https://doi.org/10.1080/10739149.2017.1340896.
[19] A. Zandi, A. Gilani, H. Ghafoori fard, J. Koohsorkhi, An optimized resistive CNT-based gas sensor with a novel configuration by top electrical contact, Diam. Relat. Mater. (2019), https://doi.org/10.1016/j.diamond.2019.01.020.
[20] H. Elhaes, A. Fakhry, M. Ibrahim, Carbon nano materials as gas sensors, Mater. Today Proc, 2016, https://doi.org/10.1016/j.matpr.2016.04.166.
[21] D.R. Kauffman, A. Star, Carbon nanotube gas and vapor sensors, Angew. Chem. Int. Ed. (2008), https://doi.org/10.1002/anie.200704488.
[22] S. Brahim, S. Colbern, R. Gump, A. Moser, L. Grigorian, Carbon nanotube-based ethanol sensors, Nanotechnology 20 (2009), https://doi.org/10.1088/0957-4484/20/23/235502.
[23] S.J. Young, Z.D. Lin, Ethanol gas sensors based on multi-wall carbon nanotubes on oxidized Si substrate, Microsyst. Technol. (2018), https://doi.org/10.1007/s00542-016-3154-2.
[24] C.Y. Zhi, X.D. Bai, E.G. Wang, Enhanced field emission from carbon nanotubes by hydrogen plasma treatment, Appl. Phys. Lett. (2002), https://doi.org/10.1063/1.1503175.
[25] H. Bubert, S. Haiber, W. Brandl, G. Marginean, M. Heintze, V. Brüser, Characterization of the uppermost layer of plasma-treated carbon nanotubes, Diam. Relat. Mater. (2003), https://doi.org/10.1016/S0925-9635(02)00353-9.
[26] F. Pourfayaz, A.A. Khodadadi, Y. Mortazavi, S.H. Jafari, Plasma functionalization of MWCNTs in he followed by NH3 treatment and its application in PMMA based nanocomposites, Plasma Process. Polym. (2010), https://doi.org/10.1002/ppap.201000055.
[27] N. Santhosh, G. Filipič, E. Tatarova, O. Baranov, H. Kondo, M. Sekine, M. Hori, K. Ostrikov, U. Cvelbar, Oriented carbon nanostructures by plasma processing: recent advances and future challenges, Micromachines. 9 (2018) 565, https://doi.

org/10.3390/mi9110565.

[28] M.L.Y. Sin, G.C.T. Chow, C.K.M. Fung, W.J. Li, P. Leong, K.W. Wong, T. Lee, Ultra-low-power alcohol vapor sensors based on multi-walled carbon nanotube, Proc. 1st IEEE Int. Conf. Nano Micro Eng. Mol. Syst. 1st IEEE-NEMS, 2006, pp. 1198–1202, , https://doi.org/10.1109/NEMS.2006.334679.

[29] L. Valentini, C. Cantalini, I. Armentano, J.M. Kenny, L. Lozzi, S. Santucci, Highly sensitive and selective sensors based on carbon nanotubes thin films for molecular detection, Diam. Relat. Mater. (2004), https://doi.org/10.1016/j.diamond.2003.11.011.

[30] J. Li, Y. Lu, Q. Ye, M. Cinke, J. Han, M. Meyyappan, Carbon nanotube sensors for gas and organic vapor detection, Nano Lett. (2003), https://doi.org/10.1021/nl034220x.

[31] I.V. Zaporotskova, N.P. Boroznina, Y.N. Parkhomenko, L.V. Kozhitov, Carbon nanotubes: sensor properties. A review, Mod. Electron. Mater. (2016), https://doi.org/10.1016/j.moem.2017.02.002.

[32] P. Slobodian, P. Riha, A. Lengalova, P. Saha, Compressive stress-electrical conductivity characteristics of multiwall carbon nanotube networks, J. Mater. Sci. (2011), https://doi.org/10.1007/s10853-010-5202-0.

[33] N.M. Santhosh, G. Filipič, E. Kovacevic, A. Jagodar, J. Berndt, T. Strunskus, H. Kondo, M. Hori, E. Tatarova, U. Cvelbar, N-graphene nanowalls via plasma nitrogen incorporation and substitution: the experimental evidence, Nano-Micro Lett. 12 (2020) 53, https://doi.org/10.1007/s40820-020-0395-5.

[34] M. Scardamaglia, C. Struzzi, F.J. Aparicio Rebollo, P. De Marco, P.R. Mudimela, J.F. Colomer, M. Amati, L. Gregoratti, L. Petaccia, R. Snyders, C. Bittencourt, Tuning electronic properties of carbon nanotubes by nitrogen grafting: chemistry and chemical stability, Carbon N. Y. (2015), https://doi.org/10.1016/j.carbon.2014.11.009.

[35] R.J. Nemanich, S.A. Solin, First- and second-order Raman scattering from finite-size crystals of graphite, Phys. Rev. B (1979), https://doi.org/10.1103/PhysRevB.20.392.

[36] D. Roy, M. Chhowalla, H. Wang, N. Sano, I. Alexandrou, T.W. Clyne, G.A.J. Amaratunga, Characterisation of carbon nano-onions using Raman spectroscopy, Chem. Phys. Lett. (2003), https://doi.org/10.1016/S0009-2614(03)00523-2.

[37] M.S. Dresselhaus, G. Dresselhaus, R. Saito, A. Jorio, Raman spectroscopy of carbon nanotubes, Phys. Rep. (2005), https://doi.org/10.1016/j.physrep.2004.10.006.

[38] A.C. Ferrari, D.M. Basko, Raman spectroscopy as a versatile tool for studying the properties of graphene, Nat. Nanotechnol. 8 (2013) 235–246, https://doi.org/10.1038/nnano.2013.46.

[39] K.M. Daniels, B.K. Daas, N. Srivastava, C. Williams, R.M. Feenstra, T.S. Sudarshan, M.V.S. Chandrashekhar, Evidences of electrochemical graphene functionalization and substrate dependence by Raman and scanning tunneling spectroscopies, in: J, Appl. Phys. (2012), https://doi.org/10.1063/1.4725489.

[40] F.A. Abuilaiwi, T. Laoui, M. Al-Harthi, M.A. Atieh, Modification and functionalization of multiwalled carbon nanotube (MWCNT) via fischer esterification, Arab. J. Sci. Eng. 35 (2010) 37–48.

[41] S.C. Her, C.Y. Lai, Dynamic behavior of nanocomposites reinforced with multi-walled carbon nanotubes (MWCNTs), Materials (Basel). (2013), https://doi.org/10.3390/ma6062274.

[42] D.S. Ahmed, A.J. Haider, M.R. Mohammad, Comparesion of functionalization of multi-walled carbon nanotubes treated by oil olive and nitric acid and their characterization, Energy Procedia, 2013, https://doi.org/10.1016/j.egypro.2013.07.126.

Supporting Information

Improving sensing properties of entangled carbon nanotube-based gas sensors by atmospheric plasma surface treatment

OES was conducted for the plasma treatment of Bucky paper used as a gas sensor. The spectrometer used for optical emission analysis was a broad-range spectrometer, model LR1, from company ASEQ Instruments, Vancouver, Canada. Spectra were obtained with an exposure time of 500 ms at a distance of 3 cm from the plasma plume (length was 2 mm) at the end of jet's glass tube.

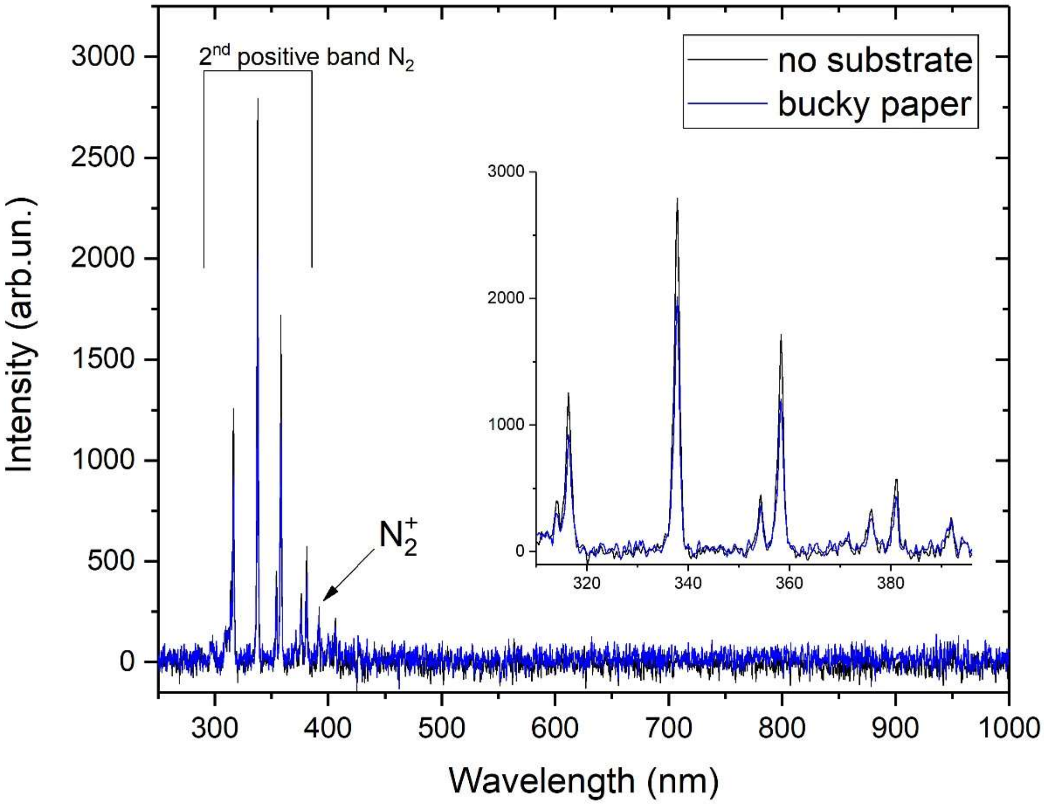

Figure 1. OES of He APPJ recorded for plasma with (blue) and without (black) Bucky paper substrate. Enlarged spectrum highlights observed nitrogen lines.

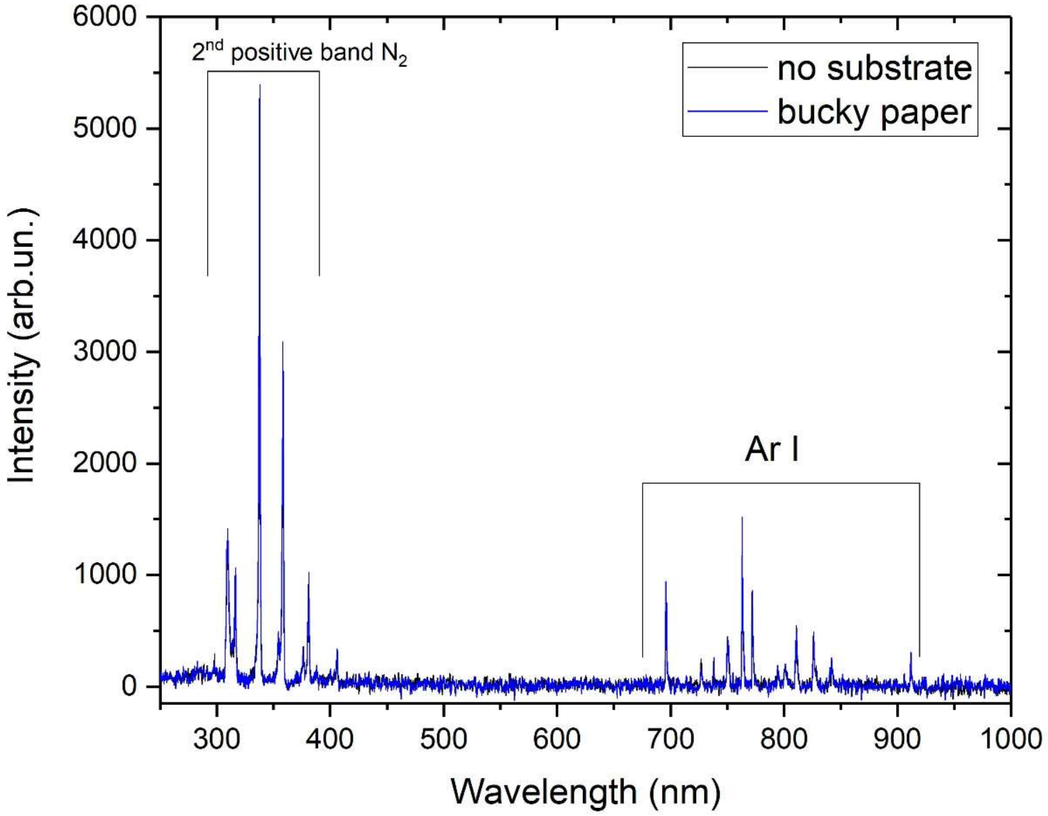

Figure 2. OES of Ar APPJ recorded for plasma with (blue) and without (black) Bucky paper substrate.

Chapter 4

Monitoring Treatment of Biological Substrates

This chapter provides an implementation of OES for monitoring cold APPJ treatments of biological samples, such as bacteria and mouse skin cells *in vivo* and *in vitro*. Atmospheric pressure plasmas are used for various treatments of surfaces, especially biomaterials, due to their beneficial effects like disinfection, stimulation of cells, apoptosis of cancerogenic cells, wound healing or topical introduction of drugs through the skin. Their application to tailoring biological surfaces is extensive. However, aggressive plasmas or too long exposure can lead to uncontrolled damage of biological materials, like cells, bacteria or tissue. The goal of this chapter is to present results for monitoring the formation and recombination of reactive species produced by APPJs in contact with substrates on the gas–surface interface. The role of the specific substrates (bacteria suspended in liquids, cells on a wet substrate or *in vivo* mouse skin) on the plasma parameters was investigated.

The gas–surface interface was diagnosed in detail with different techniques. A thorough analysis of the plasma's electrical properties and ionization processes was made to gain insight into the connection between reactive species production in the gas phase and the generation of reactive species in the plasma treated liquid/sample. These experiments showed different ways to utilize atmospheric pressure plasma properties with varying success. For some biomedical applications, the used plasma setups were too aggressive. But, in some cases, we proposed simple methods to reduce plasma-inflicted damage.

This chapter includes implementation of the optical diagnostics into treatment of different biological materials and is divided into these subchapters:

Error! Reference source not found. Error! Reference source not found.

4.2 Analyzing Mouse Skin Cell Behavior Under a Non-Thermal kHz Plasma Jet

4.3 Atmospheric Pressure Plasma Jet – Mouse Skin Interaction: Mitigation of Damages with Liquid Interfaces or Gas Flow Dynamics

This chapter addresses thesis Objective 2.

4.1 Helium APPJ Parameters and Their Influence on Deactivation of Bacteria in Medium

Bacteria are widespread organisms found in almost any habitat. They are vital in many natural processes, but some bacterial strains can be very harmful for humans. Even though different sterilization techniques are very efficient in bacteria inactivation, some strains become resistant to those methods. It is necessary to improve currently used sterilization techniques and propose new ones that might have certain advantages. We used an APPJ and showed it is capable of elimination of four different bacterial strains in a short amount of time. The research focused on finding optimal plasma parameters for this purpose.

To better understand obtained optimal parameters we did a thorough optical and electrical plasma jet diagnostics, including a detailed liquid chemistry analysis. We found a link between bacteria deactivation with higher discharge powers and gas flow rates, generation of RONS and medium solvate charges. OES helped unravel formation of gas-phase reactive species and their influence on the medium.

Regarding my contribution: I performed detailed power source and plasma diagnostics. I analyzed all data and prepared a manuscript with co-authors.

Helium atmospheric pressure plasma jet parameters and their influence on bacteria deactivation in a medium

Andrea Jurov[1,2*], Nikola Škoro[3], Kosta Spasić[3], Martina Modic[1], Nataša Hojnik[1], Danijela Vujošević[4], Milena Đurović[4], Zoran Lj. Petrović[5,6], Uroš Cvelbar[1,2]

[1]Jozef Stefan Institute, Jamova 39, 1000 Ljubljana, Slovenia
[2]Jozef Stefan International Postgraduate School, Jamova 39, 1000 Ljubljana, Slovenia
[3]Institute of Physics, University of Belgrade, Pregrevica 118, 11080 Belgrade, Serbia
[4]Center for Medical Microbiology, Institute of Public Health Montenegro, Dzona Dzeksona bb, Podgorica 81000, Montenegro
[5]Serbian Academy of Sciences and Arts, Knez Mihajlova 35, 11001 Belgrade, Serbia
[6]School of Engineering, Ulster University, Jordanstown, Co. Newtownabbey, BT37 0QB UK

*andrea.jurov@ijs.si

Abstract. Atmospheric pressure plasmas are becoming relevant in local microbial deactivation and other combined effects of plasmas on living organisms. For this reason, our research was focused on optimisation of atmospheric pressure plasma jet (APPJ) parameters to complete the deactivation of different bacteria strains in a medium. Different helium APPJ treatments with different discharge parameters were used, such as input voltages and gas flows. To better understand plasma properties behind complete bacteria deactivation at optimised discharge parameters, optical and electrical plasma jet diagnostics were performed, including electrical characterisation of the plasma source, optical emission spectroscopy of the plasma plume and intensified charged coupled device imaging of the discharge behaviour for every set of plasma parameters. Then, the resulting plasma liquid chemistry was assessed to establish the connections between reactive species generated in the gaseous and liquid phases. The most efficient deactivation was found for higher discharge powers and gas flow rates, and that was linked to higher densities of reactive oxygen and nitrogen species, especially peroxide and medium solvated charges.

1. Introduction

It is well known that some microorganisms, such as bacteria, fungi and viruses, act as pathogens and induce various diseases. Moreover, microorganisms can cause food spoilage and damage to materials such as corrosion of plumbing systems. For this reasons, several conventional sterilisation techniques which lead to complete microbial deactivation or removal have been developed, including heating, filtration, chemical liquid agents and radiation. However, a disadvantage of these sterilisation techniques is that they can be used only on thermally resistant and chemically inert substrates, as those techniques can influence substrate properties [1].

In recent years, non-thermal atmospheric pressure plasmas have been proposed as an alternative to conventional sterilisation techniques. Most frequently reported is sterilisation with atmospheric pressure plasma jets (APPJs) due to their low operating temperatures and cost-effective operation[2]–[5]. APPJs are suitable for selective treatment of specific substrates as they contain more known inactivation agents without the downsides of conventional sterilisation techniques. Research suggests that reactive oxygen species play the biggest role in bacteria inactivation, but UV radiation, electric field, other reactive species and charged particles also contribute to the process [5]–[8]. In this way, APPJs represent one of the most promising discharge candidates for different biological applications, including complete deactivation of bacteria [8]–[11].

This research tested the efficiency of a constructed APPJ on four different bacteria: *Escherichia coli*, *Staphylococcus aureus*, *Bacillus subtilis*, and *Bacillus stearothermophilus*. *B. stearothermophilus* and *B. subtilis* are spore-forming bacteria and the most commonly recognised and widely used biological indicators for monitoring the effectiveness of sterilisation processes. Spores are dormant bacterial structures, highly resistant to disinfectants and sterilising agents. Spore-forming bacteria are commonly found in processed foods and dairy products [12]–[14]. These bacteria were tested in order to see how an APPJ affects spore-forming bacteria. Additionally, *E. coli* and *S. aureus,* the most common pathogens in humans and widespread in nature (in hospitals and working and living surroundings), were selected. They are commonly found in different environments, contaminating various items, medical tools and food, and can cause hospital infections and food poisoning, as well as medically severe and sometimes fatal infections [15]–[18]. Moreover, these bacterial strains are known to be multidrug-resistant [19], [20]. In addition, these bacteria tend to form biofilms where bacteria are well protected from the outside agents. It has been shown that plasmas may sterilize even the biofilms as well as planktonic samples [21].

There have been many reports on atmospheric pressure plasma induced bacteria deactivation and decontamination [22]–[26] However, there is a knowledge gap in optimising plasma parameters so that complete bacteria deactivation in a medium can be achieved in the shortest (optimal) times. Therefore, this research focuses on finding the most efficient parameters of a non-thermal helium APPJ as one of the most frequently used sources for deactivating bacteria. For this purpose, various combinations of input DC power unit voltages and gas flows were tested and the corresponding diagnostics.

2. Experimental setup

2.1. Preparation of bacteria samples

The deactivation effect of an APPJ, operated with helium as a working gas, was investigated on four different types of bacteria: *B. stearothermophilus* (ATCC No. 7953, *B. subtilis* (ATCC No. 6633), *S. aureus* (ATCC No. 25923) and *E. coli* (ATCC No. 25922). Bacterial cultures were grown overnight on Columbia (COS) agar plates (bioMérieux SA, Marcy l'Etoile, France) at 55 °C for *B. stearothermophilus* and 37 °C for *B. subtilis, S. aureus* and *E. coli.* bacteria were picked up with a loop and resuspended in sterile saline to obtain 0.5 McF (1–2 × 10^8 CFU/ml) initial bacterial suspension. The concentration was constant in all experiments. 100 µl of these initial 0.5 McF bacterial suspensions were evenly transferred to a 96-well plate with a flat bottom. Bacterial suspensions were exposed to the He APPJ at a constant distance for different exposure times. The samples were treated each time in triplicates.

To determine viable counts and evaluate plasma treatment effects, the Miles and Misra viable count technique on COS blood agar plate (bioMérieux SA, Marcy l'Etoile, France) was used. A 20 µl properly diluted plasma-treated bacterial suspension, as well as a positive (untreated bacterial suspension) and negative control (sterile saline) were placed onto the blood agar plate. This procedure is depicted in Fig. 1. Measurements of the reactive species and pH were also conducted. Reactive species concentrations of NO_2^- and H_2O_2 were measured by a spectrophotometer (UV VIS Lambda 25) via colorimetric assays in sterile saline. The pH measurements were performed by a pH-meter (Sentron®) also in saline.

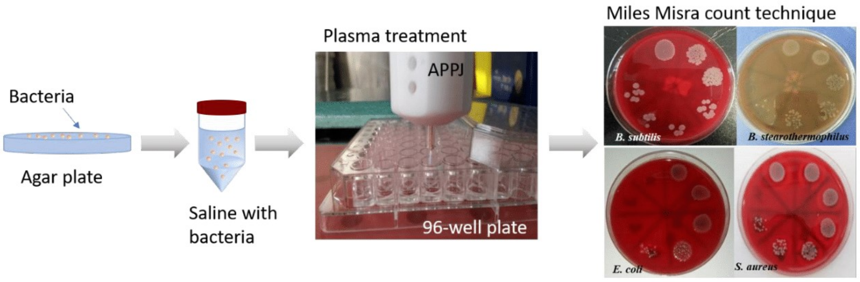

Fig. 1 Schematic representation of the experimental protocol procedure.

2.2. APPJ system

A small-size APPJ powered by a kHz high-voltage signal source was used for the treatments of a liquid medium with bacteria. The high-voltage unit was powered by a low-voltage DC source facilitating portability of the device. The APPJ consisted of a teflon casing that holds a glass tube with concentrically positioned copper wire that serves as a powered electrode. The casing has gas and electrical connections. Measurements with the needle-type APPJ were conducted with He as a working gas at a fixed distance of 15 mm between the end of the jet nozzle and the bottom of the 96-well plate with bacteria suspension. Bacteria were treated with different gas flows (0.5, 1, 1.5 and 2 slm) and several DC power unit voltages (3, 4.5, 6, 9 and 12 V). The DC power supply that gave different DC voltages was Voltcraft SPS12-12W-A. Gas flows were kept constant using mass flow meter Bronkhorst Mass-View MV-194. Detailed characterisation of the plasma source was performed employing optical measurements and electrical characterisation.

Optical characterisation comprised optical emission spectrometry and plasma imaging by using an intensified charged coupled device (ICCD) camera. Optical emission spectroscopy was performed with an Andor Shamrock 500i spectrometer equipped with iXon Ultra 897 as a detector. An optical fibre was used to receive the emission from the plasma plume and direct it to the entrance slit of the spectrometer. The fibre was positioned at a distance of 5 cm from the jet tube axis to gather the light coming from the whole channel volume. Recording of the spectra was performed for exposure times of 100 ms and with averaging of 10 spectrum acquisitions. Thus, obtained results represent space- and time-averaged emission from the plasma. Plasma imaging was performed with an Andor iStar ICCD camera DH334T-18U-03 equipped with a photographic objective. Images were taken in single-shot mode with an exposure time of 20 ms. Furthermore, electrical characterisation was performed by measuring the average power given to the jet. Voltage and current on the powered electrode were measured before the APPJ with an oscilloscope (Rigol DS1102E), high voltage probe (Rigol RP1018H) and current monitor (Pearson 8590C).

Estimation of saline solution evaporation during treatments was performed to evaluate changes in the treatment conditions throughout the experiments. For the longest treatment times, the highest DC supply voltages and He flow of 2 slm, the evaporated solution volume from the 96-well plate was not more than 50 mm^3. This change in volume caused a maximum liquid level reduction of 1.2 mm, thus increasing the distance between the plasma jet and the liquid surface. However, these changes did not drastically influence plasma properties, and these maximum values were reached only for the longest treatment times and plasma powers. For most treatment conditions, volume changes fell within the experimental error of transferring the liquid volume into the plate.

3. Results and discussion

3.1. Bacteria deactivation

At first, bacterial suspension control samples were exposed only to helium gas flow with rates of 0.5, 1, 1.5 and 2 slm, without plasma and with no voltage applied, for the same duration as required for deactivation using the plasma. The obtained results exhibit no difference in bacteria viability (Fig. 2) compared to the untreated samples (positive control; PC), which confirms that helium alone is insufficient for bacteria deactivation. The effects of the APPJ were then further tested for all bacteria and analysed with a quantitative and informative approach, which involved dynamical studies of bacterial growth after treatments. Typically, survival curves were determined as the numbers of colony-forming units (CFUs; surviving culturable bacteria as a function of plasma treatment time). However, to limit the presentation, only complete bacteria deactivation, achieving sterility of the medium, is shown in Fig. 3.

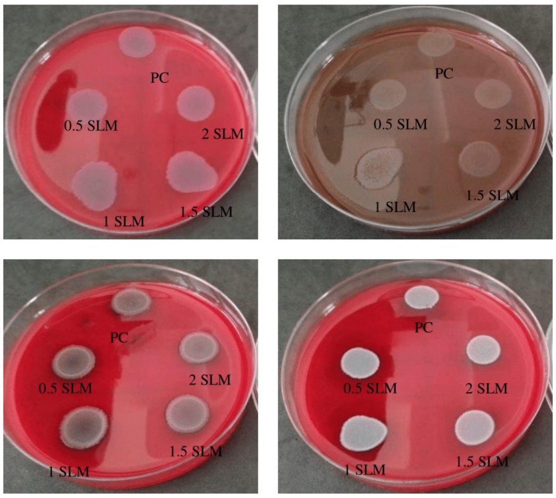

Fig. 2 Effect of gas flow-only (no plasma) treatment of bacteria (a) *B. subtilis,* (b) *B. stearothermophilus,* (c) *E. coli* and (d) *S. aureus* exposed to 0.5, 1, 1.5 and 2 slm compared to the positive control (PC) by Miles and Misra plate counting.

Furthermore, Fig. 3 presents the time needed for deactivation of *E. coli*, *S. aureus, B. stearothermophilus* and *B. subtilis* within a medium, exposed to a He APPJ generated with different DC input powers and gas flows. If there are no data shown for a specific set of parameters (usually 3 V and 0.5 slm), the bacteria were not completely deactivated (all microbiological life is killed as a result of the sterilization process) within the maximum treatment time of 240 s used in experiments. In most cases, it was found that *E. coli* was deactivated faster than other bacteria, proving to be a less plasma-resistant strain. In this case, the highest treatment time was 180 s for deactivation under the lowest gas flow of 0.5 slm, which typically did not prove very efficient. *B. stearothermophilius* strains proved the most resistant to plasma treatments. Surprisingly, the lowest flow rate deactivation curves for 0.5 slm are very similar for all types of bacterial strains, except a small deviation with *E. coli*. This indicates that the APPJ generated at these conditions and its consequent reactive oxygen and nitrogen species (RONS) chemistry within the medium are similar (although, moving to higher flow rates, the chemistries and deactivations changed significantly). The trend follows the same patterns, where 0.5 slm is the least, and 2 slm is the most efficient, which are plasma properties connected to its subsequent interaction. The exception to this general rule is *B. stearothermophilius*, the most thermally stable and resistant strain, which seems to deviate from the rule. In this case, the most efficient chemistry for deactivation is at 1 slm. Chemical analyses of the medium chemistry elucidate the reasons for this behaviour in the following paragraphs.

From the perspective of the DC input voltage parameter used for jet discharge, the general rule is: the higher the energy input into discharge, the faster the deactivation of bacterial strains. However, it seems there is a minimum level at which the jets are efficient. It was found that an input DC voltage of 3 V was not sufficient to deactivate most bacteria strains even for the highest gas flow and treatment times because the plasma plume was the shortest and was not in direct contact with the substrate. If deactivation of the bacteria strain was achieved, then the treatment time was significantly prolonged. Therefore, the results indicate that He APPJ is most efficient at bacteria strain deactivation with higher applied power and higher gas flows, considering marked limits in discharge parameters and experimental constraints. We do not reach conditions where additional heating would produce thermal necrosis (40ºC) in the covered range of powers. While increasing efficiency with power is expected as for the flow, one could expect that beyond some point, further increasing of the flow may reduce efficiency by affecting the chain of plasma chemical events needed to produce the radicals that cause sterilization.

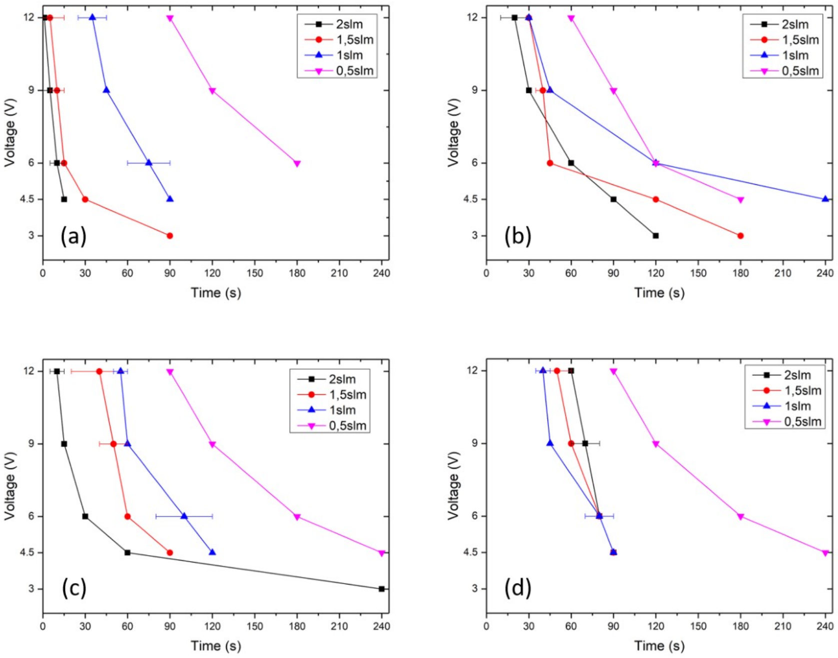

Fig. 3 Points of complete bacteria deactivation (a) *E. coli,* (b) *S. aureus,* (c) *B. subtilis* and (d) *B. stearothermophilus* exposed to He APPJ generated with powers of 3, 6, 9 and 12 V, and flow rates of 0.5, 1, 1.5 and 2 slm.

3.2. Chemical analysis of reactive species of saline medium treated by APPJ

To explain the obtained results for bacterial deactivation in a medium, the initiated medium chemistry was investigated, determining RONS species, especially H_2O_2 and NO_2^- concentrations of the APPJ treated saline solution. Immediately after treatments we performed measurements of pH changes. These parameters are known to influence the viability of bacterial strains significantly, as marked by numerous reports [27]–[30].

pH measurements were made under the same conditions as for reactive species measurement. The influence of different He plasma parameters (different gas flow rates of 0.5, 1, 1.5 and 2 slm and different input DC powers of 3, 4.5, 6, 9 and 12 V) on pH value was systematically measured. A pH value decrease was observed during the plasma treatment for most cases (Fig. 4). These decreasing trends featured an initial drop and then a steady decrease. An exception was 1 slm, which had an increasing pH trend for input DC voltage of 3 V. This could be explained by the fact that the plasma jet did not touch the surface of the liquid, and in this case, the chemistry of the medium was different than in other cases.

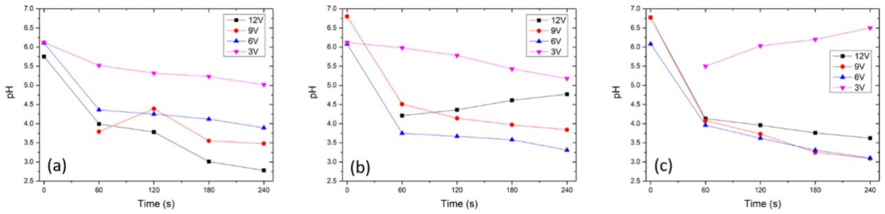

Fig. 4 pH values of He APPJ treated saline for gas flow of (a) 2 slm, (b) 1.5 slm and (c) 1 slm.

Reactive species concentrations of NO_2^- and H_2O_2 were determined after plasma treatment of saline, 50 μl of sterile saline was placed in the 96-well plate with a flat bottom. The distance between the bottom of the well and the APPJ orifice was 15 mm, as for the treatment of bacteria, and was kept constant during the treatment. The results are presented as a supplementary in Fig. S1 as they are obtained with only the parameters yielding the most efficient plasma treatment - input voltage of 12 V and a flow rate of 2 slm. An expected, steady increase of H_2O_2 concentrations was observed for increasing treatment time. In contrast, the concentration of NO_2^- increased until 30 s, where it reached its maximum value and then started decreasing. The concentration dropped to zero after 120 s. This could be explained through decreasing of the pH value during the treatment. NO_2^- is very sensitive to low pH values, which is the cause of its decomposition or transformation into other compounds [31].

3.3. Diagnostics of the plasma source

In order to analyse properties of the plasma used for treatments, we performed diagnostic experiments at the same conditions as when treating media with bacterial strains. Due to safety, a saline medium was used without bacteria for these measurements.

Power measurements were made via electrical characterisation, where the average power (P_{avg}) input into the jet was measured. This was calculated over 30 periods of current and input voltage as:

$$P_{avg} = \frac{1}{30T} * \int_{t1}^{t2} P(t)dt,$$

where T is oscillation period, and $P(t)$ is instantaneous power in every moment t calculated as $I(t) * V(t)$ from the beginning t_1 and end t_2 of 30 periods. The measurements were performed on the electrode before the plasma jet coming out of the tube and at two gas flow rates of 1 and 2 slm. The calculated values present an average power that the power source gives to the plasma jet (Fig. 5) and represents the 'real' power input into plasma. It was observed that the power was not influenced by the gas flow rate but was instead dependent on the DC input voltage and provided powers in the range of 0.1 to 1.5 W. The power that is transferred from plasma to the treated samples is somewhat lower than calculated power since part is always lost but we have made the measurements in such a way to limit the losses.

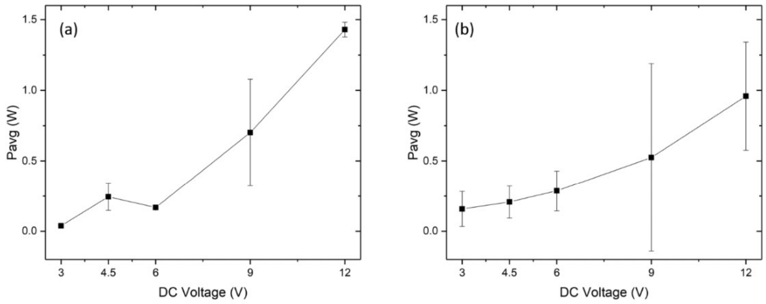

Fig. 5 Average input power to the plasma jet for He gas flows of (a) 1 slm and (b) 2 slm.

Optical emission spectroscopy was used as a plasma diagnostic tool. A typical spectrum of He discharge of an APPJ at gas flow rate of 2 slm where a jet was positioned above the distilled water target is presented in Fig. 6. The spectrum was recorded in a wide range of wavelengths, between 300 nm and 800 nm. The characteristic spectrum of excited species has already been assessed for this kind of plasma jet [32]–[34]. The most intense lines came from the molecular OH (A-X) band, atomic lines of He and O, and molecular bands of N_2; the second positive system (SPS) and the first positive system as well as from the nitrogen ion – the first negative system (FNS) [35], [36]. Excited He atoms were produced from the ground state neutrals in the working gas used in the system. At the same time, OH and N_2 bands and atomic O lines and Hα line were present since the experiments were conducted in an ambient air (with some humidity) and in contact with the distilled water. Neutral species from the surrounding air were mixed with the helium flow and therefore participated in gas phase reactions induced by plasma [37], [38]. Additionally, a spectrum of the APPJ operated under the same conditions but in contact with saline solution was also taken. In contrast to the case where solid NaCl was treated [39], the spectrum obtained with saline did not show any differences compared to distilled water, i.e. no additional lines from Na (or Cl) were observed. This suggests that these species were not excited in the gas phase above the water for the plasma source to excite them.

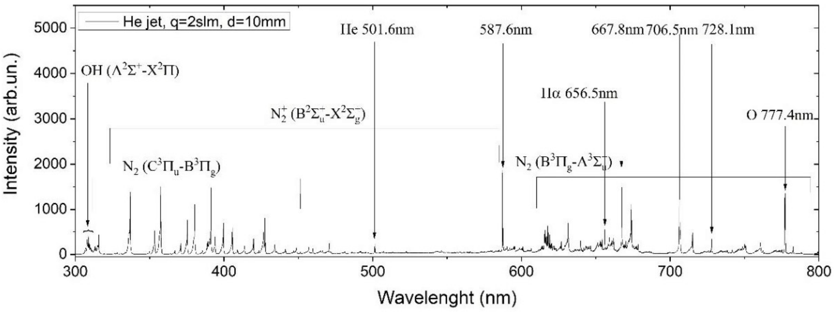

Fig. 6 Optical emission spectroscopy of the He APPJ with a characteristic spectrum generated during the treatments above the liquid medium.

Additional analysis regarding line intensity was performed on specific atomic and molecular lines for different DC input voltages used in the experiment (3, 4.5, 6, 9 and 12 V) at two gas flows (1 and 2 slm).

The intensities at different discharge parameters with two emission lines from N_2 SPS (337.1 nm and 315.9 nm), head line from FNS N_2^+ (391.3 nm), the strongest molecular OH line (309 nm), Hα (656.6 nm) and O atom line (777.4 nm) are presented in Fig. 7, while He line (706.5 nm) intensities are depicted in Fig. 8. All line intensities are normalised to the same recording conditions, thus allowing direct intensity comparison between different lines. The position of the jet and the distance to the bottom of the 96-well plate were the same as for the treatments of bacteria. There was an increase of intensities for all observed lines when the source power (DC voltage) was increased. The increase of He flow had a minor influence on line intensities, resulting in a somewhat higher line intensity. In all cases, there was a stronger or weaker 'jump' between the emission intensities recorded for 6 V and 9 V. This change in peak values occurred due to the change in plasma regime since, as observed with the naked eye, the plasma channel did not connect to the surface of the saline until the 9 V were reached [40]. Therefore, the intensities recorded for voltages below 9 V can be regarded as free-standing jet cases, while for the voltages of 9 V and 12 V, plasma plume was in contact with the liquid surface.

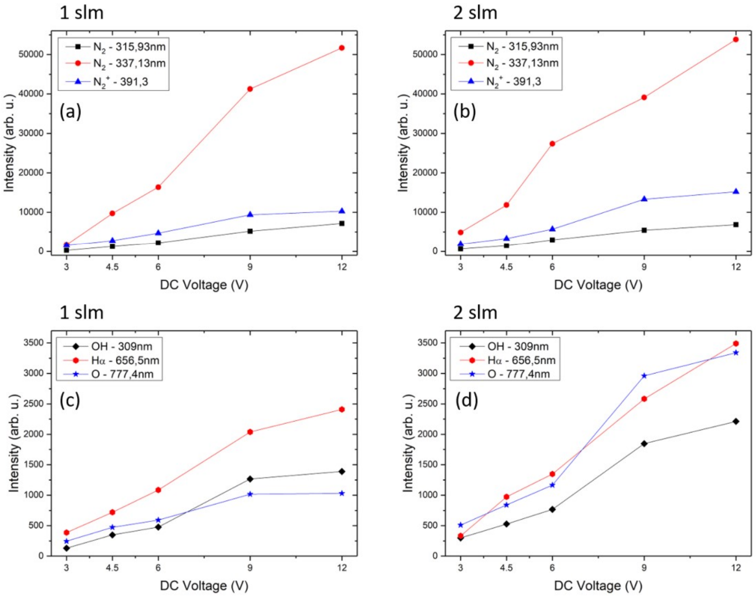

Fig. 7 Optical emission spectroscopy: intensities of certain atomic and molecular lines of nitrogen ((a) for 1 slm and (b) for 2 slm), and hydrogen, oxygen and hydroxyl (c) for 1 slm and (d) for 2 slm).

The highest line intensities belong to the mainline of N_2 SPS, and these intensities have pronounced increments between 6 V and 9 V input voltage (Fig. 7 (a) and (b)). The second strongest line of the same band has a much lower increase in intensity. However, excitation of both of the excited levels in N_2 probably happened through electron collisions with the ground state or excited N_2 molecules [34], [41]. The increasing line intensity tendency is in accordance with the dependence observed with similar jet configurations [33]. The intensity of the strongest of FNS N_2^+ lines at 391.3 nm also increased with DC voltage, yet much less than the 337.1 nm line (Fig. 7 a) and b)). This line comes from the excited state of N_2^+ ions that were efficiently produced in the Penning ionisation process, involving He metastables [42] and the direct electron impact ionisation process [41]. Consequently, an increase in He flow made the emission of the 391.3 nm line rise. On the other hand, lines from the OH band and Hα came from dissociation of water vapour molecules in plasma [34], [43]. In this jet configuration, the amount of water vapour present in the surrounding air was sufficient to produce several excited species of OH and H visible in the emission spectrum. An increase in the He flow and discharge voltage resulted in the increase of OH emission intensity (Fig. 7 c) and d)), which has been observed before [33], [44]. The atomic O (777.4 nm) line exhibited similar behaviour. Production of both OH and O species is important when it comes to the treatment of bacteria.

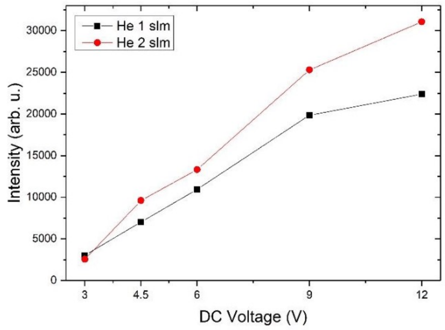

t

Fig. 8 He 706.5 nm line intensities for different gas flow and voltages.

The intensity trend of the He line at 706.5 nm was similar to that of other spectral lines, and is presented in Fig. 8. As expected, an increase was observed with the flow, and plasma plume intensity was also generated by increasing DC input power with supply voltage. This presented He line is the most intense compared to other lines observed in the spectrum (Fig. 8).

Discharge imaging gives insights into the plasma plume, showing how it forms streams and initiates more charge into the liquid. For this, ICCD imaging was employed with time-averaged images of the streamer structure obtained for all He flows and DC input powers. Typical results are presented in Fig. 9 for 1 slm and 2 slm, at only the lowest (3 V) and highest (12 V) DC voltages used in the experiments. Similar to optical emission measurements, the jet position and its distance to the liquid surface in the 96-well plate were the same as for bacteria treatments. For all conditions, a ball-shaped bright plasma was visible on the tip of the pin electrode with a plasma plume extending towards the target. For the lowest DC voltage employed, a weak plasma channel existed only for the 2 slm flow of He. Obviously, for V_{DC} = 3 V and 1 slm of He, the field attained at the electrode with these power supply conditions was not enough to achieve sufficient ionisation in the whole volume between the jet and sample surface. At the highest power, i.e. DC voltage of 12 V, a streamer-like plasma channel with strong emission bridged the distance from the electrode tip to the liquid surface. After processing all images recorded by subtracting the background intensity level, it was determined that in all applied conditions, except for 3 V at 1 slm, the plasma plume reached the liquid surface, meaning that streamer length in this range of conditions did not depend on either voltage or helium flow. On the other hand, streamer thickness varied from 0.7 mm for 3 V up to 1.9 mm for 12 V, though it also did not depend on flow. At lower DC voltages, some plasma plume flickering was noticeable at the liquid surface. This indicates that the medium chemistry of bacteria deactivation depends on streamer forming behaviour, which almost doubles the procedure's efficacy.

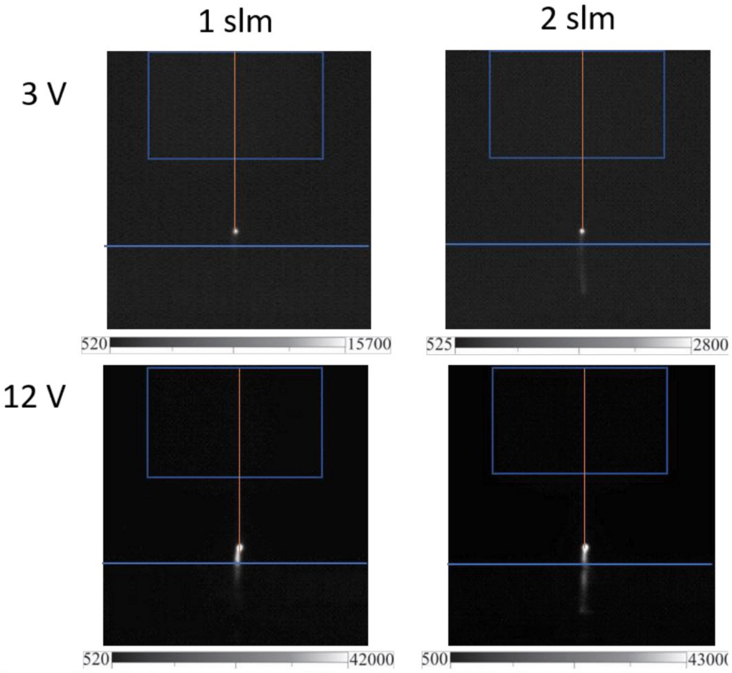

Fig. 9 Images of the discharge structure at different flows and DC voltages from the power supply. A thin vertical line represents a pin electrode protruding from the body of the jet (rectangle shape). The horizontal line in the lower part of the images signifies the upper edge of the 96-well plate.

4. Conclusion

To optimise bacteria deactivation in media and obtain sterilisation with plasmas, a parameter study involving a large number of experiments using different plasma conditions was performed. It included monitoring the viability of different bacteria strains with respect to several plasma diagnostics measurements. This research clearly shows non-thermal helium APPJs' ability to deactivate four standard strains of bacteria used in such experiments. The deactivation effects of the plasma jet were significant and dependant on the bacterial strain, exposure time and plasma configuration (gas flow rate and input DC power unit voltage). The obtained results are expected and indicate that *E. coli* is deactivated faster than other strains. Generally, all bacterial strains – *E. coli*, *S. aureus, B. stearothermophilus* and *B. subtilis* – follow the same deactivation trends. The only discrepancy is in the optimal parameters for deactivation of *B. stearothermophilus*, where optimal deactivation is reached at lower flow rate levels. This must be because of the bacterial strain's properties and its response to the changing environment by interacting plasma. The interaction of plasma and bacteria suspension (saline) was twofold – it changed the concentration of reactive species and pH in the solution with bacteria. This RONS species (He, O, N, H, photons) generated in the gas phase and high-energy electrons and ions were interacting with the liquid. As a result of the combined action of produced reactive species and chemical reactions, which also influenced the pH in the liquid phase, increased bacteria deactivation efficacy. Combining all the chemically initiated processes managed to sterilise given bacterial strains in a medium in fairly short treatment times, maximum efficacy was observed at high flow rates and DC input powers. More power transferred into the plasma shortens the deactivation process. Increasing the flow rate from 0.5 to 2 slm also shortens the inactivation process as reactive species concentration in the gas phase rises.

Supplemental material.

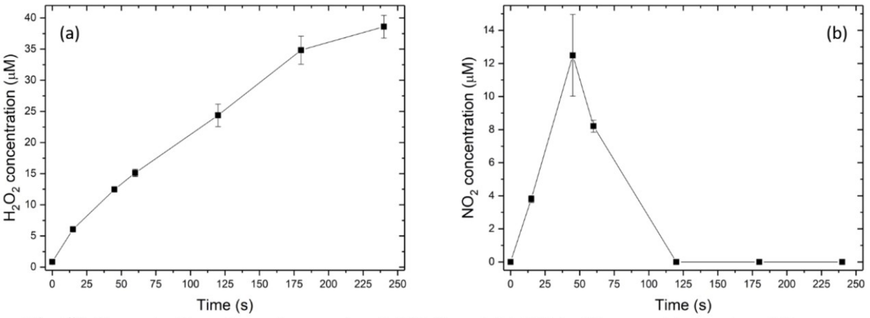

Fig. S1 Concentration of reactive species: (a) H_2O_2 and (b) NO_2^- with respect to treatment time.

Acknowledgments. This work was carried out within projects NATO SPS, and Slovenian Research Agency grant J4-1770. This article is also based upon work from COST Action PLAGRI - CA19110, supported by COST (European Cooperation in Science and Technology), www.cost.eu. K. S. acknowledge also partial funding from bilateral project Serbia-Slovenia from MESTD of Republic of Serbia. We thank Dr. Nevena Puac for useful advices related to electrical characterization.

Data Availability Statement. The data that support the findings of this study are available from the corresponding author upon reasonable request.

Autor contribution statement. U. C. and Z. Lj. P. conceived and planned the experiments. N. H., M. M., D. V. and M. Đ. performed plasma treatment of bacteria and liquid chemistry analyses along with the interpretation of those results. N.Š., K. S. and A. J. performed plasma diagnostics and electrical characterization along with interpretation of those results. A. J. wrote the original draft and all co-authors helped with manuscript revision.

References

[1] Z. Dai, J. Ronholm, Y. Tian, B. Sethi, and X. Cao, "Sterilization techniques for biodegradable scaffolds in tissue engineering applications," *J. Tissue Eng.*, vol. 7, p. 204173141664881, Jan. 2016, doi: 10.1177/2041731416648810.

[2] J. Ehlbeck *et al.*, "Low temperature atmospheric pressure plasma sources for microbial decontamination," *J. Phys. D. Appl. Phys.*, vol. 44, no. 1, 2011, doi: 10.1088/0022-3727/44/1/013002.

[3] R. Ben Gadri *et al.*, "Sterilization and plasma processing of room temperature surfaces with a one atmosphere uniform glow discharge plasma (OAUGDP)," *Surf. Coatings Technol.*, vol. 131, no. 1–3, pp. 528–541, 2000, doi: 10.1016/s0257-8972(00)00803-3.

[4] P. M. Schneider, "New technologies and trends in sterilization and disinfection," *Am. J. Infect. Control*, vol. 41, no. 5 SUPPL., pp. S81–S86, 2013, doi: 10.1016/j.ajic.2012.12.007.

[5] A. Sakudo, Y. Yagyu, and T. Onodera, "Disinfection and sterilization using plasma technology: Fundamentals and future perspectives for biological applications," *Int. J. Mol. Sci.*, vol. 20, no. 20, 2019, doi: 10.3390/ijms20205216.

[6] M. Laroussi, "Nonthermal decontamination of biological media by atmospheric-pressure plasmas: Review, analysis, and prospects," *IEEE Trans. Plasma Sci.*, vol. 30, no. 4 I, pp. 1409–1415, 2002, doi: 10.1109/TPS.2002.804220.

[7] X. Liao *et al.*, "Bacterial spore inactivation induced by cold plasma," *Crit. Rev. Food Sci. Nutr.*, vol. 59, no. 16, pp. 2562–2572, 2019, doi: 10.1080/10408398.2018.1460797.

[8] H. Halfmann, B. Denis, N. Bibinov, J. Wunderlich, and P. Awakowicz, "Identification of the most efficient VUV/UV radiation for plasma based inactivation of Bacillus atrophaeus spores," *J. Phys. D. Appl. Phys.*, vol. 40, no. 19, pp. 5907–5911, 2007, doi: 10.1088/0022-3727/40/19/019.

[9] S. Hofmann, *Atmospheric Pressure Plasma Jets - Characterisation and Interaction with Human Cells and Bacteria*, no. december. 2013.

[10] M. Keidar and E. Robert, "Preface to Special Topic: Plasmas for Medical Applications," *Phys. Plasmas*, vol. 22, no. 12, p. 121901, Dec. 2015, doi: 10.1063/1.4933406.

[11] M. Keidar, D. Yan, I. I. Beilis, B. Trink, and J. H. Sherman, "Plasmas for Treating Cancer: Opportunities for Adaptive and Self-Adaptive Approaches," *Trends Biotechnol.*, vol. 36, no. 6, pp. 586–593, Jun. 2018, doi: 10.1016/j.tibtech.2017.06.013.

[12] N. Gopal, C. Hill, P. R. Ross, T. P. Beresford, M. A. Fenelon, and P. D. Cotter, "The Prevalence and Control of Bacillus and Related Spore-Forming Bacteria in the Dairy Industry," *Front. Microbiol.*, vol. 6, Dec. 2015, doi: 10.3389/fmicb.2015.01418.

[13] S. André, T. Vallaeys, and S. Planchon, "Spore-forming bacteria responsible for food spoilage," *Res. Microbiol.*, vol. 168, no. 4, pp. 379–387, May 2017, doi: 10.1016/j.resmic.2016.10.003.

[14] S. Caulier, C. Nannan, A. Gillis, F. Licciardi, C. Bragard, and J. Mahillon, "Overview of the Antimicrobial Compounds Produced by Members of the Bacillus subtilis Group," *Front. Microbiol.*, vol. 10, Feb. 2019, doi: 10.3389/fmicb.2019.00302.

[15] J. Vila *et al.*, "Escherichia coli : an old friend with new tidings," *FEMS Microbiol. Rev.*, vol. 40, no. 4, pp. 437–463, Jul. 2016, doi: 10.1093/femsre/fuw005.

[16] J. Jang, H.-G. Hur, M. J. Sadowsky, M. N. Byappanahalli, T. Yan, and S. Ishii, "Environmental Escherichia coli : ecology and public health implications-a review," *J. Appl. Microbiol.*, vol. 123, no. 3, pp. 570–581, Sep. 2017, doi: 10.1111/jam.13468.

[17] T. J. Foster and J. A. Geoghegan, "Staphylococcus aureus," in *Molecular Medical Microbiology*, Elsevier, 2015, pp. 655–674.

[18] S. Y. C. Tong, J. S. Davis, E. Eichenberger, T. L. Holland, and V. G. Fowler, “Staphylococcus aureus Infections: Epidemiology, Pathophysiology, Clinical Manifestations, and Management,” *Clin. Microbiol. Rev.*, vol. 28, no. 3, pp. 603–661, Jul. 2015, doi: 10.1128/CMR.00134-14.

[19] S. Basak, P. Singh, and M. Rajurkar, “Multidrug Resistant and Extensively Drug Resistant Bacteria: A Study,” *J. Pathog.*, vol. 2016, pp. 1–5, 2016, doi: 10.1155/2016/4065603.

[20] L. Poirel *et al.*, “Antimicrobial Resistance in Escherichia coli,” *Microbiol. Spectr.*, vol. 6, no. 4, Jul. 2018, doi: 10.1128/microbiolspec.ARBA-0026-2017.

[21] M. Miletić *et al.*, “Inhibition of methicillin resistant Staphylococcus aureus by a plasma needle,” *Open Phys.*, vol. 12, no. 3, Jan. 2014, doi: 10.2478/s11534-014-0437-z.

[22] A. H. Asghar, O. B. Ahmed, and A. R. Galaly, “Inactivation of E. Coli using atmospheric pressure plasma jet with dry and wet argon discharges,” *Membranes (Basel).*, vol. 11, no. 1, pp. 1–20, 2021, doi: 10.3390/membranes11010046.

[23] A. Moldgy, G. Nayak, H. A. Aboubakr, S. M. Goyal, and P. J. Bruggeman, “Inactivation of virus and bacteria using cold atmospheric pressure air plasmas and the role of reactive nitrogen species,” *J. Phys. D. Appl. Phys.*, vol. 53, no. 43, p. 434004, Oct. 2020, doi: 10.1088/1361-6463/aba066.

[24] J.-W. Lackmann and J. E. Bandow, “Inactivation of microbes and macromolecules by atmospheric-pressure plasma jets,” *Appl. Microbiol. Biotechnol.*, vol. 98, no. 14, pp. 6205–6213, Jul. 2014, doi: 10.1007/s00253-014-5781-9.

[25] C. A. J. van Gils, S. Hofmann, B. K. H. L. Boekema, R. Brandenburg, and P. J. Bruggeman, “Mechanisms of bacterial inactivation in the liquid phase induced by a remote RF cold atmospheric pressure plasma jet,” *J. Phys. D. Appl. Phys.*, vol. 46, no. 17, p. 175203, May 2013, doi: 10.1088/0022-3727/46/17/175203.

[26] F. Saadati, H. Mahdikia, H. A. Abbaszadeh, M. A. Abdollahifar, M. S. Khoramgah, and B. Shokri, “Comparison of Direct and Indirect cold atmospheric-pressure plasma methods in the B16F10 melanoma cancer cells treatment,” *Sci. Rep.*, vol. 8, no. 1, pp. 1–15, 2018, doi: 10.1038/s41598-018-25990-9.

[27] S. Ikawa, K. Kitano, and S. Hamaguchi, “Effects of pH on Bacterial Inactivation in Aqueous Solutions due to Low-Temperature Atmospheric Pressure Plasma Application,” *Plasma Process. Polym.*, vol. 7, no. 1, pp. 33–42, Jan. 2010, doi: 10.1002/ppap.200900090.

[28] S. M. Hosseini, B. Hosseinzadeh Samani, S. Rostami, and Z. Lorigooini, “Design and characterisation of jet cold atmospheric pressure plasma and its effect on Escherichia coli , colour, pH, and bioactive compounds of sour cherry juice,” *Int. J. Food Sci. Technol.*, vol. 56, no. 10, pp. 4883–4892, Oct. 2021, doi: 10.1111/ijfs.15220.

[29] V. S. S. K. Kondeti *et al.*, “Long-lived and short-lived reactive species produced by a cold atmospheric pressure plasma jet for the inactivation of Pseudomonas aeruginosa and Staphylococcus aureus,” *Free Radic. Biol. Med.*, vol. 124, pp. 275–287, Aug. 2018, doi: 10.1016/j.freeradbiomed.2018.05.083.

[30] A. L. V. Cubas *et al.*, “Effect of chemical species generated by different geometries of air and argon non-thermal plasma reactors on bacteria inactivation in water,” *Sep. Purif. Technol.*, vol. 222, pp. 68–74, Sep. 2019, doi: 10.1016/j.seppur.2019.03.057.

[31] P. Lukes, M. Clupek, V. Babicky, B. Pongrac, and M. Simek, “Bulk-phase chemistry induced by nanosecond discharge plasma in water,” in *2017 IEEE 19th International Conference on Dielectric Liquids (ICDL)*, Jun. 2017, pp. 1–3, doi: 10.1109/ICDL.2017.8124702.

[32] Y. S. Seo, A. A. H. Mohamed, K. C. Woo, H. W. Lee, J. K. Lee, and K. T. Kim, “Comparative studies of atmospheric pressure plasma characteristics between He and Ar working gases for sterilization,” *IEEE Trans. Plasma Sci.*, vol. 38, no. 10 PART 2, pp. 2954–2962, 2010, doi: 10.1109/TPS.2010.2058870.

[33] E. Ilik and T. Akan, “Optical properties of the atmospheric pressure helium plasma jet generated by alternative current (a.c.) power supply,” *Phys. Plasmas*, vol. 23, no. 5, 2016, doi: 10.1063/1.4948718.

[34] A. N. Korbut, V. A. Kelman, Y. V. Zhmenyak, and M. S. Klenovskii, “Emission properties of an atmospheric-pressure helium plasma jet generated by a barrier discharge,” *Opt. Spectrosc. (English Transl. Opt. i Spektrosk.*, vol. 116, no. 6, pp. 919–925, 2014, doi: 10.1134/S0030400X14040146.

[35] J. J. Camacho, J. M. L. Poyato, L. Díaz, and M. Santos, “Optical emission studies of nitrogen plasma generated by IR CO2 laser pulses,” *J. Phys. B At. Mol. Opt. Phys.*, vol. 40, no. 24, pp. 4573–4590, 2007, doi: 10.1088/0953-4075/40/24/003.

[36] S. J. Strickler, “The identification of molecular spectra (Pearse, R. W. B.; Gaydon, A. G.),” *J. Chem. Educ.*, vol. 41, no. 5, p. A398, May 1964, doi: 10.1021/ed041pA398.

[37] T. Darny, J. M. Pouvesle, J. Fontane, L. Joly, S. Dozias, and E. Robert, “Plasma action on helium flow in cold atmospheric pressure plasma jet experiments,” *Plasma Sources Sci. Technol.*, vol. 26, no. 10, 2017, doi: 10.1088/1361-6595/aa8877.

[38] M. Foletto, V. Puech, J. Fontane, L. Joly, and L. C. Pitchford, “Evidence of the influence of plasma jets on a helium flow into open air,” *IEEE Trans. Plasma Sci.*, vol. 42, no. 10, pp. 2436–2437, 2014, doi: 10.1109/TPS.2014.2331393.

[39] R. Zaplotnik, M. Bišćan, Z. Kregar, U. Cvelbar, M. Mozetič, and S. Milošević, “Influence of a sample surface on single electrode atmospheric plasma jet parameters,” *Spectrochim. Acta - Part B At. Spectrosc.*, vol. 103–104, pp. 124–130, 2015, doi: 10.1016/j.sab.2014.12.004.

[40] P. J. Bruggeman *et al.*, “Plasma-liquid interactions: A review and roadmap,” *Plasma Sources Science and Technology*, vol. 25, no. 5. Institute of Physics Publishing, Sep. 2016, doi: 10.1088/0963-0252/25/5/053002.

[41] Q. Xiong *et al.*, “Temporal and spatial resolved optical emission behaviors of a cold atmospheric pressure plasma jet,” *J. Appl. Phys.*, vol. 106, no. 8, 2009, doi: 10.1063/1.3239512.

[42] G. Nersisyan, T. Morrow, and W. G. Graham, “Measurements of helium metastable density in an atmospheric pressure glow discharge,” *Appl. Phys. Lett.*, vol. 85, no. 9, pp. 1487–1489, 2004, doi: 10.1063/1.1784514.

[43] G. V. Naidis, “Production of active species in cold helium-air plasma jets,” *Plasma Sources Sci. Technol.*, vol. 23, no. 6, 2014, doi: 10.1088/0963-0252/23/6/065014.

[44] R. Ono, “Optical diagnostics of reactive species in atmospheric-pressure nonthermal plasma,” *Journal of Physics D: Applied Physics*, vol. 49, no. 8. 2016, doi: 10.1088/0022-3727/49/8/083001.

4.2 Analyzing Mouse Skin Cell Behavior Under a Non-Thermal kHz Plasma Jet

One possible biomedical application of a cold APPJ is exploring cell viability behavior. In this paper, we investigated the suitability of a kHz-driven APPJ for L929 murine fibroblast treatment. The research was focused on *in vitro* direct plasma treatment of mouse skin cells and was complemented with thorough gas-phase and liquid-phase analysis of plasma and plasma-treated medium. Additionally, a detailed plasma source diagnostic was conducted, which included electrical characterization and discharge imaging. The results showed that our plasma jet treatment was very destructive and even for short treatment times apoptosis occurred. An attempt was made to compare with other results in order to position us within the related experiments. However, certain issues emerged. One of the problems was the diversity of plasma systems, which makes them extremely hard to compare. There are a lot of plasma jet setups and power sources one can choose, and most are applicable for treatments of biomedical material. In addition to the diversity of plasma systems, another significant problem was non-standardized plasma diagnostics. In the end, we proposed monitoring plasma processes with OES as a first step to standardized diagnostics.

OES was complemented with a thorough electrical characterization of the power source along with ICCD imaging of the plasma plume. By investigating reactive species, we gained insight into the interaction of the gas and liquid phases of the experiment, and made presumptions on pathway for cell apoptosis. Further research is needed to tailor plasma properties for targeting specific cells.

Regarding my contribution: I performed all experiments except liquid-phase analysis and cell viability. Also, I prepared the original draft of the manuscript along with visualizations.

applied sciences

MDPI

Article

Analysing Mouse Skin Cell Behaviour under a Non-Thermal kHz Plasma Jet

Andrea Jurov [1,2], Špela Kos [3], Nataša Hojnik [1], Ivana Sremački [4], Anton Nikiforov [4], Christophe Leys [4], Gregor Serša [3] and Uroš Cvelbar [1,*]

[1] Jožef Stefan Institute, Jamova cesta 39, 1000 Ljubljana, Slovenia; andrea.jurov@ijs.si (A.J.); natasa.hojnik@ijs.si (N.H.)
[2] Jožef Stefan International Postgraduate School, Jamova cesta 39, 1000 Ljubljana, Slovenia
[3] Department of Experimental Oncology, Institute of Oncology, Zaloška cesta 2, 1000 Ljubljana, Slovenia; skos@onko-i.si (Š.K.); gsersa@onko-i.si (G.S.)
[4] Department of Applied Physics, Ghent University, Sint-Petersnieuwstraat 41, 9000 Gent, Belgium; ivana.sremacki@ugent.be (I.S.); anton.nikiforov@ugent.be (A.N.); christophe.leys@ugent.be (C.L.)
* Correspondence: uros.cvelbar@ijs.si

Abstract: Plasma jets are extensively used in biomedical applications, particularly for exploring cell viability behaviour. However, many experimental parameters influence the results, including jet characteristics, secondary liquid chemistry and protocols used, slowing research progress. A specific interest of the presented research was skin cell behaviour under a non-thermal kHz plasma jet—a so-called cold plasma jet—as a topical skin treatment. Our research was focused on in vitro mouse skin cell direct plasma treatment with argon as an operating gas. The research was complemented with detailed gas-phase diagnostics and liquid-phase chemical analysis of the plasma and plasma-treated medium, respectively. The obtained results showed that direct plasma jet treatment was very destructive, leading to low cell viability. Even with short treatment times (from 35 s to 60 s), apoptosis was observed for most L929 murine fibroblasts under approximately the same conditions. This behaviour was attributed to plasma species generated from direct treatment and the types of cell lines used. Importantly, the research exposed important points that should be taken under consideration for all further research in this field: the urgent need to upgrade and standardise existing plasma treatment protocols of cell lines; to monitor gas and liquid chemistries and to standardise plasma discharge parameters.

Keywords: atmospheric pressure plasma jet; cell viability; plasma-treated media; reactive species; optical emission spectroscopy

check for updates

Citation: Jurov, A.; Kos, Š.; Hojnik, N.; Sremački, I.; Nikiforov, A.; Leys, C.; Serša, G.; Cvelbar, U. Analysing Mouse Skin Cell Behaviour under a Non-Thermal kHz Plasma Jet. *Appl. Sci.* **2021**, *11*, 1266. https://doi.org/10.3390/app11031266

Academic Editor: Daniela Boehm
Received: 5 December 2020
Accepted: 27 January 2021
Published: 30 January 2021

1. Introduction

Non-thermal atmospheric pressure plasmas (APPs) are widely used for various applications. They show great potential in the field of medicine [1–3] because of properties such as low gas temperature, high generation rate of reactive species, affordability and simple setup compared to low-pressure plasma systems. Different frequencies can ignite plasma. The most widely used configurations are simple kHz driven jets [4–9], but microwave [10] and radio frequency [11,12] driven jets have also been reported. This type of plasma contains short-lived free radicals, charged species, neutral species, reactive oxygen and nitrogen species (RONS), UV radiation, and electric fields; all of which can influence biological samples [9].

Assuming RONS influence living cells the most out of all plasma components, their production is of interest for this research [13]. In the gas phase, plasma ionises and excites species from the ambient air which recombine into RONS. These then reach the cell culture medium and interact with liquid components. Gaseous RONS quickly recombine, leading to the formation of other species, such as nitrites (NO_2^-), nitrates (NO_3^-), hydrogen peroxide (H_2O_2) and peroxynitrite ($ONOO^-$), of which $NO_2{}^-$ and H_2O_2 are the easiest to detect and quantify.

Based on their presence in a given liquid medium, some assumptions about RONS dynamics can be made. Depending on the dosage of nitrite ($NO_2{}^-$) and hydrogen peroxide (H_2O_2), one can obtain both positive (cell proliferation, cell differentiation, angiogenesis) and negative (apoptosis, necrosis, growth arrest) effects on cells [1,2,9,14]. Both positive and negative effects can be useful in different applications. For example, in cancer treatment, it is useful to induce damage to target cells, but in open wound treatment, cells should not be damaged at all.

Depending on the required result, there are different approaches to treating cells: direct and indirect. The direct approach involves direct plasma treatment of biological cells while they are inside the cell culture medium. Indirect plasma treatment means that a liquid medium is treated with plasma (a plasma-treated medium (PAM)) and is subsequently added to the cells. One difference between these approaches is the species—produced in the gas phase—that reach and interact with the cells [15]. In the case of direct plasma treatment, both short- and long-lived species will interact with cells. In contrast, with an indirect approach, only long-lived species produced in the gas phase will interact with cells. However, this does not imply that there are no short-lived species inside the liquid; they form again when long-lived species decompose and recombine. Both direct and indirect plasma treatments influence cell processes and morphology changes [16].

This research aimed to create a simple single-electrode, kHz-driven plasma jet and examine its effect on L929 murine fibroblast cells. The motive was to explore this type of plasma jet's usability for topical skin treatment—and consequently for wound healing or gene delivery—and then compare this source with other similar approaches and investigations. To do so, we chose argon plasma, which is relatively unexplored, for direct cell treatment on healthy mouse skin cells. Direct plasma treatment was chosen in order to shorten the procedure, as indirect plasma-treated cells must be incubated in PAM for at least 24 h. Argon was chosen over helium gas because of its affordability and processing sustainability. Moreover, under the same conditions, argon plasma has higher electron density but lower electron temperature, which was considered an advantage for direct cell treatment [17].

2. Materials and Methods

2.1. Plasma Jet Configuration and Power Source Characterisation

A non-thermal APP in the form of a jet (powered by a kHz source) was used for this research. The plasma jet was constructed as a single electrode jet with no additional grounding. Therefore, a plasma plume could be formed inside a 2 mm diameter glass tube. Depending on the gas type, flow could reach up to 1.5 cm in length, measured from the end of the glass orifice outward. A schematic representation of this setup is shown in Figure 1. Diagnostic measurements (optical emission spectroscopy (OES) and I-V characterisation) were conducted while the plasma operated over a non-grounded distilled water target. This target was chosen to allow the gas-phase diagnostics to be taken closer to the cell treatment, as the cells are dispersed inside a liquid medium. Distilled water was placed in a cylindrical container of 6280 mm^3 volume at 2 cm distance from the end of the jet's glass tube.

The jet was powered by a 20 kHz power source (Amazing PMV500, Information Unlimited, Amherst, NH, USA). Based on preliminary tests, parameters were fixed at a maximum frequency and 60% power input in low operating mode (0.24 W). These conditions produced the most stable argon plasma. Current and voltage were stable sinusoidal waves without any arbitrary peaks.

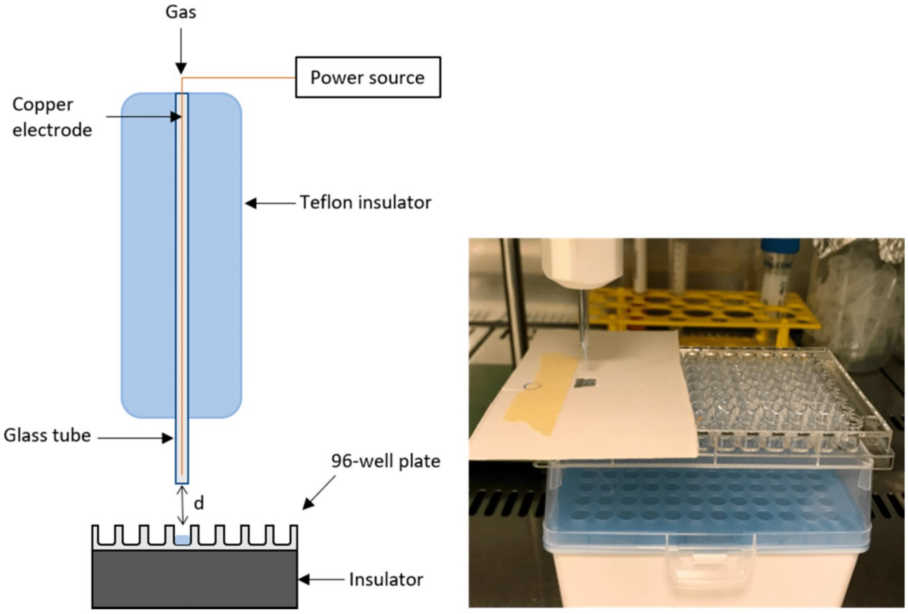

Figure 1. Schematic representation (**left**) and photograph (**right**) of the simple plasma jet system and setup for an in vitro cell treatment.

The voltage and current of the power source were monitored in real time, just before the jet. For this purpose, an HV probe (Tektronix P6105A, Tektronix Inc., Beaverton, OR, USA) and a current monitor (Pearson 2877, Pearson Electronics Inc., Palo Alto, CA, USA) were coupled with an oscilloscope (Picoscope 3204d, Pico Technology Ltd., Cambridgeshire, UK). Waveforms were monitored to ensure they were stable under the experiments' conditions but were not monitored throughout the experiments on the cell culture medium.

2.2. Gas-Phase Diagnostics

Diagnostics of plasma in the gas phase is important for monitoring the excited species' production and understanding the principles behind plasma ionisation. For this purpose, both OES and time-resolved ICCD (Intensified Charged Couple Device) imaging were used.

For OES measurements, we used broad-range, spatially-resolved and time-resolved spectroscopy. The broad-range spectra provided insight into the species that were excited in plasma, whereas the spatially-resolved spectra enabled monitoring of excited species' intensities produced in plasma, with respect to the distance from the jet. The time-resolved spectra exposed information about how chosen species form throughout one period. To obtain the broad-range and spatially-resolved spectra, an Avantes spectrometer (Avantes BV, Apeldoorn, The Netherlands) with 0.05 nm resolution was used. For time-resolved spectroscopy, a 0.75 m Zolix spectrometer (Zolix Instruments Co., LTD, Beijing, China) with a grating of 1200 grooves/mm (blazed on 500 nm) was used.

ICCD imaging was utilised to gain an insight into 'bullet' formation and propagation within the waveform, along with filament production. For these measurements, a Hamamatsu ICCD camera was used (Hamamatsu Photonics K.K., Naka-ku, Hamamatsu City, Japan). Imaging was time-resolved, and it covered the whole period. Images were obtained with an exposure time of 100 ns and at one integration.

2.3. In Vitro Cell Experiments

To investigate the effects of a kHz plasma jet on biomedical samples with a focus on skin treatment, in vitro experiments were performed with L929 murine fibroblasts. The discharge parameters were constant throughout all experiments. The argon flow rate was 1 SLM, and the source's power was fixed at 60% of the maximum available power. Different treatment times were used; more precisely, 10 s, 35 s and 60 s. The distance between the plasma jet and cell medium was 10 mm, 15 mm and 20 mm, respectively, measured from the end of the jet's glass tube to the surface of the well plate (marked as d in Figure 1). This distance was measured from the jet to the top of the well plate rather than the liquid surface, for easier monitoring. Another 7 mm should be added to these values to denote the distance from the point plasma exists in the glass tube and mixes with the ambient air to the surface of the cells dispersed in the culture medium. The distances were chosen based on the position of the plasma plume, which was either touching the surface of the substrate or its immediate or far afterglow region.

Since all in vitro cell experiments required a controlled sterile environment, they were conducted inside a laminar cabinet (Iskra PIO M12V). Laminar is essentially a large metal box, and it influences plasma intensity by acting as a grounding electrode under the sample. To mitigate this effect, a 10 cm tall dielectric was placed under the well plate. Additionally, single well treatment was assured by a barrier plate with a circular hole which was placed on top of the well plate. This provided full control over jet species in the far afterglow region and prevented their expansion to neighbouring wells. Both the dielectric under a sample and the barrier placed on top of the well-plate are shown in Figure 1.

2.4. Cell Lines

The L929 murine fibroblasts (American Type Culture Collection, ATCC, Manassas, VA, USA) were cultured in an advanced minimum essential medium (AMEM) (Gibco, Thermo Fisher Scientific, Waltham, MA, USA), supplemented with 5% fetal bovine serum (FBS; Gibco), 10 mL/l L-glutamine (GlutaMAX; Gibco), 100 U/mL penicillin and 100 μg/mL streptomycin (Pen-Strep, Sigma-Aldrich, Merck, St. Louis, MO, USA) in a 5% CO_2 humidified incubator at 37 °C.

Cell Viability Assay

For cell viability assay, L929 cells were trypsinised and counted. Prior to treatment, cells were resuspended in the cell medium (MEM (Minimum Essential Medium) without phenol red, Gibco) and 1000 L929 cells/well were placed in 96-well plates (Corning Incorporated, Corning, NY, USA) in a 0.1 mL cell culture medium. Immediately after the cell suspension was placed in plates, plasma treatment was performed as described above. Cells were incubated at 37 °C in a 5% CO_2 humidified incubator for up to three days. 24 h and 72 h after treatment, 10 μL of Presto Blue® viability reagent (Thermo Fisher Scientific, Waltham, MA, USA) was added to the wells, and 1 h later fluorescence intensity was measured by a microplate reader (Cytation 1, BioTek Instruments, Winooski, VT, USA). The percentage of viable cells was calculated and normalised to the untreated control group. Three replicates were used for each experimental group; each experiment was repeated three times. For statistical analysis, GraphPad Prism Software (version 9.0.0) was used. Data are presented as the arithmetic mean (AM) ± the mean standard error (SE). One-way ANOVA followed by the Tukey test for multiple comparisons was used for the determination of significant differences ($p < 0.05$ *, $p < 0.01$ **, $p < 0.001$ ***, $p < 0.0001$ ****) between groups.

2.5. Liquid-Phase Chemistry Analysis

Plasma-induced modifications and the liquid chemistry of culture medium MEMs were analysed using different analytical techniques. Identical plasma treatment conditions were employed as in the case of in vitro cell experiments. Immediately following treatments (0 h), the treated MEM's pH and conductivity were measured with PC 52+ DHS® (XS instruments, Italy). To obtain more information about the dynamics of the plasma-induced liquid chemistry, colourimetric tests were performed to evaluate the presence of NO_2^- and H_2O_2 using a plate reader in UV-VIS spectrometry mode (Spark 10M, Tecan, Switzerland) at 0 h, 24 h and 72 h after the treatments. The presence of NO_2^- was determined with standard Griess reagent assay (Griess reagent system; Promega, Madison, WI, USA) measuring absorbance values at 540 nm. H_2O_2 concentrations were tested with a ferric-xylenol orange complex (xylenol orange, sorbitol and ammonium iron sulphate; Sigma-Aldrich), which was added to the treated MEM. Following the chemical reaction, the absorbance of the solution was measured at 560 nm. Tests were performed in multiple independent experiments and results replicated. The obtained results were statistically analysed with 2-way ANOVA (GraphPad Prism, San Diego, CA, USA).

3. Results

3.1. Gaseous Plasma Characteristics

Broad-range spectra (Figure 2a) confirmed the presence of the usual species for an APP generated within argon gas; excited argon species from the ionisation of the working gas, and the reactive species of nitrogen (second positive band—$C^3\Pi_u \rightarrow B^3\Pi_g$), along with OH groups coming from the ambient air filled with water vapour. Given that the OH peak did not overlap with other lines, it was used to determine plasma gas temperature with LIFbase Database and spectral simulation programme (Version 2.1) [12]. The temperature measured was 318 K while plasma was in contact with a water target as described in Section 2.2.

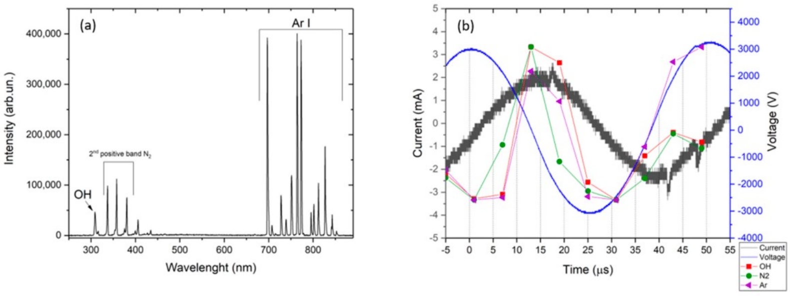

Figure 2. Broad-range emission spectrum of Ar plasma operated above a non-grounded water target (**a**) and time-resolved optical emission spectroscopy (OES) during one period (**b**).

Spatially-resolved spectra were measured at the exit of the glass tube and the plasma plume's end; approximately 1 cm apart. This distance was also the length of the used plasma plume under all experimental conditions. The spectra exhibited no specific difference when the intensity was normalised to 1 (presented in the supplementary file). Intensity normalisation allowed spectra intensity comparison, and did not influence the line intensity ratio within each recorded spectrum. Based on this result, we were confident that excited species from the gas phase delivered to the cell medium were similar at each distance used for direct cell treatment.

Intensities of OH (309 nm), N_2 (391 nm) and Ar (696 nm) were monitored throughout one period by time-resolved spectroscopy. These data were paired with I-V characteristics in Figure 2b. Our power source operated at an average maximum value of 3.4 kV and

2.8 mA at chosen discharge parameters. One period lasted for 50 µs, where maximum voltage values were fixed at 0 and 50 µs. All monitored plasma species exhibited similar behaviour. Their excitation intensity increased as the voltage dropped, and later decreased as the voltage reached its minimum value. A subsequent increase in the intensity started when voltage rose. However, Ar time-intensity more than doubled compared to the intensities of OH and N_2. This behaviour is connected to plasma 'bullet' streamer and filament formation and propagation, which ICCD images highlight in Figure 3 [18–20]. Plasma streamer formation starts around 12 µs when the voltage changes from positive to negative, and propagates until the voltage reaches its minimum value. Then, the ionisation shifts and at around 37 µs filaments start to appear, gaining their maximum intensity soon after. Time-resolved OES indicated that Ar plays the most important role in filament formation, with OH and N_2 in secondary roles.

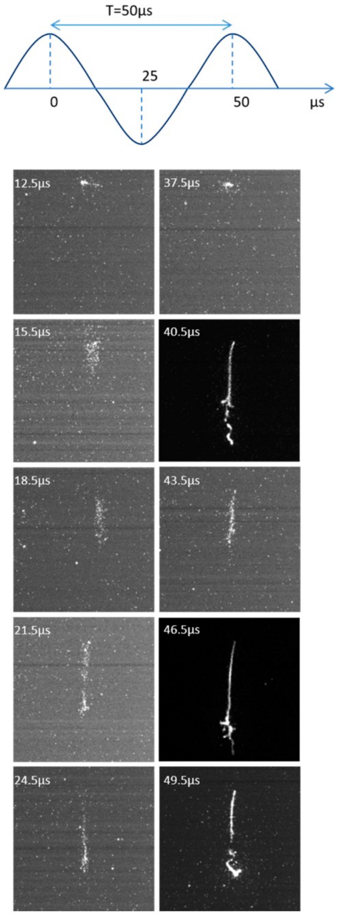

Figure 3. Plasma ionisation process. Propagation of a plasma bullet type of ionisation (**left**), from 12 µs to 25 µs, and formation of filaments (**right**), from 37 µs to 50 µs.

3.2. Plasma-Liquid Chemistry

To fully understand the plasma jet impact on cells in a liquid culture medium, the potential plasma-induced modifications in liquid chemistry need to be evaluated in detail. Firstly, as the liquid culture medium's pH is one of the most important factors that significantly influence cell viability, the pH of MEM was measured immediately after exposure to plasma. The results demonstrated no significant discrepancies from the non-treated sample's values or control (Figure 4). Thus, it was concluded that the pH level was not a contributing factor. Along with pH, conductivity was measured. As in the results obtained from pH measurements, conductivity exhibited similar stability. Data are presented in the supplementary file.

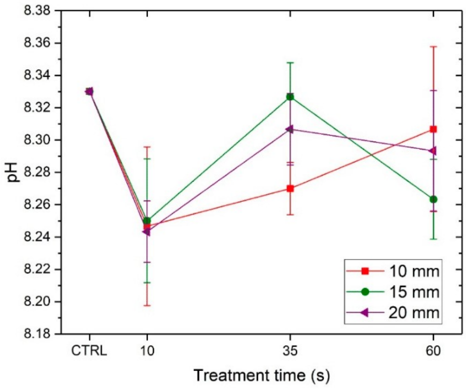

Figure 4. pH of plasma treated MEM measured right after treatment. Results are presented as mean values ± SEM (two-way ANOVA, Dunnett's post-tests; n = 3).

In contrast to the findings obtained for pH and conductivity measurements, the plasma treatments induced a slight increase in the concentrations of NO_2^- and H_2O_2. Figure 5a displays the concentrations of NO_2^- obtained immediately after treatment. As demonstrated from the results, the concentrations gradually increased with shorter distances between the plasma ignition point and MEM surface and longer exposure times. The maximum NO_2^- value (i.e., 10.5 µM) was measured at a distance of 10 mm after 60 s of exposure. Long distances led to negligible increases in NO_2^- concentrations. Similar trends were also observed for results obtained 24 h and 72 h after treatments (Figure 5c,e), where, generally, a small increase in NO_2^- concentration was noted. The shortest treatment distance and longest exposure time also led to the formation of the highest H_2O_2 concentration directly after plasma treatment (Figure 5b). A 60 s exposure of MEM to plasma at 10 mm distance resulted in the generation of 25.9 µM of H_2O_2. In contrast, concentrations of 19.5 µM and 6.3 µM were recorded at treatment distances of 15 mm and 20 mm, respectively. Unlike NO_2^-, H_2O_2 concentrations significantly shrank or completely disappeared after 24 h and 72 h (Figure 5d,f).

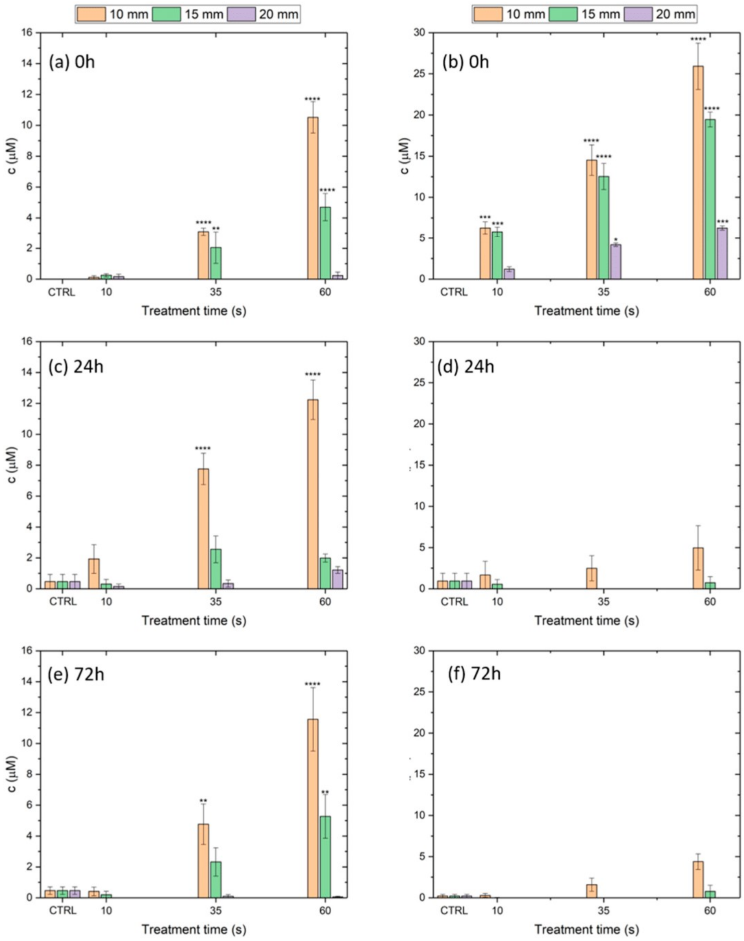

Figure 5. Concentration of NO_2^- (**left**) and H_2O_2 (**right**) in PAM measured (**a**,**b**) 0 h, (**c**,**d**) 24 h and (**e**,**f**) 72 h after plasma treatment. Results are presented as mean values ± SEM. * $p < 0.03$; ** $p < 0.002$; *** $p < 0.0002$; **** $p < 0.0001$ (two-way ANOVA, Dunnet's post-tests; n > 3).

3.3. Cell Viability

Cell viability is represented as the percentage of viable cells normalised to the control group (Figure 6) and is highly dependent on chosen parameters. As the cells were treated via direct plasma treatment, it was expected that the closest distance of 10 mm—where the plasma was in contact with the cell culture medium—would have the biggest effect on cell viability. Results show that less than 60% of cells are still viable after just 10 s of plasma treatment, and there are almost no viable cells as treatment time increases further. Consequently, greater distances, e.g., 15 mm and 20 mm, leave more viable cells in well plates. However, after just 60 s of plasma treatment, the number of viable cells dropped below 20% at a distance of 20 mm, and none were viable for shorter distances.

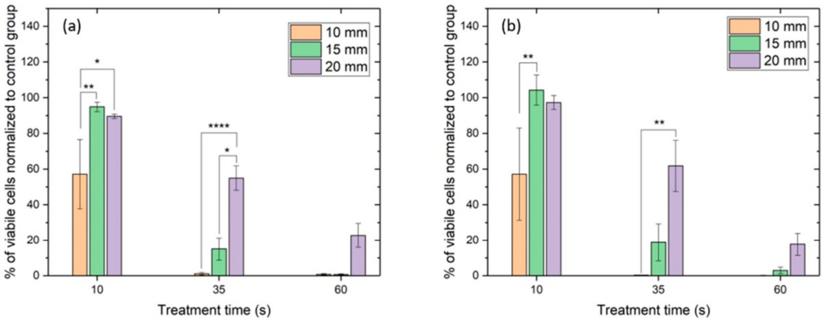

Figure 6. Cell viability test for 10 mm, 15 mm and 20 mm distance (**a**) 24 h and (**b**) 72 h after treatment. Results are presented as arithmetic mean ± SE. * $p < 0.05$; ** $p < 0.01$; **** $p < 0.0001$ (one-way ANOVA, Tukey test).

4. Discussion

Experimental results revealed that treating mouse skin cells with an atmospheric pressure kHz argon plasma jet affects cell viability. Our plasma system, used as a direct treatment, is very destructive towards L929 murine fibroblasts, highlighted by the fact that most of the cells are not viable after just 35 s of plasma treatment.

To understand what exactly causes this behaviour requires comparison with other studies and plasma systems. However, a comparison of plasma effects on cell viability with other plasma sources is extremely difficult, due to plasma source variances, plasma parameters, types of treated cells, types of plasma treatment and different approaches to the assessment of cell viability. Another problem connected to this research is repeatability, since not all researchers follow the same procedures and protocols. Similarly, researchers may not investigate all aspects needed to explain plasma effects on the treated biological samples.

Nevertheless, a comparison of approximately similar plasma systems, presented in Figure 7, highlights our plasma system's toxicity to cells. All selected sources operated in a kHz regime (20 or 40 kHz), except kINPen 09 [16], which operated in the MHz regime and was chosen as the most widely used plasma source for biomedical applications. For ease of reference, different plasma sources were given different symbols in Figure 7. The circle represents kINPen [16] (1.1 MHz, 2–6 kV, Ar—1.9 slm), the triangle represents a jet [7] (40 kHz, 4.9 kV, Ar—4 slm), the square represents a plasma torch [5] (20 kHz, 7 kV, He—5 slm), and the star represents our system. Each cited study focused on slightly different applications, so different types of cell lines were used (mHepR1, A431, HEK293, L929, LNCap, PC3 and P69). The direct approach is marked as a flat line, and the indirect approach as a dashed line. Results were selected where the distance between plasma and cell medium was 10 mm or less, and viability measured 72 h after treatment. The comparison indicates that our plasma treatment was very aggressive and the most destructive in the shortest treatment time.

To explain our jet's destructive nature on the treated cells, we must first look at the gas-phase diagnostics. OES did not show any deviation from expected species present in such plasma. The observed plasma was very stable and produced typical species for atmospheric pressure argon plasma at the beginning and end of the plasma plume (glow region) [17]. The gas temperature (measured as 318 K) is acceptable for in vitro biomedical applications and comparable to other plasma systems (e.g., kINPen 09 operates at 319–323 K [21]). Both time-resolved OES and ICCD images confirmed a regular ionisation process for a kHz-driven plasma source with the formation of pulsed streamers and filaments throughout the waveform [18–20].

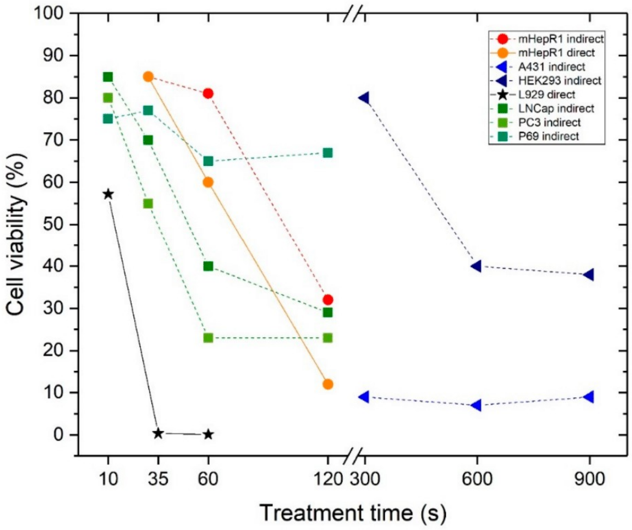

Figure 7. Comparison with other plasma sources: percentage of cell viability to direct (flat line) or indirect (dashed line) plasma treatment. Symbols represent different studies, so the circle is [16], the triangle is [7], the square is [5] and the star represents our system.

Since the gas-phase plasma parameters seem to be in accordance with other plasma sources used in cell treatment, the chemistry of the plasma-treated cell culture medium was explored. First, we made sure that the cell medium's pH and conductivity did not influence cell viability. Results were stable for all distances and treatment times. Then, we measured concentrations of NO_2^- and H_2O_2 inside the cell medium. Both concentrations were relatively low, and the NO_2^- concentration remained almost constant even 72 h after plasma treatment. In contrast, H_2O_2 concentration gradually decreased and was negligible 72 h after treatment. Comparison of H_2O_2 production with similar plasma sources is presented in Figure 8. Our results were compared to other sources that operate in the kHz region: 39.5 kHz (marked as a circle [22]), 30 kHz (marked as triangle [9]) and 17 kHz (marked as square [4]). Here, other concentrations are quite high compared to our system. One possible reason for this difference in H_2O_2 concentrations could be various cell culture media that were used; MEM was used in our research, DMEM (Dulbecco's Modified Eagle Medium) was used in [9] and RPMI 1640 was used in [22]. However, the results show that inside the same medium (DMEM), different concentrations of hydrogen peroxide can be obtained—almost a threefold difference for the longest treatment time of 60 s. Thus, we conclude that the generation of H_2O_2 is not the main source of our plasma source's destructiveness towards the L929 murine fibroblast cells. Instead, this destructiveness is thought to stem from the plasma characteristics of the argon jet used in the direct treatment conducted on these cell lines. Despite this, the argon jet is generally more aggressive towards cell lines in direct treatments than indirect ones, and as such, it should not be used for direct treatments of skin cells such as L929 murine fibroblasts.

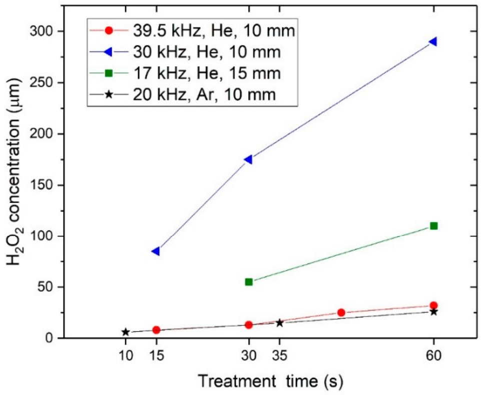

Figure 8. Comparison with other plasma sources: concentration of H_2O_2 to plasma treatment time. Symbols represent different studies: the circle is [22], the triangle is [9], the square is [4] and the star represents our system.

5. Conclusions

A non-thermal kHz argon plasma jet and its actions towards skin cells—L929 murine fibroblasts—was investigated. Although we followed reported protocols, we observed very aggressive behaviour of the jet towards the cells during direct treatment. However, neither gas-phase diagnostics nor liquid-chemistry characterisation provided a definitive answer as to why our plasma system behaved much more destructively than other sources reported. One possible reason is that such research has never been done specifically on L929 murine fibroblasts. However, there are several other possibilities for the obtained results. Firstly, plasma and its species can influence different types of cells in completely different ways. Research conducted on mHepR1 cell lines demonstrated that cell viability is higher after indirect plasma treatment than the direct approach [16]. Therefore, research must be expanded to include the indirect plasma treatment of L929 cell lines, along with additional research on other types of cells, in order to gain a deep understanding of cell behaviour. Secondly, because of the consistency of the liquid chemistry and its stability over time, it is likely that reactive species produced in the gas phase have a greater impact on cells. This is also supported by the fact that there were no major changes in viability after 24 h, from which we conclude that all cell death occurs before that time. Therefore, to gain a better insight into the timeframe for cell viability, cell viability tests—immediately or within a few hours after plasma treatment—have to be added to standard protocols. It seems that direct and short-lived plasma species could have a more extended role in cell viability than previously reported. Since this field of research is highly attractive—with many potential applications in biology and medicine—the protocols for observation of cells under plasma interaction have to be upgraded and modified.

Supplementary Materials: The following are available online at https://www.mdpi.com/2076-3417/11/3/1266/s1. Figure S1: Spatially-resolved OES with intensity normalised to 1, Figure S2: Conductivity of PAM measured right after treatment.

Author Contributions: Conceptualisation: A.J., U.C., G.S., A.N. and C.L.; Methodology: A.J., A.N. and Š.K.; Formal analysis: A.J., N.H. and Š.K.; Investigation: A.J., I.S., Š.K., A.N. and N.H.; Resources: U.C., G.S. and C.L.; Writing—original draft preparation: A.J.; writing—review and editing: G.S., N.H., I.S., Š.K. and U.C.; Visualisation: A.J.; Supervision: A.N., Š.K. and U.C.; Project administration and funding acquisition: U.C., G.S., A.N. and C.L.; All authors have read and agreed to the published version of the manuscript.

Funding: This research was funded by the Slovenian Research Agency (ARRS) and Research Foundation Flanders (FWO), grant number N3-0059 and G084917N, respectively.

Institutional Review Board Statement: Not applicable.

Data Availability Statement: The authors declare that the data supporting the findings of this study are available within the paper. All additional raw and derived data that support the plots within this paper and other finding of this study are available from the corresponding author upon reasonable request.

Conflicts of Interest: The authors declare no conflict of interest.

References

1. Laroussi, M.; Lu, X.; Keidar, M. Perspective: The physics, diagnostics, and applications of atmospheric pressure low temperature plasma sources used in plasma medicine. *J. Appl. Phys.* **2017**, *122*, 020901. [CrossRef]
2. Haertel, B.; von Woedtke, T.; Weltmann, K.D.; Lindequist, U. Non-thermal atmospheric-pressure plasma possible application in wound healing. *Biomol. Ther.* **2014**, *22*, 477–490. [CrossRef] [PubMed]
3. Laroussi, M. Plasma Medicine: A Brief Introduction. *Plasma* **2018**, *1*, 5. [CrossRef]
4. Kurita, H.; Haruta, N.; Uchihashi, Y.; Seto, T.; Takashima, K. Strand breaks and chemical modification of intracellular DNA induced by cold atmospheric pressure plasma irradiation. *PLoS ONE* **2020**, *15*, e0232724. [CrossRef] [PubMed]
5. Fofana, M.; Buñay, J.; Judée, F.; Baron, S.; Menecier, S.; Nivoix, M.; Perisse, F.; Vacavant, A.; Balandraud, X. Selective treatments of prostate tumor cells with a cold atmospheric plasma jet. *Clin. Plasma Med.* **2020**, *17–18*, 100098. [CrossRef]
6. Sato, T.; Yokoyama, M.; Johkura, K. A key inactivation factor of HeLa cell viability by a plasma flow. *J. Phys. D Appl. Phys.* **2011**, *44*, 372001. [CrossRef]
7. Schweigert, I.; Zakrevsky, D.; Gugin, P.; Yelak, E.; Golubitskaya, E.; Troitskaya, O.; Koval, O. Interaction of cold atmospheric argon and helium plasma jets with bio-target with grounded substrate beneath. *Appl. Sci.* **2019**, *9*, 4528. [CrossRef]
8. Ja Kim, S.; Min Joh, H.; Chung, T.H. Production of intracellular reactive oxygen species and change of cell viability induced by atmospheric pressure plasma in normal and cancer cells. *Appl. Phys. Lett.* **2013**, *103*, 153705. [CrossRef]
9. Gaur, N.; Kurita, H.; Oh, J.; Miyachika, S.; Ito, M.; Mizuno, A.; Cowin, A.J.; Allison, S.; Short, R.D.; Szili, E.J. On cold atmospheric-pressure plasma jet induced DNA damage in cells. *J. Phys.* **2020**, *54*, 035203. [CrossRef]
10. Jo, A.; Joh, H.M.; Chung, J.W.; Chung, T.H. Cell viability and measurement of reactive species in gas—And liquid-phase exposed by a microwave-excited atmospheric pressure argon plasma jet. *Curr. Appl. Phys.* **2020**, *20*, 562–571. [CrossRef]
11. Mehrabifard, R.; Mehdian, H.; Hajisharifi, K.; Amini, E. Improving Cold Atmospheric Pressure Plasma Efficacy on Breast Cancer Cells Control-Ability and Mortality Using Vitamin C and Static Magnetic Field. *Plasma Chem. Plasma Process.* **2020**, *40*, 511–526. [CrossRef]
12. Sremački, I.; Jurov, A.; Modic, M.; Cvelbar, U.; Wang, L.; Leys, C.; Nikiforov, A. On diagnostics of annular-shape radio-frequency plasma jet operating in argon in atmospheric conditions. *Plasma Sources Sci. Technol.* **2020**, *29*, 035027. [CrossRef]
13. Schieber, M.; Chandel, N.S. ROS function in redox signaling and oxidative stress. *Curr. Biol.* **2014**, *24*, R453–R462. [CrossRef] [PubMed]
14. Clément, M.V.; Pervaiz, S. Intracellular superoxide and hydrogen peroxide concentrations: A critical balance that determines survival or death. *Redox Rep.* **2001**, *6*, 211–214. [CrossRef]
15. Duchesne, C.; Frescaline, N.; Lataillade, J.J.; Rousseau, A. Comparative study between direct and indirect treatment with cold atmospheric plasma on in vitro and in vivo models of wound healing. *Plasma Med.* **2018**, *8*, 379–401. [CrossRef]
16. Hoentsch, M.; Von Woedtke, T.; Weltmann, K.D.; Barbara Nebe, J. Time-dependent effects of low-temperature atmospheric-pressure argon plasma on epithelial cell attachment, viability and tight junction formation in vitro. *J. Phys. D Appl. Phys.* **2012**, *45*, 025026. [CrossRef]
17. Jonkers, J.; Van De Sande, M.; Sola, A.; Gamero, A.; Van Der Mullen, J. On the differences between ionizing helium and argon plasmas at atmospheric pressure. *Plasma Sources Sci. Technol.* **2003**, *12*, 30–38. [CrossRef]
18. Laroussi, M.; Begum, A.; Karakas, E. Experimental investigations of plasma. *J. Phys. D Appl. Phys.* **2009**, *42*, 055207. [CrossRef]
19. Jarrige, J.; Laroussi, M.; Karakas, E. Formation and dynamics of plasma bullets in a non-thermal plasma jet: Influence of the high-voltage parameters. *Plasma Sources Sci. Technol.* **2010**, *19*, 065005. [CrossRef]
20. Barletta, F.; Leys, C.; Colombo, V.; Gherardi, M.; Britun, N.; Snyders, R.; Nikiforov, A. Insights into plasma-assisted polymerization at atmospheric pressure by spectroscopic diagnostics. *Plasma Process. Polym.* **2020**, *17*, 1–15. [CrossRef]
21. Bekeschus, S.; Schmidt, A.; Weltmann, K.D.; von Woedtke, T. The plasma jet kINPen—A powerful tool for wound healing. *Clin. Plasma Med.* **2016**, *4*, 19–28. [CrossRef]
22. Xu, G.M.; Hao, Y.; Sun, M.Y.; Liu, J.R.; Shi, X.M.; Zhang, G.J. Characteristics of Plasma Activated Medium Produced by Atmospheric Pressure Helium Plasma Jet and Its Selective Effect on Malignant Melanoma and Normal Fibroblast Cells. *IEEE Trans. Plasma Sci.* **2020**, *48*, 587–595. [CrossRef]

4.3 Atmospheric Pressure Plasma Jet – Mouse Skin Interaction: Mitigation of Damages with Liquid Interfaces or Gas Flow Dynamics

The presented research addressed effects of a cold APPJ on mouse skin. Even though plasma jets are often presented as a safe option for treatment of biological material, mostly because of their low gas temperature, we showed otherwise. The challenge was to reduce primary and secondary sin tissue damage induced by plasma jets. We tried to understand how and to what extent skin tissue damage can be inflicted by a kHz plasma jet generated in Ar or He. Different approaches – based on minor jet modifications through to gas flow dynamics, gas mixtures or liquid interfaces – were tested with varied but significant success. In order to investigate the cause behind plasma-inflicted skin damage, diagnostics of the power source and plasma discharge were performed. They showed that plasma was stable during the experiments, with some changes occurring when plasma breached the mouse skin. OES detected more species after the mouse skin was breached or the plasma regime became uncoupled. This difference was more prominent for Ar than He plasma, which also proved to be more harmful to the skin.

After assessing plasma induced skin damages, we proposed a few approaches to reduce the damage. Those approaches proved to be simple methods that can dramatically lessen primary skin tissue damage and, in some cases, completely avoid formation of secondary skin tissue damage. These findings are important as they will improve the safe use of cold APPJs in further research on skin treatment.

Regarding my contribution: I interpreted obtained results and prepared the original draft of the manuscript along with visualizations.

Atmospheric pressure plasma jet-mouse skin interaction: mitigation of damages by liquid interface and gas flow control

Andrea Jurov

Department F6, Jožef Stefan Institute, Jamova cesta 39, SI-1000 Ljubljana, Slovenia, EU

International Postgraduate School Jožef Stefan, Jamova cesta 39, SI-1000 Ljubljana, Slovenia, EU

Špela Kos

Department of Experimental Oncology, Institute of Oncology Ljubljana, Zaloška 2, SI-1000 Ljubljana, Slovenia, EU

Tanja Blagus

Department of Experimental Oncology, Institute of Oncology Ljubljana, Zaloška 2, SI-1000 Ljubljana, Slovenia, EU

Ivana Sremački

Department of Applied Physics, Ghent University, Sint-Petersnieuwstraar 41, 9000 Gent, Belgium, EU

Gregor Filipič

Department F6, Jožef Stefan Institute, Jamova cesta 39, SI-1000 Ljubljana, Slovenia, EU

Nataša Hojnik

Department F6, Jožef Stefan Institute, Jamova cesta 39, SI-1000 Ljubljana, Slovenia, EU

Anton Nikiforov

Department of Applied Physics, Ghent University, Sint-Petersnieuwstraar 41, 9000 Gent, Belgium, EU

Christophe Leys

Department of Applied Physics, Ghent University, Sint-Petersnieuwstraar 41, 9000 Gent, Belgium, EU

Maja Čemažar

Department of Experimental Oncology, Institute of Oncology Ljubljana, Zaloška 2, SI-1000 Ljubljana, Slovenia, EU

Faculty of Health Sciences, University of Primorska, Polje 42, SI-6310 Izola, Slovenia, EU

Gregor Serša

Department of Experimental Oncology, Institute of Oncology Ljubljana, Zaloška 2, SI-1000 Ljubljana, Slovenia, EU

Faculty of Health Sciences, University of Ljubljana, Zdravstvena pot 5, SI-1000 Ljubljana, Slovenia, EU

Uroš Cvelbar [a)]

Department F6, Jožef Stefan Institute, Jamova cesta 39, SI-1000 Ljubljana, Slovenia, EU

[a)] Electronic mail: uros.cvelbar@ijs.si

The possible benefits of an atmospheric pressure plasma jet skin treatment have been tested *in vivo* on mouse skin. Many studies have been conducted *in vitro* on mouse skin cells, but few *in vivo*, where plasma can, in certain cases, cause severe damages. For this reason, we investigated how kHz plasma generated in a jet that is known to inflict skin damage, interacts with mouse skin and explored how we can reduce skin damage. First, the focus was on exploring plasma effects on skin damage formation with different plasma gases and jet inclinations. The results pointed to a perpendicular orientation of a helium plasma jet as the most promising condition with the least skin damage. Then, skin damage caused by a helium plasma jet was explored, focusing on damage mitigation with different liquid interfaces applied on the treatment site, adding nitrogen to the gas mixture, or alternating the gas flow dynamics by elongating the jet's glass orifice with a funnel. All these mitigations proved highly efficient, but the utmost benefits for skin damage reduction were connected to skin temperature reduction, reduction of reactive oxygen species, and increase of reactive nitrogen species.

I. INTRODUCTION

Plasma medicine has been developing into an innovative and growing medical research field during the last few years. Aside from established applications of plasma for sterilization of materials and devices [1–4], a potentially transformative application is in cancer therapy [5–8] or dermatology and aesthetic surgery, with the aim to improve tissue regeneration and healing of infected or chronic wounds [9–13]. Although a growing number of atmospheric pressure plasma sources for biomedical applications are described in the literature and evaluated in in vitro studies, only limited research has been conducted so far in in vivo conditions, exploring the safety aspects of plasma treatment. Even if topical plasma treatment is mostly considered a safe and harmless approach for the skin [14–19], it could cause noticeable skin malformations, as we demonstrated in a previous study [20].

The extent of skin damage after atmospheric pressure helium plasma jet treatment is time and flow rate dependent. Besides the high concentrations of reactive oxygen and nitrogen species (RONS) and the increase of skin temperature, key discharge parameters characterized for tissue damage were shown to be gas flow dynamics, plasma jet properties, and electrical coupling of plasma and mouse skin. In the first part of this study, the aim is to explore in detail the effects of an atmospheric pressure plasma jet (APPJ) on direct and indirect skin damage formation, with an emphasis on plasma gas selection [21,22], skin temperature measurements [23–25], and jet orientation [26]. With an evaluation of different plasma parameters, the boundaries of plasma destructiveness are set, which opens the possibility of controlling and ameliorating the extent of skin damage after topical treatment with a helium plasma jet. With the obtained parameters to minimize tissue damage , the second part of the study aims to evaluate and control the extent of skin damage caused by helium jet treatment by administrating liquids with different modalities at the treatment site, adding nitrogen impurity into the gas flow [27–29] and regulating the gas flow dynamics [30]. We hypothesize that by regulating crucial parameters of the helium jet, the extent of skin damage will be reduced, leading to APPJ's improved safety and accelerating its rollout in clinical applications.

II. EXPERIMENTAL

A. Reagents

Four kDa fluorescein-isothyocianate (FITC) labelled dextran (Sigma-Aldrich, St. Louis, MO, USA) was used as an indicator of direct skin damage caused by plasma treatment since FITC labelled dextran does not leach into the area of indirect skin damage. The preparation of FITC labelled dextran for the purpose of topical administration has been described elsewhere [20]. To evaluate the effect of liquids applied topically on plasma-treated skin, 70% ethanol (prepared from ethanol absolute anhydrous, Carlo Erba Reagents, Chaussee du Vexin, France), 10% acetic acid (prepared from Acetic acid Glacial, Merck, Kenilworth, NJ, USA), phosphate-buffered saline (PBS), and saline (NaCl 0.9%, B. Braun, Melsungen, Germany) were administered to the treated skin surface prior to plasma treatment.

B. Animal and skin preparation

All procedures were performed in compliance with EU directive (2010/63/EU) guidelines for animal experiments and with the permission of the Veterinary Administration of the Ministry of Agriculture, Forestry and Food of the Republic of Slovenia (permission no. 34401-4/2012/4). 8–12 week old female Balb/c mice (Envigo, Udine, Italy) were used in the experiments. All mice were housed in pathogen-free conditions with 12-hour light cycles and provided food and water ad libitum. A day before plasma treatment, mice were shaved on the left flank, and depilatory cream (Veet® Sensitive Skin, Reckitt Benckiser, UK) was applied to remove any remaining hair. At the end of the experiment, treated mice were humanely sacrificed by cervical dislocation or inhalation of CO2.

C. Plasma system and plasma treatment

Plasma system. The plasma system was an atmospheric pressure plasma jet (APPJ) with a single inner electrode connected to a commercial 25 kHz high-voltage AC power supply from Conrad Electronic. The system was described in detail in our previous publication [20]. Additionally, a glass funnel was used to minimise ambient air influence and helped to deliver RONS directly to the mouse skin. Two different funnels were applied, both with the same dimensions; 2 cm height, an outer diameter of 10 mm, and an inner diameter of 7 mm. In addition, the second funnel had six holes at the bottom, with a height of 2 mm and width of 1 mm, and was in contact with the mouse skin during the experiments. Different plasma treatments performed in this research are depicted in Fig. 1.

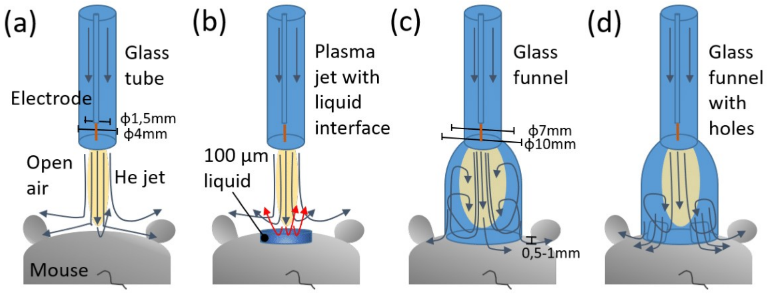

Fig. 1. Schematic representation of different plasma treatments. First, plasma operated in ambient air without a liquid interface (a) or with it (b). Second, plasma was 'contained' inside a funnel without holes (c) and in the funnel with the holes (d).

Plasma treatment. Mice were initially anaesthetised with inhalation anaesthesia in the induction chamber using a 2% isoflurane (Nicholas Piramal India, London, UK) mixture with oxygen. Mice were placed on a flat surface, with their snout in the inhalation tube to remain anaesthetised during the procedure. Prior to the plasma treatment, 100 µL of liquid (ethanol, acetic acid, PBS, or saline) was applied to target skin tissue on the mouse's left flank. Immediately after the liquid application, mice were treated with helium or argon plasma, with a fixed distance of 2 cm between the generator and the target tissue (Fig. 2). Plasma conditions were assigned based on the results of our previous study [20], *i.e.*, mice were treated with an applied gas flow rate of 1-5 L/min and a delivery time of 4 min. The used gases were helium and argon, both of purity 5.0 (Messer Slovenija, Ruse, Slovenia). Optical emission spectroscopy (OES) was conducted with spectrometer Avantes AvaSpec 3648 with a nominal spectral resolution of 0.8 nm. All spectra were obtained with the same exposure time and under the same fibre–plasma distance for easier comparison.

Immediately after plasma treatment, a patch soaked with 100 µL of FITC labelled dextran was applied to the treated skin tissue. After 1 h, the patch was removed, and fluorescence imaging was conducted.

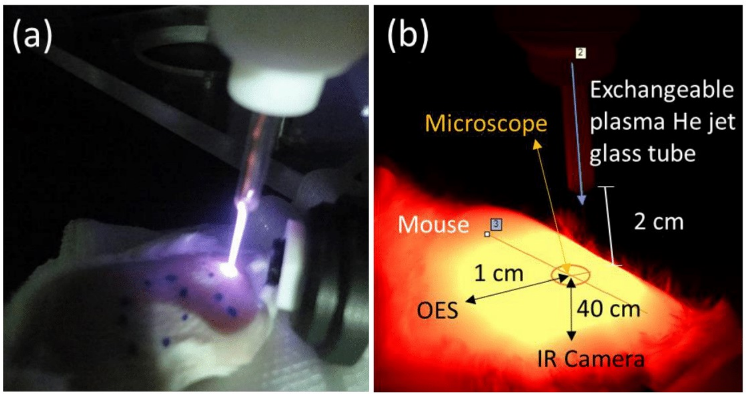

Fig. 2. Photographs of the plasma treatment (a) and distances of the plasma and diagnostic tools from the treatment surface (b).

D. Fluorescence microscopy for evaluation of skin damage

Skin damage was assessed using a Zeiss Stereo Lumar.V12 (Zeiss, Jena, Germany) fluorescence stereomicroscope equipped with an MRc.5 digital camera (Zeiss). Mice in the experiments were first anaesthetised with inhalation anaesthesia in the induction chamber (2% isoflurane in oxygen). They were then placed under the microscope with their snout in the inhalation tube to remain anesthetized during the measurement procedure. At each time point, images were taken under fluorescent light (RGB images) or under visible light (VIS images). The first image was taken 1 h post-treatment, the rest followed at 3, 24, and 48 h post-treatment. The areas of total (VIS images) and direct (RGB images) skin damages were analyzed with image analysis software AxioVision (Zeiss). The percentage of indirect damage was calculated from the total and direct skin damage, details of which are presented in [20].

E. Monitoring mouse skin surface

The thermal effects of plasma on the mouse skin were monitored with infrared (IR) imaging using a FLIR SC500 (FLIR Systems, Inc., Wilsonville, OR, USA) camera. Images recorded the surface of the mouse skin as described in our previous publication [20].

In order to control the liquid interface, it was important to measure the evaporation rate of liquids under plasma treatment. All the liquids – ethanol, saline, deionized water, PBS, and acetic acid – were treated with plasma in a cuvette on an analytical balance for 240 s. Every 15 s, the weight of the liquid was measured, and later the evaporation rate was calculated. The balance that was used was Radwag AS 220.R2 (Radwag UK Ltd, Macclesfield, UK).

F. Statistical analysis of plasma-induced cell damage

For statistical analysis, Sigma Plot software (Systat Software, London, UK) was used. Mean and standard errors were calculated for each treatment group. Comparison between groups was done using a one-way analysis of variance (ANOVA) followed by the Holm–Sidak test. A value $p < 0.05$ was considered statistically significant. The values were expressed as arithmetic mean (AM) ± standard error of the mean (SEM).

III. RESULTS AND DISCUSSION

Results are presented in two parts. First, we present an evaluation of the effects of plasma on the mouse skin and the direct and indirect damage it caused. The second part focuses on results for controlling and reducing the extent of skin damage produced with helium plasma by adding different liquids on the treatment site, adding nitrogen into the gas mixture, or changing the plasma flow dynamics via a funnel connected to the glass tube.

A. Evaluation of helium and argon APPJ effects on mouse skin

1. Gas flow dynamics and characterization

For biomedical applications, it is very important to use a stable plasma system. To monitor plasma source stability during the treatment, voltage and current measurements were measured before and during the treatments. *I–V* characterization is presented in Fig. 3, where the free or uncoupled jet (b) waveforms and coupled jet with skin (c), where the streamers are generated, can be seen. The waveform was uniform with constant maximum values of current and voltage of 2.2 mA and 3.8 kV in cases when a jet is not coupled to mouse skin, which typically happens at low flow rates, low powers, or when mouse skin is breached and an underlayer is exposed. However, after the plasma coupled with skin and the streamers were formed, the waveform changed, which manifested as an additional period of 0.4 ms width in which values of current and voltage rose from 0.8 mA and 0.2 kV to their maximum values 4.3 mA and 1.5 kV, respectively.

Discharge's electrical characteristics are complemented with OES, which reveals excited species in plasma and gives an insight into the presence of the reactive species present in the experiments (Fig. 3(d)). As observed from the spectra, obtained of helium plasma jet in the non-coupling mode, only a few lines from a second positive band of N_2 were detected. Lack of helium emission lines indicates that helium species recombined very fast and were undetectable with this setup. After the streamers were generated, more energy was transferred to the mouse skin surface and detected emission lines were more prominent. Along with the nitrogen lines from the air present at the beginning of the experiment, additional nitrogen lines appeared in the same band, particularly the prominent nitrogen molecule ion line at 391.3 nm. Furthermore, the helium line at 706.5 nm started to appear, although it was barely observable. In the argon plasma jet in non-coupling mode, some lines from the second positive nitrogen band were observed along with Ar I lines in the range 695–915 nm. Moreover, the intensity of all emission lines increased after the streamers formed. The spectra include 309 nm OH line partially overlapping with 315 nm N_2 line, emission lines in the range 315–380 nm from second positive nitrogen band, lines in the range 390–435 nm from the first negative nitrogen molecule band, 777 nm oxygen line, and many Ar I emission lines in the range 695–925 nm. Both experiments showed a rise in the number and intensity of observed emission lines after the streamers formed, which implies severe and fast recombination processes occurring during mouse skin plasma treatment. More excited species appeared after the mouse skin was breached or the regime became uncoupled, especially in the argon plasma. However, the presence of hydrogen and oxygen emission lines was not detected in any spectra which in combination with the rise of nitrogen lines, could suggest a high production rate of biologically important reactive species such as H_2O_2, NO_2^-, NO_3^- at the non-coupling stages of the experiment [31].

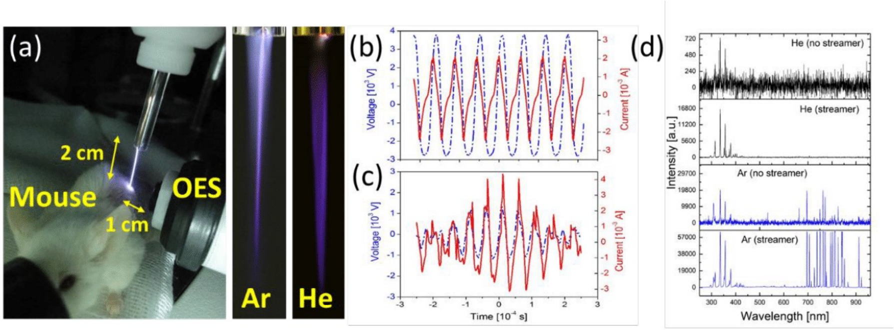

Fig. 3. Photograph of the procedure and plasma jet (a), I–V characterization of He plasma discharge without (b) and with streamers (c), and corresponding OES of He and Ar plasma (d).

2. *Influence of helium and argon plasma on mouse skin tissue*

The early effects of the plasma jet on treated mouse skin were observed immediately after treatment. These effects were noticed as skin burns at the site where the plasma jet was in contact with mouse skin and were considered as direct skin damage [20]. To evaluate temperature-related direct skin damage, IR imaging was applied (Fig. 4 and 5). The results indicate that argon plasma was significantly more harmful to skin tissue than helium plasma. Under the same flow rate of 1 L/min and treatment time of 4 min, the maximum detected temperature at the treatment site was 36 °C in the case of helium plasma, while the temperature increased to 103 °C with argon plasma. It caused severe skin burns, observed instantly after treatment.

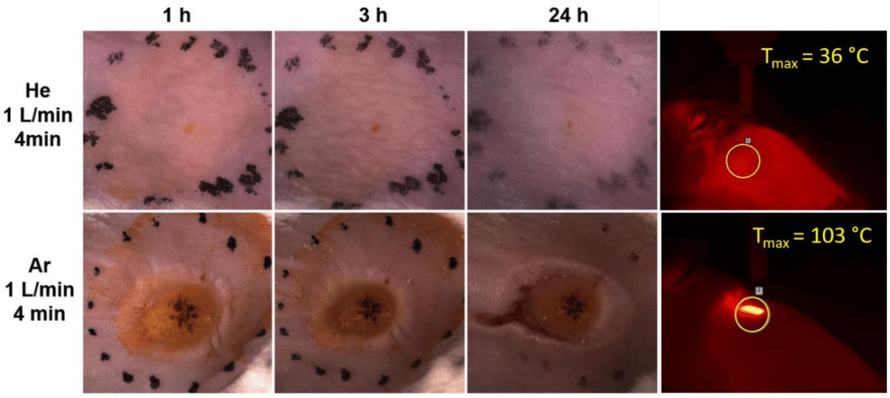

Fig. 4. Photographs of skin damage induced by helium or argon plasma taken 1 h, 3 h, and 24 h after the experiment, along with temperature measurements of the skin taken during the experiment.

Since the increase of skin temperature and observed skin damage were minimal after treatment with 1 L/min helium plasma, the flow rate was then increased to 4 L/min, and IR imaging was applied at different time points during the treatment. As presented in Fig. 5, the temperature rose with increased treatment duration, resulting in notable early direct skin damage. Here it is worth noting that in the case of argon plasma, the high skin damage that occurred could also be due to the higher concentration of reactive oxygen species (ROS) inside the plasma. It is known that ROS play an important role in biological processes, but when their concentrations rise, they can induce more damage [31–35]. The influence of oxygen concentration on skin damage is further discussed in Section 3.2.3.

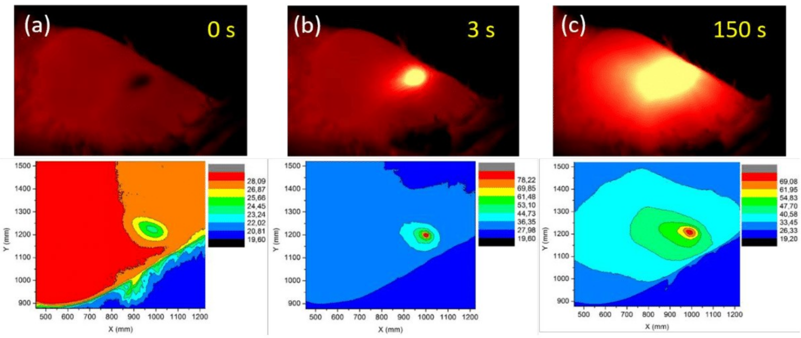

Fig. 5. Example of IR imaging of helium plasma during *in vivo* treatment (a) without plasma and just an impinging He jet, (b) at the beginning when the plasma is turned on, and (c) towards the end of the experiment. The gas flow rate was 5 L/min.

Besides the early effects of skin heating, additional skin damage was noticed 24–48 h post plasma treatment as oedema around the treated area. Oedema was ascribed to RONS formation at the plasma–surface interface and late effects of plasma treatment and is considered as indirect skin damage [36,37]. As already presented in the previous study [20], indirect skin damage depends on the angle of the plasma jet stream, *i.e.*, when the stream is not perpendicularly oriented to the treated skin, the extent of indirect skin damage is more severe. Results presented in Fig. 6 show that a smaller inclination broadens the indirect skin damage. For helium plasma with a reduced inclination of 45˚, the damaged area grew by 2–14 times depending on the treatment time compared to a 90˚ inclination. See supplementary material at [URL will be inserted by AIP Publishing] for photographs of helium and argon plasma induced skin damage areas under different jet inclinations. This is attributed to the larger contact surface area that the plasma had with the skin, which enabled a higher bombardment rate of reactive species and led to broader skin heating. Additionally, argon plasma inflicted greater damage to the skin when it was directed perpendicular to skin comparing to helium plasma: a 4–40 times larger damaged skin area. For this reason, no further *in vivo* experiments were done with argon plasma in the presented study.

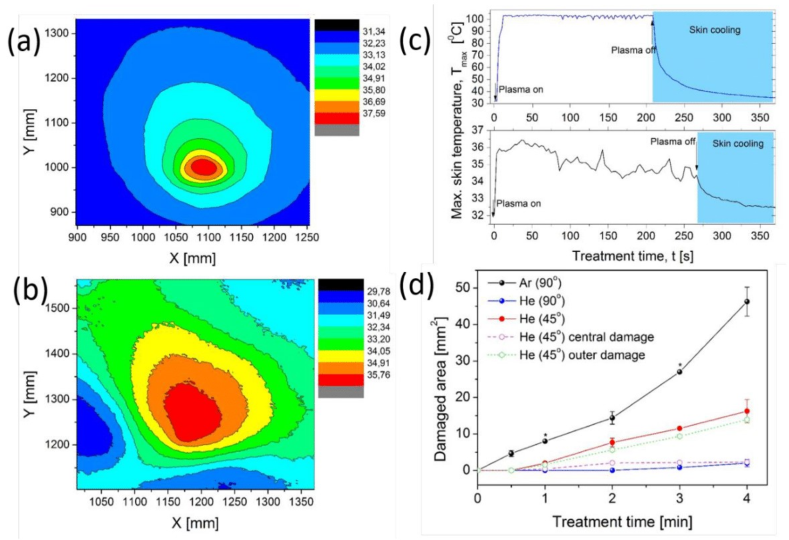

Fig. 6. Temperature profile distribution of mouse skin with a 90˚ (a) and 45˚ (b) inclined He plasma jet. (c) Time evolution of skin temperature in the centre during the plasma treatment (top – Ar plasma, bottom – He plasma at flow rate 1L/min). (d) Evaluated damaged skin area for different plasma jet inclinations and its central part where the skin was bridged.

B. Minimizing skin tissue damage

1. Application of the liquid interface

Due to the large extent of direct and indirect damages from both gases, we had to find new ways to control or prevent them. The first approach to skin damage reduction is the addition of different interfacial liquids, which could add some beneficial properties, such as a high evaporation effect for cooling the treatment site, antiseptic ability, and maintaining constant pH. Thus, liquids (ethanol, acetic acid, PBS, or saline) were applied to the mouse skin prior to plasma treatment. Following plasma exposure, areas of direct skin burns and the presence of indirect skin damage were evaluated (Fig. 7 and 8(a)). Results indicate that skin damage could be ameliorated if ethanol was applied to the treatment site prior to plasma treatment. Plasma treatment with the ethanol pre-treatment resulted in minimal direct skin damage, whilst indirect damage was not observed. In contrast, pre-treatment with acetic acid, PBS, and saline led to extensive skin burns at the site where the plasma jet was in contact with mouse skin. Additionally, after 48 h post-treatment, severe indirect plasma jet effects were noticed, especially in the case of saline application.

A factor that could interpret demonstrated differences is that the plasma system was not connected to any ground. As a result, the mouse skin and used liquids took over the function of a ground electrode, leading to coupling. This effect was demonstrated by I–V characterization in Fig. 3(b) and (c), where different waveforms are observed. Similarly, adding a liquid to the mouse skin before treatment impacted the conductivity of the treated mouse skin and consequently modified the ‘electrode’ properties and thus plasma–mouse interactions. The electrical conductivity of liquids is dependent on the concentration of the ionized chemical species in the solution. Among all the liquids used in this study, PBS possesses the highest electrical conductivity (10.6 S/m [38]), followed by 0.9% saline (1.45 S/m [39]), and 10% acetic acid (0.2 S/m [40]). Ethanol and deionised water are not electrically conductive; however, after the plasma treatments, their conductivity was modified due to the addition of plasma ionised species and their diffusion into the liquid. As plasma-induced skin damage cannot be explained only with electrical conductivity, thermal effects must also be considered. Since plasma was heating the skin, liquid evaporation and gas flow produced a cooling effect. Volume loss measurements reveal (Figure 8(b)) that all liquids had roughly the same linear evaporation rate, except ethanol, the only liquid that evaporated completely after 240 s of plasma treatment. The proposed conclusion is that ethanol's cooling effect and low electrical conductivity greatly reduce skin damage. Therefore, ethanol represents the best intermediate liquid stage for minimizing skin damages during plasma treatments. However, even more efficient skin damage control was obtained in gas mixtures, where nitrogen gas was added to the He gas flow, as detailed below.

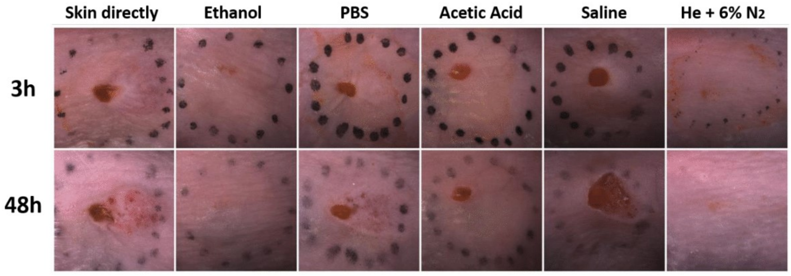

Fig. 7. Photographs of skin damage after 3 h and 48 h without and with different liquid interfaces after 4 min of the most severe helium plasma treatment at a gas flow rate of 5 L/min. The liquid interface on the skin was ethanol, PBS, acetic acid, and saline. Additionally, plasma damages with a mixture of He 6% and N_2 are presented.

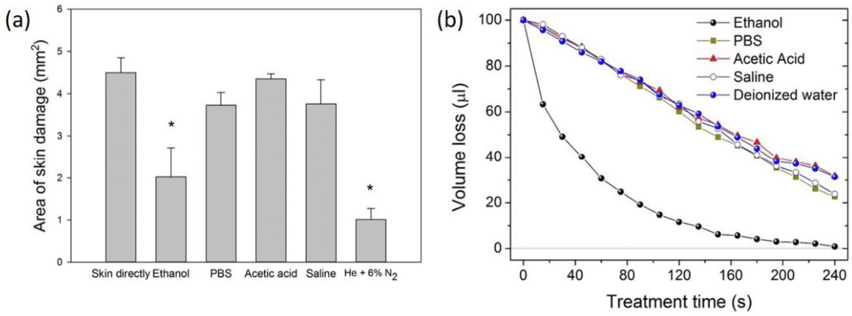

Fig. 8. (a) Numeric representation of direct skin damage for different liquid interfaces and gas mixtures observed 3h after the treatment. (b) Volume loss at the liquid interface for ethanol, PBS, acetic acid, saline, and deionized water under the plasma treatment.

2. Combining He and N_2 plasma minimizes the extent of skin damage

In order to minimize skin tissue damage, a mixture of helium and 6% nitrogen was used as the plasma gas. At a gas flow rate of 5 L/min – the most severe condition for He plasma treatment – this was the maximum concentration of nitrogen we could add to the plasma system and still ignite the plasma jet.

When adding 6% N_2 to the helium gas mixture, only minimal tissue damage at the plasma treatment site was observed (Fig. 7 and 8) without notable oedema, typical for the development of indirect damage (Fig. 7). See supplementary material at [URL will be inserted by AIP Publishing] for additional optical and fluorescence photographs of skin damage under pure helium plasma and a mixture of helium and 6% nitrogen plasma. According to the research, the addition of nitrogen as an impurity in helium plasma influences the propagation of plasma and affects the generation and transport of reactive species [41,42]. Regardless of the lower ionisation energy of nitrogen compared to helium, having higher nitrogen concentrations, such as 6% in our case, led to the reduction of the total plasma ionization degree. In the gas mixture helium helps ionizing nitrogen, via Penning ionization, leading to reduced concentrations of helium ions and augmentation of nitrogen molecule ions [27]. One of the main reasons behind skin damage mitigation might have been the change of the reactive species delivered to the mouse skin. The addition of 6% nitrogen impurity modified the jet profile, producing a more uniform structure than the pure helium jet plasma. With increasing nitrogen impurity, reactive nitrogen species' intensity also rises, especially NO.

3. The extent of tissue damage controlled by regulating gas flow dynamics

The third approach to regulating skin damages was to explore the potential of turbulent flow dynamics. This was done by changing plasma jet design by adding a funnel (Fig. 2) with or without holes at the treatment site. This enabled two benefits: a) limiting access of neighbouring air and generated air radicals, and b) using gas circulation within the funnel with chaotic gas dynamics retaining ionised species for longer periods at the treatment site. The glass funnel ameliorated the extent of skin damage, especially when helium was combined with N_2 (Fig. 9). Only minor direct skin damage was observed where the funnel was in contact with the skin. When the funnel was applied, indirect damage was absent. There was no significant difference in skin damage within measurement errors when the funnel with holes was used compared to the funnel without holes (Fig. 10). Since, in the case of the funnel without holes, the funnel itself could not be in complete contact with the skin (due to the mouse shape and the necessity of a gas outlet), this result was expected. However, the reason behind damage mitigation by funnel use (with or without holes) could be that there is a smaller concentration of ROS because the funnel reduces the amount of oxygen diffused to plasma from the ambient air.

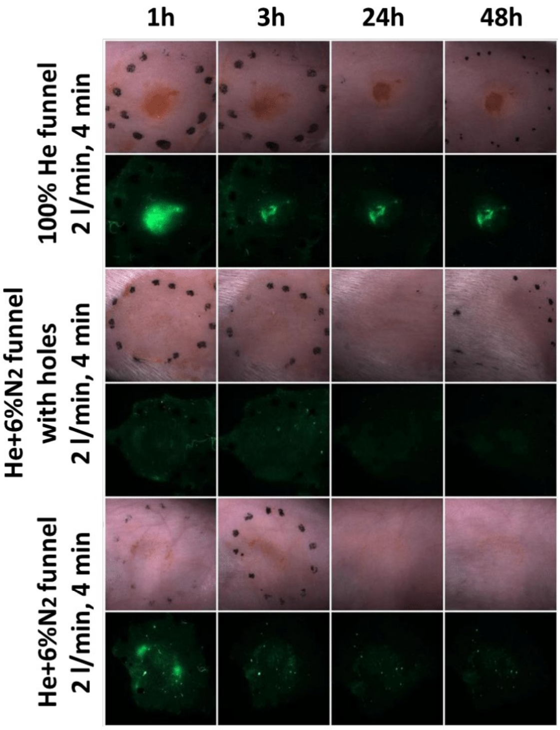

Fig. 9. Optical and FTIC labelled dextran fluorescence photographs of skin damage with two funnel types and nitrogen addition.

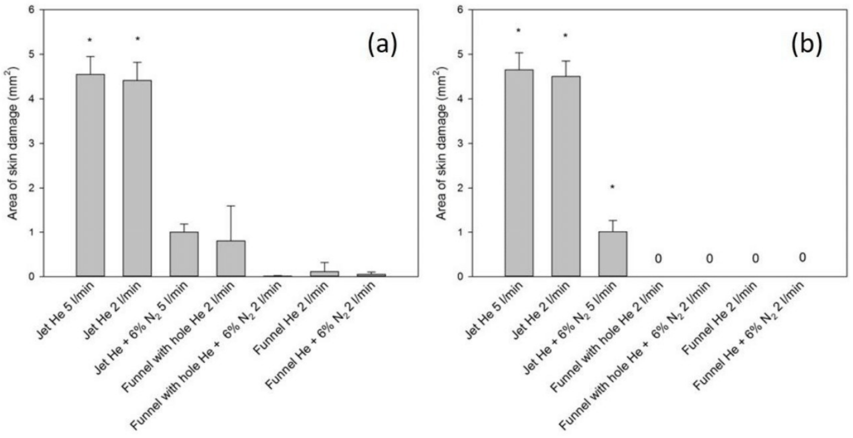

Fig. 10. Summarized numerical representation of skin damage for all different funnel combinations and gas mixtures: direct skin damage measured 1 h post-treatment (a), and direct skin damage measured 24 h post-treatment (b).

IV. SUMMARY AND CONCLUSIONS

Mouse skin damage using a kHz plasma jet is highly dependent on gas selection and jet inclination, which also influences direct and indirect skin damage. This damage relates to immediate effects and skin penetration or additional subsequent effects after 48 h when RONS species diffuse into the skin. The extend of damages is larger for argon than helium gas, which is attributed to much greater skin heating and production of ROS. The damage was so severe that any further *in vivo* experiments with argon plasma were discontinued. Surprisingly, even changing the jet inclination from 90° to 45° increased skin damage by 2–14 times, which was attributed to the larger surface area in contact with the plasma.

For this reason, the subsequent experiments to control damages were conducted only with helium plasma treatment. Damage control was explored via three different approaches: adding a liquid interface, adding nitrogen into the gas flow, and regulating flow dynamics with a funnel.

Liquids tested on the skin treatment site were ethanol, PBS, acetic acid, and saline. The application of ethanol gave the best result, with more than two times less skin damage compared to treatment without liquid, whereas other media contributed to even more severe damages. Beneficial skin damage mitigation effects via ethanol application have been attributed to ethanol's cooling effect and low electrical conductivity. The 6% addition of nitrogen to helium gas resulted in even better damage mitigation – more than four times less damage than direct helium plasma skin treatment. Finally, limiting the ambient gas surrounding interaction with the plasma plume by adding a funnel at the end of the jet's glass tube reduced damage by more than five times compared to the lone helium plasma jet treatment. This was due to reduced oxygen content and lower production of ROS, which reduced the plasma's negative impact on the mouse skin.

These results describe several promising routes to reducing skin damage caused by plasma jets, and by further developing the reported approaches could help in designing safer plasma skin treatments in clinical settings.

SUPPLEMENTAL MATERIAL

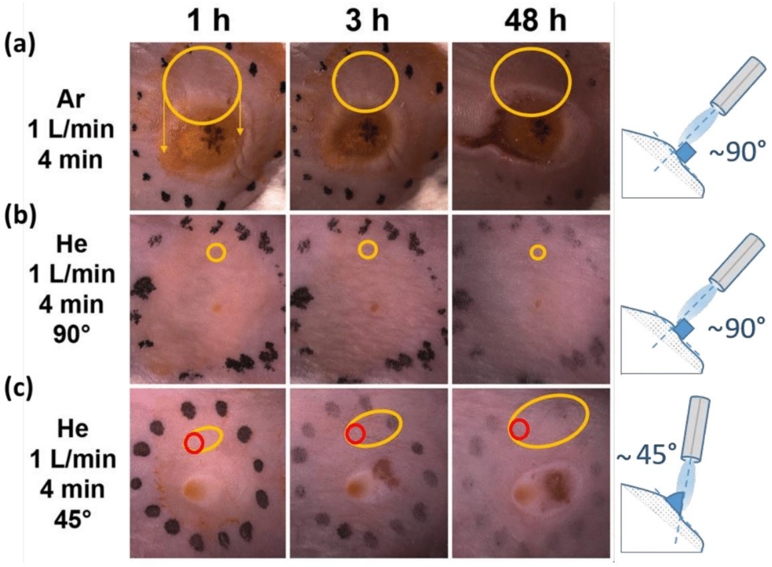

Fig. S1. Photographs of plasma-induced skin damage under different plasma conditions: (a) argon plasma perpendicular to the skin surface, (b) helium plasma perpendicular to the skin surface, and (c) helium plasma with a 45˚ inclination to the skin surface. Pictures contain marked inner damage and outer damage.

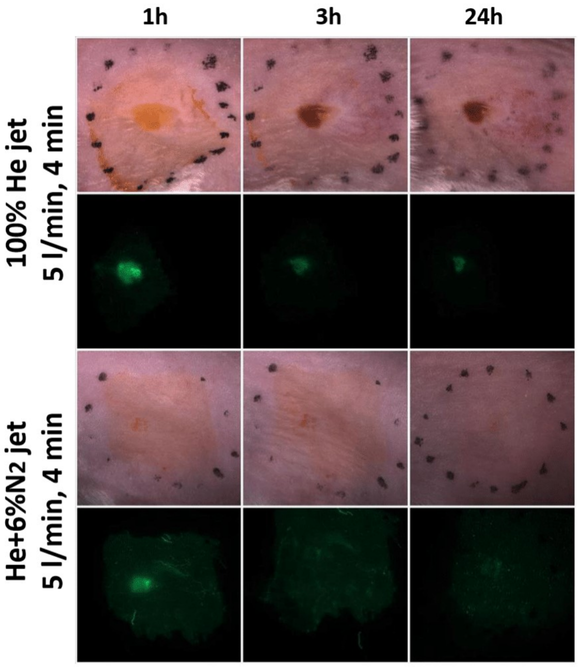

Fig. S2. Optical and fluorescence photographs of skin damage under pure helium plasma and a mixture of helium and 6% nitrogen plasma.

ACKNOWLEDGMENTS

Acknowledge grants and other people who have contributed to the work (other than authors) here. Any funding information provided in your Acknowledgements should also be listed in your manuscript details in the submission system. Under “Manuscript Information”, please click on "Publication Charges and Funding". Enter any funding sources in the "Funding Sources" section. Please be concise. Acknowledgements text should be styled as *AckText.* Acknowledgement title should be styled as *AckHead.*

DATA AVAILABILITY

The data that support the findings of this study are available from the corresponding author upon reasonable request.

REFERENCES

[1] M. Moisan, J. Barbeau, S. Moreau, J. Pelletier, M. Tabrizian, and L. Yahia, Int. J. Pharm. **226**, 1 (2001).

[2] T. Akitsu, H. Ohkawa, M. Tsuji, H. Kimura, and M. Kogoma, Surf. Coatings Technol. **193**, 29 (2005).

[3] M. Laroussi, Plasma Process. Polym. **2**, 391 (2005).

[4] M. Laroussi, IEEE Trans. Plasma Sci. **30**, 1409 (2002).

[5] M. Keidar, A. Shashurin, O. Volotskova, M. Ann Stepp, P. Srinivasan, A. Sandler, and B. Trink, Phys. Plasmas **20**, (2013).

[6] J. Schlegel, J. Köritzer, and V. Boxhammer, Clin. Plasma Med. **1**, 2 (2013).

[7] M.L. Semmler, S. Bekeschus, M. Schäfer, T. Bernhardt, T. Fischer, K. Witzke, C. Seebauer, H. Rebl, E. Grambow, B. Vollmar, J.B. Nebe, H.R. Metelmann, T. von Woedtke, S. Emmert, and L. Boeckmann, Cancers (Basel). **12**, 1 (2020).

[8] M. Keidar, R. Walk, A. Shashurin, P. Srinivasan, A. Sandler, S. Dasgupta, R. Ravi, R. Guerrero-Preston, and B. Trink, Br. J. Cancer **105**, 1295 (2011).

[9] T. von Woedtke, H.-R. Metelmann, and K.-D. Weltmann, Contrib. to Plasma Phys. **54**, 104 (2014).

[10] G. Lloyd, G. Friedman, S. Jafri, G. Schultz, A. Fridman, and K. Harding, Plasma Process. Polym. **7**, 194 (2010).

[11] T. Bernhardt, M.L. Semmler, M. Schäfer, S. Bekeschus, S. Emmert, and L. Boeckmann, Oxid. Med. Cell. Longev. **2019**, (2019).

[12] R.S. Tipa and G.M.W. Kroesen, IEEE Trans. Plasma Sci. **39**, 2978 (2011).

[13] Nasruddin, Y. Nakajima, K. Mukai, H.S.E. Rahayu, M. Nur, T. Ishijima, H. Enomoto, Y. Uesugi, J.

Sugama, and T. Nakatani, Clin. Plasma Med. **2**, 28 (2014).

[14] G. Daeschlein, S. Scholz, R. Ahmed, A. Majumdar, T. von Woedtke, H. Haase, M. Niggemeier, E. Kindel, R. Brandenburg, K.D. Weltmann, and M. Jünger, JDDG J. Der Dtsch. Dermatologischen Gesellschaft **10**, 509 (2012).

[15] T. Bernhardt, M.L. Semmler, M. Schäfer, S. Bekeschus, S. Emmert, and L. Boeckmann, Oxid. Med. Cell. Longev. **2019**, 1 (2019).

[16] A. Shashurin, M. Keidar, S. Bronnikov, R.A. Jurjus, and M.A. Stepp, Appl. Phys. Lett. **93**, 181501 (2008).

[17] B. Kleineidam, M. Nokhbehsaim, J. Deschner, and G. Wahl, Clin. Oral Investig. **23**, 1941 (2019).

[18] J.W. Fluhr, S. Sassning, O. Lademann, M.E. Darvin, S. Schanzer, A. Kramer, H. Richter, W. Sterry, and J. Lademann, Exp. Dermatol. **21**, 130 (2012).

[19] X. Lu, M. Keidar, M. Laroussi, E. Choi, E.J. Szili, and K. Ostrikov, Mater. Sci. Eng. R Reports **138**, 36 (2019).

[20] S. Kos, T. Blagus, M. Cemazar, G. Filipic, G. Sersa, and U. Cvelbar, PLoS One **12**, (2017).

[21] H.M. Joh, S.J. Kim, T.H. Chung, and S.H. Leem, AIP Adv. **3**, (2013).

[22] S. Reuter, T. von Woedtke, and K.-D. Weltmann, J. Phys. D. Appl. Phys. **51**, 233001 (2018).

[23] M. Laroussi and X. Lu, Appl. Phys. Lett. **87**, 113902 (2005).

[24] G. Daeschlein, S. Scholz, R. Ahmed, T. von Woedtke, H. Haase, M. Niggemeier, E. Kindel, R. Brandenburg, K.-D. Weltmann, and M. Juenger, J. Hosp. Infect. **81**, 177 (2012).

[25] E. Stoffels, Contrib. to Plasma Phys. **47**, 40 (2007).

[26] J. Schäfer, F. Sigeneger, J. Šperka, C. Rodenburg, and R. Foest, Plasma Phys. Control. Fusion **60**, 0 (2018).

[27] I. Korolov, M. Leimkühler, M. Böke, Z. Donkó, V. Schulz-Von Der Gathen, L. Bischoff, G. Hübner, P. Hartmann, T. Gans, Y. Liu, T. Mussenbrock, and J. Schulze, J. Phys. D. Appl. Phys. **53**, (2020).

[28] D. Rankovic, M. Kuzmanovic, M.S. Pavlovic, M. Stoiljkovic, and J. Savovic, Plasma Chem. Plasma Process. **35**, 1071 (2015).

[29] J.-P. Sarrette, S. Cousty, F. Clement, C. Canal, and A. Ricard, Plasma Process. Polym. **9**, 576 (2012).

[30] M.H. Qaisrani, Y. Xian, C. Li, X. Pei, M. Ghasemi, and X. Lu, Phys. Plasmas **23**, (2016).

[31] X. Lu, G. V. Naidis, M. Laroussi, S. Reuter, D.B. Graves, and K. Ostrikov, Phys. Rep. **630**, 1 (2016).

[32] M. Schieber and N.S. Chandel, Curr. Biol. **24**, R453 (2014).

[33] B. Haertel, T. von Woedtke, K.D. Weltmann, and U. Lindequist, Biomol. Ther. **22**, 477 (2014).

[34] C. Dunnill, T. Patton, J. Brennan, J. Barrett, M. Dryden, J. Cooke, D. Leaper, and N.T. Georgopoulos, Int. Wound J. **14**, 89 (2017).

[35] S. Reuter, J. Winter, K. Wende, S. Hasse, D. Schroeder, L. Bundscherer, K. Masur, N. Knake, V.S. Der Gathen, and K. Weltmann, Icpig 28 (2011).

[36] S.J. Kim and T.H. Chung, Sci. Rep. **6**, 20332 (2016).

[37] A. Khlyustova, C. Labay, Z. Machala, M.-P. Ginebra, and C. Canal, Front. Chem. Sci. Eng. **13**, 238 (2019).

[38] C. V. Chaparro, L. V. Herrera, A.M. Meléndez, and D.A. Miranda, J. Phys. Conf. Ser. **687**, (2016).

[39] R. Sauerheber and B. Heinz, Chem. Sci. J. **6**, 4 (2016).

[40] T.H.C. Salles, C.B. Lombello, and M.A. D'Ávila, Mater. Res. **18**, 509 (2015).

[41] M. Włodarczyk and W. Zyrnicki, Spectrochim. Acta - Part B At. Spectrosc. **58**, 511 (2003).

[42] Y. Jiang, Y. Wang, S. Cong, J. Zhang, and D. Wang, Phys. Plasmas **27**, (2020).

Chapter 5

Conclusions and Future Outlook

The experimental results presented in this dissertation demonstrate that optical emission spectroscopy (OES) is a convenient multipurpose diagnostic tool for monitoring and controlling atmospheric pressure plasma jet (APPJ) characteristics and processes. OES was chosen for its availability and ease of use. It is especially convenient for monitoring APPJs as their plumes have small volumes and cannot be analyzed by any methods that would induce changes in them. A simple setup is sufficient for analyzing emission spectra before and during experiments along with temperature and density measurements. OES can also be used for identifying spatial and temporal evolutions of specific energetically excited species, which is beneficial for tracking plasma processes during plasma treatments of different materials.

Further discussion regarding the results center on both stated objectives:

Objective 1: Tracking atmospheric pressure plasma jet surface modification

APPJ properties were used for surface modifications of thermally sensitive materials. We presented two different applications – changing surface properties of a polymer in order to prepare it for nanoparticle impregnation and consequently creating a polymer/nanoparticle composite, and modifying surface properties of a carbon nanotube (CNT)-based gas sensor to improve sensing properties. In both surfaces, properties of treated materials were changed but the bulk was left intact, which was supported by spectroscopy. We took emission spectra before the experiments to identify plasma species and parameters while plasma operated in ambient air, and we tracked how emission changed during the treatments. Comparison of two recorded spectra, before and during the experiment, showed that APPJ systems used for these experiments did not have sufficient energy to burst out any or enough (to be detected) volatile degradation products from the treated surfaces. However, spectra changed by intensity, which implied there was an interaction between discharge and the material. This was confirmed by surface analysis conducted on each treated material. Moreover, a detailed analysis of substrates was conducted to see the effect of the plasma treatments.

In the case of CNT-based gas sensors, besides conducting detailed electrical and sensing characterizations, sensor surface morphology and chemical composition were analyzed with scanning electron microscopy (SEM), transmission electron microscopy (TEM), Raman spectroscopy and Fourier-transform infrared spectroscopy (FTIR). We found that plasma treatment did not change surface morphology on the macroscale, but TEM suggested that the treatment led to the removal of amorphous structures from the nanotube surface, which improved crystalline behavior and consequently sensing capabilities. Raman and FTIR analyses confirmed that plasma improved graphitic behavior of the CNTs, which was attributed to plasma-enhanced etching by creating vacancies with the removal of the amorphous carbon.

After gold nanoparticle (AuNP) impregnation into polyvinyl chloride polymer, the polymer/nanoparticle composite's surface morphology was analyzed by atomic force microscopy, SEM and X-ray photoelectron spectroscopy. The results showed that surface morphology and AuNP distribution was highly influenced by the treatment procedure, which was especially noticeable in the changes of surface roughness and wettability after plasma treatment. All analyses confirmed that plasma treatment only affected the polymer's surface and that nanoparticles became embedded into the ripples created by the increased roughness on the surface of the composite.

If OES is used alone for tracking APPJ surface modifications, it can only give information about the changes induced in the gas phase and not the ones induced in the treated surfaces. However, when OES is complemented by a thorough surface morphology analysis, the combined results very well explain the effect plasma has on the surface.

Thesis Objective 1 was addressed, and the goal to track changes in the process of plasma surface modification was achieved in Chapter 3.

Objective 2: Monitoring treatment of biological substrates

One of the important applications of APPJs is studying various effects on biological material, like bacteria, viruses, cells, tissue, etc. Biological systems can be very sophisticated and their interaction with plasma is complex. This makes it important to do all necessary diagnostics and analyses of the power source, plasma gas phase, plasma/substrate interaction and substrate. Plasma treatment of biological matter is an interdisciplinary field and often researchers focus on one aspect of diagnostics while ignoring the complete setup. This makes comparison and consequently interpretation of the results quite difficult. We proposed implementing a standard for plasma diagnostics by means of OES, adding significant value to the research and allowing a better understanding and faster improvement of this field. To support this goal, the results were presented with three different applications – plasma treatment of bacteria, murine fibroblast and mouse skin cells *in vivo*.

APPJ treatment of bacteria was successful and fast in deactivation. Different strands of bacteria were sterilized in under two minutes for most plasma conditions. In order to understand the processes that led to bacteria sterilization, a thorough analysis of every step of the experiment was conducted. Diagnostics of the power source included electrical characterization supported by gas-phase diagnostics that included OES and intensified charged coupled device imaging. The results showed that the used plasma was not energetically strong enough to ionize the volatile components of the treated saline in which the bacteria were suspended. However, liquid-phase diagnostics indicated that the generation of reactive species (hydrogen peroxide, nitrogen dioxide) was dependent on the plasma treatment time and influenced by changes of pH. OES gave an important insight into formation of active species and their influence on the formation of liquid-phase reactive components.

Next, we analyzed mouse skin cell behaviour under APPJ treatment. For this purpose, murine fibroblast cell line L929 was treated with an argon plasma jet. The results showed that the used plasma jet was very aggressive, as short treatment times, from 35 to 60 s, led to cell apoptosis; attributed to the used type of cell lines and to reactive species generated by plasma. Since cells were treated inside culture medium Minimal Essential Medium (MEM), a thorough analysis of the liquid-phase chemistry was conducted. In order to find a connection between gas-phase generation of reactive species and formation of reactive species in the liquid phase, we also conducted detailed gas-phase diagnostics. Spatially resolved OES revealed that excited species from the gas phase are delivered to the cell medium regardless of distance. Time-resolved OES appointed argon as the most important factor in plasma filament formation, with OH and N_2 in secondary roles. All of them influenced formation of reactive species inside the cell medium which, consequently, played a role in cell apoptosis. However, all data implied that the reason behind such plasma aggressiveness toward cells was the plasma characteristics of the argon APPJ that was used for direct cell treatment.

Another example of possible plasma destruction was the effect a plasma jet had on mouse skin tissue when experiments were conducted *in vivo*. Since we found that the used plasma jet induced a lot of skin damages, both primary and secondary, the focus was on understanding processes behind those damages and implementing additional steps that would help reduce them. Monitoring the excited species, we concluded that an argon plasma jet, which induced significantly more damage than a helium plasma jet, has a high production of reactive oxygen species (ROS). Also, argon plasma induces greater skin heating than helium plasma, which proved to be a contributing factor for skin damage. However, it was easily avoided by addition of ethanol on the treatment site, which cooled the skin. Optical diagnostics showed stable plasma with some changes occurring after the mouse skin was breached – more excited species were detected. Again, OES served as a great tool to gain a lot of information on reactive species formation in the gas phase, which helped in understanding how those species interacted with the skin cells.

Thesis Objective 2 was addressed, and the goal to monitor plasma treatments of biological substrates was addressed in Chapter 4.

5.1 Conclusions and Propositions for Future Work

This dissertation hypothesized that OES is an efficient method for monitoring parameters of APPJs generated within inert gases, and can provide all necessary data on plasma parameters and plasma conditions in order to understand physical and chemical processes occurring on surfaces or during depositions. The results and discussions in this dissertation confirmed the hypothesis. OES was identified as a feasible tool for monitoring plasma. OES can give us spatial and temporal evolutions of excited species generated in plasma, help measure temperatures and densities of plasma species, and identify elements involved in plasma/substrate interaction. However, OES has its limitations, and therefore complementary methods should be used in order to gain a full analysis.

For plasma treatments of material surfaces, emission spectroscopy alone was not enough to investigate processes occurring at the plasma/substrate interface. Plasmas used in this part of the dissertation proved to be energetically soft, in regard of surface modifications, and OES did not manage to detect any influence treated material might have on plasma. However, by supplementing gas-phase diagnostics with a comprehensive surface morphology analysis, we managed to understand some of the processes that occurred on the material surface due to the plasma treatment. We confirmed plasma did not influence bulk material properties, only surface modifications were made. Depending on the material, surface modifications included surface functionalization, roughness and wettability alterations, and formation of nanoscale defects.

Monitoring plasma treatments of biological substrates with OES was successfully implemented before and, when possible, during the experiments. Since most biological materials are suspended in a liquid medium, the interaction of plasma and medium is more easily observed than in the case of solid material surface treatments. In these cases, OES seemed more beneficial as it provided us with more information – identification of reactive species, temperature, temporal and spatial evolution of species, gas temperatures, etc. Indubitably, reactive species, especially reactive nitrogen species (RNS), play an important role in biological processes. Since atmospheric pressure plasmas are a great source of RNS, it was essential to investigate their generation. We concluded that reactive species produced in the gas phase were not transferred into the liquid medium, but a secondary formation of reactive species occurred. With a detailed liquid-chemistry analysis, we managed to track the presence of reactive species and their reduction or stability over time. Moreover, biological substrates, bacteria, murine fibroblasts and mouse skin were analyzed with appropriate methods which completed the diagnostics.

To conclude, OES is a great sensoric tool for monitoring processes occurring in various atmospheric presure plasma treatments, but should always be accompanied with appropriate analysis on the treated substrates and additional media used within the treatment process. There are some possibilities to upgrade proposed methods – addition of comparable diagnostics techniques, enhanced versions of OES, merging of known diagnostic techniques, modeling atmospheric pressure plasma processes and many more. The simplest next step would be enhancing OES with optical laser diagnostics, like Raman and Rayleigh scattering, to check and supplement current results and to overcome natural OES limitations. As an extension to the current technique, OES can be upgraded as tomographic optical emission spectroscopy that allows a three-dimensional representation of the non-symmetric plasma jets [77]. Moreover, we could merge OES with Fourier-transform infrared spectroscopy or ultraviolet–visible spectroscopy for *in situ* monitoring of plasma changes. However, the most useful would be to improve the mathematical model of atmospheric pressure plasmas so that it is on par with the model for low-pressure plasmas. This is quite a challenge due to the vast number of parameters influencing plasmas at atmospheric pressure, most of which are influenced by the environment in which those plasmas operate.

References

[1] X. Lu, S. Reuter, M. Laroussi, and D. Liu, *Nonequilibrium Atmospheric Pressure Plasma Jets*, 1st ed. Boca Raton : CRC Press, Taylor & Francis Group, [2019]: CRC Press, 2019.

[2] S. Eliezer and Y. Eliezer, "The fourth state of matter: An introduction to plasma science, second edition," *Fourth State Matter An Introd. to Plasma Sci. Second Ed.*, pp. 1–215, 2001.

[3] J. Winter, R. Brandenburg, and K. D. Weltmann, "Atmospheric pressure plasma jets: An overview of devices and new directions," *Plasma Sources Science and Technology*, vol. 24, no. 6. 2015, doi: 10.1088/0963-0252/24/6/064001.

[4] V. N. Ochkin, *Spectroscopy of Low Temperature Plasma.* Wiley, 2009.

[5] A. Grill, *Cold Plasma Materials Fabrication: From Fundamentals to Applications.* IEEE, 1994.

[6] P. J. Bruggeman, F. Iza, and R. Brandenburg, "Foundations of atmospheric pressure non-equilibrium plasmas," *Plasma Sources Sci. Technol.*, vol. 26, no. 12, p. 123002, Nov. 2017, doi: 10.1088/1361-6595/aa97af.

[7] B. Surowsky, O. Schlüter, and D. Knorr, "Interactions of Non-Thermal Atmospheric Pressure Plasma with Solid and Liquid Food Systems: A Review," *Food Eng. Rev.*, vol. 7, no. 2, pp. 82–108, Jun. 2015, doi: 10.1007/s12393-014-9088-5.

[8] M. Šimek and T. Homola, "Plasma-assisted agriculture: history, presence, and prospects—a review," *Eur. Phys. J. D*, vol. 75, no. 7, p. 210, Jul. 2021, doi: 10.1140/epjd/s10053-021-00206-4.

[9] M. Ito, T. Ohta, and M. Hori, "Plasma agriculture," *J. Korean Phys. Soc.*, vol. 60, no. 6, pp. 937–943, Mar. 2012, doi: 10.3938/jkps.60.937.

[10] N. Puač, M. Gherardi, and M. Shiratani, "Plasma agriculture: A rapidly emerging field," *Plasma Process. Polym.*, vol. 15, no. 2, p. 1700174, Feb. 2018, doi: 10.1002/ppap.201700174.

[11] M. Ito, J.-S. Oh, T. Ohta, M. Shiratani, and M. Hori, "Current status and future prospects of agricultural applications using atmospheric-pressure plasma technologies," *Plasma Process. Polym.*, vol. 15, no. 2, p. 1700073, Feb. 2018, doi: 10.1002/ppap.201700073.

[12] N. Hojnik, U. Cvelbar, G. Tavčar-Kalcher, J. Walsh, and I. Križaj, "Mycotoxin Decontamination of Food: Cold Atmospheric Pressure Plasma versus 'Classic' Decontamination," *Toxins (Basel).*, vol. 9, no. 5, p. 151, Apr. 2017, doi: 10.3390/toxins9050151.

[13] R. Múgica-Vidal *et al.*, "Production of Antibacterial Coatings Through Atmospheric

Pressure Plasma: a Promising Alternative for Combatting Biofilms in the Food Industry," *Food Bioprocess Technol.*, vol. 12, no. 8, pp. 1251–1263, Aug. 2019, doi: 10.1007/s11947-019-02293-z.

[14] U. Cvelbar *et al.*, "White paper on the future of plasma science and technology in plastics and textiles," *Plasma Process. Polym.*, vol. 16, no. 1, p. 1700228, Jan. 2019, doi: 10.1002/ppap.201700228.

[15] D. Mariotti and R. M. Sankaran, "Perspectives on atmospheric-pressure plasmas for nanofabrication," *J. Phys. D. Appl. Phys.*, vol. 44, no. 17, p. 174023, May 2011, doi: 10.1088/0022-3727/44/17/174023.

[16] D. Mariotti, J. Patel, V. Švrček, and P. Maguire, "Plasma-liquid interactions at atmospheric pressure for nanomaterials synthesis and surface engineering," *Plasma Process. Polym.*, vol. 9, no. 11–12, pp. 1074–1085, 2012, doi: 10.1002/ppap.201200007.

[17] S. E. Babayan, J. Y. Jeong, V. J. Tu, J. Park, G. S. Selwyn, and R. F. Hicks, "Deposition of silicon dioxide films with an atmospheric-pressure plasma jet," *Plasma Sources Sci. Technol.*, vol. 7, no. 3, pp. 286–288, Aug. 1998, doi: 10.1088/0963-0252/7/3/006.

[18] F. Massines, C. Sarra-Bournet, F. Fanelli, N. Naudé, and N. Gherardi, "Atmospheric Pressure Low Temperature Direct Plasma Technology: Status and Challenges for Thin Film Deposition," *Plasma Process. Polym.*, vol. 9, no. 11–12, pp. 1041–1073, Dec. 2012, doi: 10.1002/ppap.201200029.

[19] O. V. Penkov, M. Khadem, W.-S. Lim, and D.-E. Kim, "A review of recent applications of atmospheric pressure plasma jets for materials processing," *J. Coatings Technol. Res.*, vol. 12, no. 2, pp. 225–235, Mar. 2015, doi: 10.1007/s11998-014-9638-z.

[20] U. Kogelschatz, "Atmospheric-pressure plasma technology," *Plasma Phys. Control. Fusion*, vol. 46, no. 12B, pp. B63–B75, Dec. 2004, doi: 10.1088/0741-3335/46/12B/006.

[21] Xinpei Lu *et al.*, "An RC Plasma Device for Sterilization of Root Canal of Teeth," *IEEE Trans. Plasma Sci.*, vol. 37, no. 5, pp. 668–673, May 2009, doi: 10.1109/TPS.2009.2015454.

[22] E. Stoffels, I. E. Kieft, and R. E. J. Sladek, "Superficial treatment of mammalian cells using plasma needle," *J. Phys. D. Appl. Phys.*, vol. 36, no. 23, pp. 2908–2913, Dec. 2003, doi: 10.1088/0022-3727/36/23/007.

[23] Q. Xiong *et al.*, "Inactivation by helium cold atmospheric pressure plasma for Escherichia coli and Staphylococcus aureus," *J. Phys. D. Appl. Phys.*, vol. 10, no. 1, pp. 1–11, 2020, doi: 10.1038/s41598-020-59652-6.

[24] M. Laroussi, "Plasma Medicine: A Brief Introduction," *Plasma*, vol. 1, no. 1, pp. 47–60, 2018, doi: 10.3390/plasma1010005.

[25] K.-D. Weltmann and T. von Woedtke, "Plasma medicine—current state of research and medical application," *Plasma Phys. Control. Fusion*, vol. 59, no. 1, p. 014031, Jan. 2017, doi: 10.1088/0741-3335/59/1/014031.

[26] K. D. Weltmann, E. Kindel, T. von Woedtke, M. Hähnel, M. Stieber, and R. Brandenburg, "Atmospheric-pressure plasma sources: Prospective tools for plasma

medicine," *Pure Appl. Chem.*, vol. 82, no. 6, pp. 1223–1237, Apr. 2010, doi: 10.1351/PAC-CON-09-10-35.

[27] X. Lu, M. Laroussi, and V. Puech, "On atmospheric-pressure non-equilibrium plasma jets and plasma bullets," *Plasma Sources Sci. Technol.*, vol. 21, no. 3, 2012, doi: 10.1088/0963-0252/21/3/034005.

[28] J. Y. Jeong *et al.*, "Etching materials with an atmospheric-pressure plasma jet," *Plasma Sources Sci. Technol.*, vol. 7, no. 3, pp. 282–285, Aug. 1998, doi: 10.1088/0963-0252/7/3/005.

[29] J. L. Walsh and M. G. Kong, "Contrasting characteristics of linear-field and cross-field atmospheric plasma jets," *Appl. Phys. Lett.*, vol. 93, no. 11, p. 111501, Sep. 2008, doi: 10.1063/1.2982497.

[30] M. Teschke, J. Kedzierski, E. G. Finantu-Dinu, D. Korzec, and J. Engemann, "High-speed photographs of a dielectric barrier atmospheric pressure plasma jet," *IEEE Trans. Plasma Sci.*, vol. 33, no. 2, pp. 310–311, Apr. 2005, doi: 10.1109/TPS.2005.845377.

[31] Q. Li, J.-T. Li, W.-C. Zhu, X.-M. Zhu, and Y.-K. Pu, "Effects of gas flow rate on the length of atmospheric pressure nonequilibrium plasma jets," *Appl. Phys. Lett.*, vol. 95, no. 14, p. 141502, Oct. 2009, doi: 10.1063/1.3243460.

[32] X. Lu, Z. Jiang, Q. Xiong, Z. Tang, X. Hu, and Y. Pan, "An 11cm long atmospheric pressure cold plasma plume for applications of plasma medicine," *Appl. Phys. Lett.*, vol. 92, no. 8, p. 081502, Feb. 2008, doi: 10.1063/1.2883945.

[33] A. Shashurin, M. N. Shneider, A. Dogariu, R. B. Miles, and M. Keidar, "Temporal behavior of cold atmospheric plasma jet," *Appl. Phys. Lett.*, vol. 94, no. 23, p. 231504, Jun. 2009, doi: 10.1063/1.3153143.

[34] V. Léveillé and S. Coulombe, "Design and preliminary characterization of a miniature pulsed RF APGD torch with downstream injection of the source of reactive species," *Plasma Sources Sci. Technol.*, vol. 14, no. 3, pp. 467–476, Aug. 2005, doi: 10.1088/0963-0252/14/3/008.

[35] U. Fantz, "Basics of plasma spectroscopy," *Plasma Sources Sci. Technol.*, vol. 15, no. 4, 2006, doi: 10.1088/0963-0252/15/4/S01.

[36] Hans-Joachim Kunze, *Introduction to Plasma Spectroscopy*, vol. 19. Springer Heidelberg, 1991.

[37] S. Park, W. Choe, S. Youn Moon, and J. Park, "Electron density and temperature measurement by continuum radiation emitted from weakly ionized atmospheric pressure plasmas," *Appl. Phys. Lett.*, vol. 104, no. 8, p. 084103, Feb. 2014, doi: 10.1063/1.4866804.

[38] S. Park, W. Choe, H. Kim, and J. Y. Park, "Continuum emission-based electron diagnostics for atmospheric pressure plasmas and characteristics of nanosecond-pulsed argon plasma jets," *Plasma Sources Sci. Technol.*, vol. 24, no. 3, p. 034003, Apr. 2015, doi: 10.1088/0963-0252/24/3/034003.

[39] J. M. Williamson and C. A. DeJoseph, "Determination of gas temperature in an open-air atmospheric pressure plasma torch from resolved plasma emission," *J. Appl. Phys.*, vol. 93, no. 4, pp. 1893–1898, Feb. 2003, doi: 10.1063/1.1536736.

[40] S. Alexiou, "Overview of plasma line broadening," *High Energy Density Physics*,

vol. 5, no. 4. pp. 225–233, 2009, doi: 10.1016/j.hedp.2009.06.003.

[41] J. Muñoz, M. S. Dimitrijević, C. Yubero, and M. D. Calzada, “Using the van der Waals broadening of spectral atomic lines to measure the gas temperature of an argon-helium microwave plasma at atmospheric pressure,” *Spectrochimica Acta - Part B Atomic Spectroscopy*, vol. 64, no. 2. pp. 167–172, 2009, doi: 10.1016/j.sab.2008.11.006.

[42] M. Christova, E. Castanos-Martinez, M. D. Calzada, Y. Kabouzi, J. M. Luque, and M. Moisan, “Electron density and gas temperature from line broadening in an argon surface-wave-sustained discharge at atmospheric pressure,” *Applied Spectroscopy*, vol. 58, no. 9. pp. 1032–1037, 2004, doi: 10.1366/0003702041959415.

[43] L. Dong, J. Ran, and Z. Mao, “Direct measurement of electron density in microdischarge at atmospheric pressure by Stark broadening,” *Appl. Phys. Lett.*, vol. 86, no. 16, p. 161501, Apr. 2005, doi: 10.1063/1.1906299.

[44] A. Y. Nikiforov, C. Leys, M. A. Gonzalez, and J. L. Walsh, “Electron density measurement in atmospheric pressure plasma jets: Stark broadening of hydrogenated and non-hydrogenated lines,” *Plasma Sources Sci. Technol.*, vol. 24, no. 3, p. 034001, Apr. 2015, doi: 10.1088/0963-0252/24/3/034001.

[45] C. Yubero, M. D. Calzada, and M. C. Garcia, “Using the Stark Broadening of the H α , H β and H γ Lines for the Measurement of Electron Density and Temperature in a Plasma at Atmospheric Pressure,” *J. Phys. Soc. Japan*, vol. 74, no. 8, pp. 2249–2254, Aug. 2005, doi: 10.1143/JPSJ.74.2249.

[46] M. Qian, C. Ren, D. Wang, J. Zhang, and G. Wei, “Stark broadening measurement of the electron density in an atmospheric pressure argon plasma jet with double-power electrodes,” *J. Appl. Phys.*, vol. 107, no. 6, p. 063303, Mar. 2010, doi: 10.1063/1.3330717.

[47] R. Engeln, B. Klarenaar, and O. Guaitella, “Foundations of optical diagnostics in low-temperature plasmas,” *Plasma Sources Science and Technology*, vol. 29, no. 6. 2020, doi: 10.1088/1361-6595/ab6880.

[48] R. B. Miles, W. R. Lempert, and J. N. Forkey, “Laser Rayleigh scattering,” *Meas. Sci. Technol.*, vol. 12, no. 5, pp. R33–R51, May 2001, doi: 10.1088/0957-0233/12/5/201.

[49] I. Sremački *et al.*, “On diagnostics of annular-shape radio-frequency plasma jet operating in argon in atmospheric conditions,” *Plasma Sources Sci. Technol.*, vol. 29, no. 3, p. 035027, Mar. 2020, doi: 10.1088/1361-6595/ab71f7.

[50] J. M. de Regt, F. P. J. de Groote, J. A. M. van der Mullen, and D. C. Schram, “Air entrainment in an inductively coupled plasma measured by Raman and Rayleigh scattering,” *Spectrochim. Acta Part B At. Spectrosc.*, vol. 51, no. 12, pp. 1527–1534, Oct. 1996, doi: 10.1016/0584-8547(96)01519-4.

[51] P. J. Bruggeman, N. Sadeghi, D. C. Schram, and V. Linss, “Gas temperature determination from rotational lines in non-equilibrium plasmas: A review,” *Plasma Sources Science and Technology*, vol. 23, no. 2. 2014, doi: 10.1088/0963-0252/23/2/023001.

[52] “Specair.” [Online]. Available: http://www.specair-radiation.net/.

[53] “Lifbase.” [Online]. Available: https://www.sri.com/case-studies/lifbase-

spectroscopy-tool/.

[54] J. Voráč, P. Synek, L. Potočňáková, J. Hnilica, and V. Kudrle, “Batch processing of overlapping molecular spectra as a tool for spatio-temporal diagnostics of power modulated microwave plasma jet,” *Plasma Sources Sci. Technol.*, vol. 26, no. 2, p. 025010, Jan. 2017, doi: 10.1088/1361-6595/aa51f0.

[55] S. Hofmann, A. F. H. van Gessel, T. Verreycken, and P. Bruggeman, “Power dissipation, gas temperatures and electron densities of cold atmospheric pressure helium and argon RF plasma jets,” *Plasma Sources Sci. Technol.*, vol. 20, no. 6, p. 065010, Dec. 2011, doi: 10.1088/0963-0252/20/6/065010.

[56] A. F. H. van Gessel, E. A. D. Carbone, P. J. Bruggeman, and J. J. A. M. van der Mullen, “Laser scattering on an atmospheric pressure plasma jet: disentangling Rayleigh, Raman and Thomson scattering,” *Plasma Sources Sci. Technol.*, vol. 21, no. 1, p. 015003, Feb. 2012, doi: 10.1088/0963-0252/21/1/015003.

[57] T. Verreycken, A. F. H. van Gessel, A. Pageau, and P. Bruggeman, “Validation of gas temperature measurements by OES in an atmospheric air glow discharge with water electrode using Rayleigh scattering,” *Plasma Sources Sci. Technol.*, vol. 20, no. 2, p. 024002, Apr. 2011, doi: 10.1088/0963-0252/20/2/024002.

[58] M. R. Wertheimer, M. Ahlawat, B. Saoudi, and R. Kashyap, “Accurate in-situ gas temperature measurements in dielectric barrier discharges at atmospheric pressure,” *Appl. Phys. Lett.*, vol. 100, no. 20, p. 201112, May 2012, doi: 10.1063/1.4719208.

[59] H. Kersten, H. Deutsch, M. Otte, G. H. P. . Swinkels, and G. M. . Kroesen, “Micro-disperse particles as probes for plasma surface interaction,” *Thin Solid Films*, vol. 377–378, pp. 530–536, Dec. 2000, doi: 10.1016/S0040-6090(00)01439-5.

[60] K. G. Xu and S. J. Doyle, “Measurement of atmospheric pressure microplasma jet with Langmuir probes,” *Journal of Vacuum Science & Technology A: Vacuum, Surfaces, and Films*, vol. 34, no. 5. p. 051301, 2016, doi: 10.1116/1.4959565.

[61] G. Trenchev, S. Kolev, and Z. Kiss’ovski, “Modeling a Langmuir probe in atmospheric pressure plasma at different EEDFs,” *Plasma Sources Sci. Technol.*, vol. 26, no. 5, p. 055013, Apr. 2017, doi: 10.1088/1361-6595/aa63c2.

[62] L. Prevosto, H. Kelly, and B. R. Mancinelli, “Langmuir probe diagnostics of an atmospheric pressure, vortex–stabilized nitrogen plasma jet,” *J. Appl. Phys.*, vol. 112, no. 6, p. 063302, Sep. 2012, doi: 10.1063/1.4752886.

[63] J. J. Narendra, T. A. Grotjohn, and J. Asmussen, “Microstripline applicators for creating microplasma discharges with microwave energy,” *Plasma Sources Sci. Technol.*, vol. 17, no. 3, p. 035027, Aug. 2008, doi: 10.1088/0963-0252/17/3/035027.

[64] A. Shashurin, J. Li, T. Zhuang, M. Keidar, and I. I. Beilis, “Application of electrostatic Langmuir probe to atmospheric arc plasmas producing nanostructures,” *Phys. Plasmas*, vol. 18, no. 7, p. 073505, Jul. 2011, doi: 10.1063/1.3614538.

[65] H. Onishi, F. Yamazaki, Y. Hakozaki, M. Takemura, A. Nezu, and H. Akatsuka, “Measurement of electron temperature and density of atmospheric-pressure non-equilibrium argon plasma examined with optical emission spectroscopy,” *Jpn. J. Appl. Phys.*, vol. 60, no. 2, p. 026002, Feb. 2021, doi: 10.35848/1347-4065/abd0c8.

[66] H. Akatsuka, “Optical Emission Spectroscopic (OES) analysis for diagnostics of electron density and temperature in non-equilibrium argon plasma based on

collisional-radiative model," *Adv. Phys. X*, vol. 4, no. 1, p. 1592707, Jan. 2019, doi: 10.1080/23746149.2019.1592707.

[67] J. H. Kim, Y. H. Choi, and Y. S. Hwang, "Electron density and temperature measurement method by using emission spectroscopy in atmospheric pressure nonequilibrium nitrogen plasmas," *Physics of Plasmas*, vol. 13, no. 9. 2006, doi: 10.1063/1.2338282.

[68] X.-M. Zhu, J. L. Walsh, W.-C. Chen, and Y.-K. Pu, "Measurement of the temporal evolution of electron density in a nanosecond pulsed argon microplasma: using both Stark broadening and an OES line-ratio method," *J. Phys. D. Appl. Phys.*, vol. 45, no. 29, p. 295201, Jul. 2012, doi: 10.1088/0022-3727/45/29/295201.

[69] X. M. Zhu, Y. K. Pu, N. Balcon, and R. Boswell, "Measurement of the electron density in atmospheric-pressure low-temperature argon discharges by line-ratio method of optical emission spectroscopy," *J. Phys. D. Appl. Phys.*, vol. 42, no. 14, p. 142003, Jul. 2009, doi: 10.1088/0022-3727/42/14/142003.

[70] R. F. G. Meulenbroeks, M. F. M. Steenbakkers, Z. Qing, M. C. M. Van De Sanden, and D. C. Schram, "Four ways to determine the electron density in low-temperature plasmas," *Physical Review E*, vol. 49, no. 3. pp. 2272–2275, 1994, doi: 10.1103/PhysRevE.49.2272.

[71] E. Iordanova, N. de Vries, M. Guillemier, and J. J. A. M. van der Mullen, "Absolute measurements of the continuum radiation to determine the electron density in a microwave-induced argon plasma," *J. Phys. D. Appl. Phys.*, vol. 41, no. 1, p. 015208, Jan. 2008, doi: 10.1088/0022-3727/41/1/015208.

[72] R. F. Boivin, J. L. Kline, and E. E. Scime, "Electron temperature measurement by a helium line intensity ratio method in helicon plasmas," *Phys. Plasmas*, vol. 8, no. 12, pp. 5303–5314, Dec. 2001, doi: 10.1063/1.1418020.

[73] R. Mewe, "Relative intensity of helium spectral lines as a function of electron temperature and density," *Br. J. Appl. Phys.*, vol. 18, no. 1, pp. 107–118, Jan. 1967, doi: 10.1088/0508-3443/18/1/315.

[74] T. Fujimoto, "A collisional-radiative model for helium and its application to a discharge plasma," *J. Quant. Spectrosc. Radiat. Transf.*, vol. 21, no. 5, pp. 439–455, May 1979, doi: 10.1016/0022-4073(79)90004-9.

[75] A. Bogaerts, R. Gijbels, and J. Vlcek, "Collisional-radiative model for an argon glow discharge," *J. Appl. Phys.*, vol. 84, no. 1, pp. 121–136, Jul. 1998, doi: 10.1063/1.368009.

[76] X.-M. Zhu and Y.-K. Pu, "A simple collisional–radiative model for low-temperature argon discharges with pressure ranging from 1 Pa to atmospheric pressure: kinetics of Paschen 1s and 2p levels," *J. Phys. D. Appl. Phys.*, vol. 43, no. 1, p. 015204, Jan. 2010, doi: 10.1088/0022-3727/43/1/015204.

[77] T. Hermann, S. Löhle, S. Fasoulas, and A. Andrianatos, "Tomographic optical emission spectroscopy of a high enthalpy air plasma flow," *Appl. Opt.*, vol. 55, no. 36, p. 10290, Dec. 2016, doi: 10.1364/AO.55.010290.

Bibliography

Journal Articles

Andrea Jurov, Špela Kos, Nataša Hojnik, Ivana Sremački, Anton Nikiforov, Christophe Leys, Gregor Serša, Uroš Cvelbar, "Analysing Mouse Skin Cell Behaviour under a Non-Thermal kHz Plasma Jet," *Appl. Sci.*, vol. 11, no. 3, p. 1266, Jan. 2021, doi: 10.3390/app11031266.

Ivana Sremački, Špela Kos, Maša Bošnjak, Andrea Jurov, Gregor Serša, Martina Modic, Christophe Leys, Uroš Cvelbar, Anton Nikiforov, "Plasma Damage Control: From Biomolecules to Cells and Skin," *ACS Appl. Mater. Interfaces*, vol. 13, no. 39, pp. 46303–46316, Oct. 2021, doi: 10.1021/acsami.1c12232.

Kinga Kutasi, Nikša Krstulović, Andrea Jurov, Krešimir Salamon, Dean Popović, Slobodan Milošević, "Controlling: the composition of plasma-activated water by Cu ions," *Plasma Sources Sci. Technol.*, vol. 30, no. 4, p. 045015, Apr. 2021, doi: 10.1088/1361-6595/abf078.

Nataša Hojnik, Martina Modic, Dušan Žigon, Janez Kovač, Andrea Jurov, Aaron Dickenson, James L. Walsh, Uroš Cvelbar, "Cold atmospheric pressure plasma-assisted removal of aflatoxin B 1 from contaminated corn kernels," *Plasma Process. Polym.*, vol. 18, no. 1, p. 2000163, Jan. 2021, doi: 10.1002/ppap.202000163.

Damjan Blažeka, Julio Car, Nikola Klobučar, Andrea Jurov, Janez Zavašnik, Andrea Jagodar, Eva Kovačević, Nikša Krstulović, "Photodegradation of Methylene Blue and Rhodamine B Using Laser-Synthesized ZnO Nanoparticles," *Materials (Basel).*, vol. 13, no. 19, p. 4357, Sep. 2020, doi: 10.3390/ma13194357.

Neelakandan M. Santhosh, Aswathy Vasudevan, Andrea Jurov, Gregor Filipič, Janez Zavašnik, Uroš Cvelbar, "Oriented Carbon Nanostructures from Plasma Reformed Resorcinol-Formaldehyde Polymer Gels for Gas Sensor Applications," *Nanomaterials*, vol. 10, no. 9, p. 1704, Aug. 2020, doi: 10.3390/nano10091704.

Ivana Sremački, Andrea Jurov, Martina Modic, Uroš Cvelbar, Lei Wang, Christophe Leys, Anton Nikiforov, "On diagnostics of annular-shape radio-frequency plasma jet operating in argon in atmospheric conditions," *Plasma Sources Sci. Technol.*, vol. 29, no. 3, p. 035027, Mar. 2020, doi: 10.1088/1361-6595/ab71f7.

Andrea Jurov, Dean Popović, Iva Šrut Rakić, Ida Delač Marion, Gregor Filipič, Janez Kovač, Uroš Cvelbar, Nikša Krstulović, "Atmospheric pressure plasma jet–assisted impregnation of gold nanoparticles into PVC polymer for various applications," *Int. J. Adv. Manuf. Technol.*, vol. 101, no. 1–4, pp. 927–938, Mar. 2019, doi: 10.1007/s00170-018-2988-4.

Uroš Cvelbar, James L. Walsh, …, Andrea Jurov, … , Klaus-Dieter Weltmann, "White paper on the future of plasma science and technology in plastics and textiles," *Plasma Process. Polym.*, vol. 16, no. 1, p. 1700228, Jan. 2019, doi: 10.1002/ppap.201700228.

Werner Schlemmer, Wolfgang Fischer, Armin Zankel, Tomislava Vukušić, Gregor Filipič, Andrea Jurov, Damjan Blažeka, Walter Goessler, Wolfgang Bauer, Stefan Spirk, Nikša Krstulović, "Green Procedure to Manufacture Nanoparticle-Decorated Paper Substrates," *Materials (Basel).*, vol. 11, no. 12, p. 2412, Nov. 2018, doi: 10.3390/ma11122412.

Andrea Jurov, Špela Kos, Tanja Blagus, Ivana Sremački, Gregor Filipič, Nataša Hojnik, Anton Nikiforov, Christophe Leys, Maja Čemažar, Gregor Serša, Uroš Cvelbar, "Atmospheric pressure plasma jet-mouse skin interaction: mitigation of damages by liquid interface and gas flow control," *Biointerphases*, 2021 (Under revision)

Andrea Jurov, Nikola Škoro, Kosta Spasić, Martina Modic, Nataša Hojnik, Danijela Vujošević, Vineta Vukasinović, Milena Đurović, Zoran Lj. Petrović, Uroš Cvelbar, "Helium atmospheric pressure plasma jet parameters and their influence on deactivation of bacteria in medium," *European Physical Journal D*, 2021 (Submitted)

Published Scientific Conference Contribution

Ivana Sremački, Lei Wang, Andrea Jurov, Martina Modic, Uroš Cvelbar, Christophe Leys, Anton Nikiforov. Radio-frequency plasma in combination with aerosol injection for biomedical applications. In: Final program. ISCP24, 24th International Symposium on Plasma Chemistry, 9–14 June, 2019, Naples (Italy). Antwerp: Universitet Antwerpen, 2019.

Andrea Jurov, Uroš Cvelbar, Zoran Lj. Petrović, Nikola Škoro, Kosta Spasić, Martina Modic, Nataša Hojnik,Danijela Vujošević, Vesna Vuksanović, Marina Đurović. Influence of atmospheric pressure plasma jet parameters on decontamination of bacteria. In: Proceedings of the XXIInd International Conference on Gas Discharges and their Applications, 2–7 September 2018, Novi Sad, Serbia. Vol. 2. Belgrade: Serbian Academy of Sciences and Arts: Institute of Physics, University of Belgrade, 2018.

Published Scientific Conference Contribution Abstract (Invited Lecture)

Uroš Cvelbar, Andrea Jurov, Ana Kračun, Gregor Filipič, Branka Mušič, Bojan Podgornik. Plasma-enabled catalytic properties of nanostructures for applications. In: International Workshop on Plasma Synthesis of Nanomaterials and its Applications for Sensor Devices, 11–14 March, 2018, Gifu, Japan. [S. l.: s. n.], 2018.

Uroš Cvelbar, Andrea Jurov, Gregor Filipič. Designing catalytic properties of nanostructures for applications with plasma. In: Miglena Dimitrova (ed.), M. Damyanova (ed.), Chavdar Ghelev (ed.). VEIT 2017: program, abstracts. Twentieth International Summer School on Vacuum, Electron and Ion Technologies, 25–29 September 2017, Sozopol, Bulgaria. Sofia: Institute of Electronics, Bulgarian Academy of Sciences, 2017.

Published Scientific Conference Contribution

Jože Kotnik, Igor Živković, Jan Gačnik, Andrea Jurov, Uroš Cvelbar, Milena Horvat. Novel plasma oxidized mercury source. In: Abstract volume. 14th International Conference on Mercury as a Global Pollutant, ICMGP 2019, 8–13 September 2019, Krakow, Poland. [S. l.: s. n.], 2019.

Andrea Jurov, Nikša Krstulović, Martina Modic, Nataša Hojnik, Anton Nikiforov, Andre Zille, Christophe Leys,Uroš Cvelbar. Plasma-laser assisted synthesis of nanoparticles for antibacterial coatings. In: Luís Lemos Alves (ed.), Antonio Tejero-del-Caz (ed.). ICPIG 2017. XXXIII International Conference on Phenomena in Ionized Gases, Estoril, Portugal, 9–14 July 2017. Lisboa: Instituto de Plasmas e Fusão Nuclear: Instituto Superior Técnico: Universidade de Lisboa, 2017.

Professional Entry in Dictionary, Encyclopaedia or Lexicon

Andrea Jurov, Uroš Cvelbar, Martina Modic, Zoran Lj. Petrović, Nikola Škoro, Kosta Spasić, Nataša Hojnik,Danijela Vujošević, Vesna Vuksanović, Marina Đurović. Optimal atmospheric pressure plasma Jet parameters for bactria sterilization. In: IX. International Conference Plasma Physics and Plasma Technology, Minsk, Belarus, 17–21 September 2018 : contributed papers. [Minsk]: B. I. Stepanov Institute of Physics of the National Academy of Sciences of Belarus, 2018.

Biography

The author of this work graduated from the Department of Physics, Faculty of Science (PMF), University of Zagreb, Croatia, with the thesis entitled »Cold plasma assisted laser synthesis of nanoparticles in liquids and applications« under the supervision of Doc. Dr. Nikša Krstulović. The experimental work for the thesis was conducted at the Institute of Physics, Zagreb, Croatia, where the author continued research for another half a year after graduation. In 2016, she started her doctoral studies at the Jožef Stefan International Postgraduate School (IPS), Ljubljana, Slovenia. At the same time, she became a student representative for the program Sensor Technologies, IPS and remained in that position for the next four years. In the last five years at the Jožef Stefan Insitute, she focused on cold plasma diagnostics, more precisely on optical emission spectroscopy and was trained in techniques such as scanning electron microscopy and ultraviolet–visible spectrometry.

During her time at the Jožef Stefan Institute, she collaborated with many researchers from Slovenia and abroad. She presented her results at many internationally recognized conferences. In addition, she spent a month working at the Department of Applied Physics, Faculty of Engineering and Architecture, Ghent University, Belgium.